Turbulent Combustion Modelling of Fast-Flames and Detonations Using Compressible LEM-LES

by

Brian McN. Maxwell

Thesis submitted to the
Faculty of Graduate and Postdoctoral Studies
In partial fulfillment of the requirements
For the Ph.D. degree in
Mechanical Engineering

Ottawa-Carleton Institute for Mechanical and Aerospace Engineering
Faculty of Engineering
University of Ottawa

Abstract

A novel approach to modelling highly *compressible* and *reactive* flows is formulated to provide high resolution closure of *turbulent*-scale reaction rates in the presence of very rapid transients in pressure and energy. For such flows, treatment of turbulent-micro scales are generally unattainable through traditional modelling techniques. To address this, the modelling strategy developed here is based on the **Linear Eddy Model for Large Eddy Simulation** (LEM-LES); a technique which has only previously been applied to weakly compressible flows. In the current formulation of the Compressible LEM-LES (CLEM-LES), special treatment of the energy balance on the model subgrid is accounted for in order for the model reaction rates to respond accordingly to *strong shocks* and *rapid expansions*, both of which may be present in reactive and supersonic flow fields.

In the current study, the model implemented is verified and validated for various 1D and 2D flow configurations in a compressible Adaptive Mesh Refinement (AMR) framework. In 1D test cases, laminar and turbulent flame speeds and structure have been reproduced. Also, detonation speeds and initiation events are also captured with the model. For 2D model validation, unsteady and turbulent detonation propagation and initiation events, in a narrow channel, are simulated. Both test cases involve premixed methane-oxygen mixture at low pressures. The model is found to capture well the two-dimensional detonation cellular structure, behaviour, and initiation events that are observed in corresponding shock tube experiments. Furthermore, the effect of *turbulent mixing rates* is investigated though a single tuning constant. It was found that by increasing the intensity of turbulent fluctuations present, detonations exhibit larger and more irregular cell structures. Furthermore, the intensity of turbulent fluctuations is found to also have an effect on initiation events.

Acknowledgements

Funding for the work presented in this thesis has been provided by the Ontario Ministry of Training, Colleges and Universities via an Ontario Graduate Scholarship, a CFD Society of Canada Graduate Scholarship, and NSERC through an Alexander Graham Bell Scholarship, the Discovery Grant, and the H2Can strategic network. Further acknowledgement is given to Andrzej Pekalski from Shell for financial support in the later stages of the project. Finally, two academic visits to the University of Leeds, UK, were made possible through additional funding from the University of Ottawa Mobility Scholarship, NSERC Michael Smith Foreign Study Supplement, and also the H2Can strategic network.

The author would like to personally thank his supervisor, Matei Radulescu, for his invaluable guidance, mentorship, discussion, and support throughout the project duration. Additional thanks goes to Sam Falle, at the University of Leeds, and Gary Sharpe, of Blue Dog Ltd. (UK), for their additional mentorship, suggestions, training, and hospitality during the author's academic visits to Leeds. Finally, further acknowledgement goes to the fellow graduate students, at both the University of Ottawa (Department of Mechanical Engineering), and the University of Leeds (Department of Mathematics).

Dedication

This work is dedicated to family, friends, and loved ones, for their patience, support, and understanding.

Table of Contents

List of Tables

List of Figures

Nomenclature

Roman Symbols

A	Pre-exponential factor
b	Finest grid scale
C	Model constant (C_ν, C_ϵ, C_κ, C_λ)
c	Speed of sound
c_p	Specific heat capacity at constant pressure
c_v	Specific heat capacity at constant volume
D	Mass diffusivity
D_a	Damkohler number
D_{CJ}	Detonation Mach number
D_T	Turbulent diffusivity
e	Total specific sensible and kinetic energy per unit mass
E_a	Activation energy
e_T	Total specific energy per unit mass
e_u	Specific internal energy per unit mass
$\dot{F}$	Turbulent stirring source term
f	External force per unit mass
H	Computational domain height
h	Specific enthalpy
I	Identity matrix
k	Heat conductivity
K_a	Karlovitz number

k^{sgs}	Subgrid kinetic energy
L	Reference length scale
l	Eddy size
L_e	Lewis number
m	Mass or mass coordinate
M	Mach number
N	Number of subgrid elements
N_η	Model constant
$\dot{P}$	Subgrid kinetic energy production rate
p	Pressure
P_r	Prandtl number
Q	Heat release
q	Heat flux vector
R	Specific gas constant
R_e	Reynolds number
R^o	Universal gas constant
S_c	Schmidt number
S_L	Laminar flame speed
T	Temperature
t	Time
u, v	Velocity
u_d	Molecular diffusion velocity
V	Volume
W	Molecular weight
X	Mole fraction of reactant
x, y	Cartesian distance coordinate
Y	Mass fraction of reactant

Greek Symbols

α	Heat diffusivity
$\bar{\Delta}$	Filter length scale

δ	Laminar flame width
Δ_H	Hydrodynamic thickness of detonation wave
ϵ	Dissipation rate per unit mass
γ	Ratio of specific heats
η	Kolmogorov scale
κ	Wave number
λ	Stirring event frequency per unit length
$\lambda_{1/2}$	Detonation half reaction length
μ	Dynamic viscosity
ν	Kinematic viscosity
ξ	Exothermicity
$\dot{\omega}$	Reaction rate
Ω	Vorticity
ρ	Density
τ	Stress

Superscripts

$\bar{}$	Spatially averaged quantity
$\dot{}$	Rate form
$'$	Fluctuating quantity
$\hat{}$	Dimensional quantity
^{sgs}	Unclosed subgrid scale term
$\tilde{}$	Favre (mass) averaged quantity
^{T}	Transpose

Subscripts

δ	Inner flame structure scale
D	Detonation quantity
F	Outer flame structure scale
i	Subgrid node number or species index
o	Quiescent reference state
$*$	Pre-compression reference state

s	Shock quantity
t	Turbulent quantity

Acronyms

AMR	Adaptive Mesh Refinement
BC	Boundary Condition
CJ	Chapman-Jouguet
CLEM	Compressible Linear Eddy Model
CPU	Central Processing Unit
DDT	Deflagration to Detonation Transition
DNS	Direct Numerical Simulation
IC	Initial Condition
KH	Kelvin-Helmholtz
LDKM	Localized Dynamic subgrid Kinetic energy Model
LEM	Linear Eddy Model
LES	Large Eddy Simulation
LKM	Localized subgrid Kinetic energy Model
NS	Navier-Stokes
ODE	Ordinary Differential Equation
RANS	Reynolds-Averaged Navier-Stokes
RM	Richtmyer-Meshkov
SCRAMJET	Supersonic Combustion Ramjet
VN	von Neumann
ZND	Zel'dovich-Neumann-Doring

Chapter 1

Introduction

1.1 Motivation

Supersonic combustion research is a fast growing field in engineering as there exists a wide range of practical problems of engineering interest to study, from explosion safety assessment to the development of propulsion technology. In this thesis, the role of turbulent mixing, and the application of a novel modelling technique (Compressible LEM-LES), is under investigation for several compressible turbulent combustion problems that relate to gaseous explosion safety. The present work focuses primarily on the rapid ignition of natural gas mixtures in the presence of strong pressure waves, but is also motivated by rapid ignition of mixtures involving pure-hydrogen and air. Of particular interest are the roles that turbulent mixing of burned and unburned fuel has on the enhancement of combustion rates of compressed gas for potentially dangerous scenarios, such as high speed *deflagration* propagation or *detonation* initiation.

Focus in this particular area of research has become of vital importance in the wake of a number of recent accidents involving compressed gases. Two well publicized incidents, the Fukushima Daiichi nuclear disaster [1] and the Buncefield explosion [2], highlight a major physical fundamental problem, which is not clearly understood; the

Deflagration to Detonation Transition (DDT) phenomenon. For example, the explosion in reactor unit 3 at the Fukushima nuclear power plant, in 2011, was believed to be a detonation involving hydrogen [1], yet it is unclear what specific mechanisms triggered the powerful blast. Also, in 2005, release of hydrocarbon vapours at the Buncefield oil storage depot, England, triggered an explosion much more powerful than anyone had anticipated probable. It has been speculated that detonation occurred as the ensuing reactive wave propagated along a row of trees [3]. It is believed that the presence of obstacles allowed for increased turbulent mixing in the reaction zone and thus gave rise to enhanced combustion rates. To highlight the importance of understanding of turbulent deflagrations and how they may transition to detonation, for the purpose of mitigating further serious accidents, a partial time line of recent explosions involving compressible gases is presented here:

- 13 May 2014: Soma mine disaster involving a buildup of methane (Turkey) [4].
- 31 July 2014: Kaohsiung natural gas explosions below city streets (Taiwan) [5].
- 6 August 2013: Rosario natural gas explosion (Argentina) [6].
- 11 March 2011: Fukushima Daiichi nuclear disaster involving hydrogen (Japan) [1].
- 29 October 2009: Jaipur oil depot fire involving petrol vapour (India) [7].
- 10 August 2008: Sunrise Propane incident (Toronto, Canada) [8].
- 18 November 2007: Zasyadko mine disaster involving methane (Ukraine) [9].
- 11 December 2005: The Buncefield fire involving hydrocarbon vapour (England) [2].
- 25 September 1998: Esso Longford natural gas explosion (Australia) [10].

In order to understand how detonations, or powerful explosions occur on the industrial scale, it is necessary to understand the underlying physics of how flames

accelerate in compressed fluids, how such flames transition to detonation, and the mechanisms by which detonations can sustain propagation. Furthermore, due to the dangerous nature and expense of performing large-scale experiments, efficient numerical strategies must be developed. This is to increase confidence of industrial-scale designs and to ensure public safety. Unfortunately, many flows of practical interest, that are highly turbulent, remain difficult to simulate and resolve, due to the wide range of scales present; from the integral length scales of the problem to the turbulent Kolmogorov and chemical scales [11, 12]. Furthermore, the difficulty of resolving the full spectrum of length scales is compounded by the presence of large flow velocities associated with high Mach numbers (M_a) and Reynolds numbers (R_e). What sets these types of problems apart from traditional low speed turbulent flows is that high M_a flows are highly compressible and involve shock waves, very fast transients, and very high shears for large R_e. To address scale-limitations of the problems described above, and to isolate the specific roles of the turbulent-scale physics, the focus of this thesis is to examine the role of turbulent mixing, numerically, for experiments which address detonation propagation dynamics and initiation events through wave interactions with obstacles of irregular fuel-oxygen mixtures [13–15]. To resolve the turbulent scales of the experiments, simulations are conducted using a state of the art Large Eddy Simulation (LES) approach, as described below. First, a brief review is given in the next section to provide background, and to justify the need to address turbulent mixing in various supersonic combustion problems. Following this review, the specific objectives and outline of this thesis are presented.

1.2 Turbulent Mixing in Supersonic Combustion

In this section, a review of several supersonic combustion experiments is presented in order to provide the necessary background state-of-knowledge, identify the key physics that are believed to influence supersonic combustion behaviour, and to expose difficulties modelling such phenomena. In each problem below, combustion occurs in flow fields that are highly turbulent. Thus, burning rates cannot be described by

laminar theory, unless Direct Numerical Simulation (DNS) is used. Furthermore, the presence of rapid compressions (i.e., shock waves) and expansions further complicate the understanding and predictability of such flows by further introducing and enhancing turbulence through various flow instabilities; namely, but not limited to, the Richtmyer-Meshkov (RM) and Kelvin-Helmholtz (KH) instabilities. Turbulent flows, therefore, become highly unstable, which has implications on burning rates, flow patterns, and ignition behaviour. In all cases presented below, the need to address and understand the role of turbulent mixing in highly compressible and reactive flow fields is highlighted. More specifically, turbulent mixing of unignited gas with burned products, in each case, is believed to influence ignition events, flow patterns, and rate at which burning occurs. Hence, each example below demonstrates a need to model turbulent mixing, in a numerical framework, in order to gain further insight. In addition to a review of physical experiments and their outcomes, a review of state-of-the art modelling approaches, applied to each scenario, is presented. Furthermore, difficulties associated with each modelling attempt are discussed in each subsection. Following this review, a novel solution methodology which addresses current modelling difficulties in supersonic combustion is recommended as a fundamental focus of the thesis, see section 1.3.

1.2.1 Detonation cellular dynamics

To date, it is well known that multi-dimensional detonations exhibit a characteristic *cellular* pattern on their fronts, as they propagate in a reactive medium. This cell pattern is associated with wave interactions whose directions are predominantly transverse to the direction of flow. At each transverse wave collision, whose natural spacing is on the order of 100 reaction-zone lengths [16], a new cell is formed as triple points are reflected from each other. This process is illustrated in Figure 1.1. The *triple-point* is a key feature of detonation waves. It is the location where three-principle shock waves meet: the transverse wave, and also the Mach stem and incident shocks. The two latter are both associated with the front of the wave as indicated in

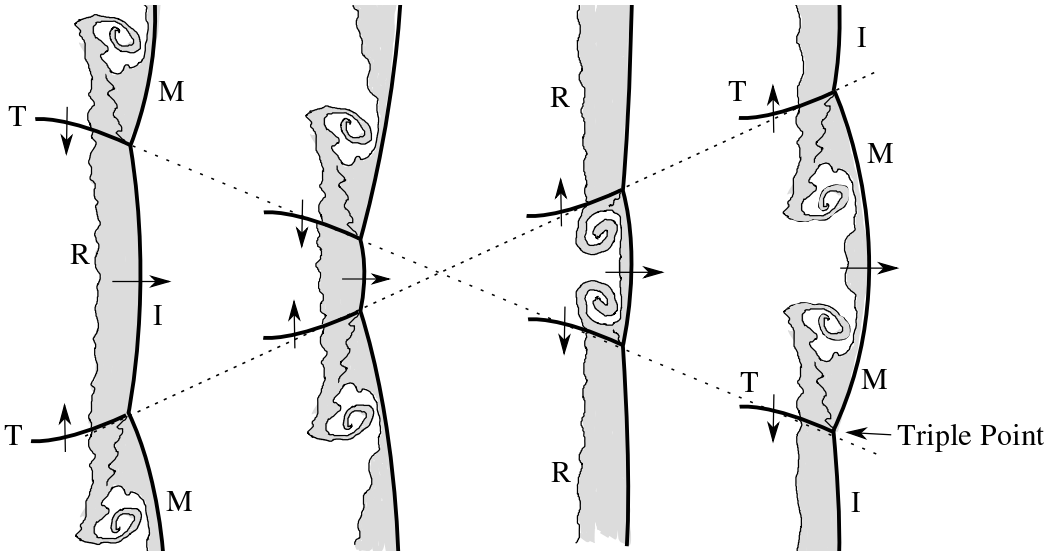

Figure 1.1: Sketch showing a triple point collision process. Various waves indicated are the incident shocks (I), Mach shocks (M), and transverse shocks (T). The extent of the turbulent reaction zones are also shown (R).

the sketch. Furthermore, these wave interactions, or cell patterns, are generally classified as either having a *regular* structure or an *irregular* structure. Figure 1.2 shows soot foils obtained from two different experiments, one showing a regular structure [17] and one irregular [18].

Regular detonation experiments [19–21] exhibit very structured-looking fish-scale patterns with consistent, and repeating, cell sizes. In general, regular detonations are associated with fuel mixtures having low-activation energies [20]. Typical examples are $H_2 + O_2$ (pure hydrogen-oxygen), $C_2H_2 + O_2$ (acetylene-oxygen), or fuel-oxygen mixtures diluted with argon. Owing to the relatively low activation energies, regular mixtures typically have very little variation of ignition delays for the reactive gas mixture which passes through the wave front structure. For this reason, it is generally believed that the principle mechanism which drives the detonation is by shock-compression alone [22]. This was shown to be the case for regular detonations where the structure is well predicted by considering only the ignition delay history of a shocked particle, where transport mechanisms have been neglected [23]. In fact, for an ideal steady wave, the ignition history of a shocked particle would recover the

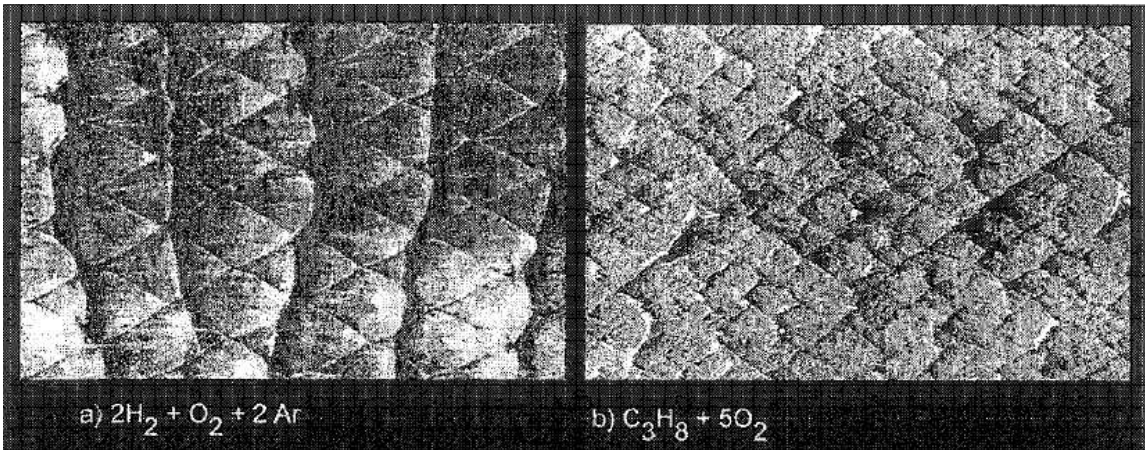

Figure 1.2: Soot-foils showing a) a regular structure in $2H_2 + O_2 + 2Ar$ initially at $\hat{p}_o = 13$kPa [17] and b) an irregular structure in $C_3H_8 + 5O_2$, initially at $\hat{p}_o = 5.6$kPa [18].

Zel'dovich - von Neumann - Doring (ZND) model solution [16]. The ZND model is a useful tool which provides a theoretical laminar and steady-state one-dimensional description of the detonation structure, for a given wave velocity, in terms of the density, pressure, temperature, and reactant profiles behind the leading shock wave. For *irregular* mixtures, many experiments [15, 19, 20, 22, 24, 25] have shown that a very different cell pattern exists. Typically, irregular mixtures are composed of any hydrocarbon fuel with oxygen or some oxidizer. These mixtures tend to exhibit much more stochastic-looking cell structures, as can be seen in Figure 1.2b. The cell sizes are much more variable, and sometimes contain what appears to be cells within cells; a smaller cell structure within a much larger, and more prominent, cell structure. Furthermore, a number of experiments have shown the wave front to be highly turbulent, often giving rise to shocked unburned pockets of reactive fuel in its wake [15, 19, 22, 24, 26]. Another example experiment [27] for an irregular detonation wave, involving methane-oxygen, is shown in Figure 1.3. In this figure, the turbulent structure is illustrated via Schlieren photography [28]. In the same figure, each notable feature is also illustrated and labelled in a supplemental sketch. These features include the various shock wave dynamics, shear layers, and triple points. Of particular interest are the presence of the unburned fuel pockets in the wake, also

shown in the figure, and the fine scale corrugations on their edges due to turbulence.

Owing to higher activation energies, irregular mixtures exhibit a much larger variation of shock-induced ignition delays, for unburned fuel passing through the wave structure, compared to regular detonations. Furthermore, experiments reveal that the pockets of gas in the wake burn up relatively quickly, orders of magnitude faster than expected from steady shock ignition times [22, 27]. As a result, the ZND model does not predict well the structure behind the incident and Mach shocks [22]. This suggests that any unburned pockets in the wake of irregular mixtures burn through turbulent mixing with product gases, and not by shock-compression alone. Currently, it is not yet understood how the burning rate of these pockets affects the cell pattern observed on the wave front, and is a one of the topics investigated in this thesis. One hypothesis proposes that as energy is released from the burning of unreacted fuel mixture pockets, pressure pulses can reach and perturb the leading shock, thus influencing the overall structure to generate new cells [26]. Furthermore, the triple-point appears to play a major role affecting the dynamics of how these pockets burn out. Not only is the triple-point a source of high temperature and pressure, owing to shock-compression from multiple waves, but it is also a source of enhanced turbulent mixing. The triple point has been shown to give rise to a shear layer in its wake that is susceptible to the Kelvin-Helmholtz (KH) instability [29]. This shear layer thus acts to enhance mixing between burned product gases with unburned pockets, and therefore acts to increase reaction rates.

To date, numerical investigations have been able to show that, with sufficient resolution, mildly irregular regular detonation structures are recovered quite well by solving Euler's equations of fluid motion [30–32], which do not account for turbulent mixing or molecular diffusion. More recent numerical investigations, however, have attempted the same approach for modelling highly irregular mixtures, with much higher activation energies, but with limited success [27]. Although such attempts have provided limited insight into the roles that shock compression or turbulent motions may have on detonation propagation, the solutions obtained were subject to changes in resolu-

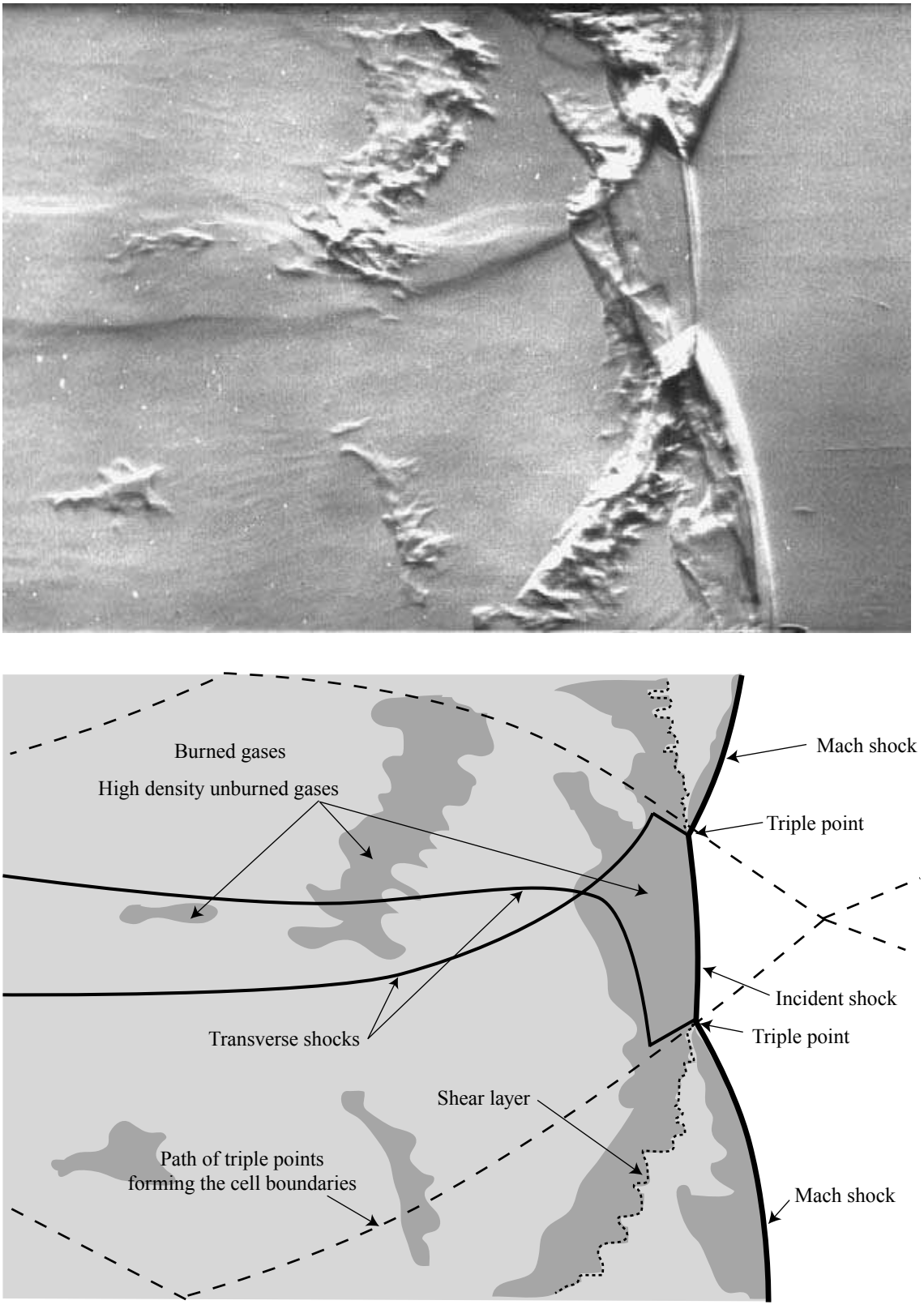

Figure 1.3: Detonation structure for $CH4 + 2O_2$, initially at $\hat{p}_o = 3.4$kPa. The top portion shows a Schlieren photograph while the bottom portion includes a corresponding explanatory sketch. [27]

tion and did not converge to unique solutions [27]. Furthermore, such investigations have confirmed that very long induction times exist, on the order of one hundred times longer than observed experimentally, and that unburned pockets burn out much more rapidly through numerical diffusion. Some recent modelling attempts through Direct Numerical Simulation (DNS) of the Navier-Stokes (N-S) equations address this problem by attempting to resolve the full spectrum of scales present, including molecular diffusion effects. Unfortunately, such investigations [25, 33] have revealed that practically attainable resolutions, in full-scale two-dimensional problems, are insufficient to capture the correct reaction rates of unburned pockets. Thus, full-scale DNS is currently limited to providing insight only on single-isolated events, such as triple point collisions [34]. Furthermore, turbulence inherently contains three-dimensional limitations. It is well known that the dissipation of turbulent motions, the *Kolmogorov energy cascade*, depends intimately on the ability of vortices to stretch in the third dimension. For this reason, two-dimensional flows tend to experience more backscatter, and hence produce larger-scale fluid motions, compared to realistic three-dimensional flows [35–37]. In order to address these fundamental shortcomings associated with Euler simulations or DNS, a reasonable compromise between accuracy of solution and resolvability is to employ Large Eddy Simulation (LES). For LES, the large scale fluid motions, governed by the N-S equations, are solved directly using numerical methods. The unresolved, micro-scale turbulence, is then modelled as a supplement to the large scale numerical solutions. Recent studies have [33, 38] demonstrated that LES can be used to provide insight on the sub-grid turbulent mixing effects that contribute to the highly irregular detonation reaction rate. Full closure to the reaction rate, however, remains difficult as it is typically obtained by assuming either instantaneous mixing or reaction at the subgrid scale. Owing to the difficulties associated with each of these strategies, adequate resolution of the reaction rate of fuel following the wake of a detonation wave remains problematic. All of this previous work clearly highlights the need to isolate and resolve turbulent mixing and combustion rates in mixtures prone to irregular structures.

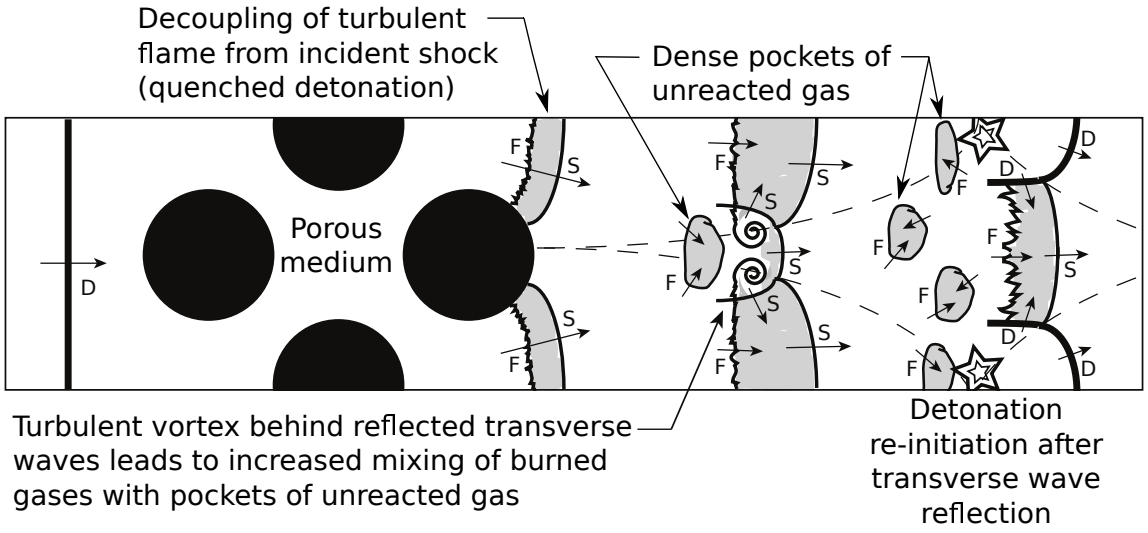

Figure 1.4: Detonation quenching and re-initiation (sketch) (D=detonation wave, S=shock wave, F=turbulent flame, - - - = path of triple point)

1.2.2 Deflagration to detonation transition (DDT) from a porous medium

In a recent attempt to isolate the ignition mechanisms that drive detonation waves, Radulescu and Maxwell [39] examined the re-ignition of fully quenched detonations following the detonation interaction with a porous media, both experimentally and numerically. This type of DDT has also been examined experimentally for detonation interactions with perforated plates [40, 41], or a series of obstacles, or blockages [42, 43]. The process of detonation quenching and re-initiation following its interaction with a porous media is illustrated in Figure 1.4.

The quenching process is currently well understood. As a detonation wave diffracts around an object, such as a sharp corner, or in this case a cylinder, the sudden change in area causes the divergence, or volumetric expansion of the gases behind the leading shock wave. This causes cooling of the gas, which in turn causes a thickening of the reaction zone owing to slower reaction rates. Eventually, the detonation can become quenched when local cooling due to volumetric expansion behind the decaying shock wave overcomes the local heating due to chemical reactions [44–46]. The

result is a de-coupling between the leading shock wave and reaction zone, as observed experimentally by Soloukhin [47], and also by Lundstrom and Oppenheim [48]. The quenched detonation in Figure 1.4 is thus a shock wave followed by a turbulent deflagration. This type of reaction quenching has also been observed numerically for rapidly expanding diffusion layers applied to jet ignition of hydrogen [49].

The mechanisms that drive the re-initiation process, however, remain unclear. To date, it has been found that re-initiation of the detonation wave following its attenuation through a porous medium, occurs through amplification of the incident shock strength resulting from shock reflections or triple point collisions [22, 39]. Furthermore, it has been found that in some cases, several shock reflections are required to accelerate the leading shock wave sufficiently in order to re-initiate the detonation [39]. At each shock reflection, or triple point collision, the incident shock is accelerated due to increased reaction rates in the unburned gases behind the incident shock. Furthermore, in some re-ignition cases, transverse detonations were observed to travel in the shocked, yet unreacted gas, as was also observed in other detonation experiments [25, 50]. The re-initiation flow field observed experimentally [39], shown in Figure 1.5, is similar to that observed in detonation diffraction studies [51–54].

In similar experiments, which examined *quasi-detonation* propagation in porous media [55–58], it has been shown that a wave can be sustained below the steady Chapman-Jouguet (CJ) velocity [16]. Due to the velocity deficit, it is believed that *adiabatic compression* alone, due to the shock interactions, cannot provide the necessary ignition to sustain a detonation wave. Thus, the recent investigation [39] and experiments [40–43, 55–58] have all come to the same conclusion; that it is unclear whether adiabatic shock compression or turbulent mixing is the dominating mechanism that drives, or initiates, the detonation.

In order to investigate the role of shock interactions on detonation re-initiation of irregular mixtures, following wave interaction with porous media, a numerical strategy based on the Euler formulation has been adopted [39]. Unfortunately, the numerical strategy, which did not address turbulent mixing, failed to capture exactly the correct

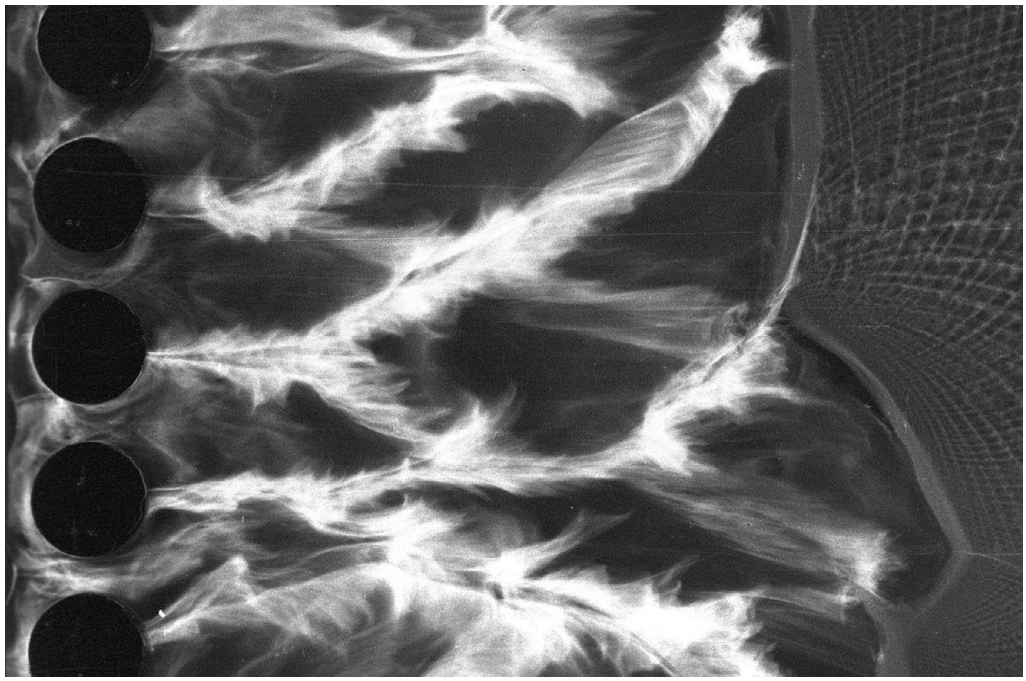

Figure 1.5: Open shutter photograph showing DDT of $C_2H_2 + O_2$ at $\hat{p}_o = 5$kPa, following detonation interaction with a porous medium [39].

number of shock reflections for detonation re-initiation to occur. Furthermore, the transverse detonations observed in the experiments have not been captured numerically. Thus, Euler simulations of the re-initiation process share the same pitfalls as Euler simulations of irregular detonation propagation; discrepancies arise due to the lack of resolution of the turbulent scales.

To address the turbulent scales, an LES investigation using a *flamelet* approach [59] has been applied to model the initial states of flame acceleration due to flame interaction with obstacles. Unfortunately, as will be demonstrated in Section 2.5.4, flamelet approaches are not appropriate for capturing the correct reaction rate in the later stages of flame acceleration, and DDT, as turbulent fluctuations are expected to increase. To address this, Gaathaug et al. [60] have applied a hybrid LES strategy to model DDT of hydrogen-air mixtures which treats combustion in both the extreme limits of *flamelet* and perfectly mixed, *well-stirred reactor*, regimes. Unfortunately, detonation initiation events were observed to occur much sooner in the simulations compared to their experiments. This is likely due to the fact that the hybrid method

does not treat combustion rates when turbulent mixing and chemical reaction rates are comparable.

To further investigate the role of turbulent mixing in this below-CJ supersonic combustion wave, or *fast-flame* phenomena, and its implication on DDT, experiments are currently being carried out at the University of Ottawa [14, 61, 62]. Unlike the previous experiments [39, 55–58], the experiment [14] uses only a cylinder to study the quenching, fast-flame propagation, and detonation re-initiation. The strategy is to scale up the porous medium problem, allowing for detailed diagnostics and higher resolution Schlieren photography to be implemented. Thus, the small scale features of the flow field are resolved experimentally, allowing for valuable comparison to validate the numerical strategy adopted in this thesis. Results from the experiments [14, 61], to date, are indicative of a common theme presented here: that *turbulent mixing* of burned product gases with unreacted pockets of gas in the wake of the incident shock gives rise to increased reaction rates, thus accelerating the flame. Furthermore, the presence of transverse shock waves due to reflections generates turbulence and thus further promotes increased reaction rates. The accelerating flame thus strengthens the leading shock wave, which can initiate a detonation [63, 64]. This problem corresponds to the last phases of flame acceleration and transition to detonation, as observed in several studies [40, 41, 65].

1.2.3 DDT from shock-flame interaction

In an alternate approach to address the stochastic nature of DDT associated with flame acceleration of irregular mixtures, and to isolate the role of turbulent mixing, Thomas et al.[66] proposed a controlled and reproducible experiment in which a single, relatively laminar, flame bubble is shocked sufficiently to induce enhanced combustion via Richtmyer-Meshkov (RM) and baroclinic instabilities. The methodology was inspired by a previous experiment [67] in which DDT was observed following the passage of a shock through a series of flame bubbles. The experiment [66] was conducted in a shock-tube, where a high pressure driver gas (helium) was used to

shock a low pressure ethylene-oxygen mixture diluted with nitrogen. Prior to experiment, a spherical flame was ignited in the centre of the test chamber. Upon arrival of the incident shock with the flame surface, the surface becomes compressed and distorted. The shock then reflects from the end wall of the test chamber and interacts with the flame a second time. Upon further shocking, instabilities rapidly appear on the flame surface giving rise to increased combustion rates. A key finding from the experiment [66] is that for a critical incident shock strength, the increased combustion rates due to the reflected shock are sufficient to sustain a highly unsteady and turbulent combustion wave that is able to drive the reflected shock speed to near-CJ velocity. In [66], this particular wave has been coined the *strange-wave*. An example of this closely coupled shock-turbulent flame complex, or strange wave, is shown in Figure 1.6. Interestingly, this wave appears to share many similarities with the *fast-flame* phenomena observed in the porous medium experiments [14, 39, 55–58, 61] and is therefore treated with particular interest. Thomas et al. [66] had found that the *strange-wave* was a regime in which energy release was dominated by turbulent mixing, rather than compression ignition alone. Finally, the onset of detonation in the shock-flame experiments is observed to occur at locations near the turbulent combustion front for sufficiently high incident shock strengths, which further supports that turbulent mixing plays an important role in DDT of high activation energy fuel mixtures.

To provide further insight on the experiments [67, 68], attempts at DNS have been conducted [69–71]. Although the simulations do not sufficiently resolve the finest scales of turbulence, and hence specific detonation initiation timings, the overall behaviour of the shock-flame interaction is captured. Findings conclude that RM instability through the shock-flame interaction is sufficient to trigger the strange-wave phenomena, and eventual transition to detonation. Furthermore the numerical investigation stresses the importance of capturing multi-dimensional shock interactions and turbulence [69]. Such shock interactions give rise to increased flame area owing to the RM instability, and hence locally increased combustion rates. Furthermore, shock bifurcations in the reflection process were found to give rise to shear layers [71],

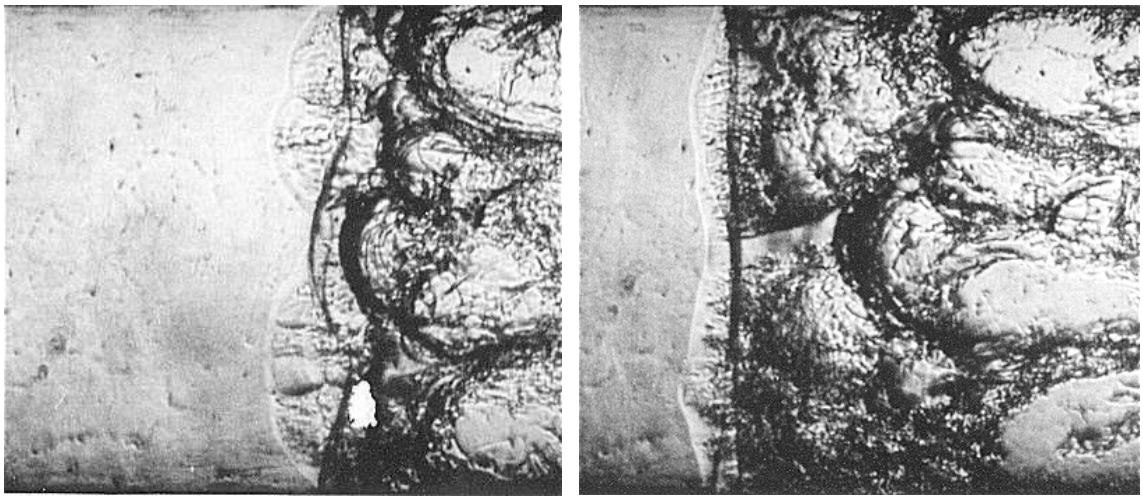

Figure 1.6: A Mach 1.7 shock emerging from a distorted flame in $C_2H_4 + 3O_2 + 4N_2$, giving rise to a closely coupled shock-turbulent flame, or *strange wave*, travelling from right to left [66].

akin to shear layers associated with triple points in detonations. It is along these shear layers that the KH instability acts to further promote turbulent mixing. It is through these mechanisms that the authors [69–71] believe detonation initiation is possible.

In a recent attempt at LES [72], the effects of turbulent mixing are addressed by applying a *flame-thickening* approach. In this regard, the application of LES is promising as the authors were able to produce grid-independent and converged results for DDT timings and locations resulting from turbulent mixing. This approach, however, has yet to be validated against experiment. Furthermore, as will be demonstrated in Section 2.5.4, the flame-thickening approach relies on the compromise of the sensitivity of the gas to shock-compression, and hence the reaction rate, in order to capture the correct laminar flame speed. This may, therefore, be problematic in predicting accurately the onset of DDT events, quantitatively, for a given fuel mixture.

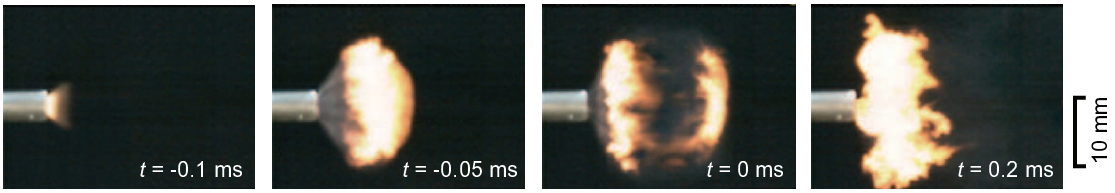

Figure 1.7: Successful ignition of pressurized H_2 released into air through a pipe [83]. ($p_o = 14,5$MPa, $d = 5$mm, $l = 185$mm)

1.2.4 Jet ignition of pressurized H_2 releases

Another significant, and related, problem of interest to the author is the spontaneous explosion phenomena and hazards associated with high pressure hydrogen leaks (i.e., from a high pressure storage facility). Although the subject matter does not pertain to the study of detonations, initial motivation for this thesis was acquired through the work presented here, funded by the NSERC H2Can Strategic Network.

In 2010, BC Transit launched the world's largest fleet of hydrogen fuel cell powered buses, consisting of 20 total, in Whistler, BC, Canada [73]. In order to power these fuel cells, hydrogen gas must be stored at fuelling stations or on-board the vehicles at very high pressures, ranging anywhere from 300 to 700 bars [74]. What is alarming is that a number of experiments [75–82] have reproducibly demonstrated that when pressurized hydrogen is suddenly released into air, spontaneous ignition of the release is possible. An example of this type of jet ignition for a release event through a tube [83] is shown in Figure 1.7. Furthermore, it has been suggested that detonation of hydrogen could be possible should sufficient turbulent mixing occur in the presence of reflected shock waves from confining geometry, or nearby obstacles [76]. Thus, the problem bears similarity to the role of turbulent mixing in jet initiation of a detonation when a jet of product gases flows into a premixed combustible mixture [68].

It is currently understood that during a release of high pressure hydrogen into air, local ignition "hot spots" form due to the shock induced *diffusion-ignition* mechanism. This has been confirmed through many numerical investigations [49, 84–92]. In this

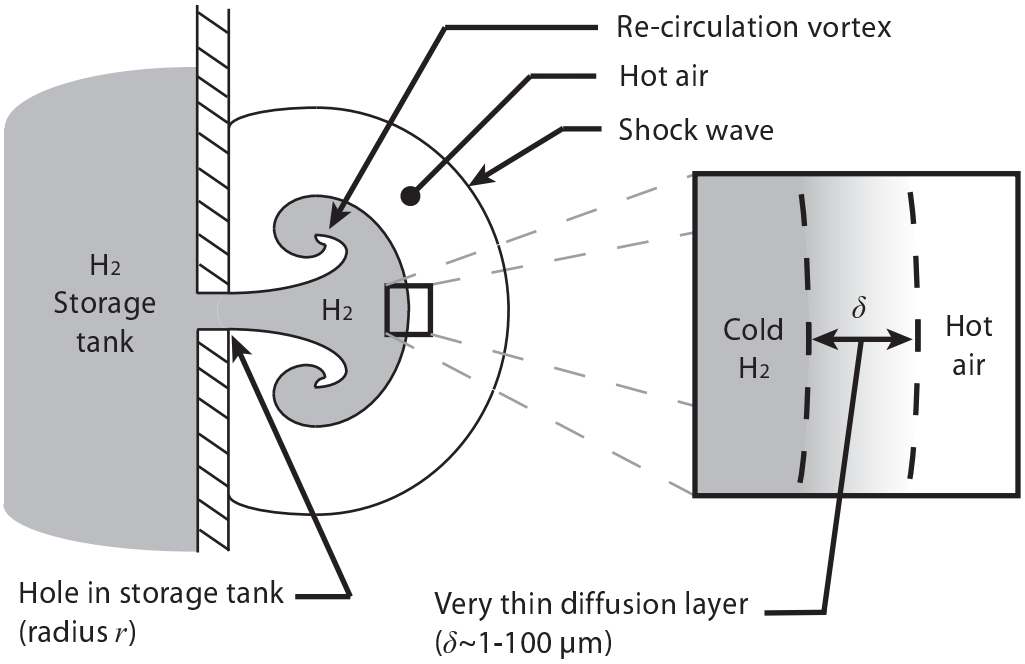

Figure 1.8: Accidental release of H_2 from a high pressure storage tank (sketch). The thin diffusion layer is where H_2 mixes with shocked air, ultimately leading to shock induced diffusion-ignition [49].

mechanism, illustrated in Figure 1.8, the rapidly expanding hydrogen jet drives a shock wave that heats the air. Since chemical reactions require both fuel and oxidizer to be present simultaneously, localized ignition spots may occur within the diffusion layer where both the cold fuel and the shock heated air co-exist. What remains unclear, however, is how these hot spots interact with each other giving rise to a jet fire, as observed in Figure 1.7, and what conditions must exist in order for a stabilized flame to form at the outflow nozzle.

To date, the experiments [76–81, 93] have only been able to determine spontaneous ignition limits, for hydrogen releases, providing the hydrogen jet is first released through a partly confining tube. Furthermore, ignition of unconfined releases was not observed when partly confined jets ignited under similar conditions (i.e., storage pressure, release hole size). Finally, specific cases were identified where ignition hot spots were blown away, or stabilized jet flames attached to the tube exit [78]. Since these observations, the influence of the tube confinement has become a subject of

active investigation [77–80, 89, 90, 93–95].

Since detailed diagnostics are not available experimentally, within the relatively narrow extension tubes used, most experiments cannot monitor the fast flow field development within the extension tubes nor explain the promoting effect that a tube has on ignition. Typical holes and extension tubes considered in these experiments are on the order of the centimetre. Instead, most studies have used numerical simulation to investigate the propensity for ignition in confined environments. Based on these simulations, different mechanisms have been proposed to explain the role of confinement on jet ignition. Maxwell and Radulescu [49] have previously suggested that confinement of the releases prevents the jet from gas dynamic expansion. The cooling due to volumetric expansion was shown to be the dominating mechanism preventing ignition in many cases [46, 49]. Likewise, Bragin and Molkov [91] have proposed that local heating in the boundary layers of the confining tube also promotes ignition. Furthermore, shock reflections from the confinement walls, and further shock focusing at the jet axis, were found to provide local temperature increases conducive to ignition. In reality, it is likely that all of these mechanisms control the local temperature in the mixing layer and its propensity for ignition. One fundamental aspect, however, that has not been adequately addressed by previous studies is the influence of *turbulent mixing* in the confined jets. Much like the fast-flame and detonation problems described above, turbulent mixing is difficult to address due to the wide range of scales that must be resolved, including molecular mixing and chemical reactions that occur at the micro-scale.

To this effect, it is currently believed that ignition of the jet not only depends on temperature in the diffusion layer alone, but also on the amount of *turbulent mixing* between the fuel and the oxidizer. Dryer et al. [76] suggested that confined releases may exhibit enhanced mixing through the RM instability that is promoted when transverse shocks interact with the mixing layer. It is thus postulated that larger volumes of premixed or reacted gases exiting the tube permits the establishment of a self-sustained jet flame at the tube exit. Bragin and Molkov [91] further sustained this

mechanism, which relies on the entrainment of burned gases into the re-circulating vortices of jets. It is thus not unreasonable to expect that ignition of the jet is controlled not only by the condition that local hot spots form inside the tube [49], but also more importantly by how much gas has ignited inside the tube. Thus, the amount of ignited gas depends intimately on *turbulent mixing* and local temperature variations through *shock reflections* [80]. In this sense, a confining extension is likely to provide both an increase in mixing rates and high temperatures to promote ignition.

To investigate the role of confining geometry and turbulent mixing on jet flame establishment, previous work has been conducted through experiments and Euler simulations [96]. Results of the investigation have confirmed that the role of confinement in hydrogen release experiments, as shown in Figure 1.9, was found to promote turbulent mixing through shock reflections and flow instabilities. Turbulent mixing thus influences how the ignition spots interact to ignite the entire jet, as shown by Figures 1.9b and c. Furthermore, inert Euler simulations of the release process have revealed that Kelvin-Helmholtz and Richtmyer-Meshkov instabilities lead to increased turbulent mixing rates and thus cause large amounts of oxygen to become entrained into the jet. For this reason, should ignition occur, much more gas is ignited experimentally than predicted by previous numerical investigations [87, 90]. This work [96], therefore, further motivates the need to treat turbulent mixing in numerical strategies applied to supersonic combustion.

1.2.5 Summary

In this section, four different types of supersonic combustion problems were presented through example experiments. The examples considered in sections 1.2.1 to 1.2.4 were detonation propagation, DDT from a porous medium, DDT from shock-flame interaction, and jet ignition of pressurized hydrogen jets, respectively. In all four types of problems, turbulent mixing of burned and unburned gases appears to influence the flow patterns and behaviour. For detonations and fast-flame acceleration leading up to DDT, it has been observed that the rate at which pockets of unreacted gas

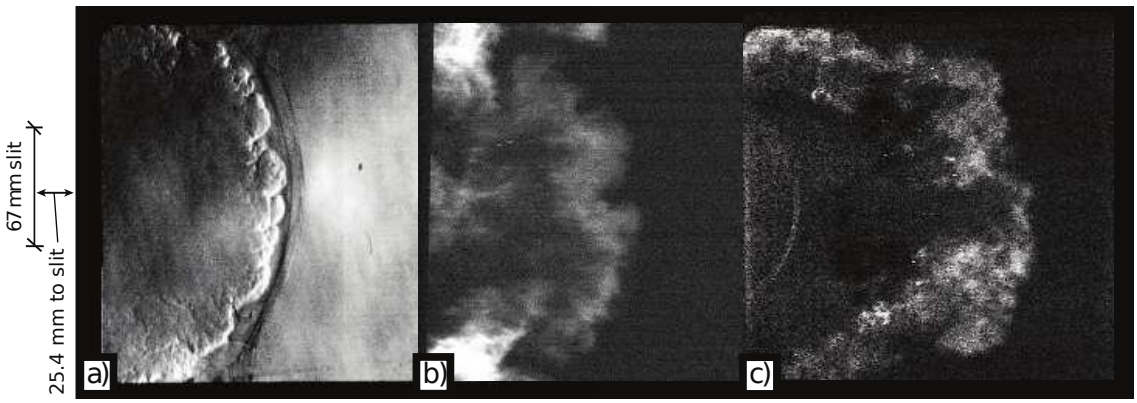

Figure 1.9: Typical cases where full jet ignition is observed experimentally [96]. Frame a) is a Schlieren image of a shock-accelerated H_2 jet flowing into pure O_2. Frames b) and c) show the combustion process at successive stages into the release process.

burn up cannot be accounted by shock compression alone. Instead, it is believed that such pockets burn at higher than expected rates owing to flow instabilities leading to turbulence near the flame surfaces. These instabilities can manifest themselves as Kelvin-Helmholtz instabilities associated with slip-lines in the flow, and are further enhanced through Richtmyer-Meshkov instabilities when shocked by transverse pressure waves. It is further believed that the burning rate of these pockets can influence detonation structure, manifested through the cell-pattern behaviour, and also DDT event timings and location. Furthermore, for supersonic jet ignition, such turbulent instabilities are believed to influence the volume of gas which is ignited during a release event, owing to increased mixing rates at the jet surface. In all cases, there is clearly a need to address turbulent mixing as a mechanism giving rise to enhanced burning through increased mixing rates. Despite recent advances in the state of knowledge of how turbulence may contribute to enhanced burning rates in supersonic combustion scenarios, numerical simulations are required to gain further insight and to develop quantitatively accurate predictive capabilities. Clearly, there exists a need to adequately model, and resolve the turbulent scales present.

To date, Euler simulations have been instrumental in providing insight on the role of pressure and turbulent instability mechanisms, and how turbulent mixing may contribute to flame acceleration and detonation initiation. However, in order to obtain

converged solutions through numerical investigation, the governing equations must be supplemented by molecular diffusion and viscosity; namely the Navier-Stokes equations. Unfortunately, DNS of the Navier-Stokes equations is not a currently feasible option as the range of scales in a large-scale multi-dimensional problem cannot be resolved adequately. While a physical problem may span several meters and seconds, the underlying turbulent mixing and chemical reactions both occur are on the order of the micrometre. LES, on the other hand, has proven to be useful at accounting for small scale turbulent effects on combustion rates of compressed gases [33, 38, 59, 72]. Although such LES investigations are useful at providing adequate closure on subgrid viscosity and mixing rates due to turbulence, closure of the reaction rate remains a challenge in turbulent combustion strategies. Typically, the reaction rate is obtained through LES by assuming the flow is either limited by chemical kinetics (i.e., the *well-stirred reactor* regime) or local mixing rates (the *flamelet* regime) [12]. The previous LES attempts [33, 38] that have assumed the well-stirred reactor regime applies have had difficulty resolving the correct reaction rates. In the flamelet approach [59], early stages of flame acceleration can be successfully modelled. However, achieving the correct reaction rate may prove difficult in the DDT limit. Unfortunately, these reaction rate assumptions break down when the mixing rates are comparable to the chemistry rates (i.e., *distributed* or *thin reaction zones* regime), which is believed to be the case for the final critical stages of fast flame acceleration and DDT. Finally, the *flame-thickening* model has been attempted [72], also with limited success. Unfortunately, the flame-thickening model is only able to produce the correct burning velocity of a turbulent flame by altering its reaction rate to compensate for increased diffusion rates. This fundamentally alters the ignition delay behaviour of the gas in the presence of shock waves, which cannot be reliably applied to study DDT events. Further details and review of supersonic combustion modelling approaches, including discussion on the complications and pitfalls that arise, are given in Chapter 2.

An alternative LES methodology which shows great promise at capturing and resolving mixing rates in the types of problems presented above, is the Linear Eddy Model for Large Eddy Simulation (LEM-LES) [97]. In the past, LEM-LES has been suc-

cessfully applied to model weakly compressible turbulent premixed and non-premixed flames [98, 99]. The method is therefore adaptable to a range of combustion regimes. Furthermore, the method has also been successfully applied to model supersonic inert mixing layers [100]. Although the method is attractive for the purpose of capturing and resolving turbulent mixing rates, it has not yet been applied to model multi-dimensional, turbulent, reactive, and highly compressible flows. It is thus a primary goal of this thesis to adapt this methodology to highly compressible and reactive flows and to verify/validate accordingly, see the next section.

1.3 CLEM-LES: A New Approach to Modelling Supersonic Combustion

In order to address the reaction rate closure problem of supersonic combustion, the primary focus of the thesis is the development, implementation, and validation of a novel modelling strategy which is based on the Linear Eddy Model for Large Eddy Simulation (LEM-LES) [97]. In the current implementation, the LEM-LES method is adapted to treat, simultaneously, highly compressible and reactive flows that involve very rapid transients in pressure and energy. It is therefore referred to as Compressible LEM-LES (CLEM-LES) for the remainder of the thesis. Although a comprehensive detailed explanation of the strategy is found in Chapter 3, the method is summarized briefly here. In the CLEM-LES context, the subgrid is treated as a one-dimensional sample of a diffusion-reaction system within each multi-dimensional LES cell, as illustrated in Figure 1.10. This reduces the expense of solving a complete multi-dimensional problem through DNS while preserving micro-scale hot spots and their physical effects on ignition. Thus, the model provides high resolution closure for the unresolved chemical reaction terms in the governing, LES-filtered, reactive Navier-Stokes equations. Furthermore, the current approach features a Lagrangian description of fluid particles on the sub-grid for increased accuracy. A principle advantage of this methodology is the ability to treat flows where chemical reactions

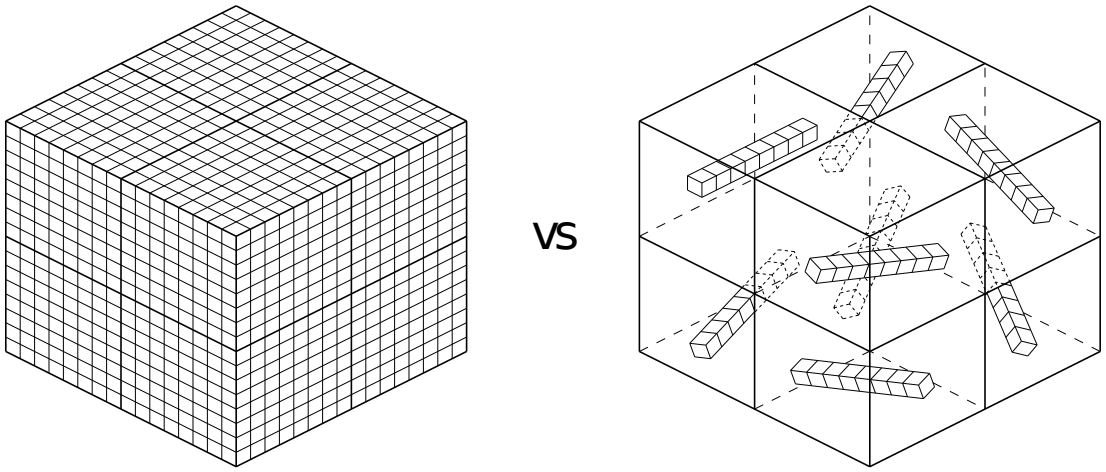

Figure 1.10: A 3D illustration showing a the computational cells required for DNS (left) compared to the number of cells required for the equivalent CLEM-LES (right).

and micro-scale mixing occur on the same scales, without the need to provide bold assumptions on the reaction rate.

In order to verify and validate the model formulation, a number of 1D and 2D test cases are considered. The primary focus is on methane-oxygen mixtures, although other fuel mixtures are also considered. In 1D, the verification exercises include inert mixing, constant volume ignition, shock tube problems, laminar flame and detonation propagation. Also verified is a hypothetical 1-D piston-driven laminar shock-flame interaction and its subsequent transition to detonation. For validation, 1D turbulent flames are simulated for lean and stoichiometric methane-air mixtures and compared to experiments [101] and also a previous LEM formulation [102]. In 2D, the structure of irregular detonation wave propagation is validated against experiments that have been conducted at the University of Ottawa [13], and also similar experiments of [15]. These validation experiments are the supersonic combustion problems described in Sections 1.2.1 and 1.2.2. Finally, the model used to provide insight on the role of turbulent mixing in fast flame propagation and detonation initiation events via detonation interaction with porous medium experiments, also conducted at the University of Ottawa [13, 14].

1.4 Objective and Organization of Thesis

1.4.1 Thesis objectives

In light of the review provided in this chapter, the specific fundamental objectives of this thesis are summarized as follows:

- To develop a solution framework (CLEM-LES) which can address the turbulent scales of highly compressible reactive flows that involve rapid transients in pressure and energy.
- To verify and validate the CLEM-LES strategy in 1D and 2D reactive flows.
- To provide recommendations on future model development.
- To identify the roles of turbulent mixing on combustion rates on detonation propagation flow patterns (example 1.2.1) and DDT events in a porous medium (example 1.2.2) through numerical modelling.

1.4.2 Organization

The organization of the thesis is as follows. First, Chapter 2 provides background information on state-of-the-art approaches to modelling turbulent combustion, including the relevant governing equations. Furthermore, this chapter details the advantages and disadvantages of various approaches that are currently used in practise. Chapter 3 then derives and details the CLEM-LES solution framework adopted in the remainder of the thesis. The CLEM subgrid formation is verified and validated for various 1D flows in Chapter 4. Then, in Chapters 5 and 6, *two-dimensional* simulations, using the CLEM-LES, are validated for the detonation propagation and DDT from a porous medium experiments [13–15] (Sections 1.2.1 and 1.2.2), respectively. Conclusions and recommendations are then provided in Chapter 7. Finally, several appendices are included to supplement the work. Appendix A contains flow charts

relevant to the CLEM-LES methodology. Appendix B is a summary of the procedure used to determine various model constants used throughout the thesis. To compliment this procedure, Appendix C describes a custom in-house computer program developed by the author, uFlame, which is used to obtain flamespeeds of fuel-oxidizer mixtures, using realistic chemistry.

Chapter 2

Governing Equations and Modelling Strategies

2.1 Governing Equations for a Reactive Gas

2.1.1 Conservation of mass, momentum, and energy

In order to describe various modelling techniques for supersonic combustion problems, and to derive the LES strategy adopted later in this thesis, it is first necessary to become familiarized with the governing reactive Navier-Stokes (N-S) equations in compressible form. The conservation of mass, momentum, and total energy, per unit volume, are presented below in Eqs.(2.1) to (2.3), respectively, in dimensional vector form. The equation set is also supplemented by N additional equations, given by (2.4), each describing the evolution of the ith out of N chemical species. The formal derivation of Eqs.(2.1) to (2.4) can be found in [103] and the meaning of each symbol presented can be found in the Nomenclature of this thesis. Vectors and tensors are

both distinguished in **bold** and tensors are further identified with an **underline**.

$$\underbrace{\frac{\partial \hat{\rho}}{\partial \hat{t}}}_{\substack{\text{local rate of change} \\ \text{in density}}} + \underbrace{\boldsymbol{\nabla} \cdot (\hat{\rho}\hat{\boldsymbol{u}})}_{\text{mass flux}} = 0 \tag{2.1}$$

$$\underbrace{\frac{\partial (\hat{\rho}\hat{\boldsymbol{u}})}{\partial \hat{t}}}_{\substack{\text{local rate of change} \\ \text{in momentum}}} + \underbrace{\boldsymbol{\nabla} \cdot (\hat{\rho}\hat{\boldsymbol{u}} \otimes \hat{\boldsymbol{u}})}_{\text{momentum flux}} + \underbrace{\nabla \hat{p}}_{\text{pressure gradient}} - \underbrace{\boldsymbol{\nabla} \cdot \underline{\hat{\boldsymbol{\tau}}}}_{\text{viscous stress}} = \underbrace{\sum_{i=1}^{N} \hat{\rho} Y_i \hat{\boldsymbol{f}}_i}_{\text{external forces}} \tag{2.2}$$

$$\underbrace{\frac{\partial (\hat{\rho}\hat{e}_T)}{\partial \hat{t}}}_{\substack{\text{local rate} \\ \text{of change in} \\ \text{total energy}}} + \underbrace{\boldsymbol{\nabla} \cdot \Big((\hat{\rho}\hat{e}_T + \hat{p})\hat{\boldsymbol{u}} \Big)}_{\substack{\text{advection of sensible energy} \\ \text{and flow work}}} - \underbrace{\boldsymbol{\nabla} \cdot (\hat{\boldsymbol{u}} \cdot \underline{\hat{\boldsymbol{\tau}}})}_{\substack{\text{viscous} \\ \text{dissipation}}} + \underbrace{\boldsymbol{\nabla} \cdot \hat{\boldsymbol{q}}}_{\substack{\text{heat} \\ \text{flux}}} = \underbrace{\sum_{i=1}^{N} (\hat{\rho}\hat{\boldsymbol{u}}_{d,i} Y_i) \cdot \hat{\boldsymbol{f}}_i}_{\text{external work}} \tag{2.3}$$

$$\underbrace{\frac{\partial (\hat{\rho} Y_i)}{\partial \hat{t}}}_{\substack{\text{local rate of} \\ \text{change in density} \\ \text{of } i\text{th specie}}} + \underbrace{\boldsymbol{\nabla} \cdot (\hat{\rho}\hat{\boldsymbol{u}} Y_i)}_{\substack{\text{advective} \\ \text{flux}}} + \underbrace{\boldsymbol{\nabla} \cdot (\hat{\rho}\hat{\boldsymbol{u}}_{d,i} Y_i)}_{\substack{\text{diffusive} \\ \text{flux}}} = \underbrace{\dot{\hat{\omega}}_i}_{\substack{\text{production} \\ \text{rate}}} \tag{2.4}$$

Here, the specific total energy is comprised of the fluids specific internal energy and its specific kinetic energy:

$$\hat{e}_T = \underbrace{\hat{e}_u}_{\text{internal energy}} + \underbrace{\frac{1}{2}\hat{\boldsymbol{u}} \cdot \hat{\boldsymbol{u}}}_{\text{kinetic energy}} \tag{2.5}$$

The specific internal energy is related to the specific enthalpy through the thermodynamic identity

$$\hat{e}_u = \hat{h} - \frac{\hat{p}}{\hat{\rho}} \tag{2.6}$$

where $\hat{e}_u = \sum_{i=1}^{N} \hat{e}_{u,i} Y_i$ and $\hat{h} = \sum_{i=1}^{N} \hat{h}_i Y_i$. Finally, the specific internal energy and specific enthalpy, of each species, are determined through the caloric equations of state:

$$\hat{e}_{u,i} = \hat{e}^o_{u,i} + \int_{\hat{T}^o}^{\hat{T}} \hat{c}_{v,i} d\hat{T} \tag{2.7}$$

$$\hat{h}_i = \hat{h}_i^o + \int_{\hat{T}^o}^{\hat{T}} \hat{c}_{p,i} d\hat{T} \tag{2.8}$$

where $\hat{e}_{u,i}^o$ and $\hat{h}_i^o$ are the internal energy and enthalpy of formation of species i at some reference temperature, $\hat{T}^o$. This set of Eqs., (2.1) to (2.4), is written in conservation form, such that the rate of change of each conserved variable per unit volume ($\hat{\rho}$, $\hat{\rho}\hat{\boldsymbol{u}}$, $\hat{\rho}\hat{e}_T$, $\hat{\rho}Y_i$) is accounted for locally within sufficiently small discreet finite-volumes, as illustrated previously in Figure 1.10. The rate of change of total mass per unit volume, in Eq.(2.1), simply accounts for the flux of mass through the volume faces. The rate of change of local momentum per unit volume, Eq.(2.2), not only accounts for momentum fluxes through its volume faces ($\boldsymbol{\nabla} \cdot (\hat{\rho}\hat{\boldsymbol{u}} \otimes \hat{\boldsymbol{u}})$), but also accounts for force imbalance due to pressure gradients ($\nabla\hat{p}$), friction due to flow shearing and bulk viscosity ($\boldsymbol{\nabla} \cdot \hat{\boldsymbol{\tau}}$), and also external body forces, f_i, which act on the fluid particles within the volume (i.e., gravity). The rate of change of total energy per unit volume, Eq.(2.3), is governed by the advection of sensible energy and flow work through its volume faces ($\boldsymbol{\nabla} \cdot (\hat{\rho}\hat{e} + \hat{p})\hat{\boldsymbol{u}}$), viscous energy dissipation ($\boldsymbol{\nabla} \cdot (\hat{\boldsymbol{u}} \cdot \hat{\underline{\boldsymbol{\tau}}})$), heat flux through the volume faces ($\boldsymbol{\nabla} \cdot \hat{\boldsymbol{q}}$), and external work due to $\boldsymbol{f}_i$. The heat flux vector, $\hat{\boldsymbol{q}}$, arises due to several influencing factors. In its full form, $\hat{\boldsymbol{q}}$ comprises of primary and secondary diffusion effects, Dufour effects [103], and radiation:

$$\hat{\boldsymbol{q}} = - \underbrace{\hat{k}\nabla\hat{T}}_{\substack{\text{heat}\\ \text{conduction}}} + \underbrace{\sum_{i=1}^{N} \hat{\rho}\hat{\boldsymbol{u}}_{d,i} Y_i \hat{h}_i}_{\substack{\text{secondary heat}\\ \text{diffusion}}} + \underbrace{R^o\hat{T} \sum_{i=1}^{N}\sum_{j=1}^{N} \left(\frac{X_j \hat{D}_{T,i}}{W_i \hat{D}_{i,j}}\right)(\hat{\boldsymbol{u}}_{d,i} - \hat{\boldsymbol{u}}_{d,j})}_{\text{Dufour effect}} + \underbrace{\hat{\boldsymbol{q}}_{\text{rad}}}_{\substack{\text{radiation}}} \tag{2.9}$$

Finally, the rate of change of density of each ith reactive specie is governed by its advective mass flux due to bulk fluid motion ($\boldsymbol{\nabla} \cdot (\hat{\rho}\hat{\boldsymbol{u}}Y_i)$), its mass flux due to molecular diffusion to neighbouring volumes ($\boldsymbol{\nabla} \cdot (\hat{\rho}\hat{\boldsymbol{u}}_{d,i}Y_i)$), and its net rate of production due to chemical reaction ($\dot{\hat{\omega}}_i$).

2.1.2 Assumptions and simplifications

In order to isolate the direct role that turbulent mixing has on the overall reaction rate of the equations set, (2.1) to (2.4), while simplifying the governing physics, a number of assumptions are made. The list of assumptions applied directly to the governing equations are as follows:

- Calorically perfect gas with constant specific heats.
- Newtonian fluid.
- Fickian diffusion.
- Kinematic viscosity, heat conductivity, and mass diffusivity are constants.
- No radiation effects.
- No external body forces (i.e., gravity).
- Reactants form products according to a one-step global reaction mechanism.
- Negligible change in molecular weight as reactants form products.
- Reactants and products have equal specific heats.

First and foremost, a calorically perfect gas with constant specific heats is assumed. Thus, pressure, density, and temperature are related through

$$\frac{\hat{p}}{\hat{\rho}} = \hat{R}\hat{T} \tag{2.10}$$

where the specific gas constant

$$\hat{R} = R^o \sum_{i=1}^{N} (Y_i/W_i). \tag{2.11}$$

This assumption also simplifies the caloric equation for specific internal energy and enthalpy. Thus, the specific internal energy component of Eq.(2.5) can be simplified to

$$\hat{e}_u = \underbrace{\frac{\hat{p}/\hat{\rho}}{\gamma - 1}}_{\text{sensible energy}} + \underbrace{\sum_{i=1}^{N} \hat{h}_i^o Y_i}_{\text{chemical energy}} \tag{2.12}$$

where γ is the ratio of specific heats

$$\gamma = \hat{c}_p/\hat{c}_v. \tag{2.13}$$

Next, the viscous stress is assumed to behave as a Newtonian fluid [104]. Thus, the shear and normal stress is assumed to vary linearly with the fluid strain rate through

$$\underline{\hat{\boldsymbol{\tau}}} = \hat{\mu}\left(\nabla\hat{\boldsymbol{u}} + (\nabla\hat{\boldsymbol{u}})^T - \frac{2}{3}(\boldsymbol{\nabla}\cdot\hat{\boldsymbol{u}})\underline{\boldsymbol{I}}\right) \tag{2.14}$$

where $\hat{\mu}$ is the dynamic viscosity of the fluid. To further simplify the governing equations, Fickian diffusion according to the Hirschfelder and Curtiss approximation [11, 105] has been assumed. Thus, upon further neglecting radiation, secondary diffusion, and higher order diffusion, such as Dufour (and Soret) effects [103], the heat flux and species diffusion terms become:

$$\hat{\boldsymbol{q}} \approx -\hat{k}\nabla\hat{T} \tag{2.15}$$

$$\hat{\rho}\hat{\boldsymbol{u}}_{d,i}Y_i \approx -\hat{\rho}\hat{D}_i\nabla Y_i. \tag{2.16}$$

The equations are then further simplified by neglecting other body forces, such as gravity. Thus, $\hat{\boldsymbol{f}}_i = 0$ for all i. Finally, the chemistry is simplified by assuming that reactants form products according to a single-step global reaction with no intermediate reactions: *Reactants* $\rightarrow$ *Products* directly and irreversibly. In reality, the reaction rate ($\hat{\dot{\omega}}$) is governed by chemistry involving multiple species. This requires significant computational overhead due to the requirement of accounting for hundreds, or thousands, of equations and reactions in reactive flows. Instead, the one-step global reaction mechanism [103] considers a single premixed reactant, with mass fraction Y, that forms products according to the single step Arrhenius expression [103]:

$$\hat{\dot{\omega}} = -\hat{\rho}\hat{A}Ye^{(-\hat{E}_a/\hat{R}\hat{T})} \tag{2.17}$$

where $\hat{E}_a$ is the activation energy of the reactant mixture.

Thus, by applying the assumptions above, the system of governing Eqs.(2.1) to (2.4) become:

$$\frac{\partial \hat{\rho}}{\partial \hat{t}} + \boldsymbol{\nabla} \cdot (\hat{\rho}\hat{\boldsymbol{u}}) = 0 \tag{2.18}$$

$$\frac{\partial (\hat{\rho}\hat{\boldsymbol{u}})}{\partial \hat{t}} + \boldsymbol{\nabla} \cdot (\hat{\rho}\hat{\boldsymbol{u}} \otimes \hat{\boldsymbol{u}}) + \nabla \hat{p} - \boldsymbol{\nabla} \cdot \underline{\hat{\boldsymbol{\tau}}} = 0 \tag{2.19}$$

$$\frac{\partial (\hat{\rho}\hat{e})}{\partial \hat{t}} + \boldsymbol{\nabla} \cdot \left((\hat{\rho}\hat{e} + \hat{p})\hat{\boldsymbol{u}} - \hat{\boldsymbol{u}} \cdot \underline{\hat{\boldsymbol{\tau}}} \right) - \boldsymbol{\nabla} \cdot (\hat{k} \nabla \hat{T}) = -\hat{Q}\dot{\hat{\omega}} \tag{2.20}$$

$$\frac{\partial (\hat{\rho} Y)}{\partial \hat{t}} + \boldsymbol{\nabla} \cdot (\hat{\rho}\hat{\boldsymbol{u}} Y) - \boldsymbol{\nabla} \cdot (\hat{\rho}\hat{D} \nabla Y) = \dot{\hat{\omega}} \tag{2.21}$$

where the conservation of total energy has been re-cast in terms of the total sensible energy plus kinetic energy such that

$$\hat{e} = \frac{\hat{p}/\hat{\rho}}{\gamma - 1} + \frac{1}{2}\hat{\boldsymbol{u}} \cdot \hat{\boldsymbol{u}}. \tag{2.22}$$

Since the specific heats of both the reactants and the products have been assumed equal and constant, this reformulation of the conservation of energy has been conveniently written in conservative form. Furthermore, this assumption does not introduce any secondary diffusion terms. To balance the conservation of energy, Eq.2.20 now introduces the rate of heat released during chemical reaction as a source term, $(\hat{Q}\dot{\hat{\omega}})$. Here, $\hat{Q}$ is the total amount of heat released during a complete constant volume reaction of the reactants.

Finally, changes in molecular weight are neglected, as reactants form products. Thus the gas constant $\hat{R}$ is treated as having a constant value through the reaction process. The application of this assumption is particularly useful for further simplifying to the final non-dimensional form of the equation of state (2.31), as will be presented in the next section.

2.1.3 Non-dimensional form

To further generalize the set of equations, it is useful to normalize the flow properties to some reference state, denoted below by the subscript 'o'. Here, the various state

variables are normalized such that

$$\rho = \frac{\hat{\rho}}{\hat{\rho_o}}, \quad \boldsymbol{u} = \frac{\hat{\boldsymbol{u}}}{\hat{c_o}}, \quad p = \frac{\hat{p}}{\hat{\rho_o}\hat{c_o}^2} = \frac{\hat{p}}{\gamma\hat{p_o}}, \quad T = \frac{\hat{T}}{\gamma\hat{T_o}}, \quad x = \frac{\hat{x}}{\hat{L}}, \quad t = \frac{\hat{t}}{\hat{L}/\hat{c_o}}. \tag{2.23}$$

Also, the activation energy (E_a), heat release (Q), and pre-exponential factor (A) are normalized by

$$E_a = \frac{\hat{E_a}}{\hat{c_o}^2}, \qquad Q = \frac{\hat{Q}}{\hat{c_o}^2}, \qquad A = \frac{\hat{A}}{\hat{c_o}/\hat{L}}. \tag{2.24}$$

Furthermore, it is useful to define the following transport relationships in order to relate viscosity to heat and mass diffusion in terms of Prandtl (P_r), Schmidt (S_c), and Lewis numbers (L_e):

$$\mu = \rho\nu = \frac{1}{R_e} = \frac{\hat{\mu}}{\hat{\rho_o}\hat{c_o}\hat{L}}, \qquad \alpha = \frac{\mu}{P_r} = \frac{\hat{k}/\hat{c_p}}{\hat{\rho_o}\hat{c_o}\hat{L}}, \qquad L_e = \frac{S_c}{P_r} = \frac{\hat{k}/\hat{c_p}}{\hat{\rho}\hat{D}}. \tag{2.25}$$

The final form of the governing equations, (2.18) to (2.21) may now be expressed in non-dimensional form:

$$\frac{\partial\rho}{\partial t} + \boldsymbol{\nabla}\cdot(\rho\boldsymbol{u}) = 0 \tag{2.26}$$

$$\frac{\partial(\rho\boldsymbol{u})}{\partial t} + \boldsymbol{\nabla}\cdot(\rho\boldsymbol{u}\otimes\boldsymbol{u}) + \nabla p - \boldsymbol{\nabla}\cdot\underline{\boldsymbol{\tau}} = 0 \tag{2.27}$$

$$\frac{\partial(\rho e)}{\partial t} + \boldsymbol{\nabla}\cdot\Big((\rho e + p)\boldsymbol{u} - \boldsymbol{u}\cdot\underline{\boldsymbol{\tau}}\Big) - \left(\frac{\gamma}{\gamma-1}\right)\boldsymbol{\nabla}\cdot\left(\frac{\mu}{P_r}\nabla T\right) = -Q\dot{\omega} \tag{2.28}$$

$$\frac{\partial(\rho Y)}{\partial t} + \boldsymbol{\nabla}\cdot(\rho\boldsymbol{u}Y) - \boldsymbol{\nabla}\cdot\left(\frac{\mu}{S_c}\nabla Y\right) = \dot{\omega} \tag{2.29}$$

where

$$e = \frac{p/\rho}{\gamma-1} + \frac{1}{2}\boldsymbol{u}\cdot\boldsymbol{u} \tag{2.30}$$

$$T = p/\rho \tag{2.31}$$

$$\underline{\boldsymbol{\tau}} = \mu\left(\nabla\boldsymbol{u} + (\nabla\boldsymbol{u})^T - \frac{2}{3}(\boldsymbol{\nabla}\cdot\boldsymbol{u})\underline{\boldsymbol{I}}\right) \tag{2.32}$$

and

$$\dot{\omega} = -\rho A Y e^{(-E_a/T)}. \tag{2.33}$$

2.2 Reactive Euler Methods: Inviscid Calculations

To date, the most common approach for modelling detonation waves has been to neglect viscosity and diffusion, and thus solve Euler's equations of motion [104]. This approach assumes that in the high R_e limit, advection dominates over diffusion. Thus, the model is suitable for modelling flows where shock compression is the dominant ignition mechanism governing the overall fluid flow evolution. In non-dimensional form, the reactive and inviscid conservation of total mass, momentum, energy, and chemical reactant mass for a calorically perfect gas become

$$\partial\rho/\partial t + \boldsymbol{\nabla}\cdot(\rho\boldsymbol{u}) = 0 \tag{2.34}$$

$$\partial(\rho\boldsymbol{u})/\partial t + \boldsymbol{\nabla}\cdot(\rho\boldsymbol{u}\otimes\boldsymbol{u}) + \nabla p = 0 \tag{2.35}$$

$$\partial(\rho e)/\partial t + \boldsymbol{\nabla}\cdot(\boldsymbol{u}(\rho e + p)) = -Q\dot{\omega} \tag{2.36}$$

$$\partial(\rho Y)/\partial t + \boldsymbol{\nabla}\cdot(\rho\boldsymbol{u}Y) = \dot{\omega}. \tag{2.37}$$

This Reactive-Euler approach, which neglects diffusion effects, is often justified by the fact that the hydrodynamic scales of high R_e flows (i.e., detonations) are much larger than the micro-scales [27]. In fact, the reactive Euler method coupled with the one-step ignition model has been adopted by many to study detonation behaviour and structure [27, 29–32, 39, 106–108]. These types of simulations, however, only give a picture of the larger gas dynamic process evolving in the problems when chemical reactions are not limited by diffusive mixing. Furthermore, despite the fact that the one-step chemistry model is computationally simple and maintains the physics of the overall global chemistry, the reaction zone lengths cannot be independently controlled compared to the induction zone lengths. It has been reported that the energy released in the reaction zone of the model occurs over a much larger distance than in reality [39]. To circumvent this problem, the Euler method has also been coupled with a

two-step model [109–111] to study detonation behaviour. Despite these efforts, it has recently become apparent that there is a need to resolve the turbulent mixing scales for DDT and irregular detonation propagation [27, 39]. Thus, in order to address the specific goals of the research outlined in Chapter 1, the full N-S equations must be considered.

2.3 Direct Numerical Simulation (DNS)

In order to account for the turbulent scale effects that may contribute to the fast-flame and detonation phenomenon, the governing equations must include molecular mixing and friction effects. This is done by supplementing the Euler formulation with viscosity and diffusion. Although the Euler equations describe the bulk gas-dynamic fluid motion of a fluid, in reality the small scale diffusive effects give rise to large-scale influence on the global fluid evolution through mixing layer growth influenced by turbulent instabilities, namely the RM and KH instabilities. Thus, the compressible N-S equations, (2.26) to (2.29) must be considered.

Despite the computational resources available, simulations of compressible combustion problems, at present, are difficult to resolve through DNS of the N-S equations due to the wide range of scales involved. To demonstrate this, consider a single energy carrying eddy, in the wake of a fast-flame or detonation, whose integral length scale is anywhere from $\hat{l}_t = 1 - 10$cm and whose tangential velocity is on the order of $\hat{u}' = 500 - 1000$m/s [62]. For a hydrocarbon fuel mixture whose temperature is $\hat{T} > 1000$K, the kinematic viscosity is on the order of $\hat{\nu} \approx 1 \times 10^{-4}$m^2/s, see Tables 5.1 and 6.1. The corresponding Reynolds number is:

$$R_{e,t} = \frac{\hat{l}_t \hat{u}'}{\hat{\nu}} \approx 50,000 - 1,000,000. \tag{2.38}$$

The Kolmogorov scale [112], or scale at which turbulent eddies are dissipated through viscosity, is estimated to be $\eta \approx l_t / {R_{e,t}}^{3/4} = 2 - 5\mu$m. Furthermore, it has previously been demonstrated that mixing layers [49] and flame thicknesses [101] are on the order

of $1 - 100\mu$m. Since combustion occurs within these thin layers, where burned and unburned gases mix, it is clear that a very high resolution is required. In fact, to model and resolve the single eddy, above, would require trillions of nodes. This revealed limitation explains why previous DNS attempts at modelling detonation propagation [25, 33] have been unable to capture the correct burning rates of unburned pockets in full-scale problems. This also explains why application of DNS is limited to single-isolated events, i.e., triple point collisions [34]. Since the DNS technique is not yet realizable for problems that contain length scales of practical interest, it is necessary to *model*, rather than simulate, the micro-scale physics of the problems (i.e., through RANS or LES).

2.4 Reynolds Averaged Navier-Stokes (RANS)

An alternative approach to DNS is to apply Reynolds Averaging to the Navier-Stokes equations (RANS). In this approach, only the very large scale fluid motion is simulated, while the small scale fluctuations to the flow field are modelled [112]. This approach, however, provides only mean values of the flow field properties (p, ρ, T, u) which are averaged across rather large time steps. To date, the method has been applied to model relatively steady operation of Supersonic Combustion Ramjet engines (SCRAMJETs) [113] and also fully developed supersonic jets and jet fires involving hydrogen, beyond the start-up phase [85, 114]. Unfortunately, the detonation and fast-flame problems under investigation in this study are highly transient in nature, where large fluctuations in flow properties are expected in very short time scales [39, 115]. For this reason RANS is not considered.

2.5 Large Eddy Simulation (LES): State of the Art

A compromise, and realizable alternative, to both DNS and RANS, is to model the turbulent scales in a Large Eddy Simulation (LES) formulation. This approach is a reasonable compromise between the computational efficiency of RANS and the solution accuracy of DNS. In this approach, the exact N-S equations are solved down to the inertial scales of the problem [112], such that the energy carrying eddies are resolved. Models are then applied to describe only the small scale turbulent mixing and combustion. These models apply Kolmogorov scaling laws to describe the self-similar nature of the energy cascade associated with vortical motion in order to account for the small scale fluctuations with higher accuracy than RANS. As a result, LES is a favourable approach to solving the problems under investigation here, and is currently regarded as the state-of-the-art approach to solving compressible turbulent combustion problems. With LES, however, there are many fundamentally different modelling approaches. The most appropriate modelling technique must be chosen that captures the correct expected combustion regime with the appropriate flow assumptions. A brief discussion regarding combustion regimes is given below followed by discussion of the governing equations and applicable modelling techniques.

2.5.1 Premixed combustion regimes

Turbulent premixed combustion regimes have traditionally been categorized by characteristic Damkholer and Karlovitz numbers [116, 117]. Although regimes have also been categorized for non-premixed combustion [11], they are not discussed here since only premixed combustion is considered in this thesis. The Damkholer number, given by Eq.(2.39), relates the integral time scales of the problem to laminar flame chemical time scales (i.e., the inverse of the rate at which burning occurs over the entire flame structure). The Karlovitz number on the other hand, given by Eq.(2.40), relates the

flame chemical time scales to the Kolmogorov scale, which is the dissipation time scale of the smallest eddies.

$$D_a = \frac{t_F}{t_c} = \frac{l_t/u'}{l_F/S_L} = \frac{l_t/u'}{\nu/S_L^2} \tag{2.39}$$

$$K_a = \frac{t_c}{t_\eta} = \frac{l_F^2}{\eta^2} \tag{2.40}$$

Specifically, three major turbulent combustion regimes have been identified. As $D_a \ll 1$, mixing times are much faster than burning rates, and hence the flow is treated as a *well-stirred reactor*. Conversely, as $K_a \ll 1$, the turbulent scales are much larger than the laminar flame structure. Thus, burning is almost instant compared to the mixing time. In this *flamelet* regime, the flow is treated as a collection of infinitely thin laminar flame sheets, where reactants are converted to products, instantaneously, as they contact the flame surface. Of particular interest, however, is when $D_a > 1$ and $K_a > 1$. In this regime, traditionally called the *distributed reaction zones* regime, the scales at which turbulent mixing occurs are comparable to the scales at which burning occurs. Alternatively, the distinction between distributed reaction zone and well-stirred reactor has also been categorized in terms of a Karlovitz number associated with the inner-flame structure rather that a Damkholer number [118]. This inner-flame Karlovitz number, $K_{a,\delta}$, relates the chemical time scales associated with the inner-flame structure to the dissipation time scales and is given by

$$K_{a,\delta} = \frac{t_{c,\delta}}{t_\eta} = \frac{l_\delta^2}{\eta^2} = \frac{(\delta l_F)^2}{\eta^2} \tag{2.41}$$

where $l_\delta = \delta l_F$ is the inner flame thickness and δ is a scaling constant on the order of 0.1 [118]. In this classification, a *thin reaction zones* regime is alternatively defined when $K_a > 1$ and $K_{a,\delta} < 1$, i.e. when turbulent motions begin to disrupt the inner flame structure. These three major regimes, and their limits, are indicated in Figure 2.1, for premixed combustion, which is categorized in terms of K_a and $K_{a,\delta}$. As will now be demonstrated, the combustion regime of particular interest, for fast-flame acceleration and DDT, is the thin reaction zones regime.

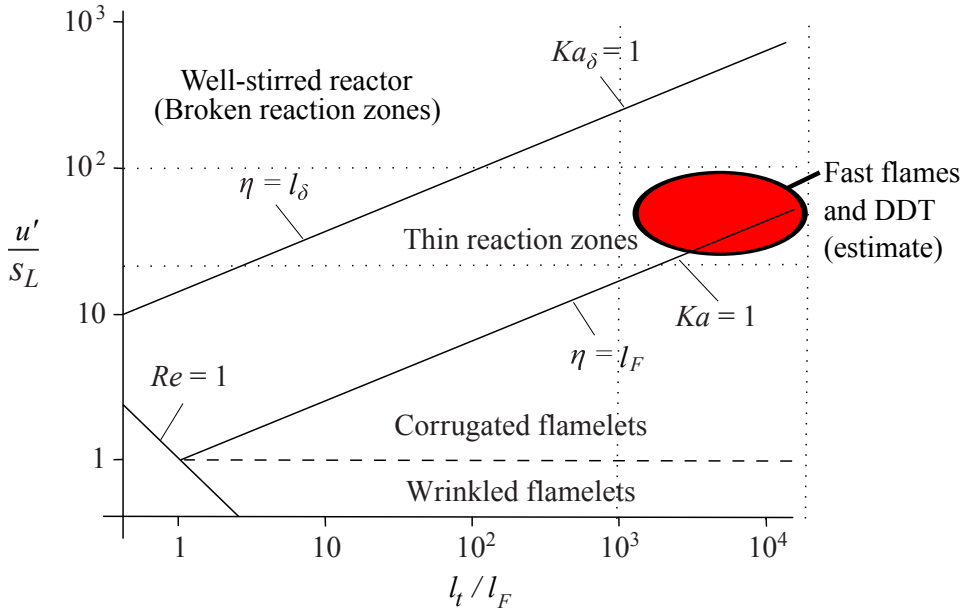

Figure 2.1: Regime diagram for premixed turbulent combustion [118]. (u'/S_l) is the ratio of turbulent velocity fluctuations relative to the laminar flame speed, and (l_t/l_F) is the integral scale relative to the inner flame thickness. K_a and $K_{a,\delta}$ represent the ratio of chemical to dissipation time scales associated with the outer and inner flame structures, respectively.

Consider the $\hat{l}_t = 1-10$cm integral scale eddy with velocity fluctuations on the order $\hat{u}' = 500-1000$m/s, from Section 2.3. For a hydrocarbon fuel mixture at $\hat{T} > 1000$K, in the wake of a strong shock wave, the laminar flame speed is $S_L \approx 10-20$m/s, see Appendix C. Thus, the flame outer-length scales are on the order $l_F = \nu/S_L \approx 5-10\mu$m. Therefore, $(\hat{l}_t/\hat{l}_F) \approx 1000-20000$ and $(u'/S_L) \approx 25-100$. For the Reynolds numbers in Section 2.3, $K_a \approx 1-25$ and $K_{a,\delta} \approx 0.01-0.25$. Also, $D_a \approx 1-40$. Thus, the expected combustion regime is the thin reaction zones regime. Unfortunately, this regime remains a very difficult challenge to model since the fluid motion time scales are on the same order as the chemical time scales, hence the motivation for adopting the CLEM-LES strategy in the next chapter. Current popular LES approaches for turbulent combustion, and their pitfalls, are described below. First, however, it is necessary to present the governing equations for LES in order to further elaborate the closure problems of modern modelling approaches.

2.5.2 Filtered LES equations

Starting with the full reactive N-S set of Eqs., (2.26)-(2.29), each term is filtered uniformly (spatially averaged) at a desired length scale, $\bar{\Delta}$. In most cases, but not necessarily, this length scale is equal to the finest grid spacing of the numerical scheme. Formally, a resolved spatially filtered quantity, $\overline{\phi}$ is defined as

$$\overline{\phi} = \int_{-\infty}^{\infty} G(r)\phi(x-r)dr \tag{2.42}$$

where $G(r)$ is the filter type. For uniform filtering, box filters are assumed for $G(r)$ [112]. Thus, $\overline{\phi}$ is effectively treated as a spatially averaged mean value of ϕ. Furthermore, density-weighted, or Favre-filtered quantities are introduced for variable density flows [112] such that

$$\tilde{\phi} = \frac{\overline{\rho\phi}}{\bar{\rho}}. \tag{2.43}$$

Therefore, upon spatially averaging each term in Eqs.(2.26)-(2.29), and then applying the Favre-averaging relations through Eq.(2.43), the filtered N-S equations that govern the large scale fluid motion for reactive compressible flows (i.e., conservation of mass, momentum, sensible and kinetic energy, and reactant mass) become:

$$\frac{\partial\bar{\rho}}{\partial t} + \boldsymbol{\nabla}\cdot(\bar{\rho}\tilde{\boldsymbol{u}}) = 0 \tag{2.44}$$

$$\frac{\partial(\bar{\rho}\tilde{\boldsymbol{u}})}{\partial t} + \boldsymbol{\nabla}\cdot(\bar{\rho}\tilde{\boldsymbol{u}}\otimes\tilde{\boldsymbol{u}}) + \nabla\bar{p} - \boldsymbol{\nabla}\cdot\underline{\bar{\boldsymbol{\tau}}} = -\boldsymbol{\nabla}\cdot\underline{\boldsymbol{\tau}}^{sgs} \tag{2.45}$$

$$\frac{\partial(\bar{\rho}\tilde{e})}{\partial t} + \boldsymbol{\nabla}\cdot((\bar{\rho}\tilde{e}+\bar{p})\tilde{\boldsymbol{u}} - \tilde{\boldsymbol{u}}\cdot\underline{\bar{\boldsymbol{\tau}}}) - \left(\frac{\gamma}{\gamma-1}\right)\boldsymbol{\nabla}\cdot\left(\frac{\bar{\rho}\nu}{P_r}\nabla\tilde{T}\right) = -Q\overline{\dot{\omega}} - \boldsymbol{\nabla}\cdot(\boldsymbol{H}^{sgs}+\boldsymbol{\sigma}^{sgs}+\boldsymbol{q}^{sgs}) \tag{2.46}$$

$$\frac{(\partial\bar{\rho}\tilde{Y})}{\partial t} + \boldsymbol{\nabla}\cdot(\bar{\rho}\tilde{\boldsymbol{u}}\tilde{Y}) - \boldsymbol{\nabla}\cdot\left(\frac{\bar{\rho}\nu}{S_c}\nabla\tilde{Y}\right) = \overline{\dot{\omega}} - \boldsymbol{\nabla}\cdot(\boldsymbol{Y}^{sgs}+\boldsymbol{\theta}^{sgs}) \tag{2.47}$$

where the equations of state become

$$\tilde{e} = \frac{\bar{p}/\bar{\rho}}{\gamma-1} + \frac{1}{2}(\tilde{\boldsymbol{u}}\cdot\tilde{\boldsymbol{u}}) + k^{sgs} \tag{2.48}$$

$$\bar{p} = \bar{\rho}\tilde{T}. \tag{2.49}$$

Also, the source terms, on the right side of Eqs.(2.45)-(2.47), are comprised of left over terms from the filtering process that require modelling:

$$\underline{\boldsymbol{\tau}}^{sgs} = \bar{\rho}(\widetilde{\boldsymbol{u}\boldsymbol{u}} - \tilde{\boldsymbol{u}}\tilde{\boldsymbol{u}}) \tag{2.50}$$

$$\boldsymbol{H}^{sgs} = \bar{\rho}(\widetilde{e\boldsymbol{u}} - \tilde{e}\tilde{\boldsymbol{u}}) + (\overline{p\boldsymbol{u}} - \bar{p}\tilde{\boldsymbol{u}}) \tag{2.51}$$

$$\boldsymbol{\sigma}^{sgs} = \widetilde{\boldsymbol{u}\cdot\underline{\boldsymbol{\tau}}} - \tilde{\boldsymbol{u}}\cdot\bar{\underline{\boldsymbol{\tau}}} \tag{2.52}$$

$$\boldsymbol{q}^{sgs} = \left(\frac{\gamma}{\gamma-1}\right)\left(\frac{\bar{\rho}\nu}{P_r}\nabla\tilde{T} - \overline{\frac{\rho\nu}{P_r}\nabla T}\right) \tag{2.53}$$

$$\boldsymbol{Y}^{sgs} = \bar{\rho}(\widetilde{\boldsymbol{u}Y} - \tilde{\boldsymbol{u}}\tilde{Y}) \tag{2.54}$$

$$\boldsymbol{\theta}^{sgs} = \frac{\bar{\rho}\nu}{S_c}\nabla\tilde{Y}_i - \overline{\frac{\rho\nu}{S_c}\nabla Y_i} \tag{2.55}$$

$$k^{sgs} = \frac{1}{2}(\widetilde{\boldsymbol{u}\cdot\boldsymbol{u}} - \tilde{\boldsymbol{u}}\cdot\tilde{\boldsymbol{u}}). \tag{2.56}$$

2.5.3 LES closure challenges

Filtering the N-S equations introduces many unclosed quantities, most of which are denoted with the superscript 'sgs'. All of these terms, and also the filtered reaction rate, $\bar{\dot{\omega}}$, require modelling. The subgrid stress and kinetic energy terms, $\underline{\boldsymbol{\tau}}^{sgs}$ and k^{sgs}, are relatively straightforward to close using a static Smagorinsky or dynamic Germano type turbulence model suitable for high R_e flows [112]. The subgrid enthalpy flux and convective species flux terms, $\boldsymbol{H}^{sgs}$ and $\boldsymbol{Y}^{sgs}$, are often approximated using rather ad hoc gradient assumptions [11, 12], which may be subject to error [11]. Furthermore, the remaining subgrid terms, $\boldsymbol{\sigma}^{sgs}$, $\boldsymbol{q}^{sgs}$, and $\boldsymbol{\theta}^{sgs}$, are often neglected altogether due to lack of available models [11, 119]. Finally, filtering the reaction rate, $\bar{\dot{\omega}}$, is where the greatest difficulty of turbulent combustion modelling lies. Modelling this term often requires very bold assumptions, such as perfect instantaneous mixing($K_{a,\delta} \gg 1$) or very fast chemistry ($K_a \ll 1$). For cases where $K_{a,\delta} < 1$ and $K_a > 1$ (or

$D_a \to 1$), both molecular mixing and chemical reaction become important to consider on the micro-scales. Furthermore, the reaction rates are very sensitive to the local temperature. When hot spots form on the micro-scales, the locally rapid increase in temperature may influence the overall large scale combustion. Since most turbulent combustion models only consider the average temperature over the entire LES cell for the computation of the reaction rates, the micro-scale combustion is effectively unaccounted for, or "washed out". The next section is a brief review of turbulent combustion models currently used to simulate supersonic combustion, which further highlights many of the pitfalls and difficulties in capturing the correct reaction rate, $\overline{\dot{\omega}}$, effectively.

2.5.4 Turbulent combustion models for LES of supersonic combustion problems

The following section gives a brief review of LES strategies that are typically applied to simulate problems which are turbulent, reactive, and highly compressible, containing rapid transients in both pressure and energy. These examples include strategies applied to the types of problems described in Chapter 1 (the detonation phenomena and compressible jet ignition involving hydrogen), and also to Supersonic Combustion Ramjet engine (SCRAMJET) operation. All of these problems involve both very large R_e and M_a. Details on the methods summarized here, as well as information on other methods which may be available for turbulent combustion of both subsonic and supersonic flow, can be found in the following references [11, 120–122].

Well-stirred reactor methods

Well-stirred reactor methods assume that combustion is entirely limited by the chemistry alone. That is, the turbulent mixing time scales are much quicker than the chemical reaction time scales ($D_a \ll 1$). This is the simplest assumption to implement numerically, as each computational cell can be assumed to be perfectly mixed at

each time step. Thus, each computational cell is treated as a constant volume reactor with a uniform reactant concentration and temperature at each time step. In this approximation, $\overline{\dot{\omega}} \approx \dot{\omega}$. Thus, Eq.(2.17) can be solved directly in each cell. This approach has been attempted [33, 38] to study irregular detonation propagation. Also, both investigations were supplemented by models to describe the unclosed turbulent mixing terms in Eqs.(2.50)-(2.56). Unfortunately, this approach has proven to be unsuccessful in capturing converged reaction rates. [33] was only able to reproduce the burning rate of unburned pockets for a methane-oxygen detonation at a very high resolution (600 cells per half reaction length). Furthermore, convergence beyond this resolution was not verified. At much lower resolutions (120 cells per half reaction length), the presence of unburned pockets in ethylene-oxygen detonations was not observed [38], suggesting a much faster than expected burning rate. Clearly, irregular detonations cannot be treated as well-stirred reactors. Thus, results from [33, 38] confirm the need to provide adequate closure to $\overline{\dot{\omega}}$.

Wrinkled flame and flamelet methods

Flamelet methods are at the opposite end of the regime spectrum from the well-stirred reactor regime. In the wrinkled flame or flamelet method, the chemical reaction time scales are much quicker than the rate at which turbulent energy is dissipated ($K_a \ll 1$). In this assumption, burning occurs instantly once the reactant is in contact with the flame surface. Thus, reaction rates are controlled and limited by the turbulent motions. The wrinkled flame can then be viewed as an ensemble of very thin laminar flames, or flamelets within each LES cell [11, 12]. The wrinkling of the flame causes increased reaction rates through increased surface area associated with the convolution of the flame. The reaction rates can then be easily estimated from the turbulence intensity of the flow. Unfortunately, this assumption does not hold for the current problems under investigation, where distributed or thin reaction zones are expected. Wrinkled flame techniques, however, are very popular and have been applied to a variety of supersonic turbulent combustion problems. This method

has been applied to model SCRAMJETs [123–125], large-scale hydrogen detonations [126, 127], and the early stages of fast flame acceleration [128–130]. As fast-flames accelerate toward DDT limits, however, they are expected to become more turbulent with much greater velocity fluctuations. Should the flow reach the *thin reaction zones regime*, when $K_a > 1$ and $K_{a,\delta} < 1$, the inner flame structure becomes disrupted by the turbulent motions present. Thus, the flamelet model is expected to longer remain applicable at some point within this regime. However, it is noted that it remains unclear to what extent into this regime, when $K_a > 1$, flame structures remain intact, and to what extent the flamelet models remain applicable.

Hybrid methods: the Eddy Dissipation Concept (EDC)

The Eddy Dissipation Concept (EDC) is an another approach that combines well-stirred reactor and flamelet methods in an attempt to model the full spectrum of regimes possible. The approach has been successfully applied to model supersonic jet ignition of pressurized hydrogen releases [91, 92]. It has also been used to model SCRAMJETs [131]. The advantage of the model is that it can be applied to both turbulent mixing controlled combustion regimes ($K_a \ll 1$), and also kinetically controlled combustion regimes ($K_{a,\delta} \gg 1$) [132]. For the mixing controlled regime, the chemical reactions are limited by the turbulent eddy dissipation rates [12, 133]. For the kinetically controlled regime, the fuel and oxidizer react as soon as they meet in a perfectly well stirred reactor within each LES cell at each time step [12]. This hybrid approach has also been applied to model DDT of hydrogen-air mixtures [60]. The findings of [60], however, have revealed that simulated detonation initiation events occurred much sooner compared to physical experiments. Although the model is computationally efficient, it fails to describe, accurately, the small scale diffusive mixing and combustion that occur as $D_a \to 1$. In fact, since reaction rates depend not only on the availability of reactants, but also largely on temperature, the appearance of hot spots which appear on the micro-scale are effectively washed out, as the temperature within each LES cell is taken as the average. Thus, contributions due to the

formation of micro-scale hot spots are not accounted for. For the problems described in Chapter 1, diffusive mixing and micro-scale combustion must be accounted for.

Flame thickening model

An alternative approach to modelling the turbulent scales, in the LES context, is to artificially thicken the flame structure such that it can be resolved at much lower resolutions than required by DNS [134]. In this approach, thickening is achieved by artificially increasing the diffusion coefficients by a factor F, which gives rise to increased flame thickness that can be easily resolved by solving directly the DNS Eqs.(2.26)-(2.29). This factor, F, must be chosen such that the desired turbulent burning rates are obtained for the resolution chosen. This requires experimental data, or resolved DNS data, for validation. Furthermore, a fundamental drawback of this method is that in order to maintain the theoretical laminar flame speed, S_L, the reaction rate, $\dot{\omega}$ must also be decreased by a factor of $1/F$ [134]. This is done in order to satisfy the requirement that laminar flame speed squared is proportional to product of diffusivity and reaction rate. Thus, $S_L \propto \sqrt{(FD)(\dot{\omega}/F)}$ [134]. Although this approach has been attempted to model DDT via shock-flame interaction [72], its application may be more appropriate for weakly compressible flows. Unfortunately, for highly compressible flows, the scaling of $\dot{\omega}$ by $1/F$ severely modifies the ignition delay and sensitivity of the reactant gas mixture to compression arising from shocks. Furthermore, the interaction between turbulent mixing and the chemistry is altered since the Damkholer number must also decrease by a factor of $1/F$ [134]. This leads to an artificial decrease in wrinkling of the flame front, and hence the available surface area of the flame. Thus, enhanced mixing arising from turbulent instabilities may be filtered out. While this approach addresses the problem of resolving the turbulent scales in DNS, it is not be suitable for modelling problems where capturing the correct ignition delays and turbulent-flame interactions may both be important.

Implicit LES (ILES)

ILES was previously applied to model jet ignition of pressurized hydrogen releases [87] and also to model blast waves involving TNT explosions [135]. This approach, however, assumes that discretization errors in the numerical scheme for solving the N-S equations implicitly account for the contributions of the turbulent scales [136]. Thus, intimate knowledge of how numerical diffusion scales with resolution, and what expected burning rates would be are both required in order to have confidence on solution results. In this sense, the scheme is essentially unresolved DNS. For this reason, ILES approaches are generally not adopted in reactive flows.

Statistical approach: Filtered Density Functions (FDF)

In this approach, which is analogous to Joint-Probability Density Function (PDF) modelling in RANS, it is assumed that the combustion is inherently statistical in nature. Here, rather than solve the traditional transport equations for mass, momentum, energy, and reactive scalars in 3D space, a transport equation is instead solved which describes the evolution of an LES-filtered joint PDF (the joint FDF) of all the reactive scalars and the temperature (or enthalpy) [121]. Furthermore, this transported joint FDF depends on not only space and time, but all independent scalars, and must be integrated accordingly. For supersonic combustion, this approach has been applied almost exclusively to SCRAMJET simulations [137–141]. It is an appropriate technique for treating the thin reaction zones regime which is highly stochastic in nature [132]. Furthermore, the technique inherently provides closure to the momentum equation and chemical reaction terms [132]. The main drawback is that due to the large number of possible dimensions to handle, the model is not easily implemented into standard flow solver frameworks. Furthermore, simulations can be computationally demanding [132]. Although simplifications have been proposed to reduce the computational overhead by the use of single-point statistics, doing so increases the difficulty of modelling the turbulent mixing and reaction rates. Furthermore, this simplification can lead to significant errors in the computations [119, 132].

Chapter 3

CLEM-LES Methodology

3.1 Large Eddy Simulation (LES) Closure

3.1.1 Overview

In this chapter, the details of the CLEM-LES methodology are presented. Specifically, closure to the LES Eqs.(2.45)-(2.48) is obtained at two different scales; the *supergrid* and the *subgrid* scales. As such, the content of this chapter is divided accordingly. In this section, various closure models are applied directly to the large scales, on what is referred to as the supergrid. These closure models predominantly account for the contributions of unresolved velocity fluctuations to the large-scale momentum and energy conservation equations. Then, in Section 3.2, the details of the CLEM numerical *subgrid* model are presented. In the current formulation, the sole function of the CLEM subgrid simulation is to provide closure to the reaction rate on the supergrid, through $\overline{\dot{\omega}}$ in Eqs.(2.46) and (2.47). In fact, it should be noted here that Eq. (2.47) is simply not solved on the supergrid. Instead, all reactant evolution information is handled, and stored, entirely on the subgrid, see Section 3.2. Section 3.3 then describes the numerical implementation and procedural algorithm of the CLEM-LES formulation. Finally, known limitations of the CLEM-LES approach are

presented in Section 3.4.

The LES formulation described in this chapter largely follows previous LEM-LES implementations [97, 102, 119] with a few minor differences in formulation and implementation. The most significant and novel contribution presented here is the treatment of pressure on the subgrid, and its influence on reaction rates, which allows for adequate closure of the reaction rate in the presence of shocks and strong expansions that evolve on the supergrid.

3.1.2 LES equations solved on the supergrid

In the formulation adopted here, several models are required for the closure of the 'sgs' terms and reaction rate, $\overline{\dot{\omega}}$, in Eqs.(2.45)-(2.48). First, the resolved filtered viscous stress, $\underline{\bar{\boldsymbol{\tau}}}$, is expressed in terms of the resolved filtered density, $\bar{\rho}$, and the Favre-averaged velocity, $\tilde{\boldsymbol{u}}$, through

$$\underline{\bar{\boldsymbol{\tau}}} = \bar{\rho}\nu\left(\nabla\tilde{\boldsymbol{u}} + (\nabla\tilde{\boldsymbol{u}})^T - \frac{2}{3}(\boldsymbol{\nabla}\cdot\tilde{\boldsymbol{u}})\underline{\boldsymbol{I}}\right). \tag{3.1}$$

The subgrid stress term, $\boldsymbol{\tau}^{sgs}$, in the momentum Eq.(2.45), is then closed by applying a linear-eddy-viscosity model [112]. This model is analogous to the Newtonian fluid assumption, where the subgrid stress is assumed to vary linearly with the averaged fluid strain rate, for a given fluid density, through a turbulent viscosity:

$$\underline{\boldsymbol{\tau}}^{sgs} \approx \bar{\rho}\nu_t\left(\nabla\tilde{\boldsymbol{u}} + (\nabla\tilde{\boldsymbol{u}})^T - \frac{2}{3}(\boldsymbol{\nabla}\cdot\tilde{\boldsymbol{u}})\underline{\boldsymbol{I}}\right). \tag{3.2}$$

Next, the subgrid enthalpy flux term, $\boldsymbol{H}^{sgs}$, is assumed to be gradient driven (on the supergrid) by the turbulent viscosity through

$$\boldsymbol{H}^{sgs} \approx -\left(\frac{\gamma}{\gamma-1}\right)\boldsymbol{\nabla}\cdot\left(\frac{\bar{\rho}\nu_t}{P_{r,t}}\nabla\tilde{T}\right). \tag{3.3}$$

It should be noted that although this term does not contribute to the diffusive process on the subgrid, it is formally retained on the supergrid to ensure full closure of Eq.

(2.46). The sole purpose of the subgrid is to provide closure to $\overline{\dot{\omega}}$. Then, upon neglecting the remaining subgrid terms, $\boldsymbol{\sigma}^{sgs}$ and $\boldsymbol{q}^{sgs}$, due to lack of available models [11], the filtered LES equations become:

$$\frac{\partial \bar{\rho}}{\partial t} + \boldsymbol{\nabla} \cdot (\bar{\rho}\tilde{\boldsymbol{u}}) = 0 \tag{3.4}$$

$$\frac{\partial(\bar{\rho}\tilde{\boldsymbol{u}})}{\partial t} + \boldsymbol{\nabla} \cdot (\bar{\rho}\tilde{\boldsymbol{u}} \otimes \tilde{\boldsymbol{u}}) + \nabla \bar{p} - \boldsymbol{\nabla} \cdot \bar{\rho}(\nu + \nu_t)\left(\nabla\tilde{\boldsymbol{u}} + (\nabla\tilde{\boldsymbol{u}})^T - \frac{2}{3}(\boldsymbol{\nabla} \cdot \tilde{\boldsymbol{u}})\underline{\boldsymbol{I}}\right) = 0 \tag{3.5}$$

$$\frac{\partial(\bar{\rho}\tilde{e})}{\partial t} + \boldsymbol{\nabla} \cdot \left((\bar{\rho}\tilde{e} + \bar{p})\tilde{\boldsymbol{u}} - \tilde{\boldsymbol{u}} \cdot \underline{\bar{\boldsymbol{\tau}}}\right) - \left(\frac{\gamma}{\gamma - 1}\right)\boldsymbol{\nabla} \cdot \left(\bar{\rho}(\frac{\nu}{P_r} + \frac{\nu_t}{P_{r,t}})\nabla\tilde{T}\right) = -Q\overline{\dot{\omega}} \tag{3.6}$$

Next, the subgrid kinetic energy from Eq.(2.48), k^{sgs}, is modelled using a one-equation Localized subgrid Kinetic energy Model (LKM) approach [142, 143]. In this approach, the system of equations, (3.4)-(3.6), are supplemented by a transport equation which describes the diffusion, advection, production, and dissipation of the subgrid kinetic energy associated with subgrid velocity fluctuations in the flow:

$$\underbrace{\frac{\partial(\bar{\rho}k^{sgs})}{\partial t}}_{\substack{\text{local rate of} \\ \text{change in subgrid} \\ \text{kinetic energy}}} + \underbrace{\boldsymbol{\nabla} \cdot (\bar{\rho}\tilde{\boldsymbol{u}}k^{sgs})}_{\substack{\text{advective} \\ \text{flux}}} - \underbrace{\boldsymbol{\nabla} \cdot \left(\frac{\bar{\rho}\nu_t}{P_{r,t}}\nabla k^{sgs}\right)}_{\substack{\text{diffusive} \\ \text{flux}}} = \underbrace{\dot{P}}_{\substack{\text{production} \\ \text{rate}}} - \underbrace{\bar{\rho}\epsilon}_{\substack{\text{dissipation} \\ \text{rate}}} \tag{3.7}$$

Here, the subgrid kinetic energy is produced at the same rate from which it is dissipated from the large scales through the turbulent viscosity. Hence, the rate of production of subgrid kinetic energy is given by

$$\dot{P} = \bar{\rho}\nu_t\left(\nabla\tilde{\boldsymbol{u}} + (\nabla\tilde{\boldsymbol{u}})^T - \frac{2}{3}(\boldsymbol{\nabla} \cdot \tilde{\boldsymbol{u}})\underline{\boldsymbol{I}}\right) \cdot (\nabla\tilde{\boldsymbol{u}}) \tag{3.8}$$

and the dissipation rate is modelled as

$$\epsilon = C_\epsilon (k^{sgs})^{3/2}/\bar{\Delta}. \tag{3.9}$$

Finally, a Smagorinsky-type model [112] is applied to link the turbulent viscosity to the unresolved velocity fluctuations, and thus the subgrid kinetic energy, through

$$\nu_t = C_\nu \sqrt{k^{sgs}}\bar{\Delta}. \tag{3.10}$$

Here, $\bar{\Delta}$ is the LES filter size. For simplicity, it is assumed that $\bar{\Delta} = b$, where b is the grid spacing. It is noted, however, that this assumption may introduce errors at fine-coarse cell interfaces when coupled with Adaptive-Mesh-Refinement (AMR) [144, 145]. Further discussion and justification for this choice is provided in Section 3.3. Also, it should be noted that C_ν and C_ϵ are model constants which require calibration. It is possible to obtain C_ν and C_ϵ dynamically according to local flow conditions [146, 147], however the dynamic procedure requires more computational expense and has additional requirements to ensure numerical stability [146]. Also, the presence of strong density gradients (i.e., shocks) may further introduce instability in the dynamic method [143]. For these reasons the dynamic version is not considered here, thus C_ν and C_ϵ must be prescribed. Finally, to close the system of Eqs.(3.5)-(3.6), the chemical reaction term, $\overline{\dot{\omega}}$, requires closure. This is done through the application of the CLEM subgrid within each LES cell.

3.1.3 Determination of the supergrid model constants

Although the constants C_ν and C_ϵ require calibration, it is possible to obtain an approximate estimate by applying Lilly's method [148]. This method applies Kolmogorov's hypothesis [149], which describes the kinetic energy and dissipation spectra associated with isotropic incompressible turbulence. At sufficiently high R_e, velocity fluctuations at high wave numbers (small scales), in the *inertial subrange*, follow universal behaviour such that large scale turbulence transfers kinetic energy to smaller scales through an *energy cascade* according to a well known -5/3 power law. A model which describes this power law behaviour in the inertial subrange, and also includes a description of the kinetic energy behaviour at the integral and dissipation scales, L and η, is given by [112]:

$$E(\kappa) = C_\kappa \epsilon^{2/3} \kappa^{-5/3} f_L(\kappa L) f_\eta(\kappa \eta) \tag{3.11}$$

where C_κ is the Kolmogorov constant. Typically, C_κ is estimated from experiments to be ~ 1.5, however published values range anywhere from 1.2 to 4 [150]. This

expression for $E(\kappa)$ describes the kinetic energy associated with velocity fluctuations at specific wave numbers, or frequencies, κ. In addition to the Kolmogorov power-law spectrum, $C_\kappa \epsilon^{2/3} \kappa^{-5/3}$, Eq.(3.11) also contains model behaviour for the energy-containing range of scales ($\kappa \to \pi/L$) and the dissipation scales ($\kappa \to \pi/\eta$), given by $f_L(\kappa L)$ and $f_\eta(\kappa\eta)$, respectively. For the lowest wave numbers ($\kappa \to \pi/L$) in the energy-containing range, $f_L(\kappa L)$ can be modelled by von Karman's spectrum [112, 151]:

$$f_L(\kappa L) = \left(\frac{\kappa L}{\sqrt{(\kappa L)^2 + c_L}} \right)^{11/3} \tag{3.12}$$

where $c_L \approx 6.78$ for high R_e [112]. At high wave numbers ($\kappa \to \pi/\eta$) in the dissipation range, $f_\eta(\kappa\eta)$ can be modelled using Pao's spectrum [152]:

$$f_L(\kappa\eta) = \exp\left(-\frac{3}{2} C_\kappa (\kappa\eta)^{4/3} \right). \tag{3.13}$$

An example of an arbitrary function, $E(\kappa)$, across the range of scales, $\kappa = \pi/L$ to π/η, is illustrated in Figure 3.1. A key feature of $E(\kappa)$ is that for $\kappa \ll \pi/L$, $f_L(\kappa L) \to 1$, and for $\kappa \gg \pi/\eta$, $f_\eta(\kappa\eta) \to 1$. Thus, for high R_e flows that contain wave numbers spanning several orders of magnitude, a filter length scale, $\bar{\Delta}$, placed in the inertial range would be expected to have a wave number such that $\pi/L \ll \pi/\bar{\Delta} \ll \pi/\eta$. Thus, the energy spectrum would be approximated by

$$E(\kappa) \approx C_\kappa \epsilon^{2/3} \kappa^{-5/3} \tag{3.14}$$

throughout most relevant scales of interest. Following the approach adopted by [142, 143, 148, 153], the subgrid kinetic energy, k^{sgs}, is simply the total kinetic energy from $\kappa = \pi/\bar{\Delta}$ to $\kappa \to \infty$, as indicated in Figure 3.1. Thus,

$$k^{sgs} = \int_{\pi/\bar{\Delta}}^{\infty} E(\kappa) \mathrm{d}\kappa = \frac{3 C_\kappa}{2} \left(\frac{\epsilon \bar{\Delta}}{\pi} \right)^{2/3}. \tag{3.15}$$

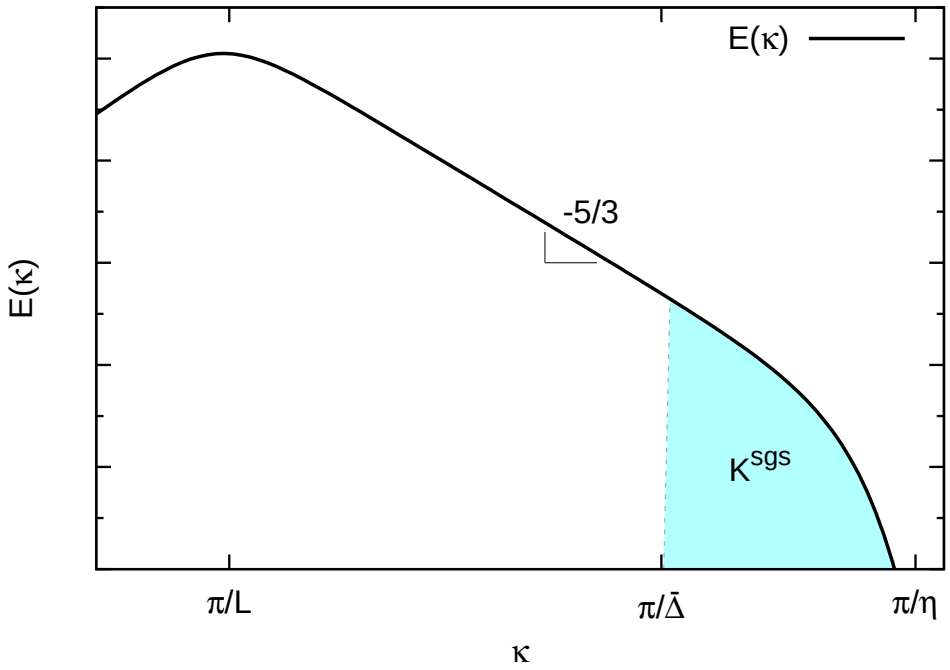

Figure 3.1: Energy spectrum for isotropic turbulence. $E(\kappa)$ is the kinetic energy of the turbulent motions that exist at various wave numbers, κ.

Isolating for the total dissipation rate, ϵ, and then equating (3.15) and (3.9) yields an expression for C_ϵ in terms of the Kolmogorov constant, C_κ:

$$C_\epsilon = \pi \left(\frac{2}{3C_\kappa} \right)^{3/2}. \tag{3.16}$$

This expression was also obtained in [142, 148].

To determine C_ν, one can consider the dissipative energy spectrum [112] given by

$$D(\kappa) = 2\nu\kappa^2 E(\kappa) \tag{3.17}$$

where the total dissipation is

$$\epsilon = \int_0^\infty D(\kappa) \mathrm{d}\kappa. \tag{3.18}$$

Following the approach by [142, 148, 154, 155], an eddy viscosity model can be introduced where energy dissipation occurs on the resolved scales through a turbulent

viscosity, ν_t, such that

$$\epsilon^{sgs} = \int_0^{\pi/\bar{\Delta}} 2\nu_t \kappa^2 E(\kappa) \mathrm{d}\kappa = \frac{3}{2}\nu_t C_\kappa \epsilon^{2/3} \left(\frac{\pi}{\bar{\Delta}}\right)^{4/3} \tag{3.19}$$

Then, by assuming that the subgrid energy dissipation rate, ϵ^{sgs}, is equivalent to the total dissipation rate, $\epsilon^{sgs} \approx \epsilon$ [148, 154–156], and equating (3.19) with (3.15), one can derive an expression for ν_t in terms of k^{sgs}:

$$\nu_t = \frac{1}{\pi}\left(\frac{2}{3C_\kappa}\right)^{3/2} \sqrt{k^{sgs}}\bar{\Delta}. \tag{3.20}$$

This expression is equivalent to that obtained in [142, 156], and holds a very similar form to that obtained from [148] applied to the Smagorinsky model [112, 155]. Finally, equating with Eq.(3.10) yields an expression for C_ν, also in terms of the Kolmogorov constant, C_κ:

$$C_\nu = \frac{1}{\pi}\left(\frac{2}{3C_\kappa}\right)^{3/2} \tag{3.21}$$

Thus, for $C_\kappa \approx 1.5$, $C_\epsilon = 0.93$ and $C_\nu = 0.094$.

3.2 The CLEM Subgrid Model

3.2.1 Overview

In order to circumvent the problem of modelling the reaction rates as $D_a \to 1$, a solution methodology based on the Linear Eddy Model [157–163] formulation as a subgrid model for LES [97, 98, 119, 164–168] is applied. In this approach, the reaction-diffusion process is simulated in a one-dimensional problem at the subgrid level within each LES grid. Thus, information regarding local hot spots and contact surfaces on the molecular level are accounted for and resolved. Furthermore, to simulate the effect of turbulent mixing, the one-dimensional flow field is randomly "stirred" by linear eddies according to a Probability Density Function (PDF) [162]. The effect of the resulting compressive strain on the flow field due to the presence of the random subgrid

eddies is to reproduce the turbulent diffusivity of the flow based on local properties of the flow at the LES level. The advantage of the model is that closure is easily provided for the species and energy equations at the LES level [119]. In addition, Lewis number effects can be accounted for if desired. Furthermore, restrictive assumptions such as infinitely fast mixing or chemical reactions, are not required. Finally, the LEM model has proven to be effective for both non-premixed [98, 164, 169] and premixed [99, 102, 165, 166, 168, 170–172] combustion applications. Although there have been no known attempts to use this method to simulate combustion problems involving large M_a, which are highly *compressible*, the model's capability to capture high R_e *inert* mixing has been demonstrated in simulations of unreactive supersonic shear layers [100].

3.2.2 Governing equations

For the CLEM subgrid modelling strategy, the large scale pressure evolution is solved separately from the small scale mixing and reactions. This is achieved through appropriate coupling of the pressure and energy fields. Thus, Eqs.(3.4) through (3.7), henceforth referred to as the *supergrid*, are solved on the large scales without the chemical reaction terms. The subgrid model is then applied to simulate the small scale molecular mixing and chemical reactions, which thus provides $\overline{\dot{\omega}}$ to the supergrid as a source term. In this particular approach, the subgrid model is a one-dimensional representation of the flow field within each supergrid cell whose orientation is assumed to be aligned in the direction of local flow. Thus, each supergrid cell, which requires closure, contains one subgrid domain. A good general summary of the model formulation for weakly compressible flows (in the context of LEM-LES) is found in [97] and a more comprehensive description of the model is found in [119].

In order to derive the subgrid model formulation, pressure gradients are locally neglected within the small scales of each supergrid cell. Thus, it is assumed that pressure waves travel much faster than the physical expansion or contraction of the local fluid relative to its convective motion. The result is that low-Mach number approxima-

tions [173] are applied to treat the small scales while the pressure on the large scales is treated using piece-wise constant discretization of the flow field. Therefore, the pressure field evolution is solved entirely on the supergrid. Also, the local temporal pressure changes determined from the supergrid are prescribed to the subgrid, as a source term, in order to account for energy changes due to rapid compression or expansions. In this sense, pressure wave locations and strengths are captured only on the supergrid. Furthermore, the subgrid energy levels within each supergrid cell responds accordingly in spatially uniform, but temporally evolving, pressure systems.

This formulation was previously applied to determine ignition limits of idealized non-turbulent and rapidly expanding hydrogen jets [49]. The previous model formulation, however, contained only pressure and energy coupling in one-direction; from the large scales to the small scales. Thus, the model could only be used to determine the onset of ignition, and not the subsequent influence of ignition on the fluid evolution. Therefore, this current model serves as an extension to the previous work [49] by providing two-way coupling between the large scale pressure evolution and small scale mixing and reactions.

The system of equations that is solved on the subgrid is formally obtained by neglecting pressure gradients in the system of Eqs.(2.26) to (2.29) and expressing the energy conservation equation, (2.28), in terms of enthalpy. Also, the subgrid equations are expressed along fluid particle paths and thus make use of the material derivative, where $\frac{D\phi}{Dt} = \frac{\partial\phi}{\partial t} + u\frac{\partial\phi}{\partial x}$. Thus, for the subgrid system, the conservation of enthalpy and reactant mass, along particle paths, are expressed in non-dimensional form as:

$$\underbrace{\rho\frac{DT}{Dt}}_{\substack{\text{rate of change}\\ \text{of enthalpy along}\\ \text{a particle path}}} - \underbrace{\left(\frac{\gamma-1}{\gamma}\right)\dot{p}}_{\substack{\text{rate of change of}\\ \text{energy due to local}\\ \text{pressure changes}}} - \underbrace{\rho\frac{\partial}{\partial m}\left(\rho\alpha\frac{\partial T}{\partial m}\right)}_{\substack{\text{heat diffusion}\\ \text{to neighbouring}\\ \text{fluid elements}}} = -\underbrace{\left(\frac{\gamma-1}{\gamma}\right)Q\dot{\omega}}_{\substack{\text{heat release}}} + \dot{F}_T \tag{3.22}$$

$$\underbrace{\rho\frac{DY}{Dt}}_{\substack{\text{rate of change of}\\ \text{reactant density along}\\ \text{a particle path}}} - \underbrace{\rho\frac{\partial}{\partial m}\left(\rho\frac{\alpha}{L_e}\frac{\partial Y}{\partial m}\right)}_{\substack{\text{reactant diffusion}\\ \text{to neighbouring}\\ \text{fluid elements}}} = \dot{\omega} + \dot{F}_Y \tag{3.23}$$

Here, the source terms, $\dot{F}_T$ and $\dot{F}_Y$ account for the effect of turbulence on the subgrid in the form of random "stirring" events [162] and m is a one-dimensional mass weighted coordinate [49] whose transformation to Cartesian spatial coordinates is given by

$$m(x,t) = \int_{x_o}^{x} \rho(x,t)dx. \tag{3.24}$$

By convention, since the subgrid nodes are assumed to be aligned in the same direction as the mean flow velocity, this implies that the positive x direction on the subgrid corresponds to the local positive $\tilde{\boldsymbol{u}}$ direction on the supergrid. Finally, the subgrid model formulation in this study differs from previous LEM-LES implementations [97, 102, 119] for two reasons. First, the pressure source term, $\dot{p}$, in Eq.(3.22) accounts for the energy changes associated with rapid changes in pressure. Second, the 1-D subgrid domains are formulated with Lagrangian mass-weighted coordinates, m, as given by Eq.(3.24). This is done in order to account for not only the expansion or contraction of the fluid along particle paths, but also changes in spatial distance between computational nodes on the subgrid (dx).

3.2.3 Subgrid-supergrid coupling through source terms

The two-way coupling between the large scale hydrodynamics (the supergrid) and the small scale mixing and reaction (the subgrid) is achieved through source terms in the energy equations, (3.6) and (3.22). Specifically, this is done by maintaining consistent pressure changes between the two energy fields. First, the large scale fluid flow, the supergrid, provides the local pressure changes in each cell at each time step to the subgrid model. For isentropic flow in the form of expansions and weak compressions, the pressure term in Eq.(3.22) is solved exactly by considering its contribution to the enthalpy change separately from the diffusion/reaction terms via operator splitting. Thus the enthalpy change of each subgrid node due to isentropic pressure changes is accounted for through

$$\frac{T_2}{T_1} = \left(\frac{p_2}{p_1}\right)^{(\gamma-1)/\gamma} \tag{3.25}$$

The diffusion terms of Eq.(3.22) are then solved separately at the updated, and spatially uniform, pressure for the entire subgrid domain within a supergrid cell. To treat irreversible shock-waves, however, the post-shock temperature of each subgrid node is determined according to the Rankine-Hugoniot jump conditions through

$$T_2 - T_* = \left(\frac{\gamma - 1}{2}\right)(p_2 + p_*)\left(\frac{1}{\rho_*} - \frac{1}{\rho_2}\right) \tag{3.26}$$

where the subscript * denotes a pre-compression reference state. In this approach, if the local flow experiences more than 0.1% pressure increase, Eq.(3.26) is solved in order to update the temperature and density of each subgrid node, according to the pressure increase, such that the equation of state (2.31) is also satisfied. This threshold is a very conservative estimate, since weak shocks can usually be treated as isentropic. In fact, the entropy generated across weak shocks are through third order effects as pressure and density increase [174]. Furthermore, the numerical shock is captured on several supergrid points, each one having a relatively small jump in pressure, even though the overall change may not be small. Thus, the value of 0.1%, presented here, was found through trial and error to work well for $\gamma = 1.2 - 1.4$. Then, if the local flow does not compress sufficiently, isentropy is assumed and Eq.(3.25) is solved. Also, the reference state (denoted by *) is reset accordingly. In order to implement this procedure, subgrid diffusion, chemical reactions, and stirring events are frozen during the irreversible compression process since a pre-compression reference state is needed.

At the end of the subgrid simulation, the model provides the energy contribution due to chemical reactions to the supergrid. This is done by prescribing the reaction rate exactly in Eq.(3.6) according to the precise amount of reactant mass consumed during the subgrid simulation. Thus,

$$\overline{\dot{\omega}} = \frac{\Delta(\rho Y)_{\text{subgrid}}}{\Delta t_{\text{supergrid}}} \tag{3.27}$$

where for each supergrid cell:

$$(\rho Y)_{\text{subgrid}} = \frac{\sum_{i=1}^{N} m_i Y_i}{V_{\text{cell}}}. \tag{3.28}$$

A key feature of this two-way energy-coupling is that the pressures (and consequently, the internal energies per unit cell volume) of both the subgrid and the corresponding supergrid cell are always returned to the same value. This ensures that energy, along with mass, is always conserved.

3.2.4 Turbulent stirring (LEM)

For the Linear Eddy Model (LEM), the turbulent "stirring" [162] on the subgrid is represented by the source terms, $\dot{F}_T$ and $\dot{F}_Y$ in Eqs.(3.22) and (3.23). The actual "stirring" events, however, are implemented as a series of random instantaneous re-mapping procedures. The remapping procedure is designed to simulate the effect that a multi-dimensional eddy would have on a one-dimensional sample of the flow field. In order to achieve this, a *triplet map* is implemented, as detailed by [162]. In this procedure, fluid properties are re-mapped in such a way that mass is conserved. The effect of this re-mapping procedure on a 1-D sample of a flow field is illustrated in Figure 3.2.

In order to implement the mapping procedure, three random variables are needed; the size of an eddy, its location, and the time of appearance. The location of each eddy is simply chosen randomly inside each subgrid domain. However, its size, l, is randomly determined according to a PDF which is derived from Kolmogorov scaling laws associated with turbulence dissipation. For eddies ranging in size from the integral scale of the LES filter width, $\bar{\Delta}$, to the Kolmogorov scale, η, the PDF of eddy sizes is given by [162]:

$$f(l) = \frac{(5/3)l^{-8/3}}{(\eta^{-5/3} - \bar{\Delta}^{-5/3})}. \tag{3.29}$$

Finally, the frequency of eddy stirring events is determined by considering a turbulent

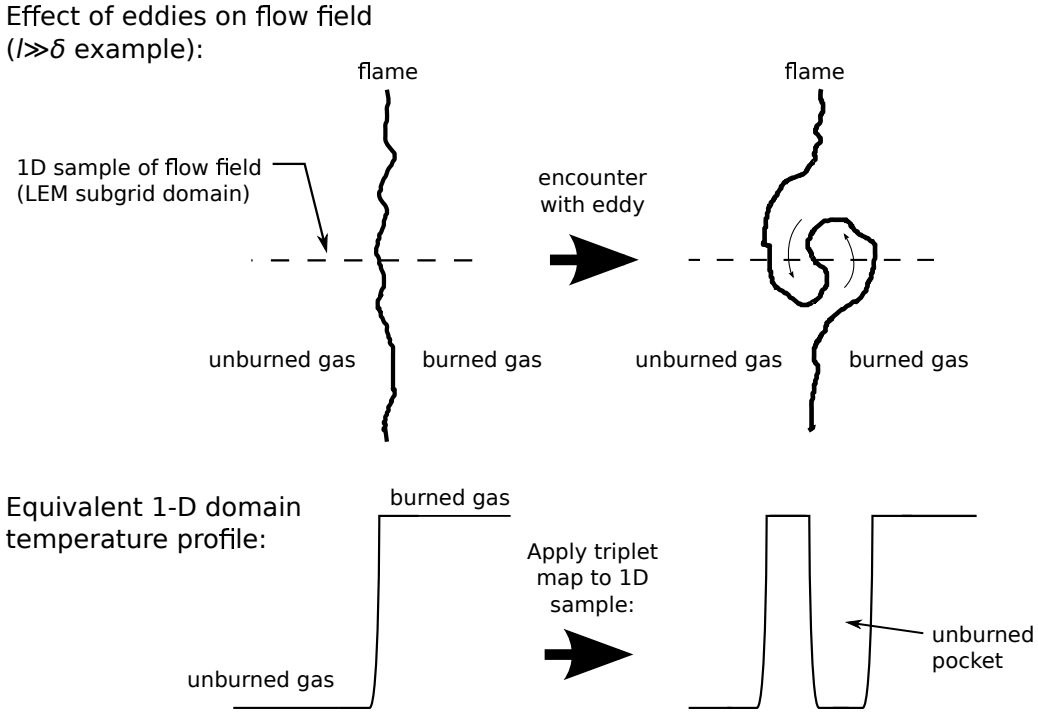

Figure 3.2: Representation of LEM triplet map to model eddies on a 1D flow field. In this example, the eddy size (l) is much bigger than the flame thickness (δ).

diffusivity resulting from a random walk of re-mapping events [162]. By considering this diffusivity as an analogue to the diffusivity resulting from random collisions of molecules in a gas [175, 176], a turbulent diffusivity of "stirring" events can derived:

$$D_T = \frac{2}{27}\lambda \int_{\eta}^{\bar{\Delta}} l^3 f(l) dl \tag{3.30}$$

where the Kolmogorov scale is estimated from [177]

$$\eta = \left(\frac{\nu^3}{\epsilon}\right)^{1/4} \tag{3.31}$$

Also, the turbulent diffusivity can be expressed in terms of the turbulent viscosity ν_t [178], which is also readily available in LES:

$$D_T = \frac{\nu_t}{S_{c,t}} \tag{3.32}$$

where $S_{c,t}$ is a single constant whose value is typically assumed to be 1.0 [178].

Eqs.(3.30) and (3.32) can then be equated in order to determine the frequency of eddy stirring events per unit space, λ. The time between stirring events is then simply

$$\Delta t_{\text{stir}} = 1/(\lambda \bar{\Delta}). \tag{3.33}$$

Finally, it should be noted that one fundamental difference between the current implementation and previous implementations [98, 99, 102, 119], is that the re-mapping procedure [162] is applied to a subgrid domain consisting of discreet nodes, each having their own mass-weighted coordinate location. Thus, the eddy size and location, which is first determined in Cartesian coordinates, must be transformed to the mass-weighted coordinate system through equation (3.24). It is possible that this procedure may introduce some error compared to their Cartesian counterpart, due to the discreet nature of the mapping procedure. The effect of this error, however, is believed to be minimal and should converge to the same solution as its Cartesian counterpart upon sufficient resolution of the subgrid. Furthermore, previous investigation [162] suggests that the turbulent diffusivity D_T has more dependence on the occurrence of the stirring event itself, rather than the specific mapping procedure applied. A comparison of the triplet mapping procedure for a hypothetical random eddy, as applied to a linear profile in ρ, for both a Cartesian grid and an equivalent mass-weighted grid is shown in Figure 3.3. Also shown, is the exact continuous map [162] which has been applied to both coordinate systems. Formally, the exact triplet map applied to a random eddy, which spans from $x = x_0$ to $x = x_0 + l$ is expressed as

$$\phi_2(x) = \begin{cases} \phi_1(3x - 2x_0) & x_0 \leq x \leq x_0 + l/3, \\ \phi_1(-3x + 4x_0 + 2l) & x_0 + l/3 \leq x \leq x_0 + 2l/3, \\ \phi_1(3x - 2x_0 - 2l) & x_0 + 2l/3 \leq x \leq x_0 + l, \\ \phi_1(x) & \text{otherwise.} \end{cases} \tag{3.34}$$

where ϕ_1 and ϕ_2 represent the various properties (ρ, T, ρ_*, T_*, Y) before and after the stirring process, respectively. For the example in Figure 3.3, relatively good agreement is observed between the Cartesian stirring and the mass-weighted stirring,

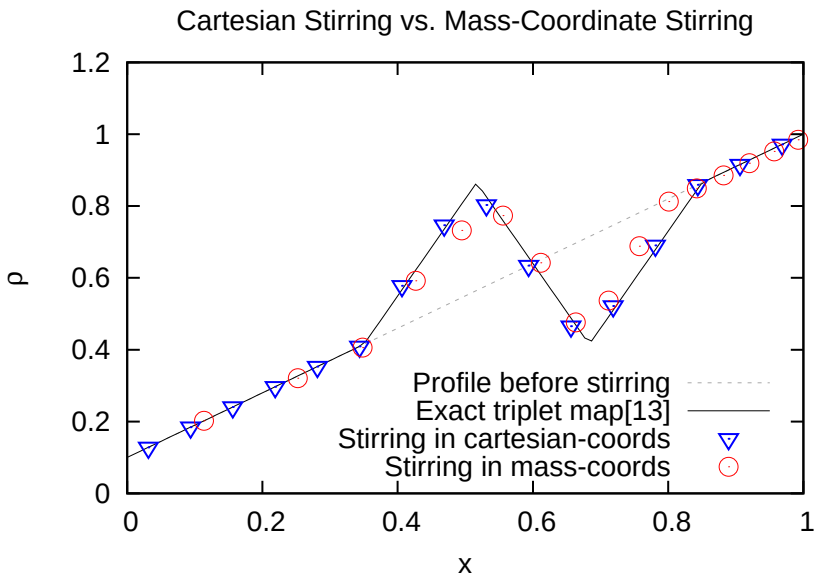

Figure 3.3: Comparison of an exact triplet mapping procedure[162] applied to a discreet Cartesian grid and a mass-weighted grid.

although some deviation does exist. It should be further noted, however, that a full investigation of this mapping procedure on wide range of density profiles, and number of subgrid nodes, has not been fully investigated.

3.2.5 Large scale advection (splicing)

Once the LEM domains evolve across each LES time step, the large scale advection of LEM elements is handled by transferring elements to or from neighbouring cells through a splicing procedure [119]. This is easily implemented and satisfies the basic mass conservation requirement since the mass flux ($\bar{\rho}\tilde{\boldsymbol{u}}$) across each LES cell face is known. Unfortunately, the method has been reported to add spurious diffusion to flows which are predominantly oblique to the grid direction [119]. Recently, this limitation has been addressed by considering a LEM domain for each Cartesian direction within each supergrid cell (LEM3D) [178]. Since this approach doubles or triples the computational expense of the simulation for 2D or 3D flows, LEM3D is not considered here. Furthermore, the flows considered in the remainder of the thesis are predominantly aligned with the grid direction, which should retain spurious

diffusion errors to a minimum. For the current implementation, following [119], the order of which elements are transferred is done according to the magnitude of the mass flux across each LES cell face. First, the LEM elements are transferred out of each LES cell through each face from the largest mass flux out to the least. Since the LEM domains are aligned with the local flow velocity, by convention, the LEM elements are moved out from the right side of each LEM domain. If an element is to be spliced, or divided into two new elements, such that the exact 1D-mass of elements transferred is equal to $(\bar{\rho}\tilde{\boldsymbol{u}})\Delta t$ across a particular face, the new elements both take on the same value of ρ, T, p, and Y as the original element. This is also true for the pre-compression reference state variables ρ_*, T_*, and p_*. Next, the LEM elements enter their destination cells through each LES cell face from the largest mass flux in to the least. Finally, to ensure that each LES cell has the same number of LEM cells of equally spaced mass coordinates, a re-gridding procedure is applied [119] prior to advancing the LEM simulation over next LES time step. See Figure 3.4 for an illustration of the splicing and re-gridding procedure.

3.2.6 Re-gridding in mass-coordinates

In order to solve the diffusive terms of Eqs.(3.22) and (3.23), in the current implementation, a uniform grid of equal mass-weighted coordinate spacing, Δm, is required for the LEM domains. Thus, prior to the diffusion/reaction (and stirring) process, each LEM domain is re-gridded such that each LES cell contains an equal number of LEM elements. Also, the procedure is only applied after the pressures of the LEM elements are updated. This ensures a uniform pressure in the LEM domain. First, suppose there are originally N subgrid elements in the cell. The grid spacing, Δm, is then computed from

$$\Delta m = \sum_{i=1}^{N} m_i/N. \tag{3.35}$$

The mass per unit area of each new LEM element, with index j, is simply $m_j = \Delta m$. Then, for each new jth element, which comprises of M original or spliced elements,

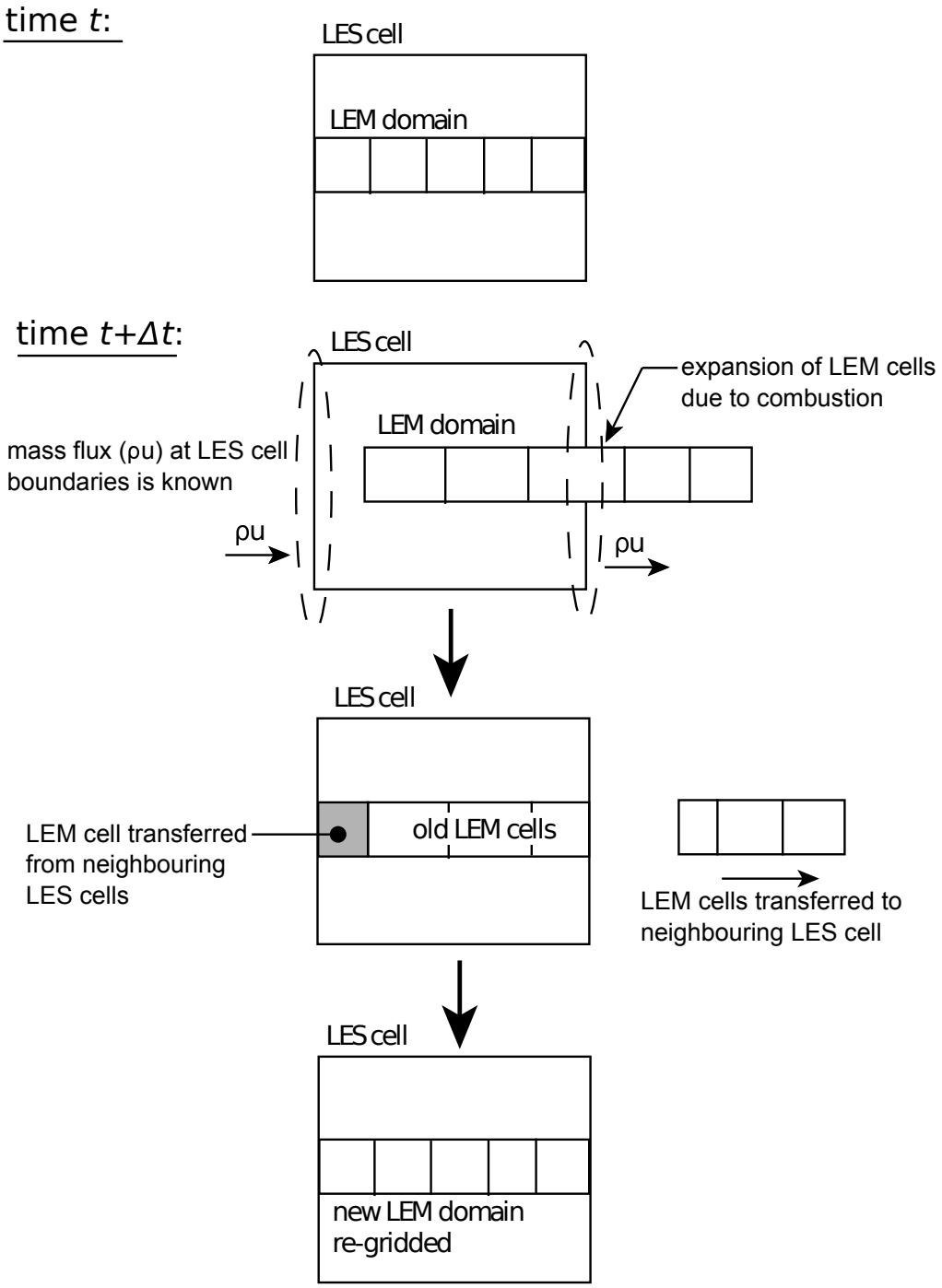

Figure 3.4: LEM splicing procedure.

the updated properties can be calculated from

$$\rho_j = m_j / V_j \tag{3.36}$$

$$T_j = \frac{p_j}{\rho_j} = \sum_{i=1}^{M} \frac{(m_i T_i)}{m_j} \tag{3.37}$$

$$Y_j = \sum_{i=1}^{M} \frac{(m_i Y_i)}{m_j} \tag{3.38}$$

where a 1-D volume of each subgrid element, useful for the computations, is given by

$$V_j = \sum_{i=1}^{M} (m_i / \rho_i). \tag{3.39}$$

Finally, the procedure is also used to re-grid the pre-compression state variables ($\rho_{j,*}$ and $T_{j,*}$) as well.

3.3 Numerical Implementation

3.3.1 The AMR-enabled LES supergrid

In order to solve the system of Eqs.(3.4) through (3.7), a numerical framework developed by Mantis Numerics Ltd. is employed. The compressible flow solver uses a second order accurate *exact* Godunov solver [179, 180], which features a symmetric monotonized central flux limiter [181], to treat the convection terms. The diffusive terms are handled explicitly. Structured Cartesian grids are applied in order to take advantage of Adaptive Mesh Refinement (AMR) [182] for increased efficiency. It should be noted, however, that the application of LEM-LES may not necessarily be limited to structured Cartesian grids [183]. In this work, AMR is implemented only on the supergrid (Eqs. (3.4) - (3.7)). Specifically, the supergrid is refined, on a per cell-basis, in regions where the density or reactant mass ($\bar{\rho}$ or $\bar{\rho}\tilde{Y}$) changes by more than 0.1% locally between existing grid levels. Furthermore, when a cell is

flagged as 'bad', or needing refinement, this badness is diffused by approximately 5-10 cells in each direction on the current grid level. For the purpose of refinement, the Favre-averaged reactant mass, $\bar{\rho}\tilde{Y}$, is obtained from information stored entirely on the subgrid. The supergrid is also refined in the presence of shocked and unburned reactant (i.e., $\bar{\rho}\tilde{Y} > 0$ & $\bar{\rho} > 1.1$). Furthermore, the subgrid model is only active on the finest cells of the supergrid system, and not the coarsest and intermediate grid levels. AMR is not applied to the subgrid domains.

The reader is cautioned, however, that AMR-LES coupling remains challenging to implement in many flow configurations. In the current formulation, the LES filter width had been assumed to be equal to the grid size, $\bar{\Delta} = b$, and is allowed to change with the mesh spacing. In some cases, however, this assumption leads to discontinuous errors in the kinetic energy field at fine-coarse cell interfaces [144, 145]. To circumvent this error, a value of $\bar{\Delta}/b = 4$ has been recommended [144]. This action, however, tends to smooth the subgrid viscosity across several fine grid cells and may affect the overall solution development. In the multi-dimensional scenarios considered in Chapters 5 and 6, the bulk of the subgrid kinetic energy would be generated from the strong shocks located near the front of the wave. Since the unrefined quiescent fluid ahead of the shock is assumed perfectly motionless, coarse-fine errors in subgrid kinetic energy are not expected to be problematic near the leading shocks. Furthermore, once the reactant is shocked, the fluid remains refined until all of the reactant is consumed. Thus, any effect that residual subgrid kinetic energy in wake of the burned products would have on the overall flow development is believed to be negligible. Thus, $\bar{\Delta} = b$ is assumed to be appropriate.

3.3.2 The CLEM subgrid implementation

Upon advancing the supergrid simulation for one time step at the finest grid level, Δt, the subgrid model, governed by the system of Eqs.(3.22) and (3.23), is then solved separately for the duration of Δt using operator splitting [184] to treat the various terms. First, the pressures of each LEM element are updated to the new pressures

computed on the supergrid. The temperature (and density) of each LEM element is then updated through

$$\frac{DT}{Dt} = \frac{1}{\rho}\left(\frac{\gamma - 1}{\gamma}\right)\dot{p}. \tag{3.40}$$

This is done by applying the procedure described in Section 3.2.3. It is noted that $p_2 = \bar{p}$ for each LEM element, and p_1 is the pressure of the element obtained at the end of the previous pressure update, which may have occurred in a different LES cell. The LEM elements thus carries pressure history information during the splicing procedure, which includes the elements pre-compression reference state, p_*. Next, the diffusion terms of Eqs.(3.22) and (3.23),

$$\frac{DT}{Dt} = \frac{\partial}{\partial m}\left(\rho\alpha\frac{\partial T}{\partial m}\right) \tag{3.41}$$

$$\frac{DY}{Dt} = \frac{\partial}{\partial m}\left(\rho\frac{\alpha}{L_e}\frac{\partial Y}{\partial m}\right) \tag{3.42}$$

are solved explicitly in time using the Forward Euler method and spatially discretized using central differences [185]. Thus, for each LEM element, with index i at the nth time step:

$$T_i^{n+1} = T_i^n + \frac{\Delta t_{\text{diff}}}{\Delta m}\left[\rho\alpha|_{i+1/2}\left(T_{i+1}^n - T_i^n\right) - \rho\alpha|_{i-1/2}\left(T_i^n - T_{i-1}^n\right)\right] \tag{3.43}$$

$$Y_i^{n+1} = Y_i^n + \frac{\Delta t_{\text{diff}}}{\Delta m}\left[\rho\frac{\alpha}{L_e}\bigg|_{i+1/2}\left(Y_{i+1}^n - Y_i^n\right) - \rho\frac{\alpha}{L_e}\bigg|_{i-1/2}\left(Y_i^n - Y_{i-1}^n\right)\right]. \tag{3.44}$$

This is done for successive and sufficiently small subgrid time-steps in order to satisfy either the CFL stability criteria associated with the explicit diffusion operation, or the time at which the next stirring event occurs, whichever is smallest. The reaction terms,

$$\frac{DT}{Dt} = -\left(\frac{\gamma - 1}{\gamma}\right)\frac{Q\dot{\omega}}{\rho} \tag{3.45}$$

$$\frac{DY}{Dt} = \frac{\dot{\omega}}{\rho} \tag{3.46}$$

are then solved, implicitly, for the same time step, Δt_{diff}, using the Backward Euler method [185]. Finally, stirring events occur as necessary. The CFL condition for the subgrid diffusion operation, in mass-weighted coordinates, is

$$\beta \frac{\Delta t_{\text{diff}}}{\Delta m^2} \leq \frac{1}{2} \tag{3.47}$$

which must be satisfied at each subgrid node interface. β is the largest diffusion coefficient associated with either Equation (3.41) or (3.42) (i.e., $\beta = \max[\rho\alpha, \rho\alpha/L_e]$) and is evaluated by taking the average value between two adjacent nodes.

Upon completion of the subgrid simulation for Δt, the contribution of $\overline{\dot{\omega}}$ is then provided to the supergrid via Eq.(3.27). This will in turn affect the large scale fluid flow evolution for the next supergrid time step, and thus the process is repeated.

3.3.3 The CLEM-LES algorithm

A summary of the CLEM-LES procedure for one global LES time step, Δt, is given below. Corresponding flow-charts of the procedure are also available in Appendix A. For each cell on the supergrid, variables that require storage are the conserved quantities ($\bar{\rho}$, $\bar{\rho}\tilde{\boldsymbol{u}}$, $\bar{\rho}\tilde{e}$, and $\bar{\rho}k^{sgs}$), the primitives ($\bar{\rho}$, $\tilde{\boldsymbol{u}}$, $\bar{p}$, $\tilde{T}$, and k^{sgs}), the local pressure increase, $\Delta\bar{p}$, the LEM resolution (Δm), and the mass flux across each cell face, ($\dot{m}$). For each LEM element on the subgrid, the primitives (ρ, p, T, Y) and the pre-compression state variables (ρ_*, p_*, T_*) require storage. It is also useful to store the 1-D volumes (V) for the stirring process, and also the location of the supergrid cell where the elements exist prior to splicing. The formal algorithm is as follows:

1. Check grid refinement criteria on the supergrid and refine/de-refine as necessary. Details are published elsewhere [182].

2. Obtain t and the time step, Δt, for the finest grid level, b. Also store the pressure in each supergrid cell, $\bar{p}_1 = \bar{p}$.

3. Check if LEM elements exist in each supergrid cell on the finest grid level. If LEM elements do not exist in a supergrid cell, create them such that $\rho = \rho_* = \bar{\rho}$, $p = p_* = \bar{p}$. Also, remove LEM elements from supergrid cells that are not refined to the finest grid level.

4. On the supergrid, get the first order convective and viscous flux contributions (including $\underline{\boldsymbol{\tau}}^{sgs}$ and $\boldsymbol{H}^{sgs}$ terms) for Eqs.(3.4) through (3.7), for $\frac{1}{2}\Delta t$, using the Godunov procedure described in [179] and explicit Forward Euler treatment of the diffusion terms [185], respectively.

5. Account for the LKM source term contributions ($\dot{P}$, $\bar{\rho}\epsilon$) in Eq.(3.7). These source terms will also have a contribution to ($\bar{\rho}\tilde{e}$) due to the presence of k^{sgs} in the equation of state (2.48).

6. Add contributions from Steps 3 and 4 and thus update the supergrid solutions for $\bar{\rho}$, $\bar{\rho}\tilde{\boldsymbol{u}}$, $\bar{\rho}\tilde{e}$, and $\bar{\rho}k^{sgs}$.

7. Repeat Steps 4, 5, and 6, but for the second order operation across the full time step, Δt. Store the computed mass flux per unit area, $\dot{m} = (\bar{\rho}\tilde{\boldsymbol{u}} \cdot \boldsymbol{n})$, across each supergrid cell face. Also store the new pressure in each supergrid cell, $\bar{p}_2 = \bar{p}$.

8. Begin the CLEM subgrid simulation in each supergrid cell. First check if $\Delta\bar{p} = \bar{p}_2 - \bar{p}_1 > 0.1\%$. If satisfied, proceed to Step 9(a). If not, proceed to Step 9(b).

9. (a) Shock compression detected. Solve Eq.(3.26) for each LEM element by letting $p_2 = \bar{p}_2$. Once finished, apply the re-gridding procedure from Section 3.2.6 and let $\overline{\dot{\omega}} = 0$. Proceed directly to Step 23.

   (b) Assume isentropic pressure change and solve Eq.(3.25) for each LEM element by letting $p_2 = \bar{p}_2$. (Note: p_1 is not necessarily equal to $\bar{p}_1$).

10. Apply the re-gridding procedure from Section 3.2.6 and obtain Δm.

11. Calculate the amount of reactant mass in each LEM domain with Eq.(3.28).

12. Obtain the stirring time step, Δt_{stir}, through Eq.(3.33).

13. Let $t_{\text{stir}} = t + \Delta t_{\text{stir}}$ and $t_\Delta = t + \Delta t$.

14. Obtain the subgrid diffusion time step, Δt_{diff}, by satisfying the CFL condition in Eq.(3.47).

15. If $t + \Delta t_{\text{diff}} > t_\Delta$ then $\Delta t_{\text{diff}} = t_\Delta - t$.

16. If $t + \Delta t_{\text{diff}} > t_{\text{stir}}$ then $\Delta t_{\text{diff}} = t_{\text{stir}} - t$.

17. Diffusion step. Solve Eqs.(3.43) and (3.44) for the time step Δt_{diff} and resolution Δm.

18. Reaction step. Solve Eqs.(3.45) and (3.46) for the time step Δt_{diff}.

19. Let $t = t + \Delta t_{\text{diff}}$. If $t \geq t_{\text{stir}}$ apply the stirring procedure described in Section 3.2.4 and let $t_{\text{stir}} = t + \Delta t_{\text{stir}}$.

20. If $t < t_\Delta$ then repeat Steps 14-19.

21. Update the pre-compression state variables. I.e. $\rho_* = \rho$, $p_* = p_2$, $T_* = T$.

22. Calculate the amount of reactant mass with Eq.(3.28), then calculate the reaction rate $\overline{\dot{\omega}}$ through Eq.(3.27).

23. Implement the splicing procedure described in Section 3.2.5. Ensure that elements move out of each supergrid cell across faces from largest mass flux out to the least. Keep track of where the element came from.

24. Check for inflow boundary conditions (or fine-coarse interfaces) and create LEM elements as necessary. Ensure that the order that elements enter each supergrid cells is from largest mass flux in to the least.

25. Account for the reaction source term, $\overline{\dot{\omega}}$, in Eq.(3.6). Thus update the solution for $\bar{\rho}\tilde{e}$.

26. Repeat steps 1-25 as required for the duration of the simulation.

3.4 Known Limitations

Finally, before proceeding to implement this CLEM-LES methodology, it is important to note and summarize the various known limitations of the solution framework. Many of these limitations, presented below, have been considered acceptable for modelling the fast-flame and detonation propagation scenarios described in Chapter 1. They are, however, presented here as a note of caution for extending the CLEM-LES methodology beyond the scope of the work conducted here.

3.4.1 Algorithm limitations

Subgrid diffusion between neighbouring supergrid cells

First, the most significant limitation is the fact that diffusion between subgrid endnodes is currently neglected between subgrid domains on neighbouring supergrid cells. At the time of writing, the implementation of diffusion in this respect remains a challenge to implement. In previous LEM-LES implementations, this limitation was also reported [97, 119], yet its effects were not investigated. It is therefore a fundamental requirement that simulations require sufficient flow velocity in order to ensure adequate transfer of subgrid nodes to neighbouring cells, which in turn allow for subgrid diffusion to occur. Thus, providing there is sufficient flow velocity, as would be the case for detonation propagation, it is believed this diffusion limitation at subgrid boundaries can be safely neglected [97, 119]. Furthermore, neglecting such diffusion limitation effects has been justified in weakly-compressible LEM-LES implementations by the fact that chemical reaction locally increases pressure, which in turn drives advective fluid motion to transfer subgrid nodes to neighbouring cells [119], and hence allows diffusion. Unfortunately, treatment of flame propagation near walls and alternate frames of reference may be influenced adversely by this limitation, and such scenarios must therefore be carefully considered before attempting the solution methodology presented above.

Spurious diffusion from the splicing procedure

As mentioned in Section 3.2.5, a by-product of the splicing procedure is that significant spurious diffusion occurs in flows which are not predominantly aligned in the grid direction [119]. In the current implementation, adopted from [119], subgrid CLEM elements can only be transferred through cell faces, to the neighbouring cells, which are in orthogonal directions. Thus, for subgrid CLEM cells that are intended to travel to supergrid cells which may not be adjacent to the current one, unwanted mixing may occur. One possibility of eliminating or mitigating such diffusive errors is to incorporate LEM3D-LES methodology [178], where each direction within a supergrid cell has its own LEM domain. This eliminates the need for requiring an ordering algorithm (in Section 3.2.5) to determine where the subgrid cells end up during large-scale advection. Furthermore, the method allows for the change in direction of subgrid cells through the stirring mechanism. Unfortunately the LEM3D-LES approach significantly increases the expense of the simulation since a subgrid domain is required for each possible flow direction. Since the fast-flame and detonation scenarios considered in this thesis are predominantly aligned with the direction of the grid, it is believed that spurious diffusion errors would be minimized. Therefore, in the interest of computational efficiency, the LEM3D-LES formulation is not currently considered.

AMR-LES: re-refinement limitations

Although coarse-fine interface errors, in terms of subgrid kinetic energy, can be mitigated by controlling LES filter width sizes $\bar{\Delta}$ relative to the finest grid size, b, as discussed in Section 3.3.1, a major limitation that remains problematic is how to treat high frequency turbulence signals upon refinement of regions which have previously been refined and de-refined. Upon de-refinement, high frequency velocity fluctuations are effectively filtered out. The problem is how to account for these fluctuations upon further local successive refinement. One solution is to randomly allocate turbulence, or to apply compression to the subgrid kinetic energy field upon refinement

[186]. In the current implementation, however, the shocked reactant of the detonations and fast-flames under investigation are always refined until fully consumed through chemical reaction. Furthermore, the fast-flames and detonations considered here propagate into quiescent and undisturbed locations which have not been previously refined. Thus, there is no need to address this re-refinement limitation in the current implementation.

3.4.2 Physical limitations

One-step model chemistry

As mentioned previously in Section 2.1.2, although the one-step model is a computationally efficient method of accounting for the overall physical ignition behaviour of a reactive mixture, its simplicity proves difficult at calibration in terms of matching every possible aspect of combustion behaviour. For example, if one desires to tune the model to give the correct theoretical detonation half-reaction length, the laminar flame structure is scaled adversely at the expense of also capturing the correct laminar flame speed [187]. Furthermore, in order to match both the laminar flame speed and the detonation half reaction length, one must choose between scaling the diffusion coefficients to match, or altering the sensitivity of the mixture to shock compression by scaling the activation energy as was done in [187]. To further complicate matters, the one-step model does not offer any ability to independently control induction and reaction zone lengths [188]. The size of the induction zone length relative to the reaction zone length is currently believed to be an important parameter which contributes to the stability of detonation wave structure and is an active topic of investigation [109–111, 188]. In order to independently control the induction and reaction zone lengths, a two-step reaction model can be used instead [188]. Although the two-step reaction model has been coupled with Euler models to investigate the stability of detonation wave structure, it remains unclear how to apply and calibrate it to a diffusion-controlled combustion regime and is therefore not considered in the scope of this thesis. Since the primary focus of the thesis is to isolate the effect of turbulent

mixing on combustion, it is desirable to first simplify the chemistry using the one-step model and then extend the chemistry models in future investigation. Finally, it should be noted that the one-step model does not allow for variable sensitivity of the mixture to wide ranges of temperatures which may affect ignition delay times due to chain-branching cross-over effects [188]. Fortunately, hydrocarbon fuels, such as methane and ethane, have been shown to have monotonic behaviour with pressure and temperature; ignition behaviour is not influenced by chain-branching cross-over effects [189].

Eddy-viscosity and gradient-driven turbulent heat diffusion

In the current formulation, closure of the subgrid stress and the subgrid enthalpy flux, $\boldsymbol{\tau}^{sgs}$ and $\boldsymbol{H}^{sgs}$, are respectively provided through eddy-viscosity and gradient-driven diffusion models, see Section 3.1.2. Although these models are relatively simple to implement, and computationally efficient, they have been reported to produce significant diffusive errors [11]. This due to the fact that both models fundamentally assume isotropic turbulence. Furthermore, the gradient-driven turbulent heat diffusion model assumes $P_{r,t}$ is constant and applies globally to the entire flow field. Thus, both models fail at mimicking the sensitivity of turbulent stress and heat diffusion to cases where mean turbulent fluctuations do not align with mean flow gradients [190, 191]. For this reason, near-wall treatments of turbulent flow remains problematic. To address this limitation, higher-moment closure models may be applied to provide higher solution accuracy. This is achieved by providing additional transport equations to represent the unclosed Reynolds stresses and heat diffusion terms. Examples are the second-moment closure model [190, 192] to close the momentum equation, and the scalar-flux model [191] to close the energy (or passive scalar) transport equation. Furthermore, higher-moment heat diffusion models allow for $P_{r,t}$ to vary spatially and temporally throughout the flow. Unfortunately these methods tend to add significant computational overhead due to the inclusion of additional transport equations and are therefore not implemented in the current LES formulation.

Furthermore, the effect of complicated geometry on flow evolution is not under investigation here. Therefore, the eddy-viscosity and gradient-driven diffusion models are considered acceptable for the multi-dimensional simulations conducted in Chapters 5 and 6. First, the next chapter formally verifies and validates the CLEM subgrid for various one-dimensional test cases.

Chapter 4

Verification and Validation for One-Dimensional Flows

4.1 Overview

In this chapter, the LES supergrid-subgrid methodology presented in Chapter 3 is verified and validated for various 1-D laminar and turbulent flow configurations. Thus, Eqs.(3.4) to (3.6) are solved on a 1D supergrid with Eqs.(3.22) and (3.23) solved on the subgrid. It should be noted that in the 1D configuration, the evolution of subgrid kinetic energy ($\bar{\rho}k^{sgs}$), Eq.(3.7), is not included on the supergrid since its production requires multi-dimensional shearing. Instead, the turbulent diffusivity on the subgrid, D_T, is determined according to a turbulent Reynolds number. Since ν_t is not readily available, Eq.(3.32) can be replaced with [102, 162]:

$$D_T \approx \frac{\nu R_{e,\bar{\Delta}}}{C_\lambda} \tag{4.1}$$

where C_λ is a constant and

$$R_{e,\bar{\Delta}} = \frac{u'\bar{\Delta}}{\nu}. \tag{4.2}$$

For the turbulent 1-D simulations carried out here, the mean turbulent velocity fluctuation, u', is also prescribed as a constant which determines $R_{e,\bar{\Delta}}$. This approach is consistent with the validation experiments [101, 102]. Also, since the dissipation rate, ϵ, is not readily available and noting that Eq.(3.30) requires the Kolmogorov scale, η, in order to determine the stirring frequency, λ, the Kolmogorov scale is estimated from [102]

$$\eta = \frac{N_\eta \bar{\Delta}}{(R_{e,\bar{\Delta}})^{3/4}} \tag{4.3}$$

where N_η is also a constant.

4.2 Model Parameters

For the verification and validation experiments below, the model parameters are calibrated predominantly for premixed fuel-lean methane-air combustion at $\hat{T}_o = 328\text{K}$ and $\hat{p}_o = 1\text{atm}$, with an equivalence ratio of $\phi = 0.717$. For further validation of turbulent flames, model parameters are also calibrated for stoichiometric methane combustion. These are consistent with the experiments of [101] and numerical simulations of [102]. The activation energy, heat release, and Lewis number are all taken from the [101] experiments. The ratio of specific heats, sound speed, fluid viscosities, and heat conductivity are computed for the unburned gas composition using Cantera 2.1 [193] and the GRI-3.0 mechanism [194]. The pre-exponential factor was chosen such that the laminar flame speeds match the experiments of [101]. Finally, the length scale $\hat{L}$ was chosen to be the laminar flame thickness, $\hat{\delta}$, also given by [101]. Dimensional quantities for the lean and stoichiometric methane-air mixture properties and the corresponding non-dimensional model parameters are given in Tables 4.1 and 4.2, respectively.

Thus, the only remaining parameters are the two empirical model constants, C_λ and N_η, and also the local velocity fluctuation of the turbulent flow, u'. N_η is calibrated to provide the Kolmogorov scale and typically has a value between 1.28 to 13 [102]. The constant C_λ is calibrated to experiments. Finally, the velocity fluctuation, u',

Table 4.1: Fluid properties and model parameters for lean methane combustion.

Dimensional properties							
$\hat{T}_o$	328 K	$\hat{\rho}_o$	1.038 kg/m^3	$\hat{\nu}$	1.88x10^{-5} m^2/s	$\hat{E}_a$	5452.1 kJ/kg
$\hat{P}_o$	1 atm	$\hat{c}_o$	368 m/s	$\hat{k}/(\hat{\rho}\hat{c}_p)$	2.62x10^{-5} m^2/s	$\hat{Q}$	1671.8 kJ/K
$\hat{S}_L$	0.36 m/s	$\hat{\delta}$	5.21x10^{-5} m				
Non-dimensional model parameters							
α/ρ	0.00137	P_r	0.716	E_a	40.3	γ	1.39
L_e	0.973	A	1.0x10^4	Q	12.4	S_L	0.001
C_λ	1.0	N_η	10.76				

Table 4.2: Fluid properties and model parameters for stoichiometric methane combustion.

Dimensional properties							
$\hat{T}_o$	328 K	$\hat{\rho}_o$	1.026 kg/m^3	$\hat{\nu}$	1.88x10^{-5} m^2/s	$\hat{E}_a$	6820.6 kJ/kg
$\hat{P}_o$	1 atm	$\hat{c}_o$	370 m/s	$\hat{k}/(\hat{\rho}\hat{c}_p)$	2.63x10^{-5} m^2/s	$\hat{Q}$	2054.5 kJ/K
$\hat{S}_L$	0.51 m/s	$\hat{\delta}$	3.68x10^{-5} m				
Non-dimensional model parameters							
α/ρ	0.00193	P_r	0.714	E_a	49.9	γ	1.38
L_e	0.975	A	4.0x10^4	Q	15.0	S_L	0.00138
C_λ	1.0	N_η	10.76				

is normally obtained according to local flow conditions through closure of the momentum Eq.(3.5) with a turbulent viscosity model. However, for the one-dimensional simulations conducted here, turbulent contributions to the conservation of momentum, Eq.(3.5), are neglected. Thus, the velocity fluctuation, u', is only considered for turbulent stirring of Eqs.(3.22) and (3.23) and is provided as a constant. This is consistent with one-dimensional LEM simulations of [102].

4.3 Freely Propagating Flames

The first series of experiments conducted was to verify the current CLEM subgrid modelling strategy, described throughout Chapter 3. This was done for the lean methane-air mixture, by comparing the laminar flame speed at different resolutions with predictions of resolved 1D Navier-Stokes computations (1D-NS), which solves only the exact N-S equations on the supergrid, (2.26) through (2.29). Also, for validation, the modelling strategy is compared against both the lean and stoichiometric

turbulent methane-air flame speed experiments of [101]. The lean turbulent flame simulation is also compared against a previously developed constant pressure LEM strategy [102]. In order to initiate the laminar and turbulent experiments, the unburned and burned fluid properties are initiated in a domain with the flame located at $(x = 0)$, according to:

$$\rho(x,0) = \begin{cases} 1 & \text{if } x < 0 \\ (1+(\gamma-1)Q)^{-1} & \text{otherwise} \end{cases}$$

$$u(x,0) = \begin{cases} 0.5 & \text{if } x < 0 \\ 0.5 + (S_L/\rho)(1-\rho) & \text{otherwise} \end{cases} \tag{4.4}$$

$$p(x,0) = 1/\gamma$$

$$Y(x,0) = \begin{cases} 1 & \text{if } x < 0 \\ 0 & \text{otherwise} \end{cases}$$

In the following simulations, the boundaries of the domain are located sufficiently far such that acoustic signals reflecting from the boundaries do not interfere with the flame itself. Also, a uniform flow velocity, $u = 0.5$, is imposed in the flow field in order to ensure that diffusion occurs between all subgrid nodes. This is necessary since the subgrid diffusion of Eqs.(3.22) and (3.23) is neglected across the supergrid cell faces [97, 119]. Therefore, in this configuration, the flame is propagating to the left, but advected to the right.

4.3.1 The lean methane-air laminar flame

For the laminar case, the resolved flame speed of the CLEM subgrid strategy for lean combustion was found to converge to the same value as that found through 1D-NS, the direct computations of Eqs.(2.26) - (2.29) without the subgrid model. The parameters used for the laminar simulations are listed in Table 4.1. For the CLEM model, the number of subgrid nodes per supergrid cell was varied from $N = 8$ to $N = 32$ and the recorded steady flame speeds are shown below in Figure 4.1. The

recorded flame speeds are determined according to the instantaneous burning rate of fuel, or the rate of reactant mass consumption at each time step. Two observations are drawn from this: 1) increasing the number of subgrid nodes per cell allows for a more coarse grid to be used on the supergrid in order to capture laminar flame speeds, and 2) providing there is fluid motion, neglecting subgrid diffusion between neighbouring supergrid cells has a negligible effect on the laminar flame speed (for this situation). Finally, the flame structures of the resolved 1D-NS and CLEM flames are presented in Figure 4.2. The minimum resolution of the 1D-NS in this figure is $b = \delta/104$ and the minimum supergrid resolution for the CLEM is $b = \delta/13$ with $N = 16$ subgrid nodes per supergrid cell. The reader is also reminded that the filter size of all CLEM simulations has been chosen such that $\bar{\Delta} = b$. Observation of Figure 4.2 reveals that the laminar flame structure is maintained by the CLEM subgrid strategy. Also, the simulated flame widths, δ_{sim}, indicated by the arrows in the figure, is consistent with [101], where $\delta = \nu/S_L = 1$. In both simulations shown, the flame width is found to be $\delta_{\text{sim}} \approx 1.15$. This was measured by the distance between spatial locations where $Y = 0.1$ and $Y = 0.9$.

4.3.2 Turbulent flames

To validate the LEM portion of the CLEM subgrid formulation, numerical turbulent flame experiments were conducted for both the lean and stoichiometric combustion parameters given in Tables 4.1 and 4.2, respectively. The minimum size of each supergrid cell was set to $b = 740$ for the lean combustion case, and $b = 1040$ for the stoichiometric case. The Kolmogorov scale was set by letting $N_\eta = 10.76$, which is consistent with the lean methane-air flame simulation "A1" in [102]. These choices effectively set the range of eddy sizes from the order of $\sim 4\delta$ to 740δ for lean combustion, or from $\sim 4\delta$ to 1040δ for stoichiometric combustion. This corresponds to turbulent combustion in the flamelet regime. Also, this choice of b (and hence $\bar{\Delta}$) is consistent with the upper range of eddy sizes reported the experiments [101]. For both experiments, the turbulence intensity, (u'/S_L), was varied from 1 to 30. All of

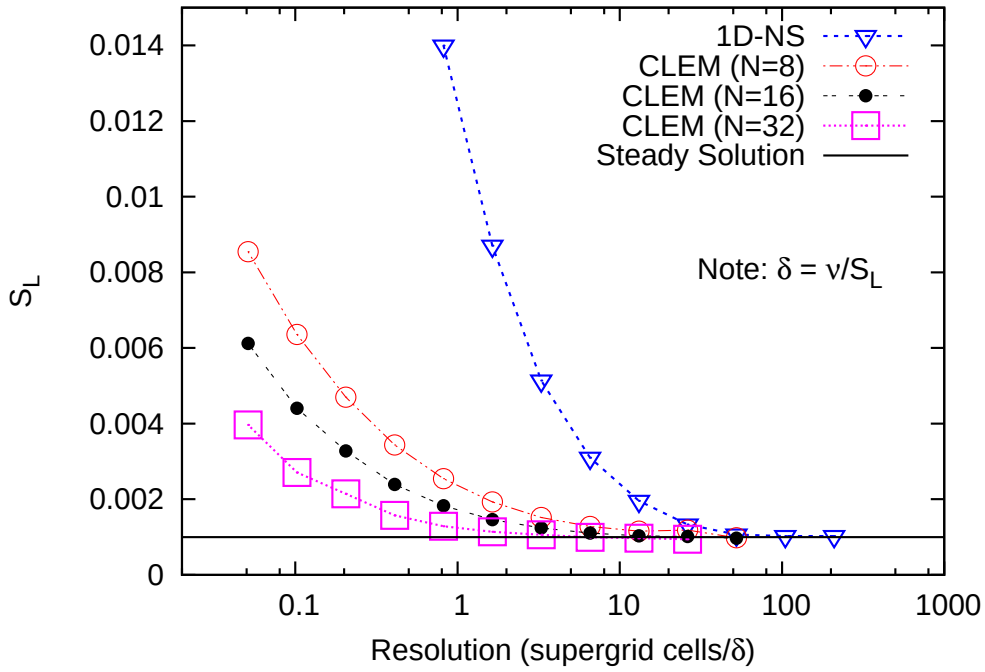

Figure 4.1: Laminar flame speed (S_L) vs. minimum supergrid resolution for 7% CH_4+Air. Note: S_L is normalized by the sound speed $\hat{c}_o$.

the simulations were run up to $t = 500,000$. This corresponds to eddy turn over times, defined in Eq. (4.5), which range from 0.7 to 20, depending on u'.

$$t_\tau = \bar{\Delta}/u' \tag{4.5}$$

The results of the experiments are presented in Figures 4.3 and 4.4 for lean and stoichiometric combustion, respectively.

For the lean methane-air flames, the resolution on the subgrid was varied from $N = 370$ to $N = 2960$ nodes per supergrid cell. For the low-resolution simulations, $N = 370$ and $N = 740$, the turbulent flame speeds are generally under-predicted compared to the experiments [101] owing to insufficient resolution of the smallest eddy stirring events. The two higher-resolution simulations, however, capture much better the turbulent flame speeds when compared to experiments [101] and the stand alone LEM simulations [102]. Furthermore, the trends obtained from the $N = 1480$ simulations generally match those from the simulations where $N = 2960$. In these cases, there is

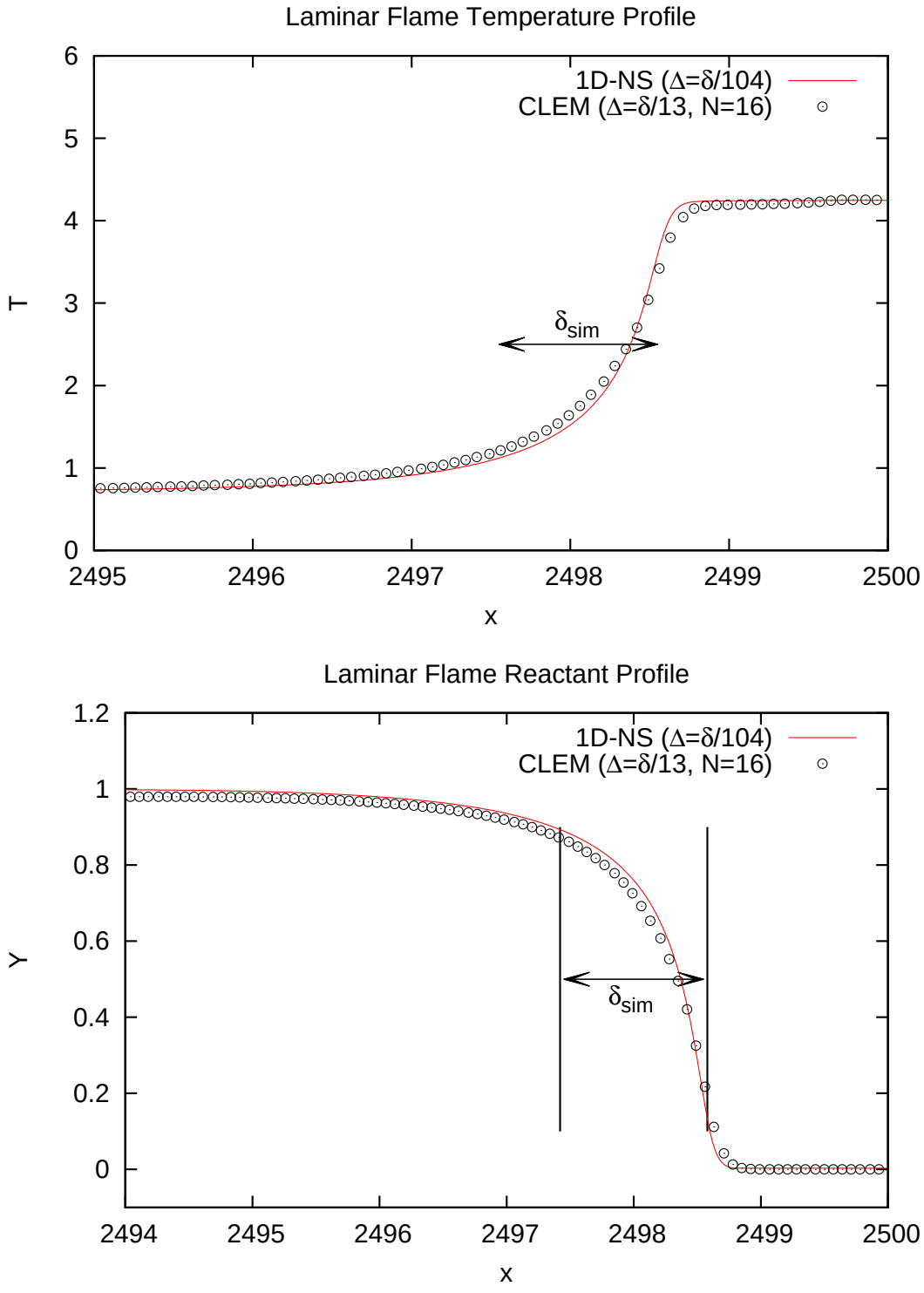

Figure 4.2: Laminar flame structure: temperature (top) and reactant mass fraction (bottom). Note: x and T are normalized by $\hat{\delta}$ and $\gamma\hat{T}_o$, respectively.

sufficient resolution to capture the smallest eddy stirring events, which occur on the order of $\sim 4\delta$. It should be noted, however, that there is a slight deviation of results between the two resolutions when $(u'/S_L) \geq 20$. It is believed that this deviation is due to the stochastic nature of the turbulent stirring mechanism. As (u'/S_L) is increased, the range of random eddy sizes also increases. This leads to increased variation in turbulent diffusivities associated with each stirring event, thus causing increased statistical deviation with an increase in u'. The statistical error estimation for u' vs. simulation run time is a topic currently under investigation, but preliminary work showing the scatter for $(u'/S_L) \geq 5$, using the CLEM with $N = 1480$, is included in Figure 4.3. A total of 10 simulations, each with a different random seeds, have been conducted for each value of (u'/S_L). The average values obtained are indicated in the figure along with the total scatter, indicated by the error bars. In general, the statistical variation of the simulations match well the experimental scatter of [101].

For the turbulent stoichiometric methane-air flames, a resolution of $N = 2080$ was used on the subgrid. This resolution is equivalent to the lean combustion simulations were $N = 1480$ subgrid nodes per supergrid cell. As observed in the lean case, the trend for stoichiometric combustion, shown in Figure 4.4, also captures well the the experiments of [101], thus further validating the CLEM formulation. The same value for $C_\lambda = 1.0$ was used for both the lean and stoichiometric combustion simulations.

It should be noted that the choice of C_λ is quite different from the stand alone LEM simulations of [102] where they had found that $C_\lambda = 15.0$ correlates well with the experiments of [101]. It is believed that this difference can be attributed to several factors. First, there are significant differences in the model parameters used. Q and A, for example, are calibrated differently in [102]. Since C_λ is a model constant, there may be dependence on the selection of other constants, E_a, Q, and A. Also, [102] is formulated in a purely constant pressure system on a single grid. Due to the nature of the subgrid-supergrid coupling in the current CLEM formulation, the eddy stirring events in the current model do not extend beyond subgrid domain boundaries. All subgrid stirring events are self-contained within each supergrid cell.

The flame speeds given in Figures 4.3 and 4.4 for the CLEM are taken as the ensemble-averaged speeds, determined from instantaneous burning rates at each time step, recorded throughout the duration of each numerical experiment. A typical flame speed history, including the cumulative and final mean velocities, is shown in Figure 4.5. Also, a typical turbulent flame structure is shown in Figure 4.6. Both figures are shown for lean combustion when $u'/S_L = 30$ and $N = 1480$. The action of the eddy stirring events under high turbulence causes a one-dimensional "Flame brush" to form. This leads to pockets of un-reacted gas to form behind the leading flame front. This effectively increases the total surface area of the flame, which increases the burning rate, or flame speed due to the large-scale turbulence. This was also observed in [102]. Finally, it should be noted that although the flamelet regime was simulated here, a recent study [195] has used a stand-alone LEM to investigate turbulent flames with average eddy sizes are comparable to δ. In [195], LEM has been shown to capture straining of the flame profiles that result from smaller scale turbulent-flame interactions.

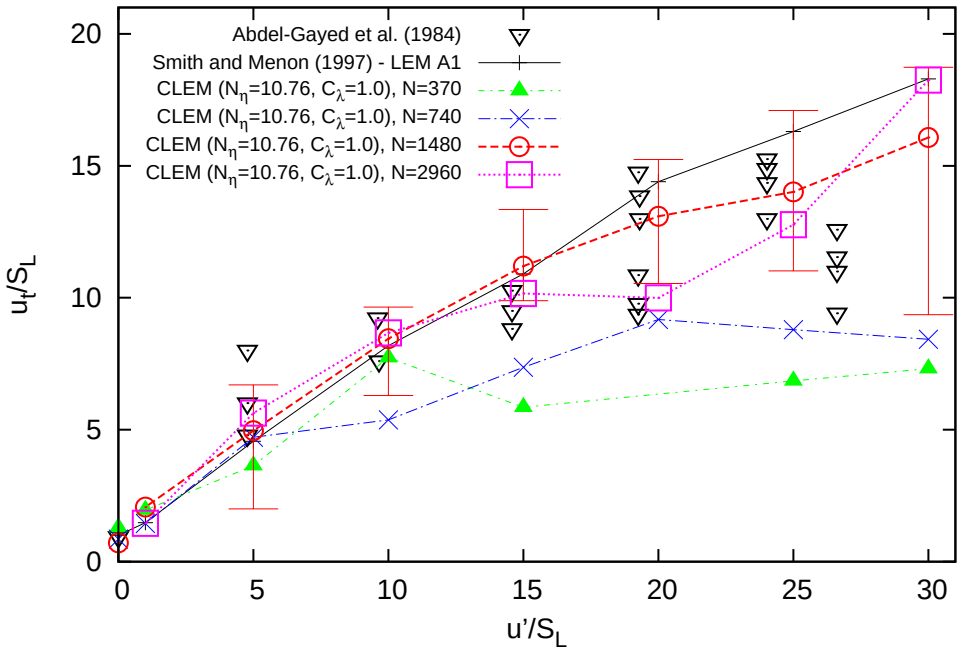

Figure 4.3: Turbulent flame speeds vs. intensity (u'/S_L) for lean methane combustion (7% CH_4+Air) for various resolutions. The current simulations are also compared against previous experiments of Abdel-Gayed et al. [101] and simulations of Smith and Menon [102].

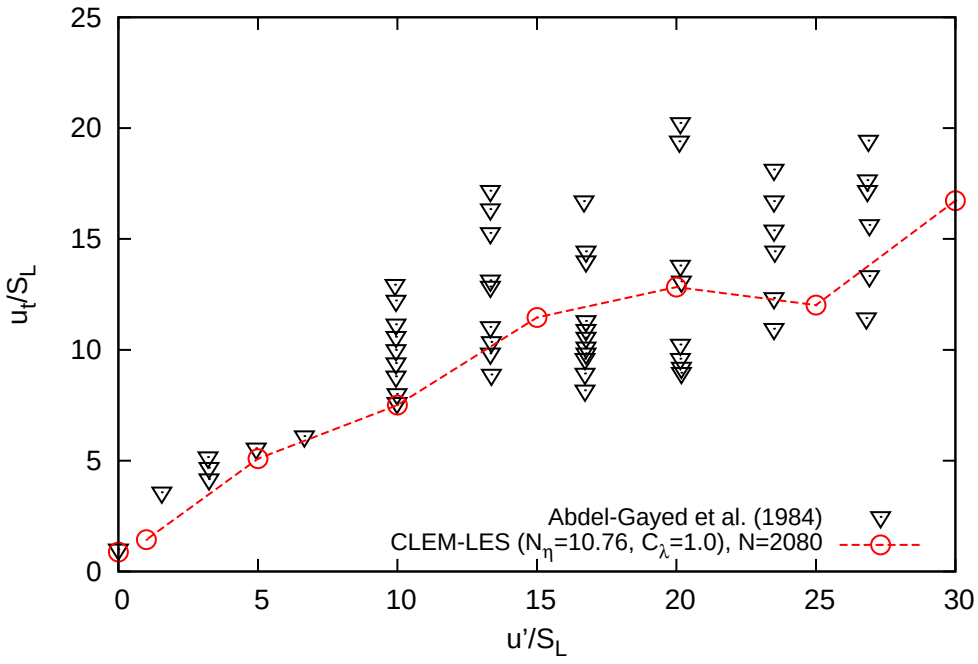

Figure 4.4: Turbulent flame speeds vs. intensity (u'/S_L) for stoichiometric methane combustion (9.52% CH_4+Air), and compared against experiments [101].

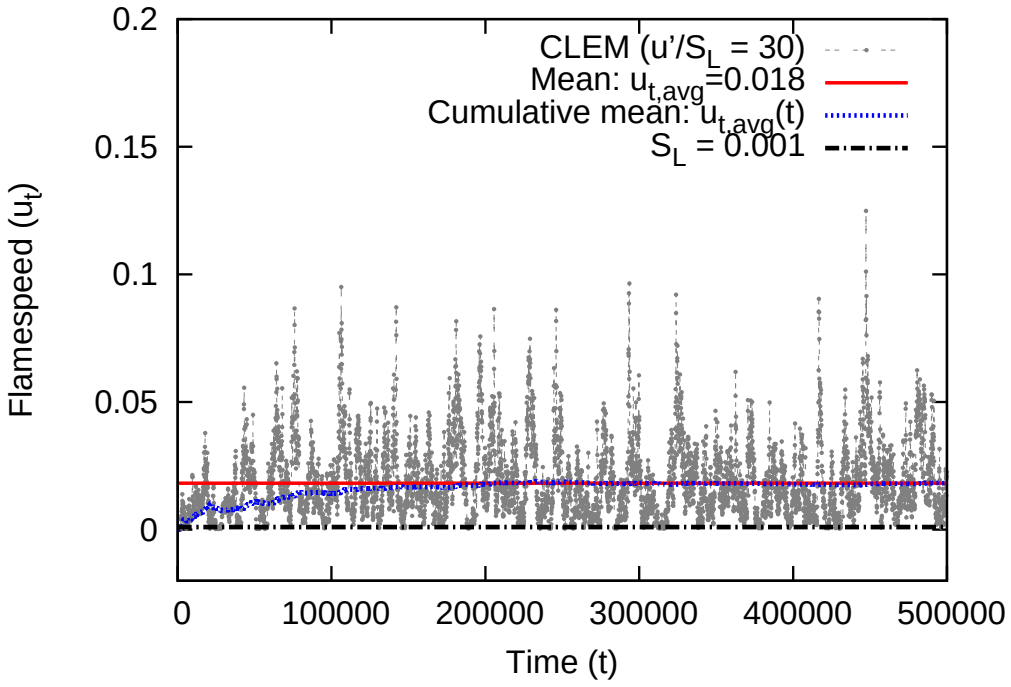

Figure 4.5: Turbulent flame speed history for lean combustion (7% CH_4+Air) at $(u'/S_L) = 30$, with CLEM ($N = 1480$). Note: u_t and t are normalized by $\hat{c}_o$ and $(\hat{\lambda}_{1/2}/\hat{c}_o)$, respectively.

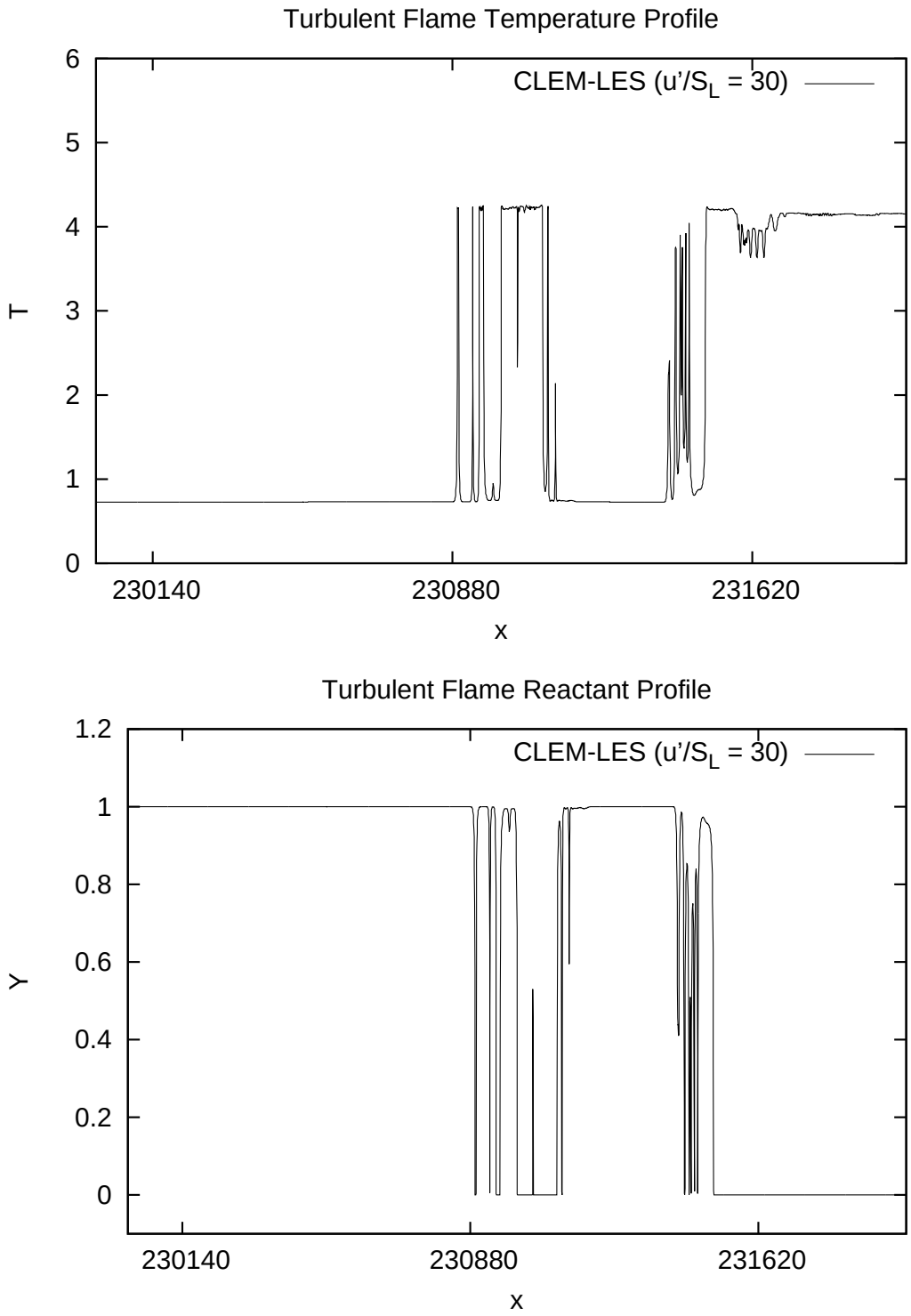

Figure 4.6: Turbulent flame structure for lean combustion: temperature (top) and reactant mass fraction (bottom). Note: x and T are normalized by $\hat{\delta}$ and $\gamma\hat{T}_o$, respectively.

4.4 Detonation Initiation via Shock-Flame Interaction

In this numerical experiment, laminar detonation initiation through a shock-flame interaction for lean combustion was modelled using the CLEM subgrid modelling strategy and compared against 1D-NS computations at two different resolutions using the model parameters given in Table 4.1. The LEM turbulence in 1-D was not considered in this experiment. The simulation set-up, illustrated in Figure 4.7, was conducted in the frame of reference of a piston, whose surface is initially located 4000 laminar flame thickness widths (4000δ) downstream from the flame in the burned products (on the left of the domain). An inflow boundary of unburned gas is specified 1000δ upstream from the flame (on the right of the domain). The speed at which the unburned gas flows into the domain is sufficient to drive a shock through the products with a strength of $M_s = 2.2$ relative to the burned gas. In this context, the flame propagates toward the right, however it is advected to the left (toward the piston). Mathematically, the domain is initialized according to

$$\rho(x,0) = \begin{cases} (1+(\gamma-1)Q)^{-1} & \text{if } x < 4000 \\ 1 & \text{otherwise} \end{cases}$$

$$u(x,0) = \begin{cases} -u_p & \text{if } x < 4000 \\ (S_L/\rho)(1-\rho) - u_p & \text{otherwise} \end{cases} \tag{4.6}$$

$$p(x,0) = 1/\gamma$$

$$Y(x,0) = \begin{cases} 0 & \text{if } x < 4000 \\ 1 & \text{otherwise} \end{cases}$$

where the piston velocity in the absolute frame of reference is given by

$$u_p = 2\Big(1+(\gamma-1)Q\Big)^{1/2}\frac{(M_s - 1/M_s)}{(\gamma+1)}. \tag{4.7}$$

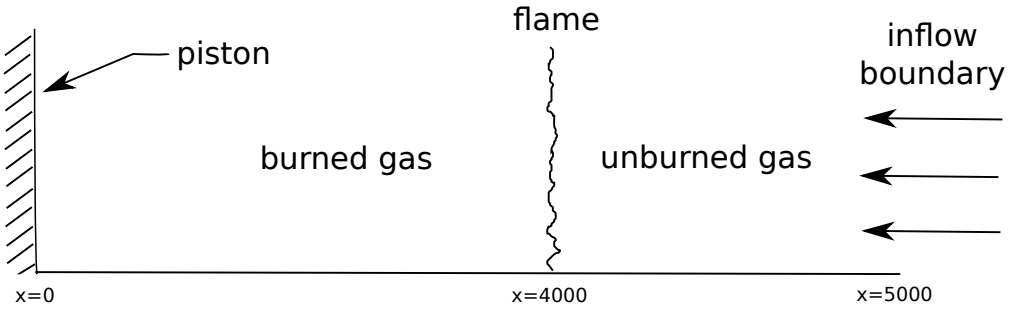

Figure 4.7: Setup for the shock-flame interaction simulation.

The 1D-NS computations are conducted for minimum resolutions of $b = \delta/64$ and $b = 10\delta$, which correspond to the high resolution and low resolution case, respectively. The CLEM is simulated for a minimum supergrid resolution of $b = 10\delta$ containing $N = 640$ subgrid nodes per supergrid cell, thus with diffusion and chemical reaction resolved to the same scale as the high resolution 1D-NS case. The density and reactant mass fraction evolution for all three cases is shown in Figure 4.8. For the high resolution 1D-NS, a detonation wave was found to initiate ahead of the flame, in the unreacted gas, at approximately $(x, t) = (1000, 1500)$. Specifically, the location where detonation initiation occurred was found to coincide with the shock-shock interaction involving the initially transmitted shock into the unreacted gas, and a second transmitted shock originating a shock reflection at the piston wall. In this case, detonation initiation occurs due to sufficient shock-compression. In the low resolution 1D-NS, however, a detonation wave was found to initiate almost immediately after the incident shock from the piston reached the flame, at approximately $(x, t) = (1400, 900)$. In this case, increased reaction rates owing to numerical diffusion (and a faster moving flame) at the flame surface are sufficient to initiate the detonation wave prematurely. For the CLEM, on the other hand, detonation initiation occurs at approximately the same instant and position as the 1D-NS. Differences between the CLEM and high resolution 1D-NS, however, are observed where subsonic burning of reactant gas occurs in the near zero velocity region between the original flame and newly formed detonation wave. This error in the CLEM prediction is due to insufficient diffusive mixing across supergrid cell faces since the model relies on sufficient flow velocity across the cell boundaries.

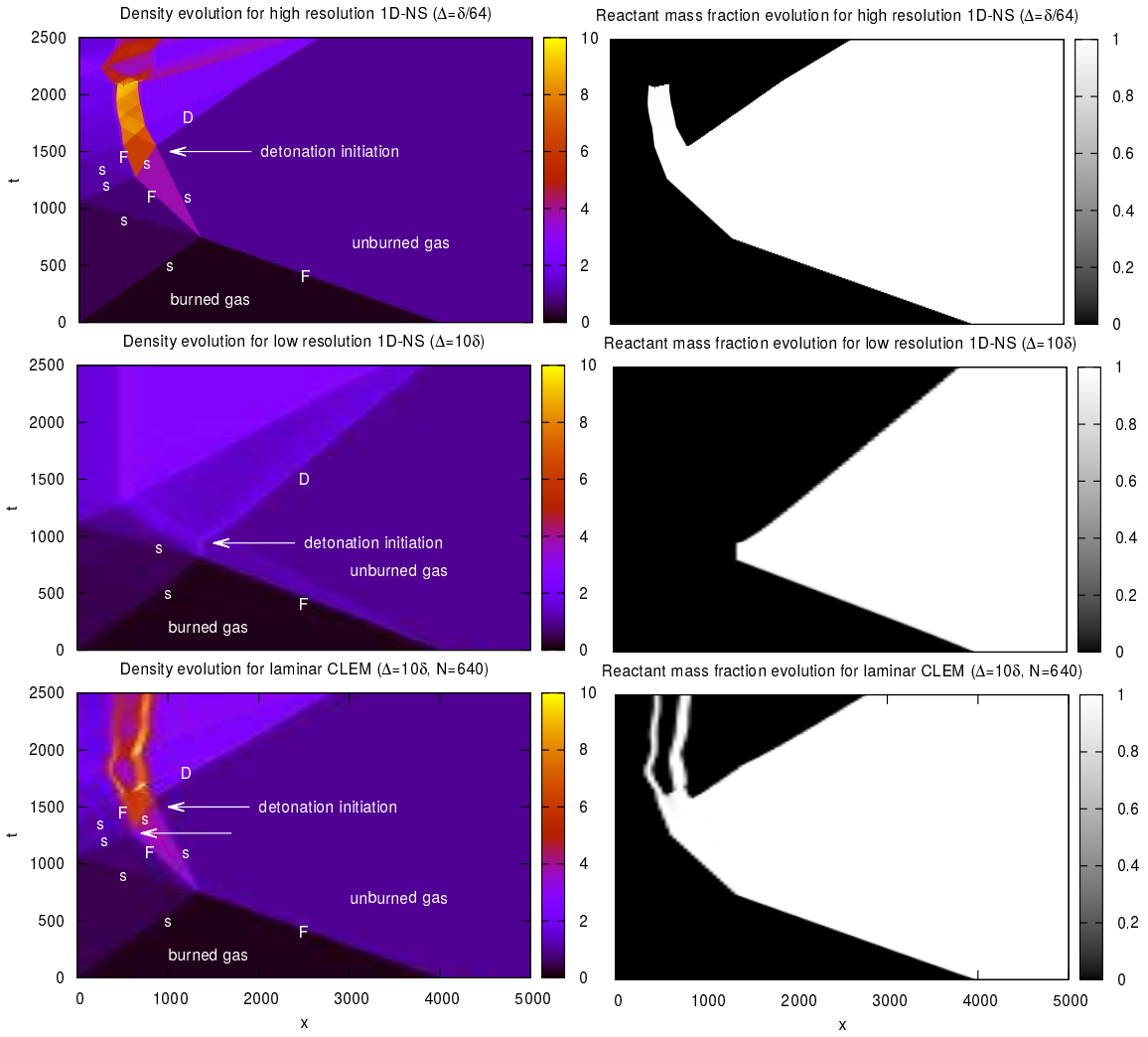

Figure 4.8: Shock-flame interaction for 1D-NS computations (at high and low resolution) and the CLEM strategy (laminar). The left frames show density (ρ) while the right frames show the reactant mass fraction (Y). The diagrams show the various shock, flame, and detonation features in the frame of reference of a piston (the left boundary). The right boundary is an inflow boundary. Note: x and t are normalized by $\hat{\delta}$ and $(\hat{\delta}/\hat{c}_o)$, respectively. (s=shock, F=flame, D=detonation)

4.5 Detonation Propagation and Structure

The final numerical test case conducted here assesses the performance of the model in highly compressible and reactive flows. Specifically, a highly resolved detonation was simulated for the lean combustion parameters given in Table 4.1. The resulting structure and propagation characteristics were subsequently analyzed. In order to initiate the detonation, the Zel'dovich - von Neumann - Doring (ZND) structure [16] is imposed with the leading shock wave located at $(x = 0)$, as illustrated in Figure 4.9. The length scale, $\hat{L}$, is given in terms of the half-reaction length, $(\hat{\lambda}_{1/2})$ and is obtained from explicit numerical integration of the steady ZND solution, given by

$$\frac{d(\rho u)}{dx} = 0 \tag{4.8}$$

$$\rho u \frac{du}{dx} + \frac{dp}{dx} = 0 \tag{4.9}$$

$$\rho u \frac{d}{dx}\left(e + \frac{p}{\rho}\right) = -Q\dot{\omega}(x) \tag{4.10}$$

$$\rho u \frac{dY}{dx} = \dot{\omega}(x). \tag{4.11}$$

The non-dimensional distance, time, and pre-exponential factor are scaled accordingly. The left boundary, located at $x = -90$, is fixed at the Chapman-Jouguet (CJ) conditions [16], while the right boundary, located at $x = 1200$, is an outflow boundary with zero gradients. The initial quiescent fluid, located at $x > 0$, has the properties $\rho(x, 0) = 1$, $u(x, 0) = 0$, $p(x, 0) = 2$, and $Y(x, 0) = 1$. The simulation is run up to $t = 180$ for a minimum supergrid resolution of $b = 1/128$. The results are compared against the theoretical ZND model and also 1D-NS with the same minimum resolution. For the CLEM formulation, only a few subgrid nodes are included $(N = 4)$.

Figure 4.10 shows the velocity of the wave as a function of time for both the 1D-NS computations and the CLEM formulation. For both simulations at sufficient resolution, the initial disturbance (numerical errors) at $(x, t) = (0, 0)$ is sufficient to

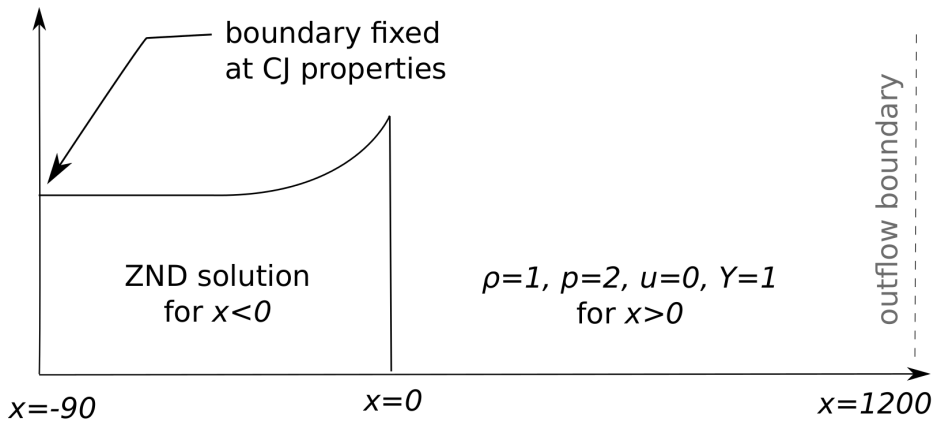

Figure 4.9: Initial conditions for the detonation propagation experiment.

induce the oscillatory unstable (pulsating) behaviour associated with high activation numbers and low reaction orders [108, 196]. For the CLEM procedure, this oscillatory behaviour is triggered faster than the 1D-NS. Despite this transient difference at the simulation start up, the amplitude, period, and mode of velocity fluctuations are the nearly same for both simulations despite being out of phase. Furthermore, the detonation velocities recorded in both simulations was found to oscillate about the Chapman-Jouguet (CJ) velocity of $D_{CJ} = 5.33$. The steady-state amplitude and period for the 1D-NS is found to be $\Delta D = 2.602$ and $\Delta t = 0.572$, respectively. For the CLEM, the amplitude and period are $\Delta D = 2.617$ and $\Delta t = 0.574$, respectively. Thus, the CLEM yields respective errors of 0.576% and 0.3% for the amplitude and period. The difference in behaviour at start up is believed to be influenced by differences in resolution of the diffusive scales between the two simulations, but is not further investigated here. Finally, comparison of an instance where the unsteady detonation structure of the CLEM modelling strategy and the 1D-NS is shown in Figure 4.11. Excellent agreement is observed between CLEM and the 1D-NS computations for the reactant and density profiles. Furthermore, the numerical simulation profiles periodically match those of the steady ZND solution, also shown in Figure 4.11.

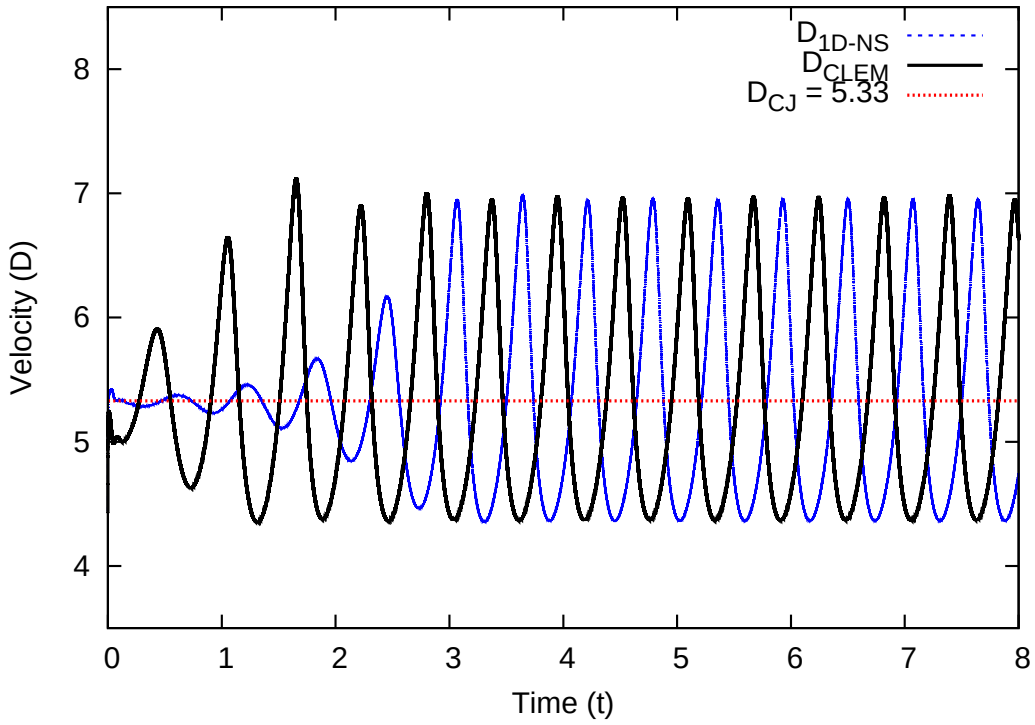

Figure 4.10: Comparison of detonation velocities for 1D-NS and the CLEM strategy. Note: D and t are normalized by $\hat{c}_o$ and $(\hat{\lambda}_{1/2}/\hat{c}_o)$, respectively.

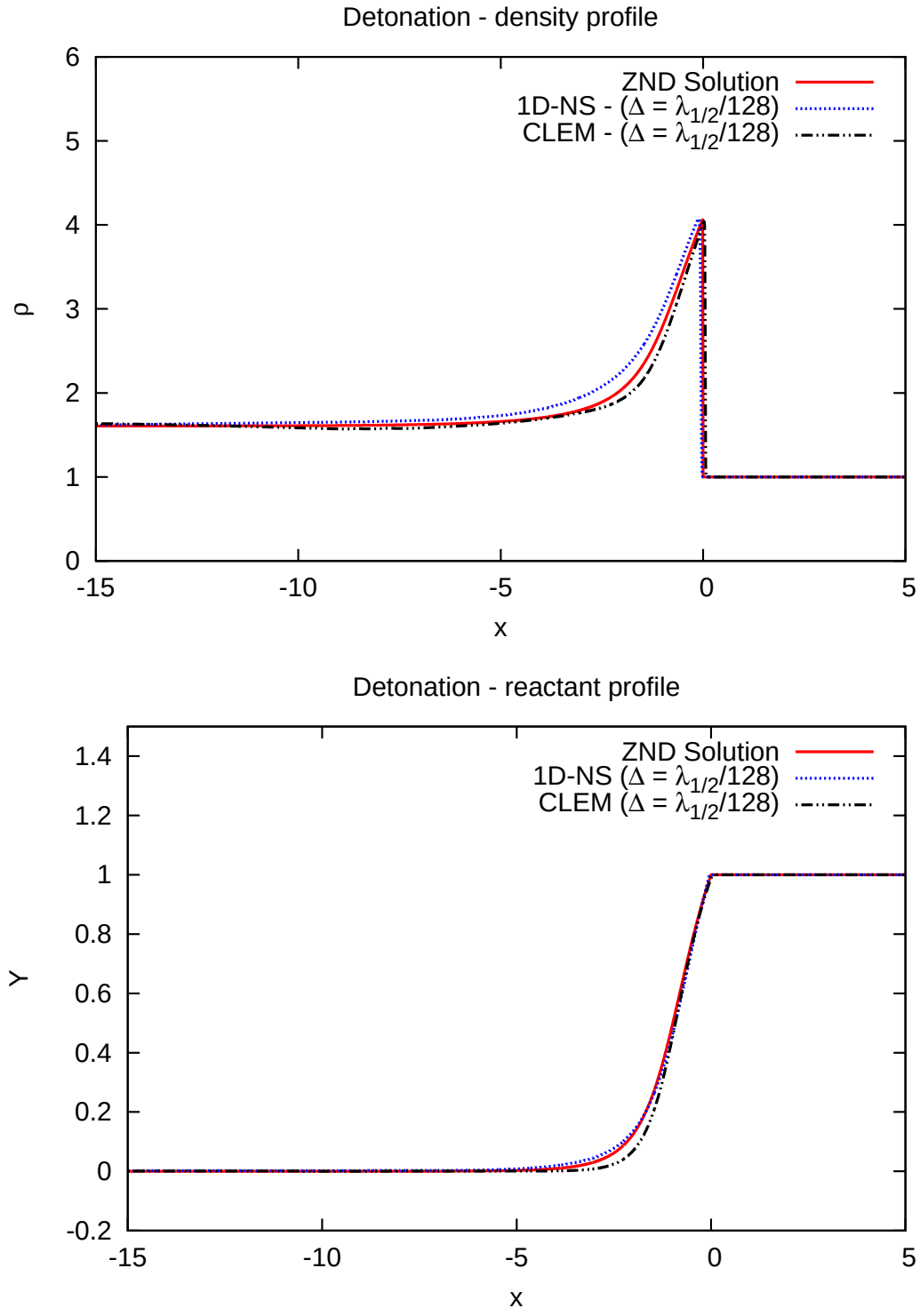

Figure 4.11: Detonation structure: density (top) and reactant (bottom) profiles. Note: x and ρ are normalized by $\hat{\lambda}_{1/2}$ and $\hat{\rho}_o$, respectively.

4.6 Summary

In this chapter, the subgrid modelling strategy (CLEM), inspired by LEM-LES [97], has been verified and validated for various one-dimensional laminar and turbulent combustion scenarios, respectively. The model has been demonstrated to resolve and capture laminar flame speeds and structure when compared against 1D-NS computations. Also, the simulations support the assumptions made by [97] regarding the negligible effect that subgrid diffusion between neighbouring supergrid cells has on the laminar flame speed, providing there is sufficient fluid motion. Furthermore, the model is able to reproduce the turbulent flame speed trends observed experimentally [101] and also numerically [102]. It is worthwhile to note that for the 1-D turbulent flame calculations presented here, the turbulent production on the subgrid scale is prescribed as a constant. In a multi-dimensional simulation, however, adequate closure to the momentum equation would be required. In this case, multi-dimensional fluid motion would generate turbulence, which would then be reflected on the subgrid through the stirring events. These stirring events would then influence the energy and reactant evolution, through source terms, which would then further influence fluid motion and turbulence. Furthermore, a multi-dimensional implementation of the CLEM subgrid model would allow for large-scale curvature effects on flame propagation and extinction to be taken into account. In the current 1-D formulation, such effects are neglected and therefore extinction limits associated with much higher levels of turbulence cannot be predicted, as is demonstrated in [102].

Piston-driven shock-flame interaction experiments showcase the ability of the model to simulate detonation initiation resulting from complex gas-dynamics and rapid chemical reactions in the presence of shock waves. The model has been found to address difficulties with associated with unresolved (low resolution) computations of the Navier-Stokes equations in terms of detonation initiation resulting from increased reaction rates and faster flame speeds that are driven by numerical diffusion. It was found that the CLEM modelling strategy captures correctly detonation initiation

events when compared to high resolution 1D-NS. Furthermore, these events are captured with the CLEM formulation despite the fact that the shock wave propagation is only simulated on the supergrid. Since the supergrid has a lower resolution, it is likely that shock structure is smeared by numerical diffusion, but would still exhibit the correct speed and strength. Thus, it has been demonstrated that the response of the subgrid to the pressure changes on the supergrid is sufficient to provide the correct high resolution burning rates leading up to detonation initiation. Despite this, however, errors in the burning rates of reactant gas in near-zero velocity regions are observed, which further confirms the model requirement of sufficient flow velocity to ensure adequate diffusive mixing across cell boundaries. Finally, detonation structure and stability characteristics arising from perturbations in the flow field are also captured by the CLEM formulation.

As a final note, it was found that computational expense of the subgrid model was comparable to the direct computations of the Navier-Stokes equations for 1-D simulations. The model, however, has the potential to reduce computation expense by a square-root or cubic-root factor in two and three-dimensional simulations when compared to 2-D and 3-D DNS, respectively. This is attributed to the fact that multi-dimensional problems would effectively be reduced to one-dimensional problems on the finest scales. To conclude, the CLEM subgrid formulation has been demonstrated to improve on previous LEM-LES formulations [97–99, 119] by simultaneously treating rapid pressure changes and chemical reactions in turbulent environments.

In the next two chapters, 5 and 6, the CLEM-LES extension to two-dimensional flows is validated against the detonation propagation and DDT from a porous medium experiments presented earlier in Sections 1.2.1 and 1.2.2, respectively.

Chapter 5

Validation for 2D Flows Part I: Irregular Detonation Propagation

5.1 Overview

In this chapter, the CLEM-LES methodology was validated against experiments of detonation propagation in an unobstructed channel, for premixed methane-oxygen at low pressure, which have been conducted at the University of Ottawa [13] and also elsewhere [15, 27] for the same conditions. As mentioned previously, in Section 1.2.1, mixtures involving premixed methane-oxygen are characteristic of having an irregular cell structure. In this sense, they tend to have a spectrum of cell sizes and patterns, and occasionally contain smaller cell structures within larger, and more prominent, cell structures. Furthermore, irregular detonation waves have been found, experimentally, to be highly turbulent and quite often contain shocked un-burned pockets of reactive fuel in their wake [15, 19, 22, 24, 26, 27]. To date, it is believed that such pockets burn through enhanced mixing associated with hydrodynamic instabilities leading to turbulence, and not through shock compression alone. Experiments have shown that pockets of gas in the wake of irregular mixtures burn up orders of magnitude faster than steady shock ignition times [22, 27]. Thus, in this chapter, it is of particu-

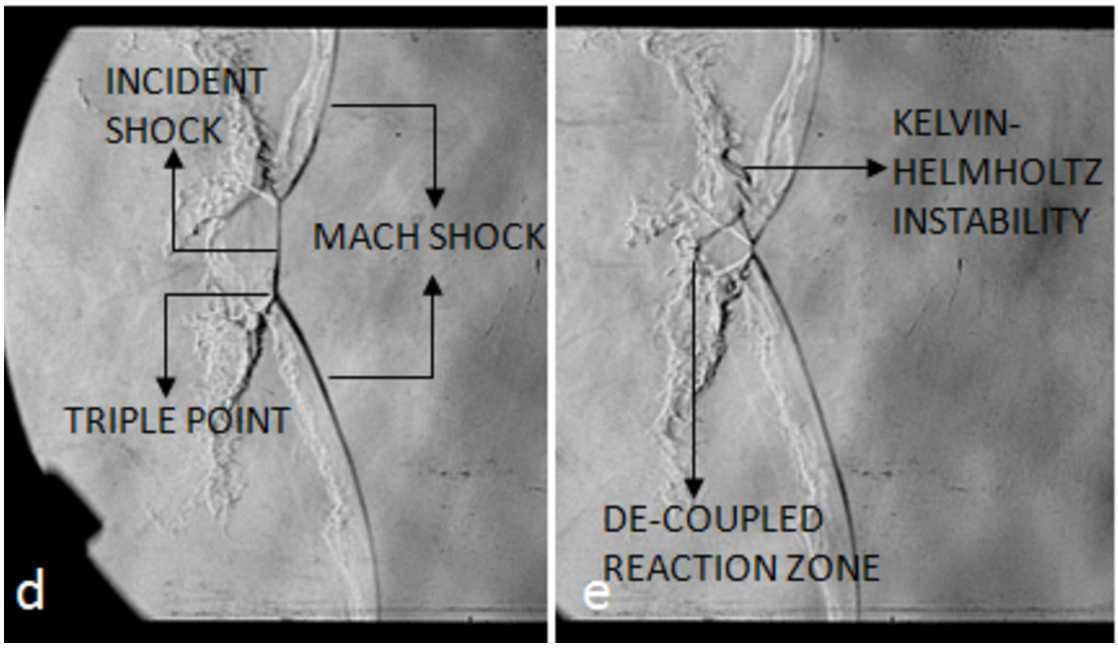

Figure 5.1: Detonation structure for $CH_4 + 2O_2$, initially at $\hat{p}_o = 3.5kPa$, obtained for two successive frames, 11μs apart [13]. Indicated in the figure are various features of interest; the incident and Mach shocks, triple points, de-coupled reaction zone (pocket of unreacted gas), and shear layers where KH instability is present.

lar interest to examine how turbulent mixing, driven through turbulent instabilities, can impact the overall cell structure and propagation characteristics of a detonation wave. An example of an irregular detonation wave, which exhibits the characteristic cellular structure, is shown in Figure 5.1. In the figure, taken from Bhattacharjee [13], the various features expected for a detonation wave, in a methane-oxygen mixture, are shown. These include the incident and Mach shocks, triple points, and pockets of unreacted gas (labelled as de-coupled reaction zone). Also shown in the figure are shear layers that give rise to Kelvin-Helmholtz (KH) instability.

To validate the CLEM-LES with experiments [13, 15], results are first presented for a single arbitrary C_κ value to gain insight on the performance of the strategy and the expected flow patterns that emerge. Then, a resolution study is first performed in order to determine the most appropriate resolution which resolves both the correct reaction rate, and also the qualitative cellular patterns observed throughout the propagation process. Next, numerical simulations are conducted to determine the role that

turbulent fluctuations, or turbulent mixing rates, has on the reaction zone structure, and how the hydrodynamic thickness (i.e., how the pockets burn out), and also the cell size and regularity. This is achieved though varying the C_κ variable, whose value is proportional the turbulent kinetic energy present, or mixing rates experienced, as was explained previously in Section 3.1. Finally, comparison to experiment [13, 15] is made in order to determine which C_κ value produces the correct expected qualitative and quantitative features.

5.2 Numerical Domain and Model Parameters

A schematic showing the setup for the numerical experiment is shown in Figure 5.2. In all experiments, the total domain length is $900\hat{\lambda}_{1/2}$ long, which is sufficient to allow adequate sampling and analysis of the detonation structure beyond the time it takes for the CJ-speed to be recovered. A domain height of $20\hat{\lambda}_{1/2}$ corresponds to experiments of [13], while a height of $10\hat{\lambda}_{1/2}$ corresponds to experiments of [15]. For the wall boundary, shown in Figure 5.2, $u = v = k^{sgs} = 0$ and the normal gradients of all remaining variables are zero. For the symmetry boundary condition, only the normal velocity component is taken as zero. Thus $v = 0$, while the normal gradients of all other variables are also zero. Finally, the zero gradient boundary condition assumes that all normal gradients for all variables are zero. To initiate the planar detonation wave, an initially over-driven ZND-profile is initialized in the first $20\hat{\lambda}_{1/2}$ lengths of the computational domain. The initial ZND-profile corresponds to an over-driven detonation by 10% or 20% in order to overcome start-up errors associated with the initially sharp discontinuity at the shock. A section ahead of the ZND-profile, $4\hat{\lambda}_{1/2}$ long, contains random perturbations to the quiescent density field. This allows for the two-dimensional cellular structure to develop further down the channel. Formally, the initial conditions for ρ, u, p, and Y are given according

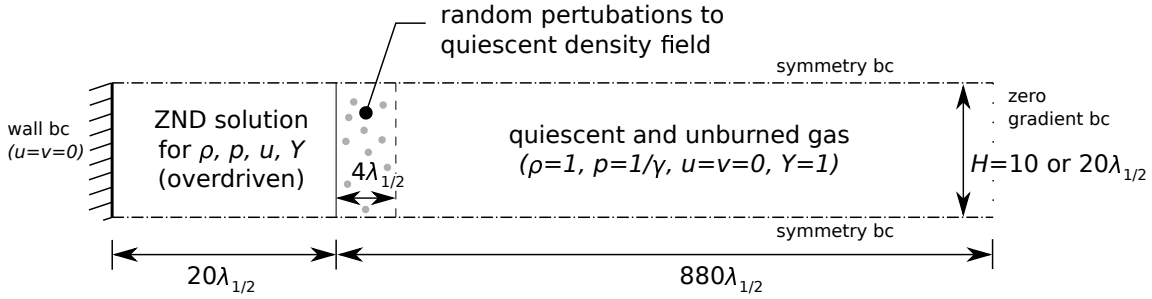

Figure 5.2: Initial and boundary conditions for the 2D planar detonation propagation experiment (Not to scale). Note: $\hat{\lambda}_{1/2} = 9.68$mm.

to:

$$\rho(x,y,0) = \begin{cases} \text{ZND solution Eqs.(4.8)-(4.11)} & \text{if } x < 0 \\ 1.25 - 0.5n & \text{if } 0 \le x \le 4 \\ 1 & \text{otherwise} \end{cases}$$

$$u(x,y,0) = \begin{cases} \text{ZND solution Eqs.(4.8)-(4.11)} & \text{if } x < 0 \\ 0 & \text{otherwise} \end{cases} \tag{5.1}$$

$$v(x,y,0) = 0$$

$$p(x,y,0) = \begin{cases} \text{ZND solution Eqs.(4.8)-(4.11)} & \text{if } x < 0 \\ 1/\gamma & \text{otherwise} \end{cases}$$

$$Y(x,0) = \begin{cases} \text{ZND solution Eqs.(4.8)-(4.11)} & \text{if } x < 0 \\ 1 & \text{otherwise} \end{cases}$$

where n is a random real number from 0 to 1. For the turbulent kinetic energy, $k^{sgs}(x,y,0) = 0$ everywhere, and is therefore self-generating throughout the simulation.

Then, in order to determine the required model parameters, for the one-step model described in Section 2.1.2, that mimic the experimental premixed methane-oxygen mixtures [13, 15], the various dimensional and non-dimensional properties are obtained using the procedure detailed in Appendix B. To summarize the procedure, the global activation energy, heat release, post-shock flame speed, and the ZND structure [16] are first obtained using realistic chemistry using the Cantera libraries [193] and the GRI-3.0 detailed kinetic mechanism [194]. The pre-exponential factor, A, and dif-

Table 5.1: Dimensional and non-dimensional fluid properties and model parameters for methane combustion at $\hat{T}_o = 300$K and $\hat{p}_o = 3500$Pa.

Dimensional properties					
$\hat{\rho}_o$	0.04 kg/m^3	$\hat{c}_o$	356.36 m/s	$\hat{E}_a/\hat{R}$	18357.4 K
$\hat{D}_{CJ}$	2243.31 m/s	$\hat{D}_{70\%CJ}$	1571.55 m/s	$\hat{S}_{L,70\%CJ}$	16.39 m/s
$\hat{T}_{CJ}$	3159.60 K	$\hat{p}_{CJ}$	90.7 kPa	$\hat{\rho}_{CJ}$	0.07 kg/m^3
$\hat{T}_{70\%CJ}$	1085.39 K	$\hat{p}_{70\%CJ}$	81.0 kPa	$\hat{\rho}_{70\%CJ}$	1.038 kg/m^3
$\hat{T}_{VN}$	1726.74 K	$\hat{p}_{VN}$	169.5 kPa	$\hat{\rho}_{VN}$	0.24 kg/m^3
$\hat{\nu}$	1.9x10^{-4} m^2/s	$\hat{k}/(\hat{\rho}\hat{c}_p)$	4.8x10^{-4} m^2/s	$\hat{D}$	2.0x10^{-4} m^2/s
$\hat{Q}$	6388.0 kJ/kg	$\hat{\lambda}_{1/2}$	9.68 mm		
Non-dimensional model parameters					
ν	3.68x10^{-3}	M_{CJ}	6.30	$M_{70\%CJ}$	4.41
L_e	1.32	P_r	0.709	S_c	0.933
$P_{r,t}$	1.0	$S_{c,t}$	1.0	γ	1.17
E_a	45.0	Q	50.3	A	8.96x10^3

fusion coefficients are then scaled such that the one-step model reproduces the correct half reaction length, $\hat{\lambda}_{1/2}$, and also the post-shock flame speed for a shock travelling at 70% the theoretical CJ speed [16] for the given quiescent mixture. This particular state of reference (70% CJ) has been chosen since experiments have reported that wave velocity deficits of 20-30% exist during propagation [13, 27]. Furthermore, pockets of unreacted gas, where significant burning occurs, are more likely to form in regions where the shock strength is weaker. Such velocity deficits give rise to a significant increase in ignition delay by several orders of magnitude [27], thus allowing the pocket to decouple from the wave front. The various dimensional and corresponding non-dimensional parameters relevant to one-step combustion model are given in Table 5.1.

5.3 Results

5.3.1 Preliminary simulation results

Here, a CLEM-LES simulation was conducted for a typical C_κ value of 1.5. The maximum resolution of the supergrid was set arbitrarily to $b = 1/32$ (32 cells per

$\hat{\lambda}_{1/2}$), while the number of subgrid elements within each LES cell was set to $N = 16$. For the AMR implementation, the base grid (G1) has a resolution of $b_{G1} = 1$ with 5 additional levels of refinement for a total of 6 grid levels on the supergrid. Also, the domain height for this simulation was $H = 20$, consistent with the Bhattacharjee experiment [13]. As mentioned in the previous section, the simulation was initiated on the left of the domain with an overdriven ZND wave structure. Random disturbances to the density field ahead of the wave were sufficient to allow the unstable cellular structure to develop with time. In the simulation, the wave was allowed to travel approximately $\sim 850\hat{\lambda}_{1/2}$ downstream, which was more than sufficient to allow the wave to reach a quasi-steady state, in terms of velocity and exhibited cell patterns. A snapshot of the density and temperature fields of the wave, for a particular instance in time near the end of the channel, are shown in Figure 5.3. This particular figure shows that a very irregular pattern emerges on the front. Clearly, there is one large cell that spans half of the domain height, and several much smaller cells above it. Also shown in the figure, is the formation of a typical unburned pocket of reactive gas that appears in the wake. Such pockets are much more cool and dense compared to the surrounding burned products. Also, to compliment Figure 5.3, the corresponding grid topology, which indicates the locations of each grid level (G) in a portion the flow field, is shown in Figure 5.4 for the same instance in time. From this Figure, it is demonstrated that the reaction zone is always refined to the finest level, G6 in this case.

To gain insight on how the observed cells evolve as the wave propagates through the channel, a numerical soot foil was obtained by integrating the local vorticity $\Omega(x, y)$ throughout the duration of the simulation, locally at each spatial location. Thus

$$\Omega(x, y) = \int_{t=0}^{t} \Big(\boldsymbol{\nabla} \times \bar{\boldsymbol{u}}(x, y, t) \Big) dt \tag{5.2}$$

Figure 5.5 shows a portion of the numerical soot foil obtained for a later portion of the channel, from $700 < x < 800$. This particular portion is shown as it highlights in detail the complex nature of the cellular pattern that emerges. In this figure, the

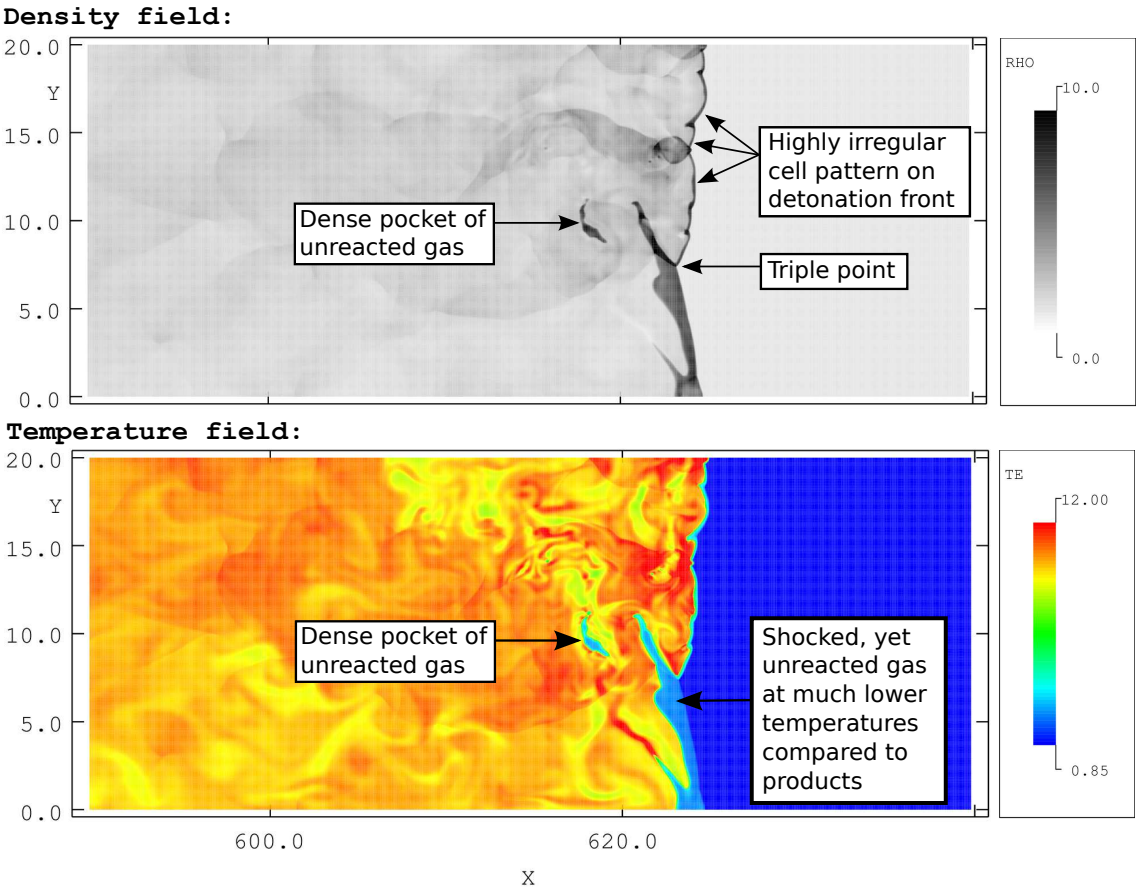

Figure 5.3: Density (top) and temperature (bottom) fields for the CLEM-LES simulation with $C_\kappa = 1.5$. This preliminary result shows the irregular cellular pattern that emerges on the detonation front, and the occasional formation of unburned pockets of reactive gas that appear in the wake. Note: density, temperature, and distances are normalized by $\hat{\rho}_o$, $\gamma\hat{T}_o$, and $\hat{\lambda}_{1/2}$, respectively.

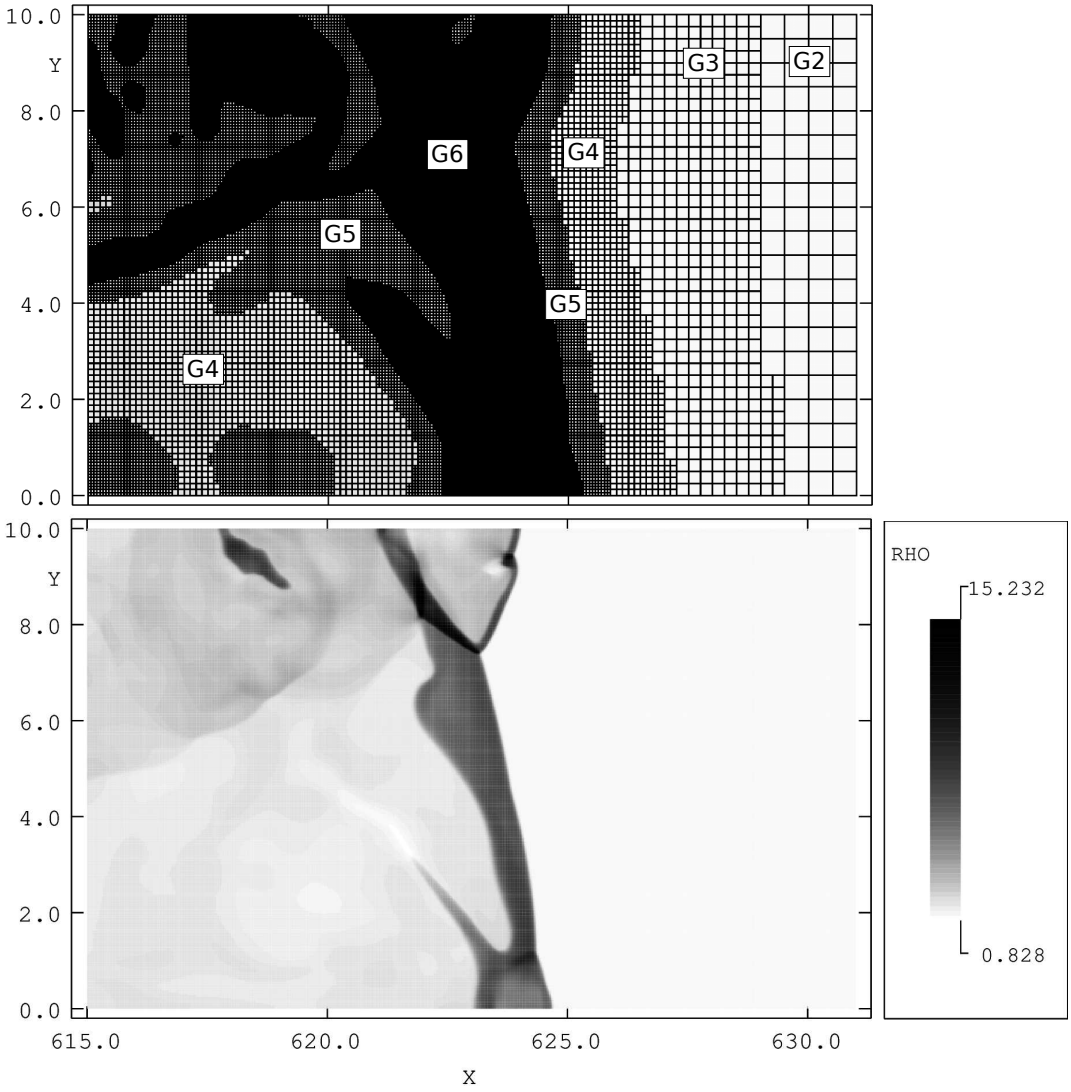

Figure 5.4: Grid topology (top) and corresponding density field (bottom) for a portion of the CLEM-LES simulation shown in Figure 5.3. Also shown is the locations of the various grid levels (G2-G6). Note: The base grid G1 is always refined to at least grid level G2, everywhere.

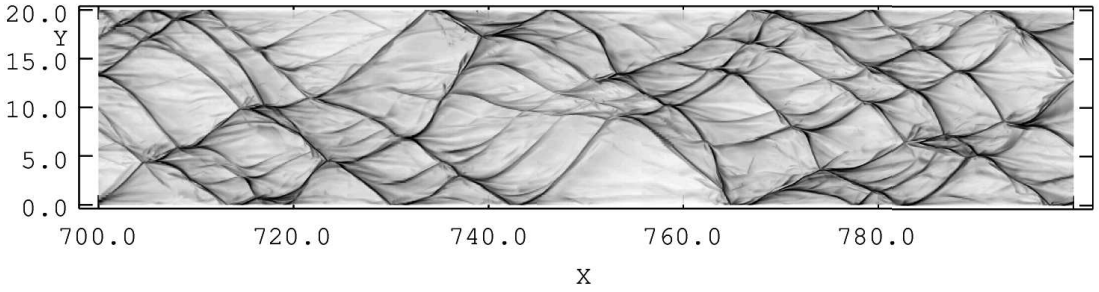

Figure 5.5: Portion of the numerical soot foil obtained for the CLEM-LES with $C_\kappa = 1.5$. The streak marks in the figure show the paths of high vorticity associated with triple point trajectories. Note: Distances are normalized by $\hat{\lambda}_{1/2}$.

streak marks follow paths of large vorticity associated with triple point trajectories. Clearly, in the figure, there are several different cell sizes observed. These range as large as the domain height, H, to cells as small as $\sim H/4$. Furthermore, there does not appear to be any coherent pattern to the appearance of smaller cells in the presence of larger, more prominent ones. Also, the triple point paths, given by the streaks on the image, do not follow perfectly straight lines, or at consistent angles. Sometimes these triple point paths curve more than others in a very irregular manner. Thus, it is of particular interest to determine how turbulence intensity, a function of C_κ, might affect the qualitative features discussed above. In particular, it is of interest to determine how turbulence affects the overall flow field at the wave front, the formation and burn out of the unreacted pockets of gas, and also the cell patterns that emerge. Furthermore, the effect of C_κ on the distance it takes for pockets of unreacted gas to burn up, i.e., the hydrodynamic thickness, is of particular interest. This will serve to validate the strategy to experiments [13, 15] from a quantitative perspective.

Next, Figure 5.6 shows the x-velocity the detonation wave as a function of time, measured along bottom wall at $y = 0$. Initially, the wave is clearly over-driven above the theoretical CJ-value. However, after $t > 40$, sufficient time has passed to allow the detonation wave to decelerate from the over-driven state and reach velocities closer to the CJ-speed. In fact, beyond $t > 40$, the averaged speed of the wave was the CJ-value of 6.3. Clearly, in Figure 5.6, the velocity peaks and valleys also appear very irregular in nature, with no coherent pattern. These velocity measurements correspond to cells

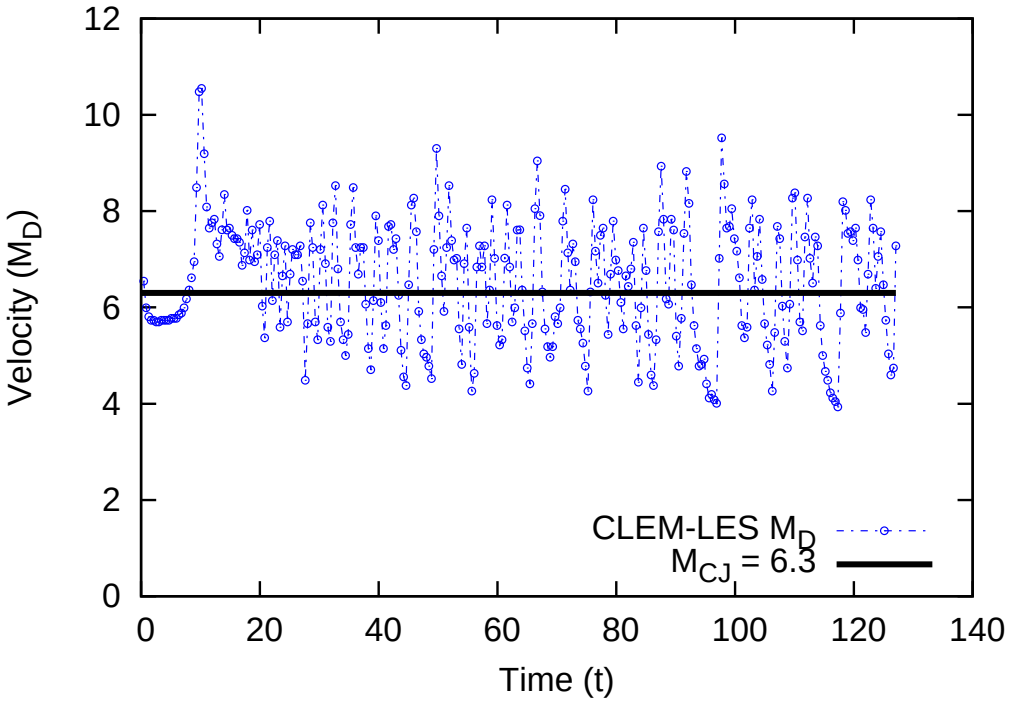

Figure 5.6: x-velocity of detonation for $C_\kappa = 1.5$ and $b = 1/32$ as a function of time, measured along bottom wall at $y = 0$. Note: M_D and t are normalized by $\hat{D}_{CJ}$ and $(\hat{\lambda}_{1/2}/\hat{c}_o)$, respectively.

which form along the wall. In fact, the maximums correspond to the start of each cell cycle observed along the bottom wall, where triple point collisions occur. The minimums represent the end of the cell cycle where the velocity has decayed below the CJ-value. Although the cell cycles appear random, much like the cells shown in the numerical soot foil of Figure 5.5, it is of particular interest to determine how the wave velocities are statistically distributed on the wave front, given the turbulence intensity (C_κ). Furthermore, it is of prime importance to compare such a velocity distribution with available experimental data [13, 15] for the purpose of CLEM-LES validation.

Finally, Figure 5.7 shows both the total resolved and subgrid kinetic energy associated with transverse turbulent motions, as a function of distance from the shock $(x - x_s)$ and along a sample line located at $y = 10$, where x_s is the shock location. The information in this figure was compiled for this simulation when $t = 127.5$. This time corresponds to an instance when the detonation approaches near the end of

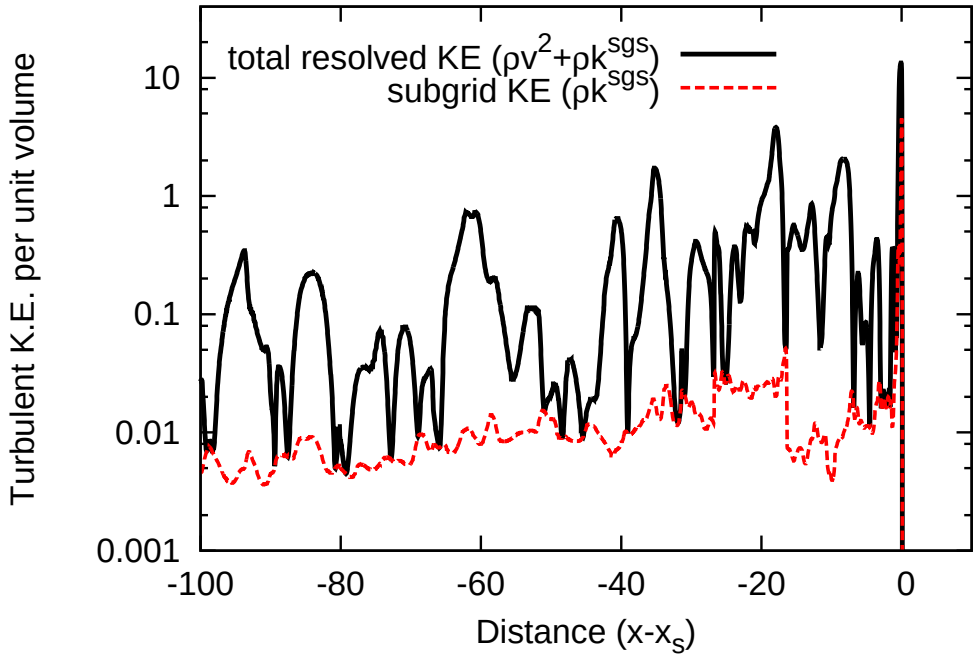

Figure 5.7: Total resolved and subgrid kinetic energy associated with transverse turbulent motions as a function of distance from the shock, measured along $y = 10$ at $t = 127.5$. Note: x_s is the location of the shock.

the computational domain. Here, the total resolved kinetic energy associated with turbulent motions is obtained by only considering the transverse velocity component, v, and the subgrid kinetic energy, k^{sgs}. This not only provides a good estimate for the performance of the CLEM-LES when eddies are encountered down stream from the shock wave, but is relatively easy information to extract since the mean traverse non-turbulent velocity of the flow is always zero. Thus, in the figure, the total resolved turbulent kinetic energy is estimated as $KE_t = \rho(v^2 + k^{sgs})$. Clearly, as transverse turbulent motions are encountered, the majority of the kinetic energy is resolved on the supergrid. At peak values of v, the total turbulent kinetic energy is approximately two orders of magnitude greater than the subgrid kinetic energy, except at the shock. This indicates good performance of the LES, since only a small fraction of the kinetic energy lies in the subgrid scale.

5.3.2 Grid convergence study

Prior to investigating the effect of turbulent mixing rates on the detonation propagation characteristics, it is important to first determine a sufficient resolution which resolves both the reaction rate, and qualitative features of the cellular structure. For this resolution study, $C_\kappa = 1.5$ is specified for the CLEM-LES simulations, and the number of subgrid elements within each LES cell is held constant at $N = 16$. Also, the domain height is kept constant at $H = 20$. Only the maximum super-grid resolution, b, is varied. As before, the base grid (G1) has a resolution of $b_{G1} = 1$, while additional levels of refinement are included to give the desired maximum value for b. This is done according to $b = 1/2^{(G-1)}$ where G is the number of grid levels present.

First, to assess the qualitative behaviour of resolution on the inherent cellular instability of the wave front, open shutter photographs are obtained, numerically, for each simulation and compared in Figure 5.8. Much like the numerical soot foils obtained in the previous section, these open shutter images are obtained by integrating the total reaction rate throughout the duration of the simulation, locally at each spatial location. Thus, the total exothermicity, $\xi(x, y)$, recorded for the open shutter image is estimated from

$$\xi(x, y) = \int_{t=0}^{t} \overline{\dot{\omega}}(x, y, t)dt \tag{5.3}$$

For all resolutions, the simulations are run up to $t = 127.5$. As observed in Figure 5.8, the lowest resolution, $b = 1/4$, produces only large cells whose size appears to be mode locked by the channel height. Furthermore, the cells at this resolution exhibit a very regular self-repeating pattern. As the resolution is increased to $b = 1/8$, the detonation wave continues to exhibit large cells on the order of the domain height. However, the cells at this resolution appear to be slightly irregular in size and shape. Also, the appearance of smaller cells within the larger cell structure are observed starting around $x \sim 550$. For $b = 1/16$, the cell sizes appear much smaller and even more irregular. Also, there appears to be much more variation in cell sizes observed throughout the channel. For example, at $x \sim 200$ there are approximately 4 cells

spanning the domain height. At $x \sim 400$, the cells are intermittently much larger, with about 1 cell spanning the domain height. At $x \sim 500$ there are 2 cells across the domain height. At $x \sim 700$, the cell size increases to 1 cell across the domain height. Then, at $x \sim 800$ there are once again approximately 2 cells spanning the domain height. For the higher resolutions, $b = 1/32$ and $b = 1/64$, the same stochastic cell size behaviour is observed as the $b = 1/8$ case. For these two higher resolution cases, however, the pattern appears even more irregular than the $b = 1/8$ case. In fact, the $b = 1/32$ and $b = 1/64$ cases are qualitatively similar to each other in terms of observed cell sizes, pattern behaviour, and irregularity.

To effectively quantify the average rate at which reactant was consumed behind the leading shock wave, at any given instant in time, the average distance for the reactant to be consumed behind the leading shock wave was measured. This was indicative of the time it takes for the the reactant burn up behind the leading shock. To measure this average *hydrodynamic thickness*, a Favre-averaging technique in spatial slices on the super-grid, dx, was applied to give a mass weighted average reactant and density profile along the channel length for any given time. This procedure is illustrated in Figure 5.9. Also, this approach was previously applied in [27]. Formally, the Favre-average reactant profile is given by the expression

$$\tilde{Y}(x,t) = \frac{\int_{y=0}^{H} \bar{\rho}(x,y,t)\tilde{Y}(x,y,t)dy}{\int_{y=0}^{H} \bar{\rho}(x,y,t)dy} \tag{5.4}$$

where the average density profile, in x, is found by

$$\bar{\rho}(x,t) = \frac{\int_{y=0}^{H} \bar{\rho}(x,y,t)dy}{H} \tag{5.5}$$

Finally, the Favre-averaged mass fractions are ensemble averaged for $k = 50$ random instances in time. Thus,

$$\tilde{Y}(x - x_s) = \frac{\sum_{i=0}^{k} \tilde{Y}(x - x_s, t_i)}{k} \tag{5.6}$$

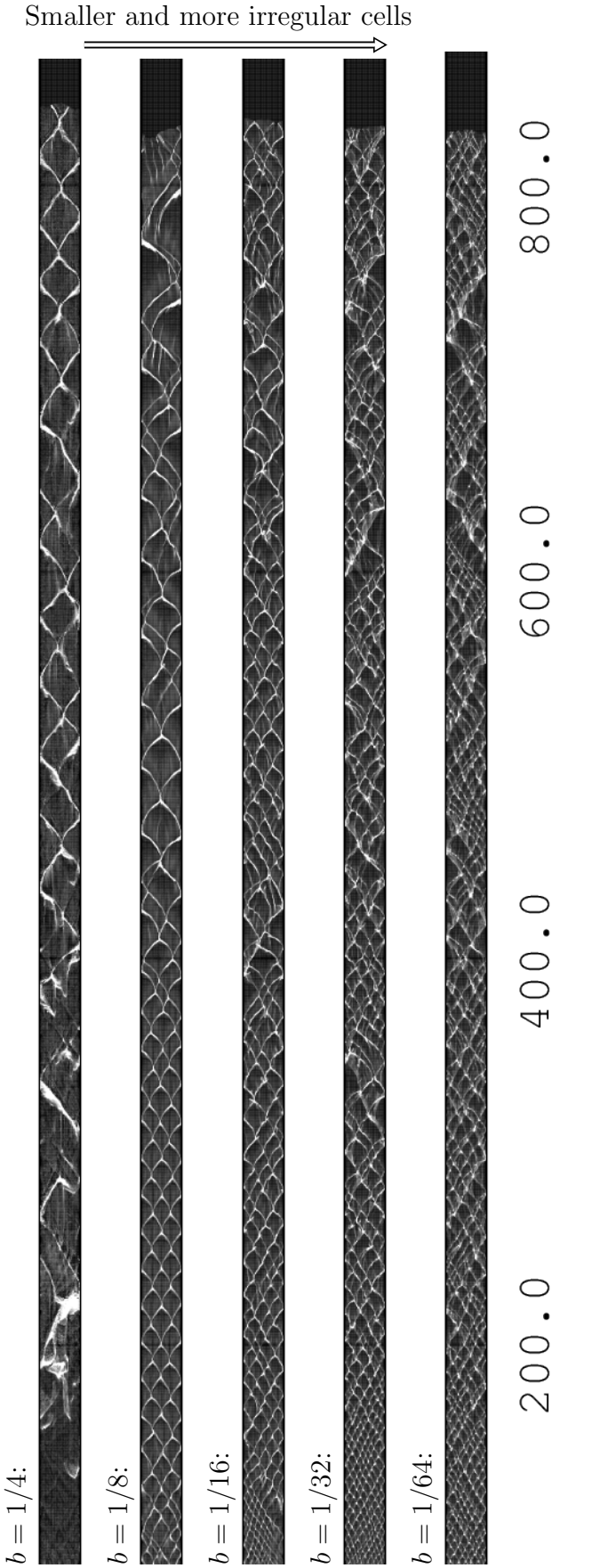

Figure 5.8: Open shutter records for $C_\kappa = 1.5$ at various resolutions, b (all with $N = 16$ elements per LES cell).
Note: Distance x is normalized by $\hat{\lambda}_{1/2}$.

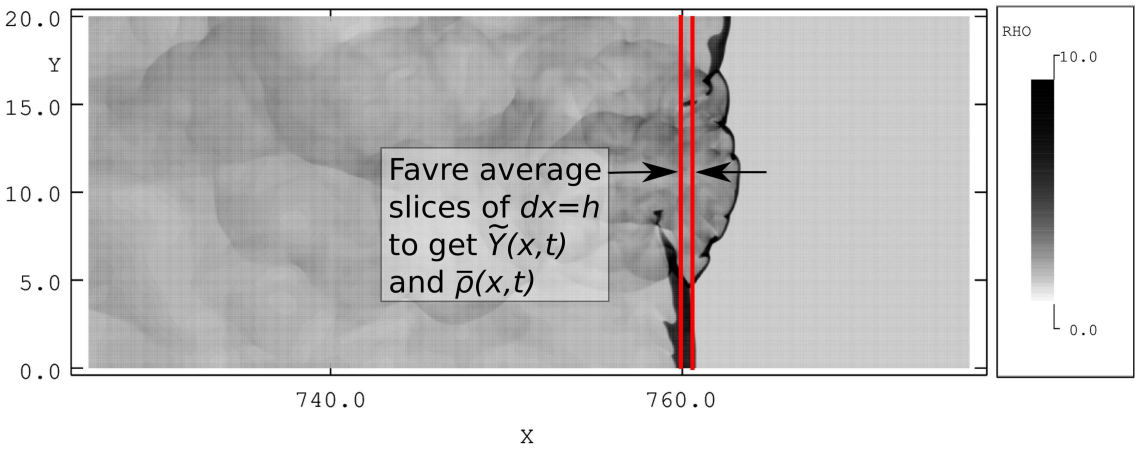

Figure 5.9: Example of how Favre-averaging is applied to an instance in time to determine $\tilde{Y}(x,t)$ and $\bar{\rho}(x,t)$. This particular image shows the density field for the CLEM-LES using $C_\kappa = 1.5$ and a resolution of $b = 1/32$ when $t = 116.9$ (3.175ms).

Here x_s was the location of the shock wave determined by the location where the right-most maximum gradients in the spatially averaged density occur. Also, the sample slices for which averaging is done is taken as the minimum super-grid resolution size, $dx = b$. Finally, it should be noted that this ensemble averaging only considers profiles when $t > 40$. As previously shown in Figure 5.6, this was sufficient time to allow the detonation wave to decelerate from the over-driven state and reach the CJ-speed.

In Figure 5.10a, the average profiles obtained for $\tilde{Y}(x - x_s)$ are presented for the CLEM-LES at various resolutions (b). For the CLEM-LES, it can clearly be seen that the average rate of depletion of $\tilde{Y}(x - x_s)$ behind the shock wave does not vary significantly across the range of resolutions tested, with the exception of $b = 1/4$ whose reactant depletion rate is slightly slower than all other cases. In fact, all of the higher resolutions ($b = 1/8$ to $b = 1/64$) appear to consume 90% of the reactant within the same average distance, $\sim 5\hat{\lambda}_{1/2}$. Finally, only the highest resolutions, $b = 1/32$ and $b = 1/64$, develop fluctuations in reactant mass fractions when $\tilde{Y}(x - x_s) < 10\%$, and thus has a slightly lengthened structure compared to lower resolution cases. These fluctuations are indicative of *pockets* of unburned fuel that form in the wake of the leading shock wave. Figure 5.11a shows an example of how such pockets of unreacted fuel form at sufficiently high resolution ($b = 1/32$), while Figure 5.11b shows how such pockets do not form at lower resolution (i.e., when $b = 1/8$). Even though the

low resolution case captures the same hydrodynamic thickness, the high frequency instabilities are effectively filtered out. This suggests that the reaction rate, in general, is not so sensitive to resolution. However, the irregular propagation behaviour and fine scale qualitative observations are sensitive to resolution. Furthermore, it is worth noting that at $b = 1/32$ resolution with $N = 16$, the laminar flame speed is resolved in 1-D (see Figure B.3 in Appendix B). To compare the performance of the CLEM-LES with the traditional use of Euler simulations, Figure 5.10b shows the average reactant profiles for $\tilde{Y}(x - x_s)$ using the Euler method (see Section 2.2) across the range of resolutions from $b = 1/4$ to $b = 1/128$. Clearly, the Euler method does not provide any convergence of solution with increased resolution. This can be observed by the lengthening of the structure, or distance it takes for reactant to become consumed, as the resolution increases. To quantify the hydrodynamic thickness of the structure of each simulation, the thickness, Δ_H, is arbitrarily taken as the distance from shock location, at $x = x_s$, to the position where $\tilde{Y}(x - x_s) < 2\%$. Figure 5.12 shows that across the range of resolutions, the average hydrodynamic thickness for the CLEM-LES is not very sensitive to resolution, whereas the Euler method clearly shows an increase in average thickness as resolution increases. Figure 5.12 also shows the range of hydrodynamic thickness observed throughout the random sampling process. The error bars thus serve as the variation in thickness for the 50 random samples used in the ensemble averaging process of each simulation. Clearly, the Euler method yields an increasing variation in thickness as the resolution is increased. Also at high resolutions, $b \geq 1/64$, the Euler method yields larger, and more stochastic, range in thickness compared to the CLEM-LES. The CLEM-LES, on the other hand, appears to converge to a statistically consistent range of thickness observed with each random sample. This can be seen for $b = 1/32$ and $b = 1/64$ where the hydrodynamic thickness is found to vary stochastically between $\Delta_H = 3-16\hat{\lambda}_{1/2}$ for both resolutions. Furthermore, the average thickness for the CLEM-LES remains consistent around $\Delta_H = 6 - 9\hat{\lambda}_{1/2}$ for all resolutions.

In terms of performance, Figure 5.13 shows the run times for the CLEM-LES and Euler simulations, conducted in this section, at various supergrid resolutions. Also

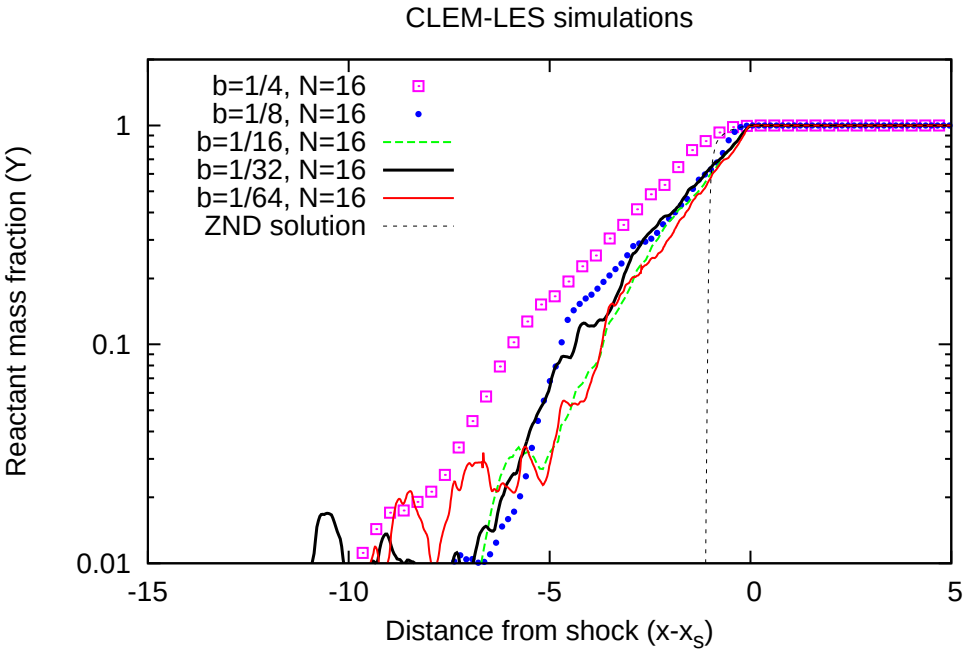

a)

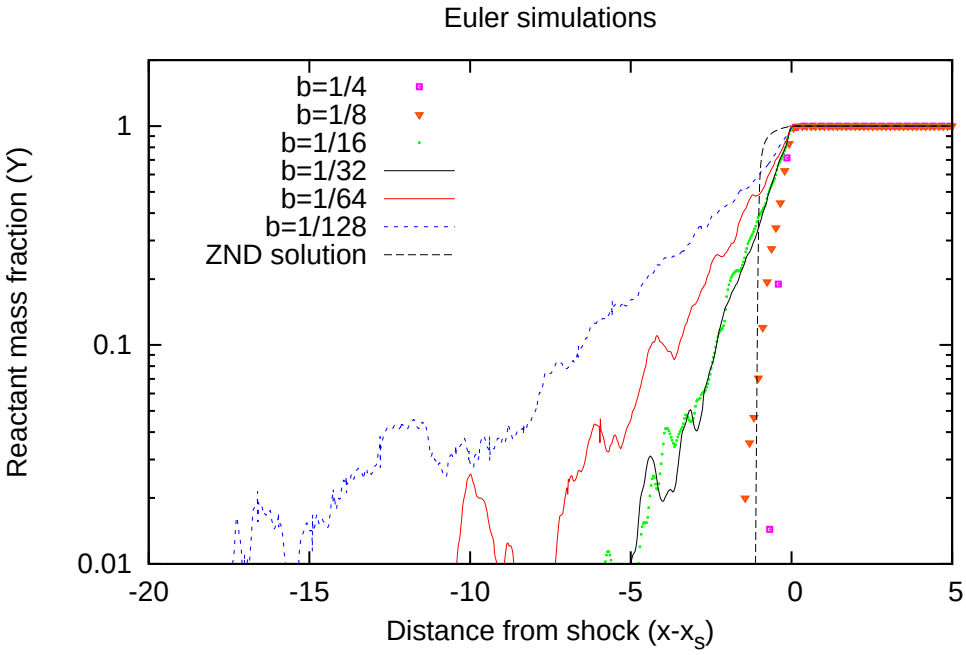

b)

Figure 5.10: Effect of resolution on average reactant profiles for a) the CLEM-LES and compared to b) Euler methods. Note: Distances x and x_s are normalized by $\hat{\lambda}_{1/2}$.

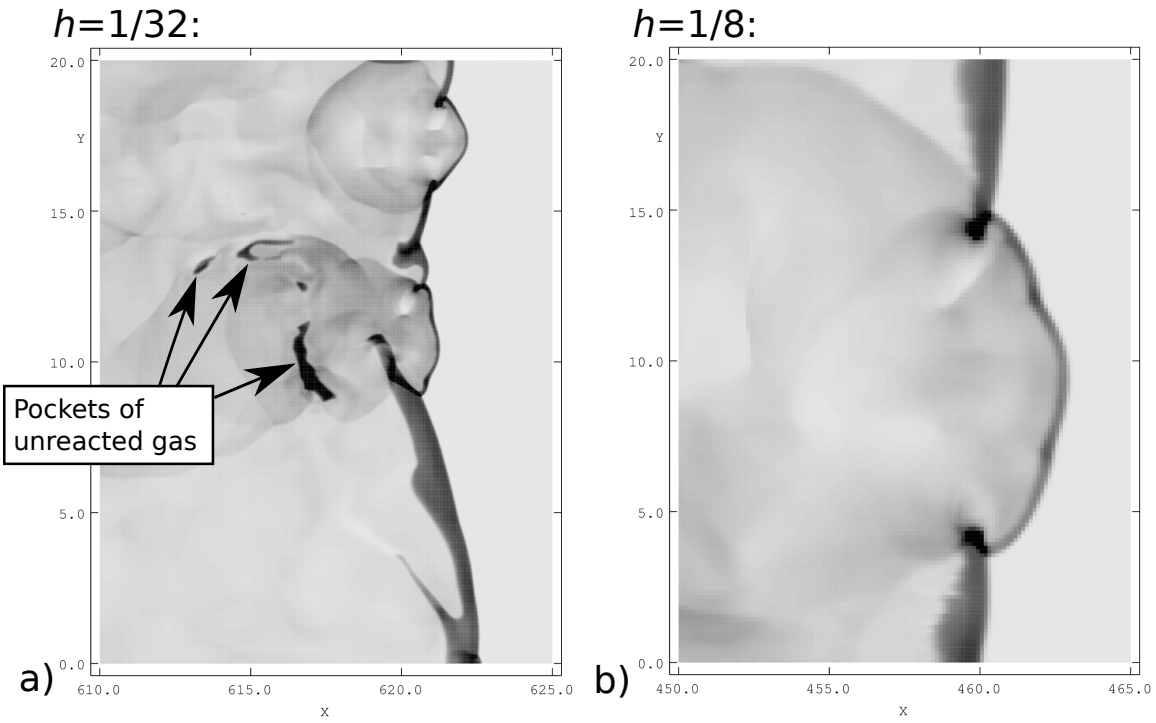

Figure 5.11: The left frame (a) reveals how pockets of unreacted gas form in the wake of the detonation front at high resolution ($b = 1/32$), while (b) shows how such pockets do not form at low resolution ($b = 1/8$). Both images show the density field at a randomly chosen instance in time.

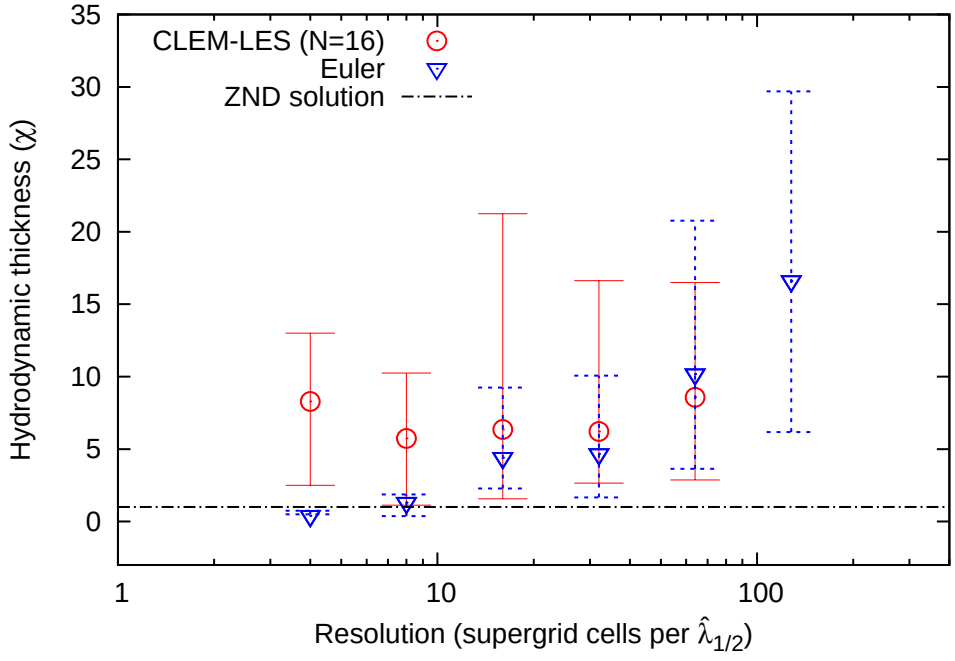

Figure 5.12: Effect of resolution on hydrodynamic thickness (Δ_H) for CLEM-LES and compared to Euler methods. Note: Δ_H is normalized by $\hat{\lambda}_{1/2}$.

indicated in the figure are the number of CPUs used to evolve each simulation. In general, both the CLEM-LES and Euler simulations have run times which appear to have a power-law dependence on the supergrid resolution chosen. Increasing the resolution by an order of magnitude requires increased run times by approximately two orders of magnitude. Furthermore, for each supergrid resolution, the CLEM-LES requires a run time that is approximately one order of magnitude greater than the corresponding Euler simulation. This is not surprising since each CLEM-LES has to compute an additional $N = 16$ subgrid elements per supergrid cell, on the finest grid level. To compliment this, Figure 5.14 shows the total number of supergrid cells and subgrid elements, for the CLEM-LES and Euler simulations, at various maximum subgrid resolutions. The information in this figure was compiled for each simulation at an instance when $t = 127.5$. This time corresponds to an instance when the detonation approaches near the end of the computational domain. In general, the resources required also exhibit a power-law dependence on supergrid resolution. For the CLEM-LES, the total number of supergrid cells, at each resolution, is comparable to its Euler simulation counterpart. Each CLEM-LES computation, however, requires a number of subgrid elements that approximately an order of magnitude greater than the total number of supergrid cells. This reflects the requirement for a larger simulation run time, also an order of magnitude greater than its Euler counterpart. In all simulations, approximately 40% of the supergrid cells are at the finest grid level.

Finally, to summarize the findings in this section, a maximum supergrid resolution of $b = 1/32$, with a further $N = 16$ subgrid elements, has been demonstrated to sufficiently resolve and capture the structure size, high frequency instabilities exhibited through cell patterns, and overall propagation behaviour. Thus, $b = 1/32$ is the resolution used throughout the remainder of the thesis.

5.3.3 Effect of the Kolmogorov parameter (C_k)

In order investigate the role of turbulent mixing rates on the detonation front cellular patterns, burning rates, and irregularity, the constant C_κ is varied. This is done using

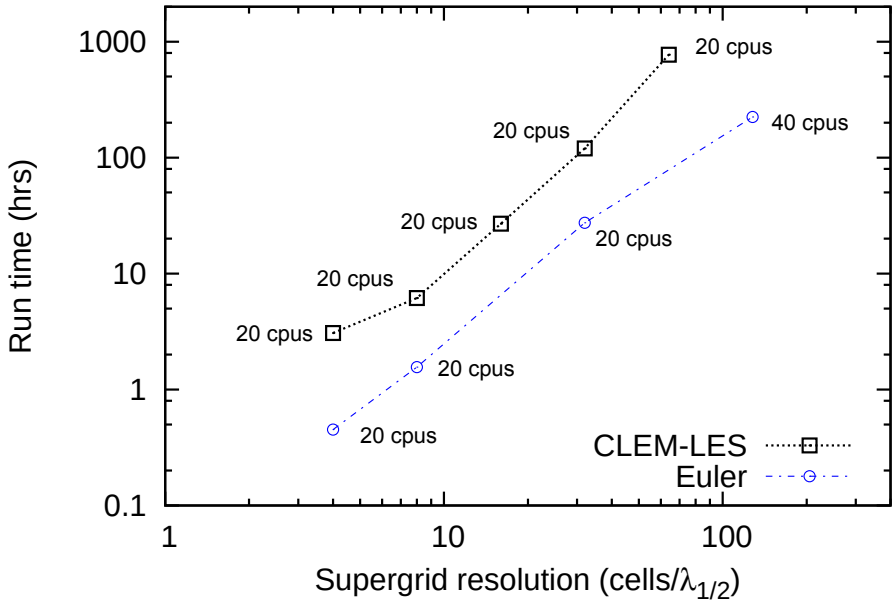

Figure 5.13: Run times for CLEM-LES and Euler simulations at various resolutions. For the CLEM-LES, $C_\kappa = 1.5$ with $N = 16$ subgrid elements per supergrid cell. Also shown are the number of CPUs used in each simulation.

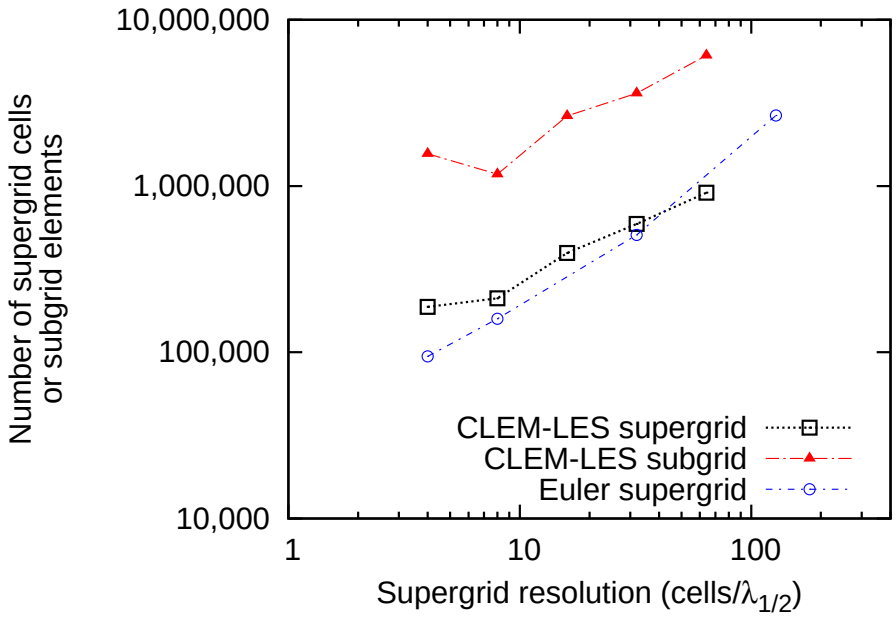

Figure 5.14: Number of total supergrid cells (on all grid levels) and subgrid elements for both CLEM-LES and Euler simulations at various resolutions. For the CLEM-LES, $C_\kappa = 1.5$ with $N = 16$ subgrid elements per supergrid cell on the finest grid level.

a maximum supergrid resolution of $b = 1/32$ with $N = 16$ subgrid elements within each supergrid cell. As before, to achieve this resolution on the supergrid, the base grid (G1) has a resolution of $b_{G1} = 1$ with 5 additional levels of refinement. It should also be noted that a formal grid resolution study for each C_κ was not conducted here. In the previous section, this particular resolution and AMR configuration was found adequate to resolve the qualitative features associated with cell sizes and patterns, and irregularity. Furthermore, this resolution was found to give converged burning rates behind the shock, which was measured quantitatively by considering the size of the observed hydrodynamic thickness (Δ_H). Also, the laminar flame speed (in 1D) is resolved at this resolution, as demonstrated in Appendix B. As discussed previously, in Section 3.1, the turbulent viscosity and dissipation rates, ν_t and ϵ, are both functions of C_κ, which are consequently functions of k^{sgs}. Thus turbulent mixing rates, and hence combustion rates, are expected to be influenced by changes in C_κ. For the numerical experiment in this section, C_κ is varied from 1.2 to 10.0. As was done in the previous section, the qualitative features are compared using numerically obtained open shutter images. The domain height for all simulations in this section is once again kept constant at $H = 20$. Also, the average hydrodynamic thickness and the statistical distribution of sizes, obtained for 50 random samples in time, are collected for each simulation.

First, open shutter images are shown in Figure 5.15 for the range of C_κ values (1.2-10). Also, the CLEM-LES open shutter images are compared against the Euler simulation, which also has $b = 1/32$ resolution. Clearly the Euler simulation exhibits much smaller cells and a more regular looking pattern compared to all of the CLEM-LES open shutter images. In fact, as previously observed in Figure 5.12, the Euler method has a much smaller statistical range of hydrodynamic thickness compared to the CLEM-LES. For the CLEM-LES at $C_\kappa = 1.2$, in Figure 5.15, the cells are still fairly small compared to the channel height, however there is some irregularity to the pattern observed. As C_κ is increased, the observed cell sizes also increase. For $C_\kappa = 3.0 - 4.0$ it is observed that the range of cell sizes span from 3 cells to 1 cell per channel height, intermittently, throughout the simulations. As C_κ is increased

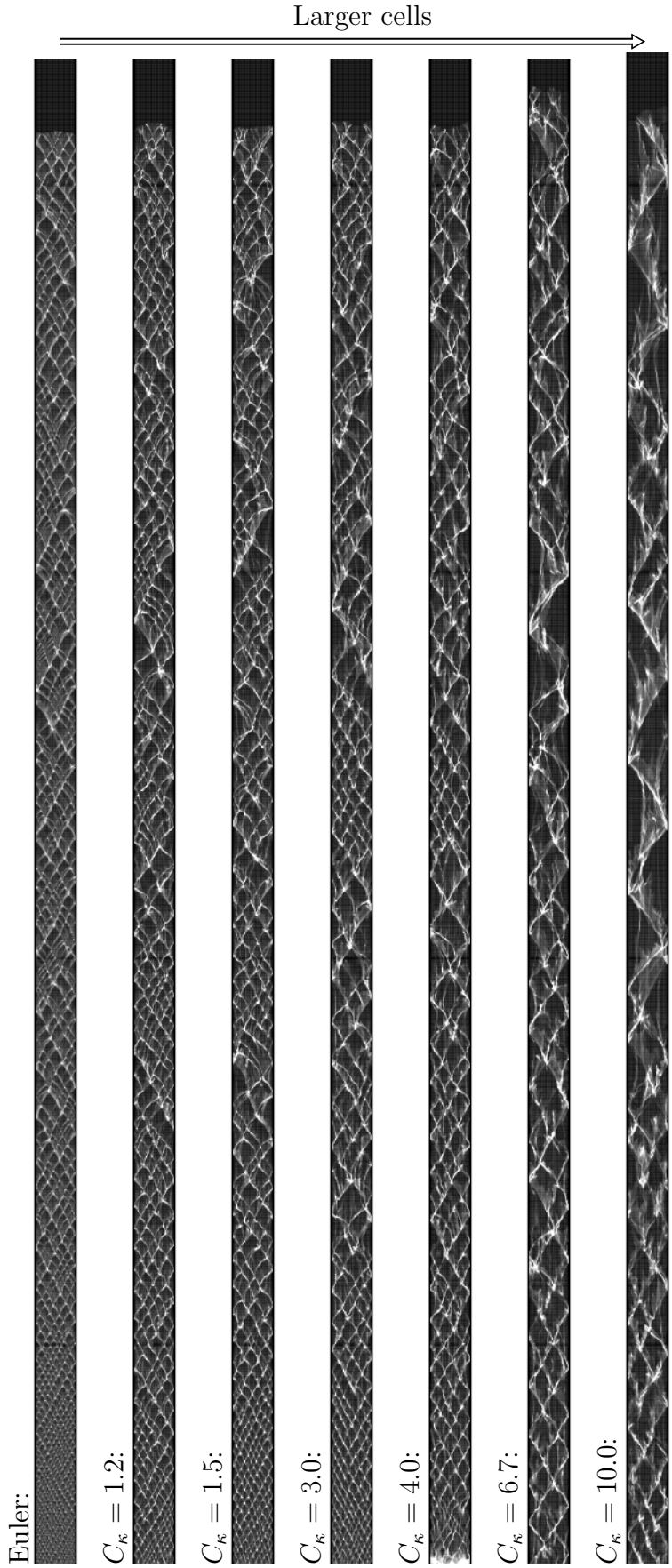

Figure 5.15: Open shutter records for various Kolmogorov parameter (C_κ) values (CLEM-LES) and an Euler simulation. All simulations have a resolution of $b = 1/32$, and for the CLEM-LES, a further $N = 16$ elements per supergrid cell. Note: Distance x is normalized by $\hat{\lambda}_{1/2}$.

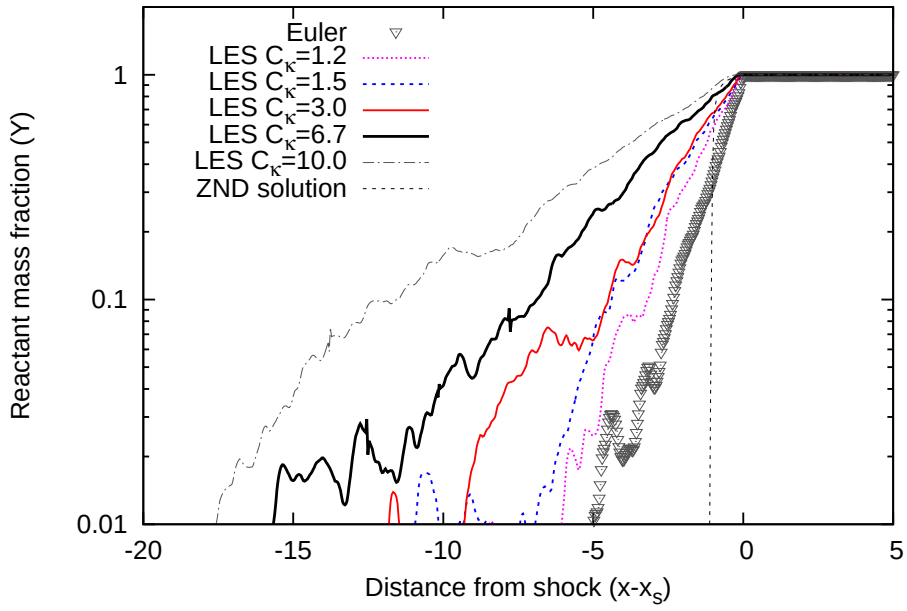

Figure 5.16: Effect of turbulent intensity (through C_κ) on average reactant profiles for the CLEM-LES (all with resolution $b = 1/32$ and $N = 16$ elements per LES cell). Also shown is the average reactant profile obtained from the Euler method at $b = 1/32$ resolution. Note: Distances x and x_s are normalized by $\hat{\lambda}_{1/2}$.

beyond 6.7, the cells become even larger, with an observed range of 2 cells to 1/2 cell per channel height.

Next, in Figure 5.16, the average reactant profiles are compared for the range of C_κ values using the procedure described in the previous section. Also, the simulations are compared to an Euler simulation, which also has a resolution of $b = 1/32$. Clearly, as C_κ increases, the average hydrodynamic thickness of the detonation wave increases. This observation is made by considering the distance it takes for $\tilde{Y}(x - x_s) \to 0$. On the other hand, the Euler method at the same resolution, which is subject to a large amount of numerical diffusion, burns fuel at a much quicker rate than all of the CLEM-LES simulations.

Finally, in terms of model performance, each simulation conducted here required a run time of approximately 100 hours. This run time and also the total number of supergrid cells and subgrid elements was found to be independent of changes in C_κ.

5.4 Discussion

5.4.1 Qualitative comparison of the flow evolution with experiments

A visual comparison of a flow field, obtained through resolved LES and the corresponding experiment [13], is shown in Figures 5.17 and 5.18 for an instance where a triple-point collision occurs for a detonation whose cell size is comparable to the channel height. For the LES, the density evolution is shown for various instances of the collision process for $C_\kappa = 6.7$. This value of C_κ was found to produce cell sizes and overall qualitative behaviour comparable to experimental observation. The maximum resolution of the simulation is $b = 1/32$ on the supergrid, with a further $N = 16$ subgrid nodes within each supergrid cell. The channel height is kept at $H = 20$. For the experiment [13], Schlieren images of each corresponding instance are obtained from high speed photography and are also shown in the figures. For comparison, many features are noted in the figures (Features 1-7). In Figure 5.17, the first feature (1) is a Mach shock with a turbulent reaction zone that follows closely. In both the simulation, and the experiment, the reaction zone is slightly decoupled from the shock owing to local unsteadiness of the wave front. This can be seen by the thickening of the shocked unburned gas region as time evolves. In the LES, however, this wave appears to be more irregular, containing what appears to be a smaller and less pronounced cell structure (cells within cells). It should be noted that experimental observations [13] report a very stochastic nature of the propagating wave. In this sense, random bifurcations on wave fronts and changes in cell patterns are expected. In some cases much smaller cells are observed experimentally and numerically for the same quiescent conditions and numerical parameters, see Figure 5.19. Feature (2), in Figure 5.17, is a completely decoupled incident shock-reaction zone, as can be seen by the large region of dense unburned gas. As the two triple-points approach each other, transverse shock waves compress this gas further. At the focal point of the

collision, owing to the increased pressure and temperature, the unburned pocket (2) ignites very rapidly. This "explosion", noted by feature (3), drives transverse shock waves and a strong Mach shock forward coupled with very rapid burning. Feature (4) is a pocket of unburned gas which is not ignited by compression associated with the original Mach shocks (1). Instead, these pockets mix and burn along turbulent shear layers. Thus, Kelvin-Helmholtz instability gives rise to increased burning rates through turbulent mixing of the burned and unburned gases. Furthermore, Richtmyer-Meshkov instability further enhances combustion of feature (4) via shock compression associated with the transverse shocks, labelled as feature (5) in Figure 5.18, which originate from feature (3). Feature (6), in Figure 5.18, is a new pocket of unburned gas that forms along slip lines associated with the collision process. Finally, feature (7), in Figure 5.18, is a bifurcation observed on the Mach shock of feature (3), owing to the unstable nature of methane-air detonations. This bifurcation also occurs in the experiment but is less pronounced. Although features (1-7) are captured by the LES, a key difference is observed in the burning rate behind behind the Mach shock originating from feature (5). In the simulation, the size of this region grows much faster compared to experiment, likely attributed to higher burning rates. It should be noted that the experiment [13] reports a velocity deficit up to $\sim 70\%$ below the CJ velocity owing to losses from the channel walls. Since external losses are not accounted in the LES, and the CJ velocity is recovered, as seen previously in Figure 5.6 for $C_\kappa = 1.5$, more rapid burning would be expected.

To further compare the performance of the LES with available experimental data [15], the simulation was repeated with a channel height of $H = 10$. Both the density evolution from the numerical simulation, and the corresponding instances obtained in the experiment [15] through Schlieren photography are shown in Figures 5.20 and 5.21. In this case, all model parameters, including C_κ, are consistent with the previous experiment [13], except the reduced channel height permits only half a cell to form. Thus the cell pattern is effectively influenced by the channel walls, or *mode-locked* into a cell size which corresponds roughly to the channel height. In this case, only a single transverse wave is observed. Again, for qualitative comparison, many features

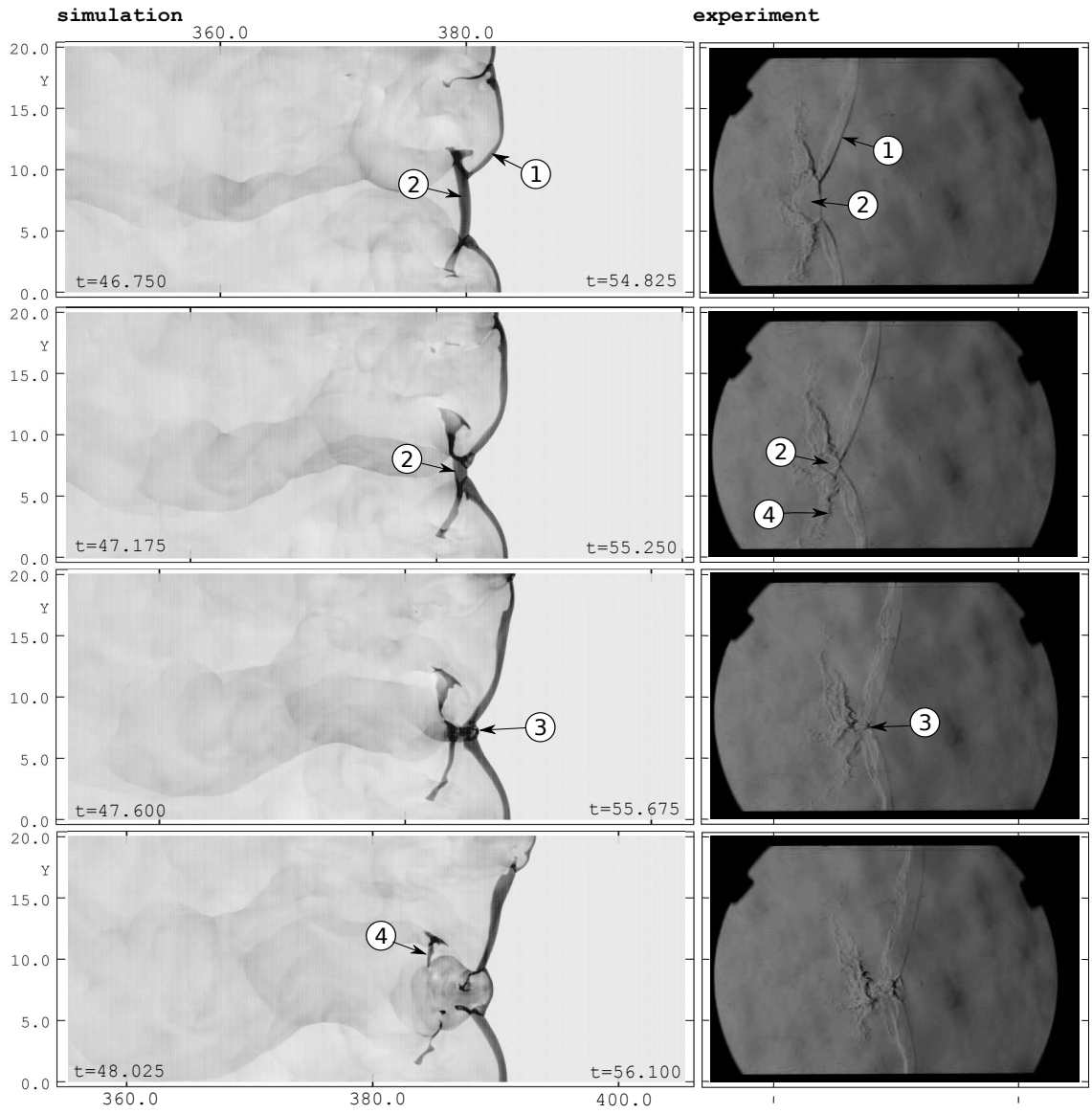

Figure 5.17: Numerical density evolution for the Kolmogorov parameter $C_\kappa = 6.7$ (left) and the corresponding experimental Schlieren photography [13] (right) of a detonation triple point collision process. The time in between each image is $\Delta t = 0.425$ (11.53μs). The remaining sequence of images are continued in Figure 5.18.

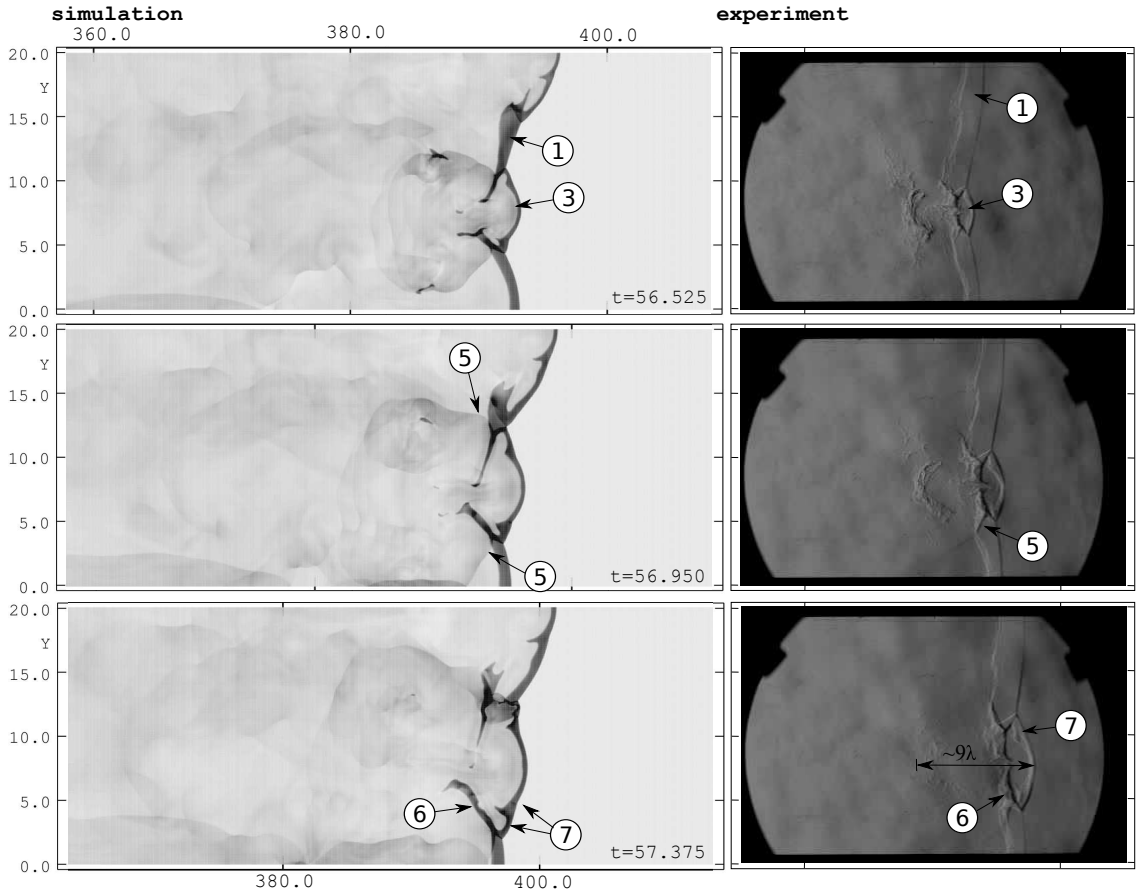

Figure 5.18: Continuation of Figure 5.17. Numerical density evolution for $C_\kappa = 6.7$ (left) and the corresponding experimental Schlieren photography [13] (right) of a detonation triple point collision process.

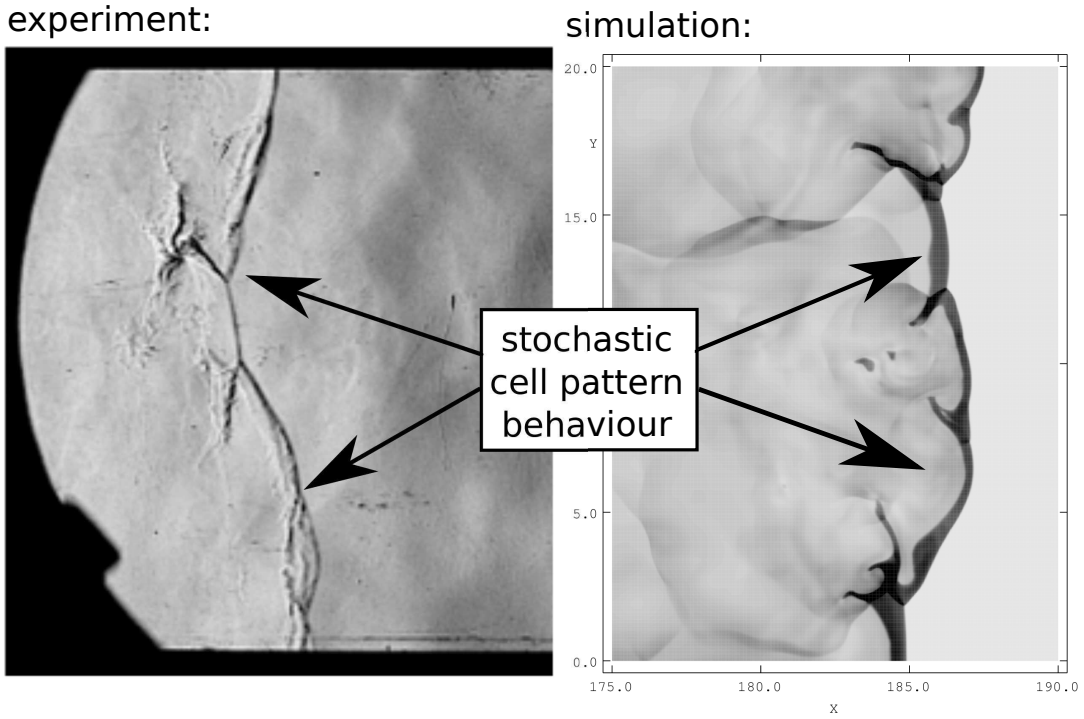

Figure 5.19: Comparison of experiments [13] and the CLEM-LES with $C_\kappa = 6.7$, both showing an instant where stochastic behaviour is observed such that a different cell pattern is observed compared to Figure 5.17

are noted in the figures (Features 1-7). Feature (1), in Figure 5.20, is the incident shock wave. Behind this shock is the de-coupled reaction zone, as observed by the region of very dense, shocked, and unburned fuel following the shock. From the top wall of the channel, Feature (2) is a Mach stem, which initially results from a transverse wave collision with the wall. This Mach stem appears to travel faster than the incident wave, owing to more intense combustion associated with the wave collision process at the wall, akin to the triple point collision process observed in Figure 5.17. Feature (3), in Figure 5.20, is a pocket of dense unburned fuel in the wake of the wave, which burns turbulently through Richtmyer-Meshkov instability associated with the transverse shock wave, Feature (4). In fact, this region burns out only slightly faster than the observed experimental rate. In the experiment, the pocket burns up completely within 7 frames (70μs), while the simulation burns up completely within 5 frames (50μs). Feature (5), in Figure 5.20, is a hot spot that forms behind a bifurcation of the Mach shock and is only clearly visible in the

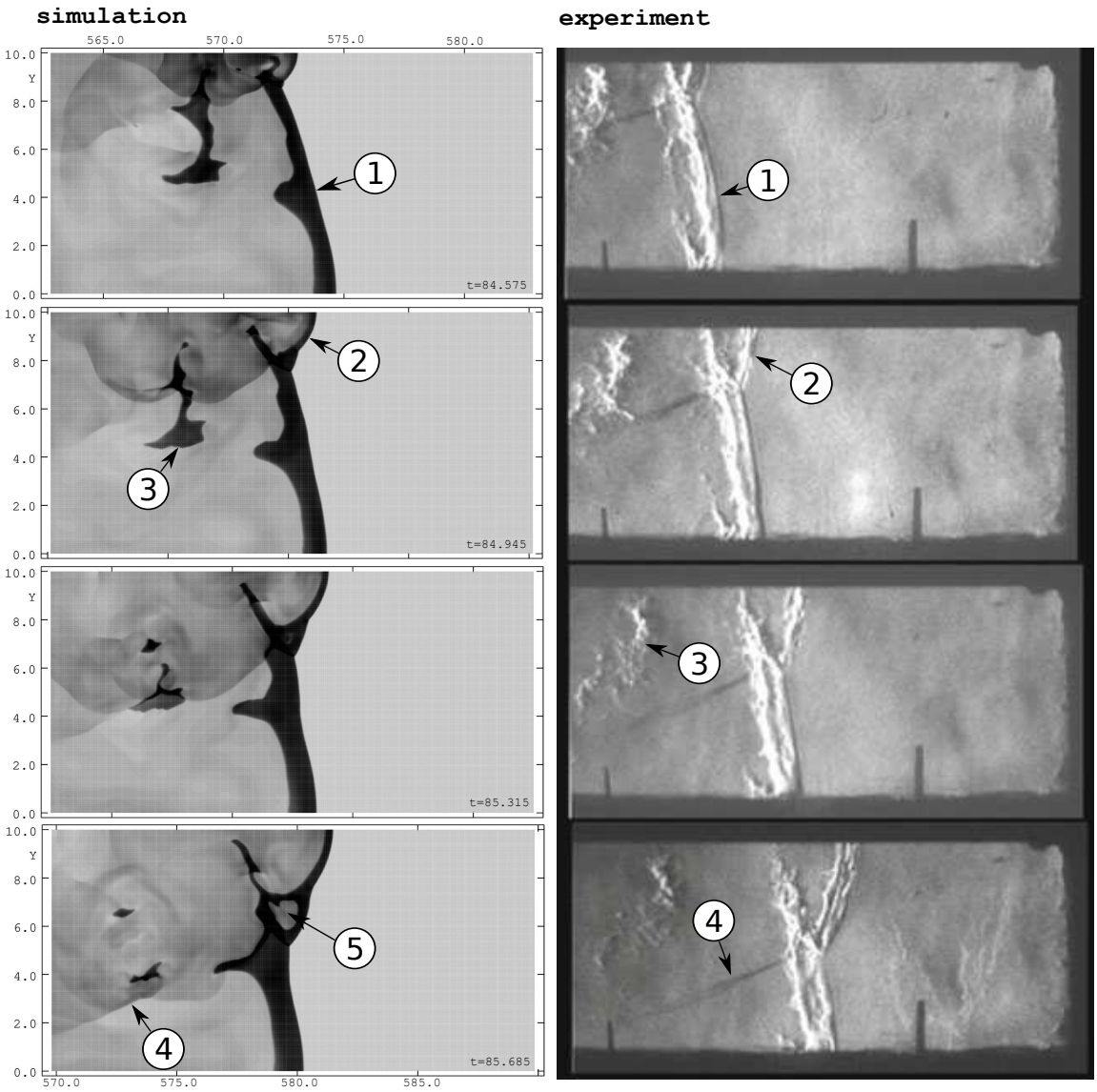

Figure 5.20: Numerical density evolution for the Kolmogorov parameter $C_\kappa = 6.7$ (left) and the corresponding experimental Schlieren photography [15] (right) of an irregular detonation propagation in a channel. The time in between each image is $\Delta t = 0.37$ (10.0μs). The remaining sequence of images are continued in Figure 5.21.

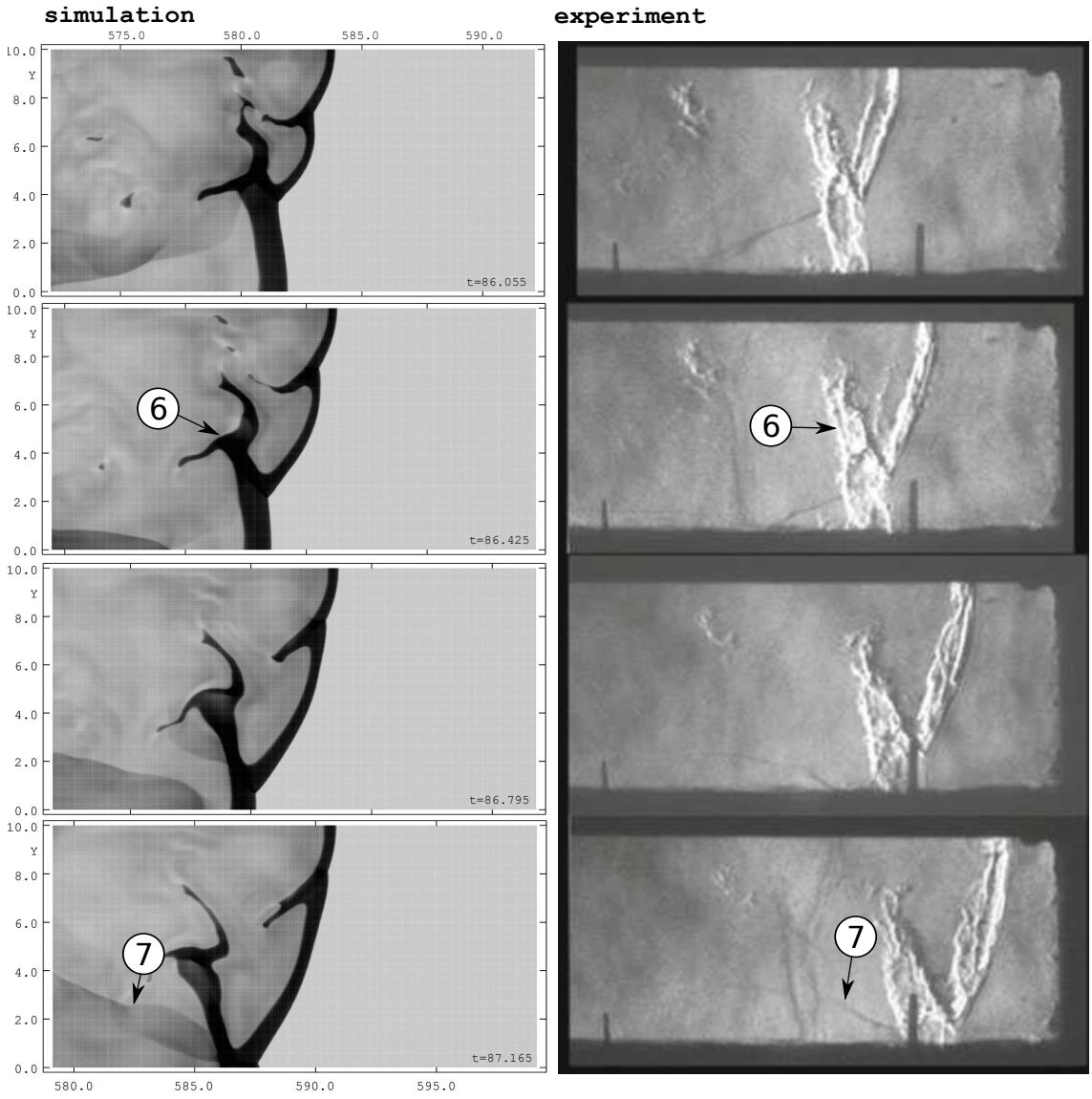

Figure 5.21: Continuation of Figure 5.20. Numerical density evolution for $C_\kappa = 6.7$ (left) and the corresponding experimental Schlieren photography [15] (right) of an irregular detonation propagation in a channel. The time in between each image is $\Delta t = 0.37$ (10.0μs).

numerical simulation. This bifurcation of the Mach stem near the triple point was also observed in the previous comparison to experiment, Figure 5.17. As the Mach stem, Feature (1) continues to evolve, the combustion zone becomes further decoupled from the shock, as observed by an increased thickness of dense unburned fuel behind the shock. Furthermore, as the Mach shock evolves, a new pocket of dense unburned fuel forms in the wake of the triple point path, denoted by Feature (6) of Figure 5.21. This pocket is initially consumed from its edges via turbulent flame, augmented locally by the intense shear through Kelvin-Helmholtz instability. The passage of the reflected transverse shock wave, Feature (7), further contributes to turbulent mixing through Richtmyer-Meshkov.

5.4.2 Qualitative comparison of cell patterns with experiments

Finally, to further compare the the CLEM-LES with experiment, in terms of cell patterns and irregularity, numerically obtained soot foils for both $H = 10$ and $H = 20$ at $C_\kappa = 6.7$ was compared to those obtained experimentally for $CH_4 + 2O_2$ at $\hat{p}_o = 3.5$kPa (courtesy M. Radulescu), and $CH_4 + 2O_2 + 0.2$Air at $\hat{p}_o = 11$kPa [19]. For $H = 20$, the numerical soot foil, presented in Figure 5.22, corresponds exactly to the open shutter image, of Figure 5.15, for $C_\kappa = 6.7$. Although the experimental soot foil, also shown in Figure 5.22, was obtained for a smaller channel height (127mm) and also for a much higher pressure, the two are comparable in terms of scaling through the half-reaction length. For the experiment [19], $\hat{\lambda}_{1/2} = 5.1$mm. This value was obtained in this study using the Cantera libraries [193] and the GRI-3.0 detailed kinetic mechanism [194], consistent with the procedure in Appendix B. Thus, the experimental soot foil was estimated to be $\sim 25\hat{\lambda}_{1/2}$ high. This is comparable to the simulation, whose domain is $20\hat{\lambda}_{1/2}$ in height. In the portion of the numerical soot foil presented in the figure, the overall cell size and pattern matches well to the experiment. In the experiment, however, a very distinct substructure was observed. This was observed by the presence of much smaller cells within the larger and more

Simulation:

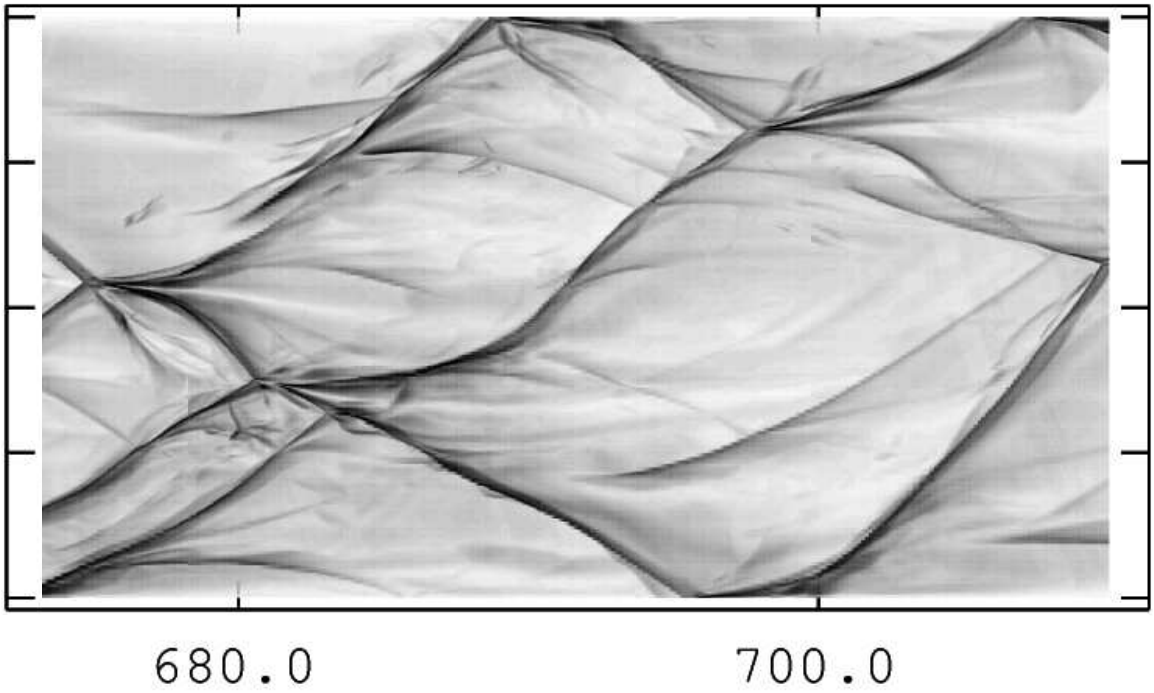

Experiment:

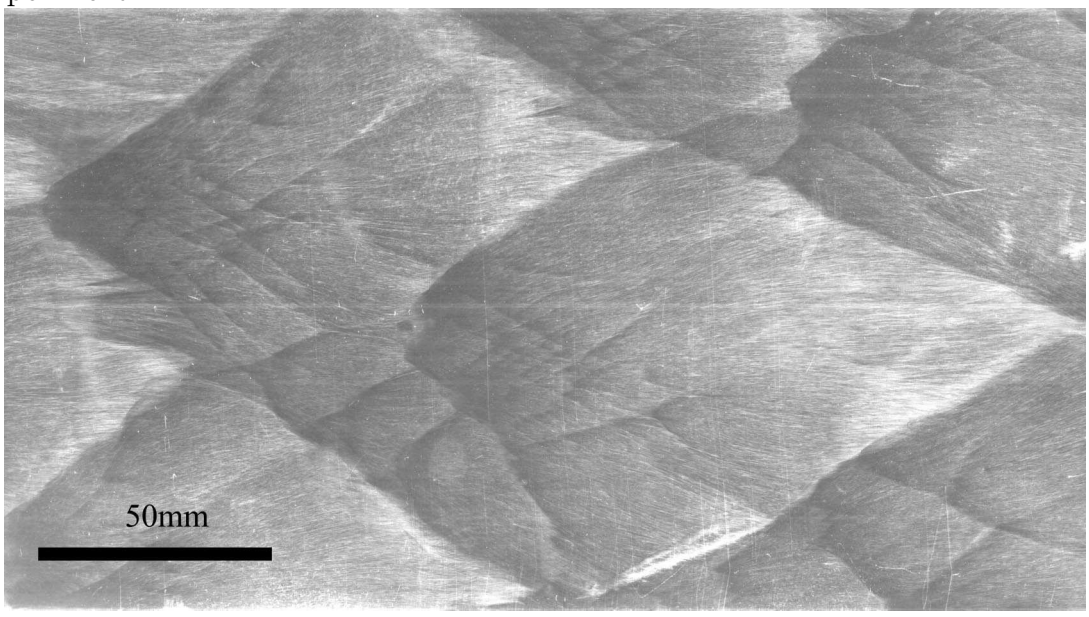

Figure 5.22: Numerical soot foil obtained for the CLEM-LES with $C_\kappa = 6.7$ and $H = 20$ (top) compared with an experimental soot foil for $CH_4 + 2O_2 + 0.2$Air at $\hat{p}_o = 11kPa$ [19] (bottom). Note: the channel height for the experiment is $\sim 25\hat{\lambda}_{1/2}$.

predominant cell structure. Although such a fine substructure is not so obvious in the simulation, there are still some streaks on the numerical soot foil, which are indicative of triple point paths associated with cell bifurcations. The lack of detailed substructure in the simulation could be an artifact of the supergrid resolution, differences in mixture properties, or most likely associated with the limitation of the one-step model in capturing the very short duration energy release of methane combustion and the associated instabilities that exists on that finer small scale. Furthermore, it is likely that at the resolution presented here, $b = 1/32$, has effectively filtered out the fine details associated with the expected substructure. It is noted that higher resolution simulations were not conducted for $C_\kappa = 6.7$. Despite this lack of fine-scale detail for the substructure, the overall cell behaviour and irregularity is captured well by the simulation.

For $H = 10$, numerical soot foils are obtained for two different portions of the numerical domain and compared to experimental soot foils, provided by M. Radulescu, in Figure 5.23. Here, the experimental soot foils were obtained using the same experimental apparatus described in Kiyanda and Higgins [15]. For both experimental soot foils, the numerical simulation captures well the cell size behaviour and irregularity. In general the channel height allows only 1/2 cell to form. The cells, however, occasionally bifurcate, giving rise to the formation of cells on the order of the channel height. This behaviour can be observed in the bottom frames of Figure 5.23. Finally, it is noted that a prominent substructure was not observed experimentally or numerically for $H = 10$, as was observed experimentally in Figure 5.22. This could be attributed to differences in the mixture or conditions (i.e., the pressure) at which tests were performed.

5.4.3 Quantitative analysis: the hydrodynamic thickness

In order to determine the effect that turbulent mixing intensity has on the hydrodynamic thickness, the average thickness of the structure (Δ_H) has been measured for various C_κ values for the domain height of $H = 20$. This was achieved by following

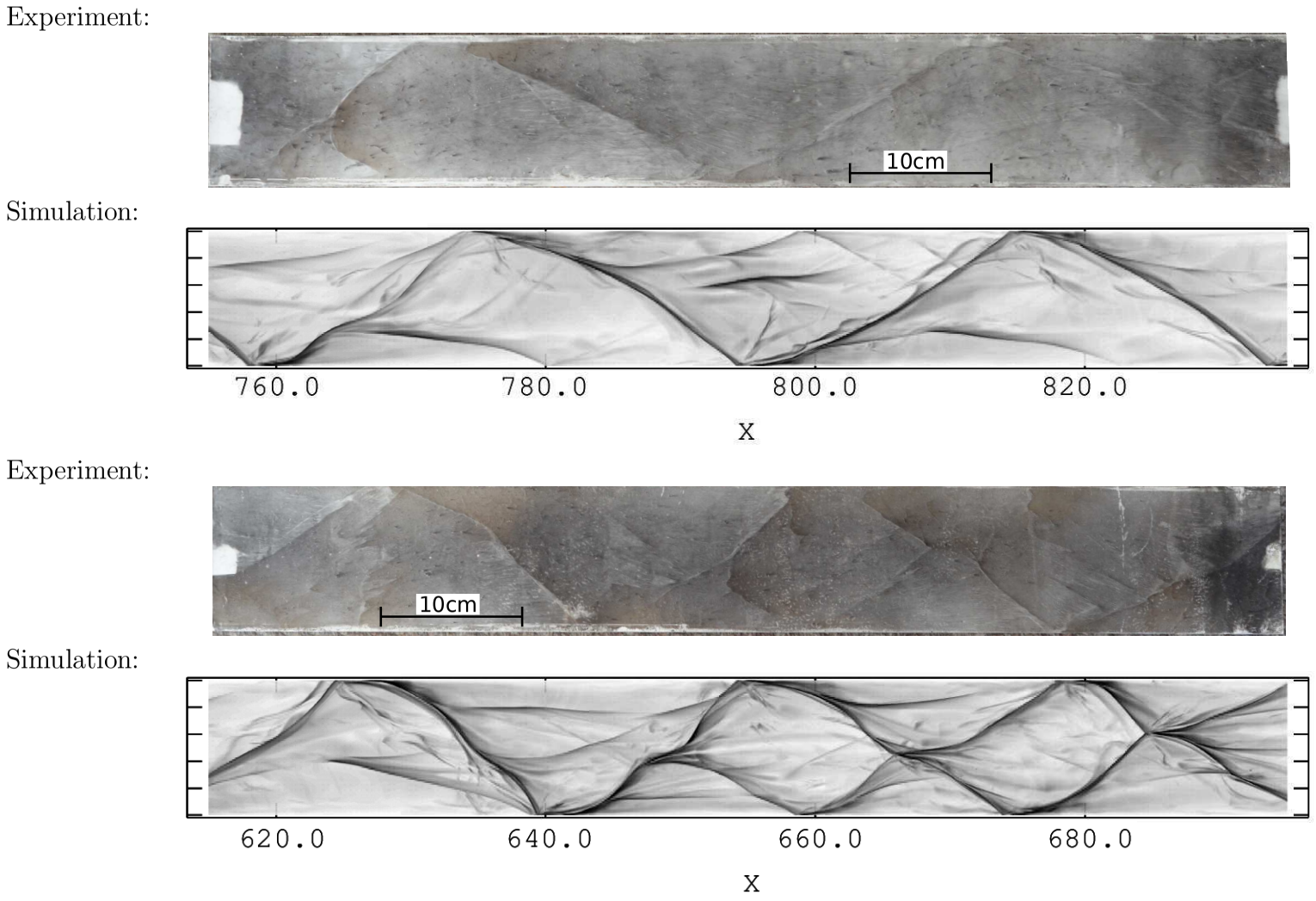

Figure 5.23: Numerical soot foils obtained for the CLEM-LES with $C_\kappa = 6.7$ and $H = 10$ compared with two experimental soot foil for $CH_4 + 2O_2$ at $\hat{p}_o = 3.5kPa$, courtesy of M. Radulescu. Note: the channel height for the experiment is also $10\hat{\lambda}_{1/2}$.

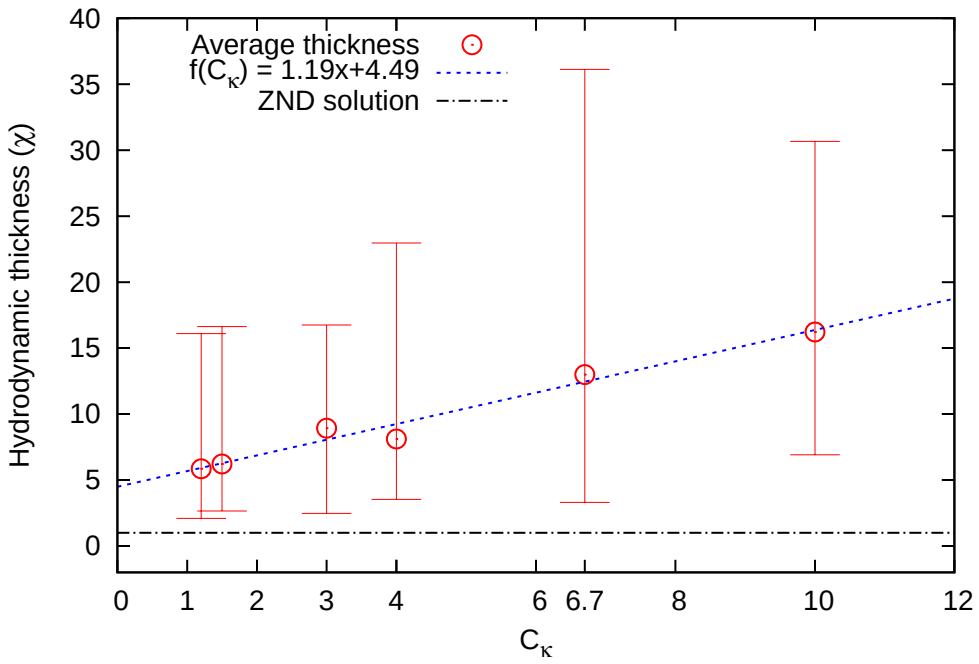

Figure 5.24: Effect of turbulence intensity (through C_κ) on hydrodynamic thickness (Δ_H) for the CLEM-LES (all with resolution $b = 1/32$ and $N = 16$ elements per LES cell). Note: Δ_H is normalized by $\hat{\lambda}_{1/2}$.

the procedure to obtain Δ_H at various resolutions in Section 5.3.2. Figure 5.24 thus shows the hydrodynamic thickness (Δ_H), measured by the distance from the shock wave, $x = x_s$, to where $\tilde{Y}(x) < 2\%$, as a function of C_κ. Clearly, there is an increasing trend in thickness with C_κ. In fact, the thickness appears to increase linearly with C_κ for the range of values simulated here. A line of best fit (obtained from linear regression of each data point), $\Delta_H = 1.19C_\kappa + 4.49$, is also indicated in the figure. Also shown in the figure are error bars indicating the variation of thickness measured from each of the 50 samples for each value of C_κ. In general, the range of expected thickness increases with C_κ, with the exception of $C_\kappa = 6.7$ having the largest range. In Figures 5.25a and b, histograms showing the statistical distribution of thicknesses observed both $C_\kappa = 1.5$ and $C_\kappa = 6.7$ are given, respectively. The figures show, for each C_κ, the probability of obtaining a certain range of thickness obtained from the 50 random samples in time. Clearly for each C_κ, there is a favoured range of thickness near the average value obtained in Figure 5.24, with a probability

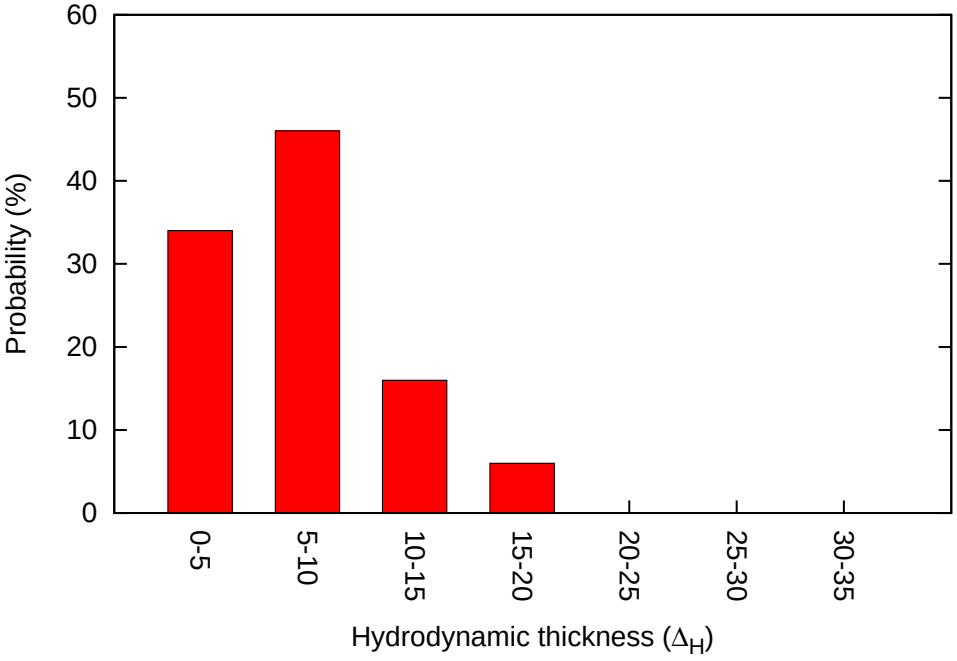

a)

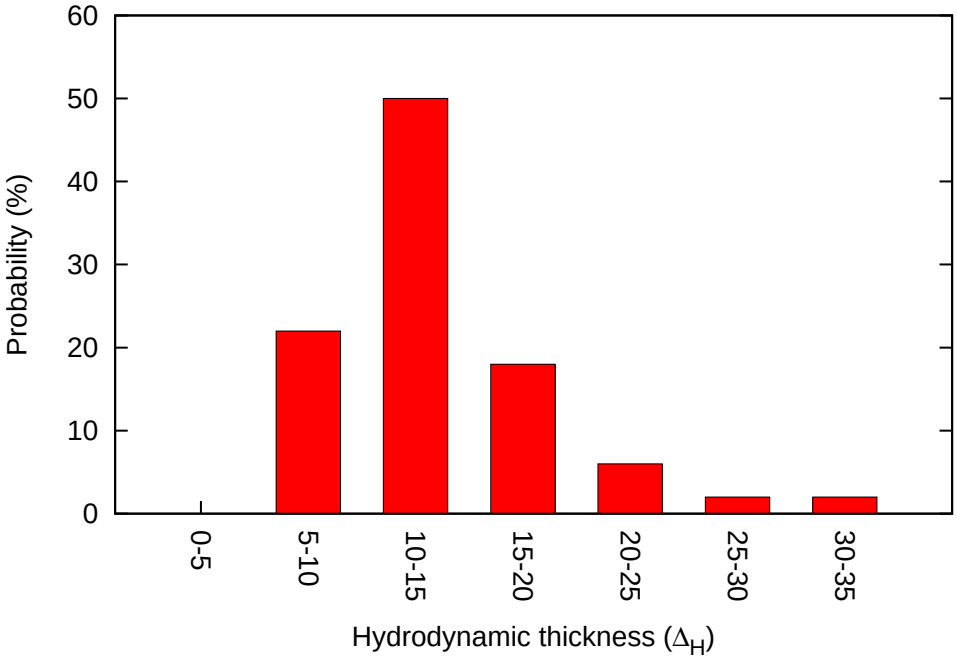

b)

Figure 5.25: Statistical distribution of hydrodynamic thickness (Δ_H) for a) $C_\kappa = 1.5$ and b) $C_\kappa = 6.7$, each compiled from 50 random instances in time. Note: Δ_H is normalized by $\hat{\lambda}_{1/2}$.

of $\sim 50\%$. Also evident from Figures 5.25a and b, is the physical shift in distribution as C_κ increases. These figures clearly show that the probability of having a larger hydrodynamic thickness increases with C_κ.

The principal finding of the numerical experiment above highlights the sensitivity of both the average hydrodynamic thickness and observed cell patterns to the constant C_κ. Specifically, increasing C_κ was found to lengthen the averaged structure thicknesses and also produce larger, and more irregular, cell patterns. This was observed previously in Figures 5.24 and 5.15, respectively.

Finally, to quantitatively compare the CLEM-LES to experimental observations in terms of the hydrodynamic thickness, or distance it takes for the pockets of unburned gas to burn, results from Section 5.3.3 are considered. In Figure 5.24, it was observed that the average hydrodynamic thickness captured by all values of C_κ, for $H = 20$, was in the range $5 < \Delta_H < 17$. More specifically, for $C_\kappa = 6.7$ and $C_\kappa = 10.0$, the average thickness was found to be $\Delta_H = 13.0$ and $\Delta_H = 16.2$, respectively. These computed average thicknesses are much higher than previous experimental reports of burn out distances between $\sim 4 - 6\hat{\lambda}_{1/2}$ [27]. Upon close inspection, however, of images published in Bhattacharjee [13], burn out distances can be estimated as high as $\sim 9\hat{\lambda}_{1/2}$, as can be seen in Figure 5.26. This can be attributed to experimental losses, which are believed to give rise to a larger observed structure [27]. Thus, compared to Bhattacharjee, $C_\kappa = 6.7$ yields an error of $\sim 44\%$, while $C_\kappa = 10.0$ yields an error of $\sim 80\%$. Despite these large errors, however, it should be noted that the simulations for $C_\kappa = 6.7$ and $C_\kappa = 10.0$ have both exhibited a large range of possible thickness anywhere from $3 < \Delta_H < 36$. Furthermore, the experiments [13, 27] are stochastic in nature and have not quantified the probability and variance of hydrodynamic thickness possible during propagation.

5.4.4 Quantitative analysis: velocity of the wave

To gain insight on why increasing C_κ has the effect of generating larger hydrodynamic structures, the subgrid kinetic energy associated with random velocity fluctuations

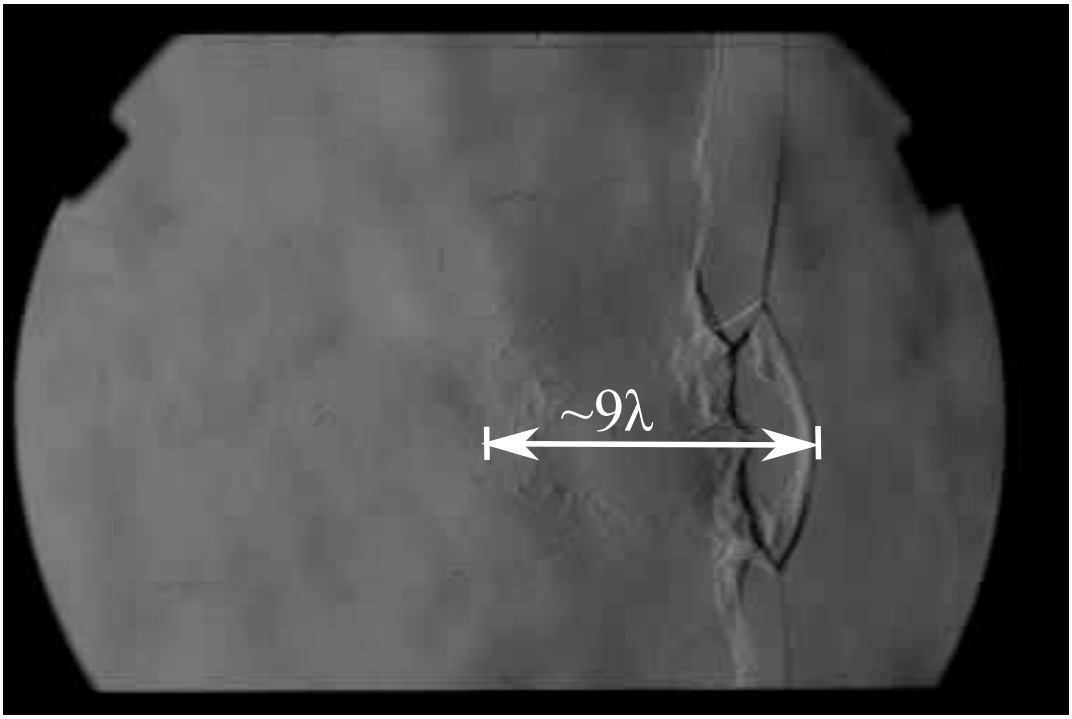

Figure 5.26: Schlieren photograph taken from Bhattacharjee [13], which shows that pockets of unburned gas can take up to $\sim 9\hat{\lambda}_{1/2}$ behind the leading shock to burn up.

(k^{sgs}) is Favre-and ensemble averaged for each C_κ case using the same procedure as was done for the reactant profiles, i.e., Eqs.(5.4)-(5.6). The averaged profiles obtained for k^{sgs} at various values of C_κ are thus shown in Figure 5.27. The principle observation made here is that as C_κ is increased, more subgrid kinetic energy is generated. This is not surprising since k^{sgs} is a direct function of C_κ in Eq.(3.15). This increase in k^{sgs} with C_κ thus generates more random velocity fluctuations, represented by stirring events on the CLEM subgrid. It is thus expected that as C_κ increases, the variation of velocities expected on the wave front should also increase.

To quantify the statistical distribution of velocities experienced by the wave front, and such a distribution was affected by C_κ, probability density functions (PDFs) were constructed and shown in Figures 5.28 and 5.29 for $H = 20$ and $H = 10$, respectively. These figures thus show the probability of the wave having a certain velocity at any random time and location. In these figures, the wave speeds expected on the front (D) are normalized by the averaged propagation speed (D_{avg}). For the CLEM-LES, conducted at various C_κ values, and also an Euler simulation at the

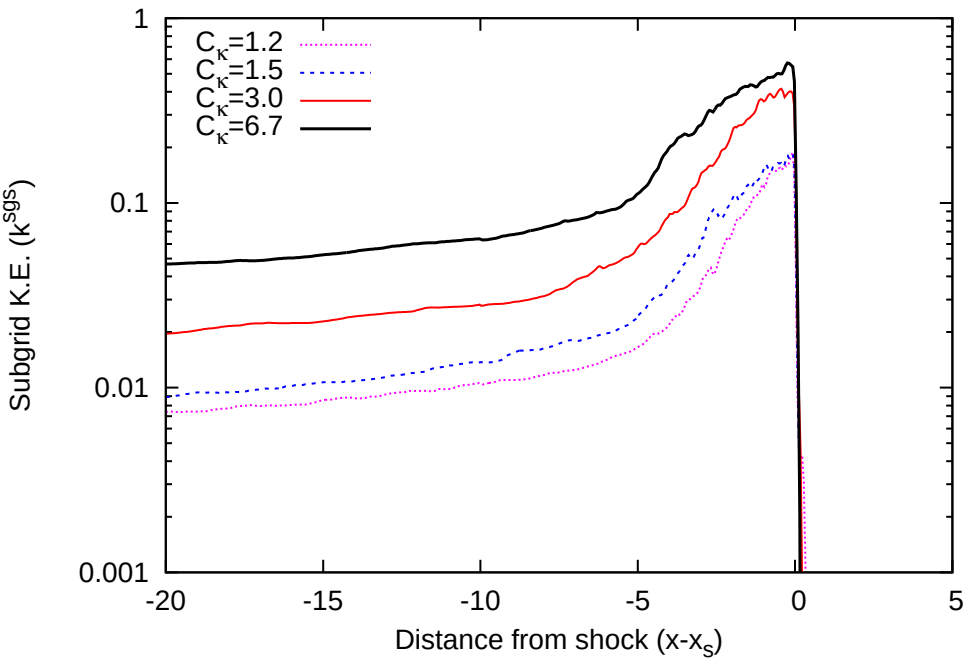

Figure 5.27: Effect of C_κ on the averaged subgrid kinetic energy (k^{sgs}) profile for the CLEM-LES. Note: Distances x and x_s are normalized by $\hat{\lambda}_{1/2}$.

same supergrid resolution ($b = 1/32$), this average propagation speed is always the CJ-value, $D_{avg} = 6.3$. Also shown in Figures 5.28 and 5.29, are the PDFs constructed from available experimental data [13, 15], for $H = 20$ and $H = 10$, respectively. From experimental data available, $D_{avg} = 5.19$ [13] for $H = 20$, and $D_{avg} = 5.53$ [15] for $H = 10$. It should be noted that the average velocities obtained from experiments are lower than CJ due to energy losses not accounted for in the simulations. To construct the PDFs from the numerical simulations, velocity measurements were taken on the top and bottom walls for a total of 500 data points in each simulation. The PDF was then evaluated at $D\pm \sim 0.5$ intervals and normalized by D_{avg} accordingly. For $H = 20$, the comparative experimental PDF, shown in Figure 5.28, was compiled from a total of 6651 velocity measurements were collected from 4 different experiments at the same conditions [13]. This PDF was evaluated at $D\pm \sim 0.2$ intervals. For $H = 10$ in Figure 5.29, 37 velocity data points are available experimentally [15] to compile the PDF for one entire cell cycle. The PDF here was compiled at each velocity measurement. Further details of how the PDFs were compiled can be found

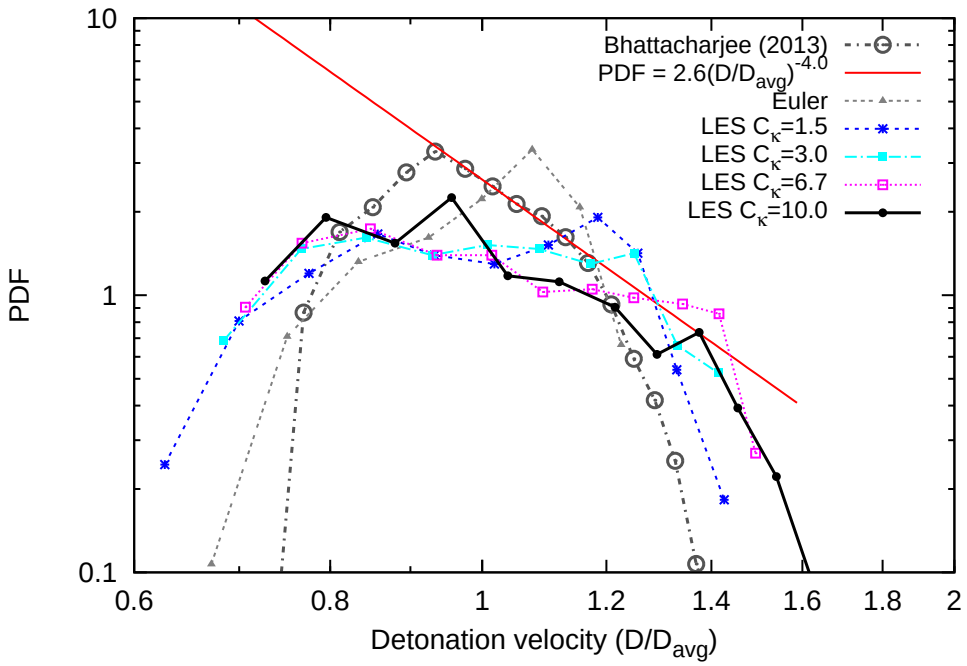

Figure 5.28: PDF of a detonation wave, in a channel with $H = 20$, having a certain velocity (D/D_{avg}) at any given moment and location. Also shown is a PDF compiled from Bhattacharjee [13].

in Appendix D.

Clearly, from Figures 5.28 and 5.29, as C_κ increases, the likelihood, or probability, of the detonation wave to travel at speeds below the average CJ value also increases. This is especially true for $C_\kappa \geq 6.7$. At these high values of C_κ, the detonation tends to favour a greater chance of having wave speeds below the average propagation speed value, i.e., when $(D/D_{avg}) < 1$. Conversely, at lower values of C_κ, and the Euler simulation, velocities above the average propagation speed are favoured. This would lead to much shorter ignition delays, thus explaining the relatively quick burning times associated with the observed shortened hydrodynamic thickness, previously shown in Figure 5.24. Thus, as C_κ increases, the detonation wave front spends more time at below average speeds. To compensate for this, the range of attainable, yet infrequent, wave speeds above the CJ-value must also increase. This leads to a larger variation of ignition delays for the unreacted gas, which travels through the leading shock at any given location, as expected for irregular detonations [27]. Furthermore, since the wave

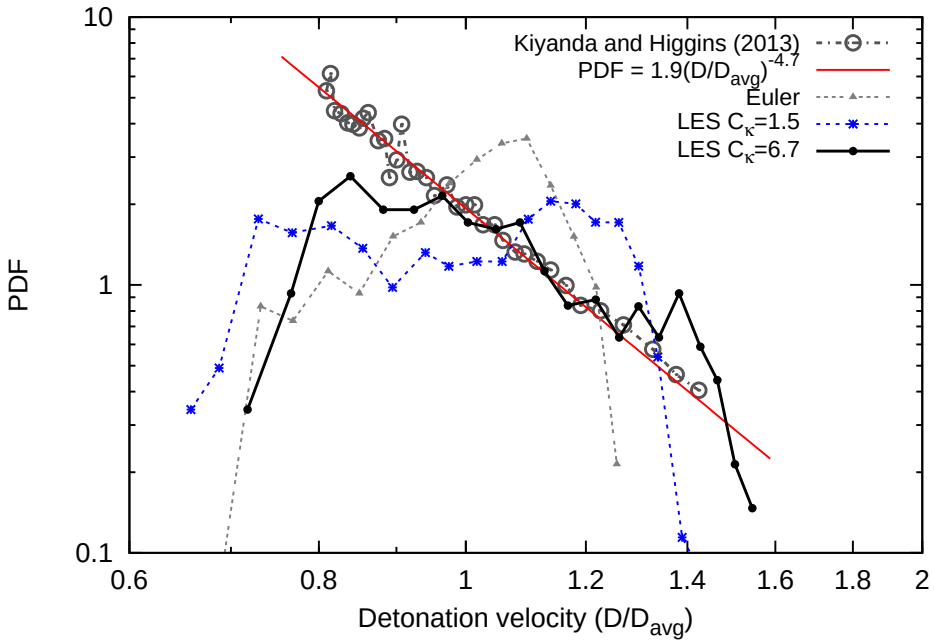

Figure 5.29: PDF of a detonation wave, in a channel with $H = 10$, having a certain velocity (D/D_{avg}) at any given moment and location. Also shown is a PDF compiled from Kiyanda and Higgins [15].

spends more time at below CJ-velocities, for higher C_κ values, most of the unburned gas that is shocked by the wave front has a much longer ignition delay compared to the ZND model. For this reason, unburned pockets of gas are able to form in the wake, which eventually burn up through turbulent mixing. This favouring of velocities below the average propagation speed thus lengthens the overall hydrodynamic structure of the wave. Consequently, the cells also increase in size and become more irregular in appearance, as observed in the cell patterns of Figure 5.15. Since higher C_κ values inherently generate more random fluctuations, the cell irregularity would also be expected to increase. This is evident as the range of expected hydrodynamic thicknesses also increases, as seen previously in Figure 5.25.

In general, the PDFs collected for $C_\kappa \geq 6.7$ compared well to experiments. In fact, simulations for $C_\kappa \geq 6.7$ reproduce well the decaying behaviour of the wave velocity, where the probability of the wave speed exhibits an power-law dependence on wave speeds above the favoured value. For $H = 20$, the experimental data [13] was found to be well predicted by PDF $= 2.6(D/D_{avg})^{-4.0}$, as shown in Figure 5.28. A similar

power-law correlation was also observed by Radulescu et al. [27] from high resolution Euler simulations, who found a -3 exponential dependence of the PDF on detonation velocity. In this case, although the numerical simulations for $C_\kappa \geq 6.7$ do not collapse onto this correlation, the same decaying trend is observed. For $H = 20$, the most probable wave speed favoured, experimentally [13], is $(D/D_{avg}) = 0.93 \pm 0.04$ with a peak PDF value of 3.3. For the simulation at $C_\kappa = 6.7$, the most probable velocity was $(D/D_{avg}) = 0.96 \pm 0.04$ with a peak PDF value of 1.74. This favoured velocity value has 8.6% error compared to experiment. For $C_\kappa = 10.0$, the most probable velocity was $(D/D_{avg}) = 0.85 \pm 0.04$ with a peak PDF value of 2.25. This agrees well for the favoured velocity value, with only 3.2% error. Despite this, however, the range of expected velocities on the wave front is much larger in the simulations compared to experiment. These differences in peak PDF values and expected ranges of velocities are believed to be influenced by several factors. First, the numerical simulations do not account for energy losses which are present in the experiments. These losses would include friction due to boundary layer effects, and heat conduction through the shock tube walls. Therefore, the detonation, in the simulations, has higher velocities. Furthermore, cell patterns for a channel height of $H = 20$ are very stochastic and irregular. The experimental PDF in Figure 5.28 was compiled for only 4 different experiments. It is likely that much more experiments are required in order to capture the events in the tails of the PDF, beyond the velocity limits currently obtained. Finally, velocity measurements are captured experimentally every 11.53μs, which may filter out any high speed and short-lived velocity fluctuations, which may occur beyond the current PDF limits. It is likely that in reality, the experimental PDF should have a larger range with a smaller peak PDF value.

For $H = 10$, the experimental data [15] was found to be well predicted by PDF $= 1.9(D/D_{avg})^{-4.7}$, as shown in Figure 5.29. Here, much better agreement to experiment is observed when $C_\kappa = 6.7$. The most probable wave speed favoured, experimentally [15], is $(D/D_{avg}) = 0.814 \pm 0.005$ with a peak PDF value of 6.15. In this case, the simulation at $C_\kappa = 6.7$ has a favoured velocity of $(D/D_{avg}) = 0.84 \pm 0.04$ with a peak PDF value of 2.55. This also agrees well for the favoured velocity value, with

only 1.0% error. This better agreement is likely attributed to the fact that a domain height of $H = 10$ effectively mode-locks the detonation in such a way that much less variation in cell size was observed. This was seen in the soot foils presented in Figure 5.23. Clearly, the analysis conducted here supports the need to calibrate C_κ in order to ensure the correct velocity probability trend, and qualitative features, are obtained numerically.

5.4.5 C_κ as a tuning parameter

From the open-shutter images presented Figure 5.15 it is clear that the C_κ parameter requires tuning in order to match the desired cell size and behaviour observed in experiments [13, 15]. From a quantitative perspective, Figures 5.28 and 5.29 have shown that numerically obtained probability density functions of detonation velocity distributions matched well the trends obtained through experiments [13, 15] when $C_\kappa \geq 6.7$. In general, higher values of C_κ allowed below average velocities to be favoured along the wave front, as was the case experimentally. As a result, it is clear that C_κ requires tuning in order to ensure the correct velocity distribution, and consequently the correct expected hydrodynamic thickness. Furthermore, as observed in Figures 5.17 to 5.23, a value of $C_\kappa = 6.7$ was found adequate to form qualitative cells and burning patterns comparable to experiments. For smaller values of C_κ, only much smaller cells appear. For larger values of C_κ, the cells increase in size until they are mode locked by the channel height. It should be noted, however, that specific 'matching' of C_κ values can prove difficult due to the stochastic nature of both the experiments and the numerical simulations. It should be further noted that even though the value of $C_\kappa = 6.7$ was found to give good agreement with experimental observation, $C_\kappa = 1.4 - 2.0$ is a more universally accepted value [150, 177]. This difference may be due to several reasons. First of all, low values of C_κ correspond to theory derived from and experiments calibrated to Kolmogorov's theory of the turbulence cascade in the incompressible limit [149]. The detonation phenomena under investigation here, on the other hand, is highly compressible. It is

possible that highly compressible regimes generate much more turbulent fluctuations than incompressible theory predicts. This is especially true for Richtmyer-Meshkov instability where turbulent motion is generated from shock waves interacting with material interfaces. Furthermore, in the presence of burned and unburned fuel interfaces, Kelvin-Helmholtz instabilities are enhanced due to shearing along slip-lines behind triple-points. Second of all, the experimental flow fields [13, 15] are essentially two-dimensional due to the very thin channel cross section widths. In fact, the aspect ratios of the channel heights to widths (H/W) in the experiments are ~ 10 [13] and ~ 4 [15]. In both cases, the channel widths are much smaller than the observed cell sizes. Thus, straining and decay of turbulent motions along the cross sectional width may not be as prominent as would be expected in a full scale three-dimensional experiment. Furthermore, turbulence in two-dimensions has been shown, theoretically, to exhibit back-scatter [35–37], and hence generate more turbulent motions. This has also been assumed to be the case for atmospheric flows, which are also considered essentially two-dimensional in nature [148]. In this sense, small scale turbulence is able to feed into, and amplify, larger scale turbulent motions. Since the experiments [13, 15] are quasi-two-dimensional, it is possible there are more turbulent motions behind the detonation front than would be expected in a naturally occurring 3D detonation wave propagation. In this sense, it is possible the corresponding 2D simulation would also require a higher C_κ value to artificially generate more turbulence. Furthermore, Kraichnan [197] predicts a theoretical value of $C_\kappa = 6.69$ for 2D turbulence, compared to 1.4 for 3D. Another review of two-dimensional turbulence [198] indicates a C_κ value of 5.8 to 7 should be adopted due to the increased turbulence associated with back-scatter. It should be noted, however, that in the current work this agreement is simply treated as a coincidence and has not been investigated further. Other sources of discrepancy may arise from errors associated with the splicing procedure, described in Section 3.2.5, or perhaps discrepancies associated with experimental losses. Finally, in terms of calibration, it should be noted that it is possible to implement a dynamic procedure to obtain the C_κ value, i.e., the Localized Dynamic Kinetic Energy Model (LDKM) method [97, 98, 142]. Although this is possible, vali-

dation and verification would still be required. Furthermore, the method may be more appropriate for three-dimensional simulations and would therefore increase computational expense significantly. Also, the dynamic procedure may not adequately account for increased turbulent fluctuations due to compressibility effects. For now, the static method of prescribing C_κ proves advantageous in two-dimensions for examining the effect of turbulence intensity on detonation propagation patterns and behaviours.

Chapter 6

Validation for 2D Flows Part II: Fast-Flames and DDT

6.1 Overview

In this chapter, the role of turbulent mixing on fast flame acceleration and transition to detonation is examined for the detonation interaction with porous medium experiments, which have previously been conducted at the University of Ottawa [13, 14]. The fundamental purpose of these experiments was to isolate the ignition mechanisms that drive detonation waves. In these experiments, whose concept was introduced previously in Section 1.2.2, an obstruction is placed in the channel whose role is to quench a detonation wave to allow its subsequent re-initiation to be studied, following the various wave dynamics in the wake of interaction with the obstacle. To this effect, the CLEM-LES methodology is validated accordingly.

To date, detonation re-initiation is believed to occur from amplification of the incident shock strength resulting from shock reflections or triple point collisions [22, 39]. In some cases, however, several shock reflections are required to accelerate the leading shock wave sufficiently in order to re-initiate the detonation. At each shock reflection, or triple point collision, the incident shock is accelerated due to increased reaction

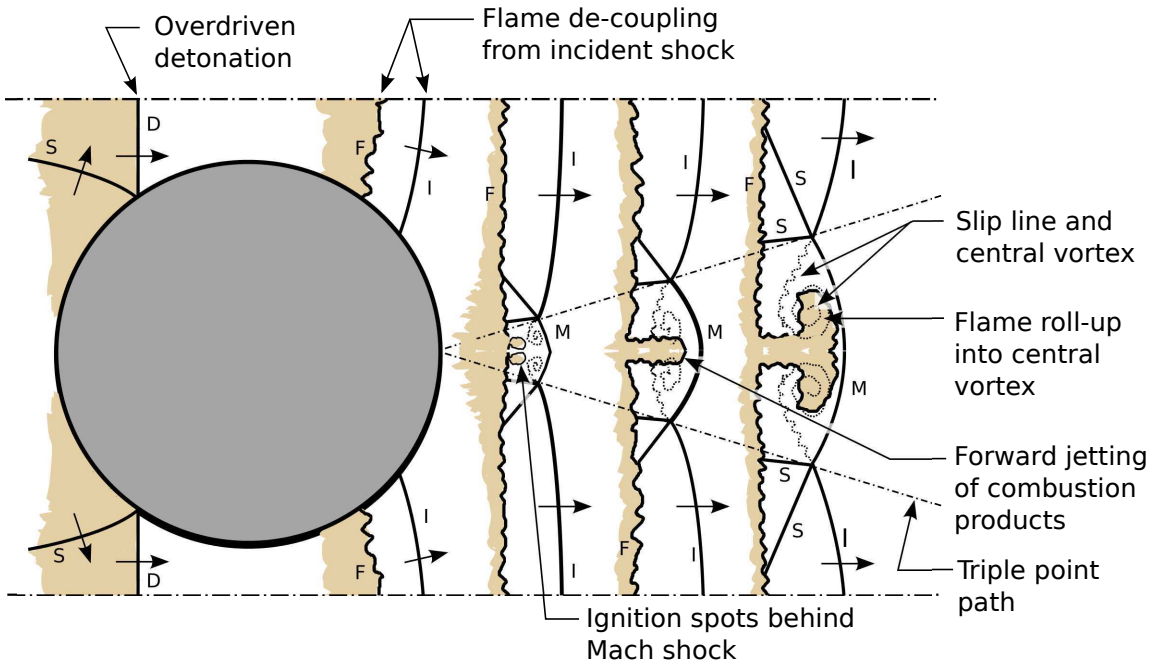

Figure 6.1: Sketch illustrating the expected flow field of a shock reflection process in the wake of an obstacle. (D=detonation, I=incident shock, M=Mach shock, S=Transverse shock, F=Turbulent deflagration)

rates in the unburned gases behind the incident shock. What remains unclear, is to what degree adiabatic shock compression or turbulent mixing contribute to DDT in this context.

For cases when DDT does not occur at a shock reflection, the presence of flow instabilities, leading to turbulence, is believed to give rise to rapid burning behind the newly formed Mach shock [13]. A sketch illustrating this particular process at the first reflection following detonation interaction with an obstacle is shown in Figure 6.1. First, as the initial detonation (D) passes over an obstacle, it gains strength due to the reduction in area. Upon its passage over the top of the obstacle, it begins to lose strength and quickly quenches. This is observed by a de-coupling between the incident shock wave (I) and the turbulent deflagration (F) that follows. When the incident shocks reflects in the wake, a Mach shock (M) forms at the wave front. Also present are newly formed transverse shock (S) and a slip-line that rolls up into a central vortex. During the reflection process, combustion products become entrained along the slip line, and into the central vortex. Rapid burning thus occurs in the

central vortex due to rapid mixing of burned and unburned product gases.

A corresponding example sequence of Schlieren photographs [13], for this particular scenario where DDT does not occur, is shown in Figure 6.2. In the experiment, conducted for methane-oxygen, forward jetting and significant turbulent mixing, through Kelvin-Helmholtz instability, give rise to very rapid burning of the shocked gas mixture behind the newly formed Mach shock. This example case is of particular interest, as it represents a critical regime where the onset of DDT is imminent. In fact, a repeated test at the same conditions has also been documented to show successful DDT [13]. To address the lack of repeatability of the experiment shown in Figure 6.2, experiments were also conducted using a roughness plate, as shown in Figure 6.3. In this figure, the same rapid burning is observed behind the Mach shock, at lower pressures. In fact, the purpose of the roughness plate, in this experiment, was to promote the formation of hot spots and turbulent motions following shock wave interactions with the plate. In this sense, a controlled turbulent environment was present experimentally, ideal for examining how turbulence influences events leading up to DDT. Therefore, in this chapter, this particular experiment (with the roughness plate) [13] has been modelled, not only to further validate the CLEM-LES strategy, but also to gain insight on the effect that turbulence intensity has on the resulting flow field.

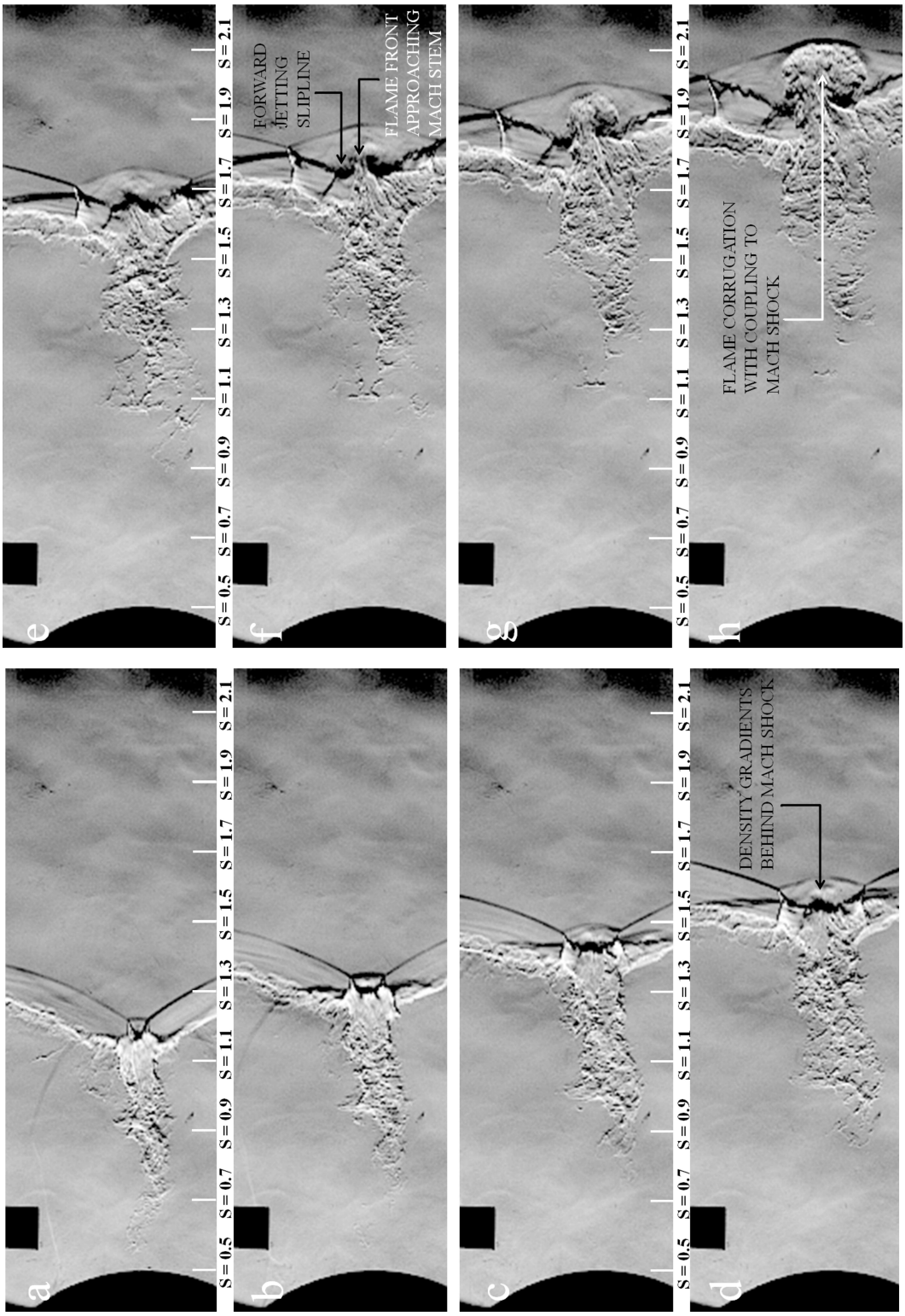

Figure 6.2: Sequence of Schlieren images showing a shock reflection process, following a detonation wave interaction with an obstacle (located to the left of each frame), where DDT does not occur. The initial mixture is $CH_4 + O_2$ at $\hat{p}_o = 10.5$kPa [13].

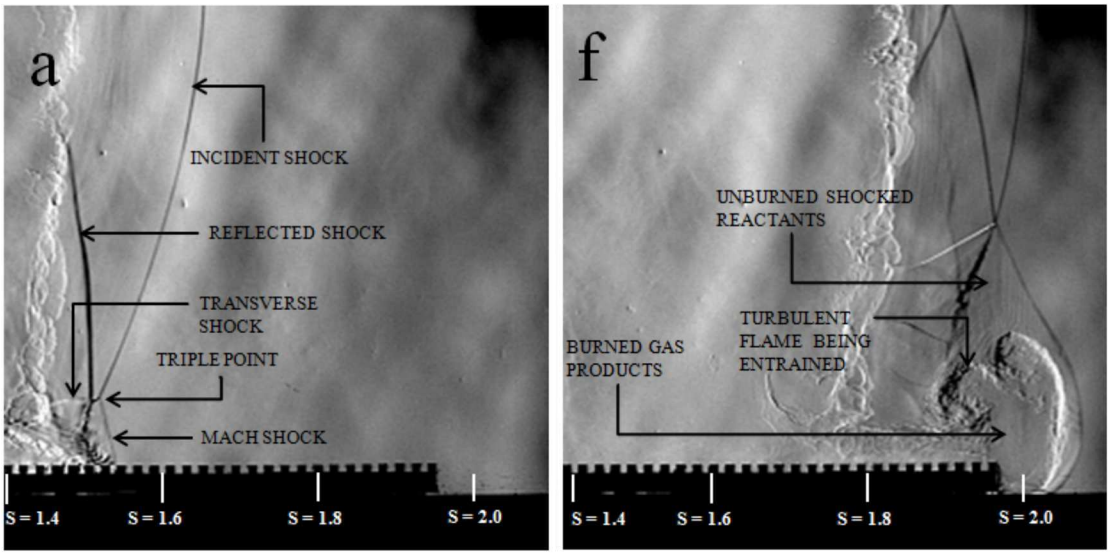

Figure 6.3: Schlieren images showing the result of a shock reflection process in the wake of an obstacle when a roughness plate is present. Here DDT does not occur, but rapid burning is observed behind the Mach shock, much like Figure 6.2. The initial mixture is $CH_4 + O_2$ at $\hat{p}_o = 7.0$kPa [13].

6.2 Numerical Domain and Model Parameters

A schematic, showing the setup for the numerical simulations, is shown in Figure 6.4. In all simulations, the domain height is $48\hat{\lambda}_{1/2}$, while the length is varied between 400-600$\hat{\lambda}_{1/2}$. For the internal boundaries associated with the obstacle and roughness plate, the wall type boundary condition is applied as described in Section 5.2. The zero gradient and symmetric boundaries are also applied to the extremities of the domain, as indicated in Figure 6.4. Here, a ZND wave profile was initiated on the left of the obstacle, and advanced to the right in time. The fluid properties, obstacle size, domain height, and roughness plate dimensions were matched to the experiment [13]. Formally, the initial conditions of the numerical experiment are expressed by

$$\rho(x, y, 0) = \begin{cases} \text{ZND solution Eqs.(4.8)-(4.11)} & \text{if } x < 0 \\ 1 & \text{otherwise} \end{cases}$$

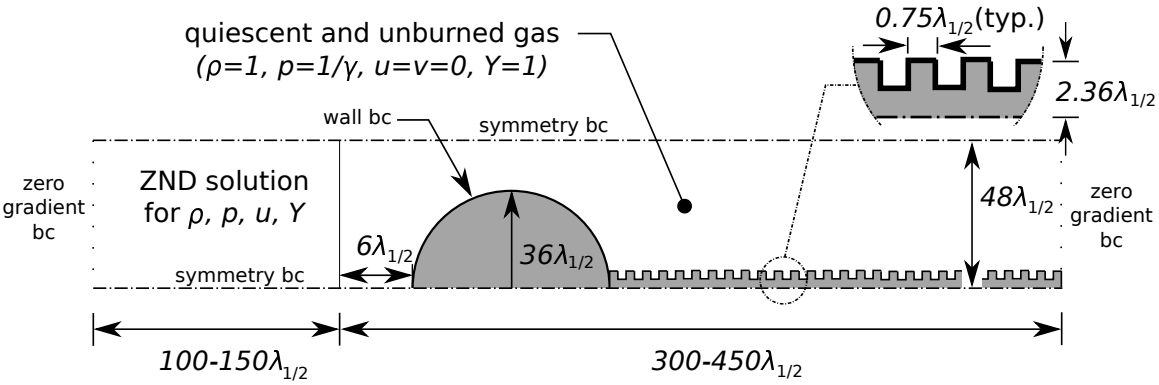

Figure 6.4: Initial and boundary conditions for detonation interaction with porous media and roughness plate (Not to scale). Note: $\hat{\lambda}_{1/2} = 4.23$mm.

$$u(x,y,0) = \begin{cases} \text{ZND solution Eqs.(4.8)-(4.11)} & \text{if } x < 0 \\ 0 & \text{otherwise} \end{cases} \tag{6.1}$$

$$v(x,y,0) = 0$$

$$p(x,y,0) = \begin{cases} \text{ZND solution Eqs.(4.8)-(4.11)} & \text{if } x < 0 \\ 1/\gamma & \text{otherwise} \end{cases}$$

$$Y(x,0) = \begin{cases} \text{ZND solution Eqs.(4.8)-(4.11)} & \text{if } x < 0 \\ 1 & \text{otherwise} \end{cases}$$

As before, the turbulent kinetic energy, $k^{sgs}(x,y,0) = 0$ everywhere initially. Furthermore, for computational savings, the simulation is advanced using the Euler scheme, Eqs.(2.34)-(2.37), up to $t = 16$. This moment is just before the shock interacts with the roughness plate. At this point the turbulence models are then activated and the solution advances by solving the LES Eqs.(3.4) through (3.7). The subgrid kinetic energy, k^{sgs} is thus generated following the wave interaction with the roughness plate in a controlled manner.

The model parameters, for the simulation, correspond to methane-oxygen ($CH_4 + 2O_2$) with an initial temperature and pressure of $\hat{T}_o = 300$K and $\hat{p}_o = 7000$Pa, respectively. The various dimensional and non-dimensional model parameters applied to this particular numerical experiment are found in Table 6.1.

Finally, the maximum resolution chosen for all simulations in this section is set to $b =$

Table 6.1: Fluid properties and model parameters for methane combustion at $\hat{T}_o = 300$K and $\hat{p}_o = 7000$Pa.

Dimensional properties					
$\hat{\rho}_o$	0.07 kg/m^3	$\hat{c}_o$	356.36 m/s	$\hat{E}_a/\hat{R}$	18685.8 K
$\hat{D}_{CJ}$	2272.97 m/s	$\hat{D}_{70\%CJ}$	1591.50 m/s	$\hat{S}_{L,70\%CJ}$	16.42 m/s
$\hat{T}_{CJ}$	3265.50 K	$\hat{p}_{CJ}$	185.9 kPa	$\hat{\rho}_{CJ}$	0.14 kg/m^3
$\hat{T}_{70\%CJ}$	1103.10 K	$\hat{p}_{70\%CJ}$	167.1 kPa	$\hat{\rho}_{70\%CJ}$	0.49 kg/m^3
$\hat{T}_{VN}$	1758.10 K	$\hat{p}_{VN}$	348.3 kPa	$\hat{\rho}_{VN}$	0.64 kg/m^3
$\hat{\nu}$	9.5x10^{-5} m^2/s	$\hat{k}/(\hat{\rho}\hat{c}_p)$	2.4x10^{-4} m^2/s	$\hat{D}$	1.0x10^{-4} m^2/s
$\hat{Q}$	6607.7 kJ/kg	$\hat{\lambda}_{1/2}$	4.23 mm		
Non-dimensional model parameters					
ν	3.82x10^{-3}	M_{CJ}	6.38	$M_{70\%CJ}$	4.47
L_e	1.32	P_r	0.709	S_c	0.933
$P_{r,t}$	1.0	$S_{c,t}$	1.0	γ	1.17
E_a	45.9	Q	52.0	A	8.30x10^3

1/32, with a further $N = 16$ subgrid elements per super-grid cell. Furthermore, for the purpose of AMR implementation, the base grid (G1) has a resolution of $b_{G1} = 1$ with 5 additional levels of refinement on the supergrid. This was previously shown to be sufficient to resolve the detonation cell structures, and overall qualitative behaviour, as observed in Chapters 4 and 5. Finally, it should be noted that although a detailed resolution study was not conducted in this Chapter, two necessary conditions which further justify the choice of this particular resolution ($b = 1/32$) have been met. First, sufficient resolution on the supergrid is chosen to allow coupling between the incident shock wave and the reaction zone. This was previously demonstrated necessary in Chapter 4 in order to recover the steady detonation structure in 1D. Also, the laminar flame speed was resolved on the subgrid at the given resolution for the parameters given in Table 6.1.

6.3 Results

6.3.1 Preliminary simulation results

Here, a simulation was first conducted for $C_\kappa = 6.7$. The simulation was run sufficiently long to determine if DDT occurs within the first few shock reflections with the wall or roughness plate. Figure 6.5 shows the density evolution of the flow field throughout the simulation. In the figure, snapshots of the density field at various times are superimposed to show the sequence of events that follow the initial detonation interaction with the obstacle. The principle observation made here is that the detonation remains quenched following the initial shock interaction with the roughness plate. In the subsequent frames following the initial shock-roughness plate interaction, there is a clear decay in shock-reaction zone coupling. This was observed by the thickening of the distance between the two features. In this case, however, DDT occurs following the reflected shock interaction with the top wall around $x \sim 200$. This is evident by the thin coupling of the shock-reaction zone that was observed in subsequent frames. Also, the resulting wave front features the characteristic cellular pattern, as observed in the detonation propagation simulations of Section 5.1.

To quantitatively confirm the existence of detonation following the shock reflection with the top wall, Figure 6.6 shows the corresponding x-velocity histories of the waves along both the top wall and the roughness plate (at $y = 2.36$). Initially, the x-velocity of the wave along the roughness plate exceeds the CJ-value at the first shock reflection with the roughness plate, around $x \sim 100$. This wave speed, however, clearly decays below the CJ-value for $x > 140$. The x-velocity of the wave along the top wall remains below the CJ-value until a sudden acceleration to values above CJ occur around $x \sim 200$. This corresponds to where the shock reflection occurs on the top wall. Also shown in Figure 6.6, for reference, are the velocities of the wave along the top wall and roughness plate recorded from the corresponding experimental investigation [13]. A formal comparison between the CLEM-LES and experiment is made in Section 6.4. First, the next section examines the effect that C_κ has on

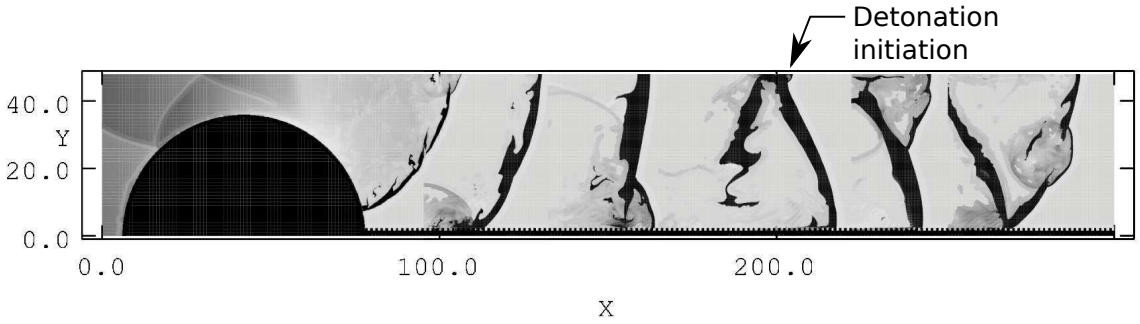

Figure 6.5: Density evolution for $C_\kappa = 6.7$. In this case, DDT occurs at the first shock interaction with the top wall. Note: dimensions are normalized by $\hat{\lambda}_{1/2}$.

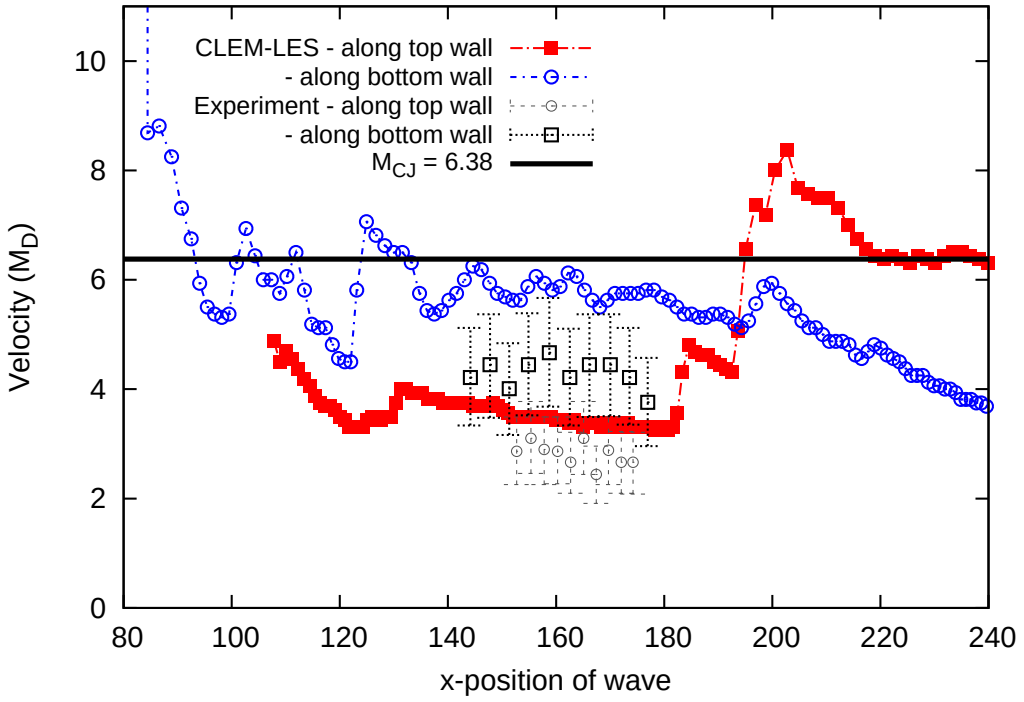

Figure 6.6: x-velocity of leading shock for $C_\kappa = 6.7$ as a function of distance from the initial wave position, measured along top and bottom walls and compared to [13].

influencing the resulting flow field from simulation. To this effect, C_κ was varied to examine effect of turbulence intensity on detonation initiation events, and to note how many shock reflections, downstream from an obstacle, it takes to initiate detonation under varying turbulence intensities.

Finally, the grid topology, which indicates the locations of each grid level (G), is shown in Figure 6.7 for an instance in time just before the wave interacts with the roughness plate, at $t = 16.5$. As was demonstrated previously, in Chapter 5, the reaction zone is always refined to the finest level, G6. Also, the grids near the solid internal boundaries, i.e. the cylinder and roughness plate, are also refined to the finest grid level, always.

6.3.2 Effect of the reaction rate through the Kolmogorov parameter (C_κ)

In this section, C_κ was varied from 3.0 to 10.0 in order to examine the effect that turbulence intensity, and hence the reaction rate, has on influencing the flow field evolution. Figure 6.8 shows the superimposed density fields for C_κ values of 3.0, 7.0, and 10.0. These values thus represent the effect of low, medium, and high turbulence intensities. Also shown in the figure is the density evolution obtained through an Euler simulation at the same supergrid resolution of $b = 1/32$, for comparison.

For a relatively low turbulence intensity, when $C_\kappa = 3.0$, a relatively low amount of subgrid kinetic energy is generated compared to higher C_κ values, as was observed in Section 5.4 and Figure 5.27. Clearly, from Figure 6.8, the detonation is initially quenched as it passes on the rear side of the obstacle, owing to volumetric expansion of the wave [46]. However, following the initial shock wave interaction with the roughness plate, the detonation wave is re-initiated. This was also the case for an Euler simulation conducted at the same resolution. This onset of DDT is much sooner compared to $C_\kappa = 6.7$, where DDT occurred at the shock reflection with the top wall. One fundamental difference between the Euler simulation and the CLEM-LES, when $C_\kappa = 3$, is the size of the cells observed after re-initiation of the detonation

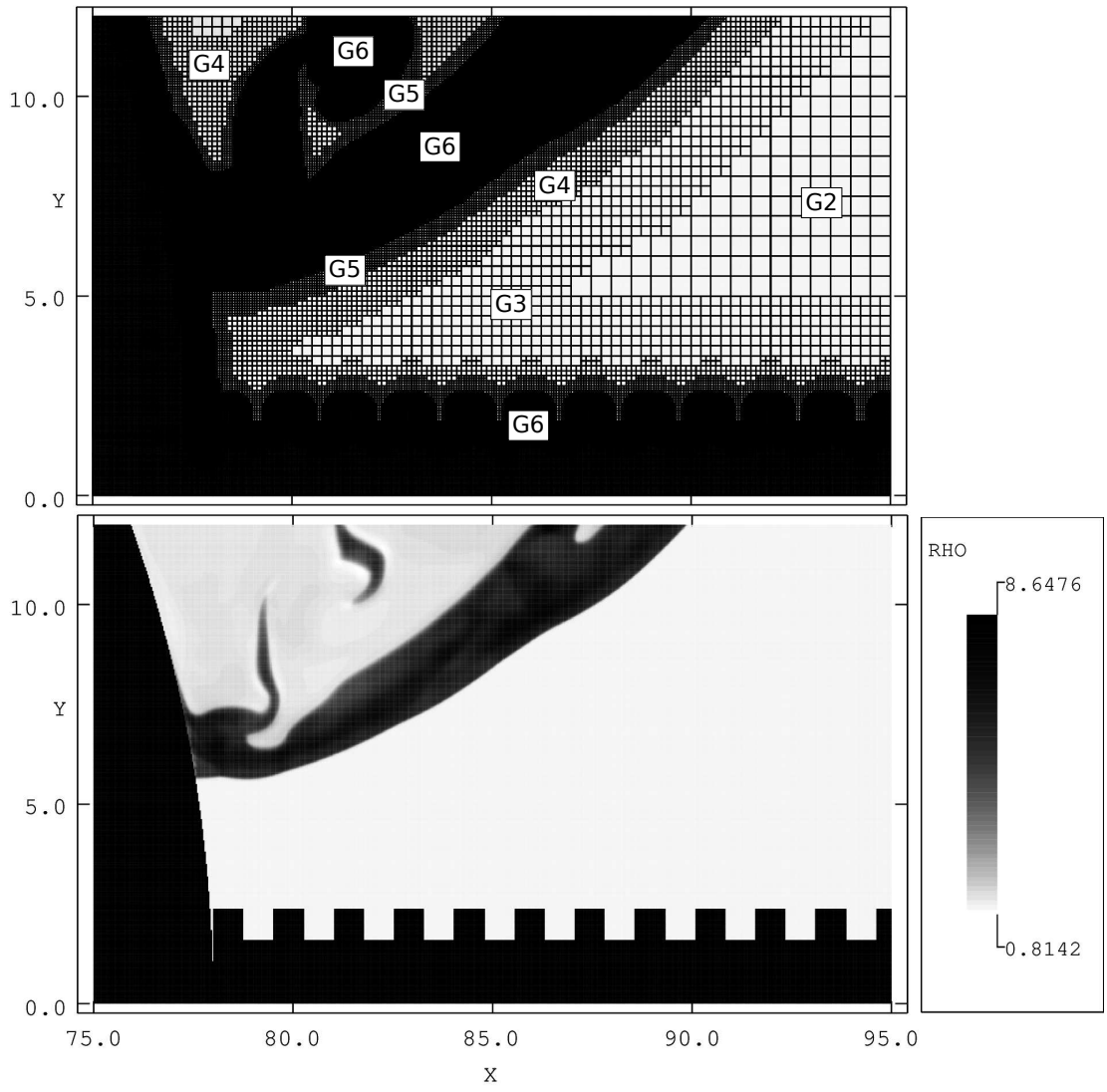

Figure 6.7: Grid topology (top) and corresponding density field (bottom) for an instance of the CLEM-LES ($C_\kappa = 6.7$) just before the wave interacts with the roughness plate ($t = 16.5$). Also shown is the locations of the various grid levels (G2-G6). Note: The base grid G1 is always refined to at least grid level G2, everywhere. Also, grids near the solid internal geometries are always refined to the finest level, G6.

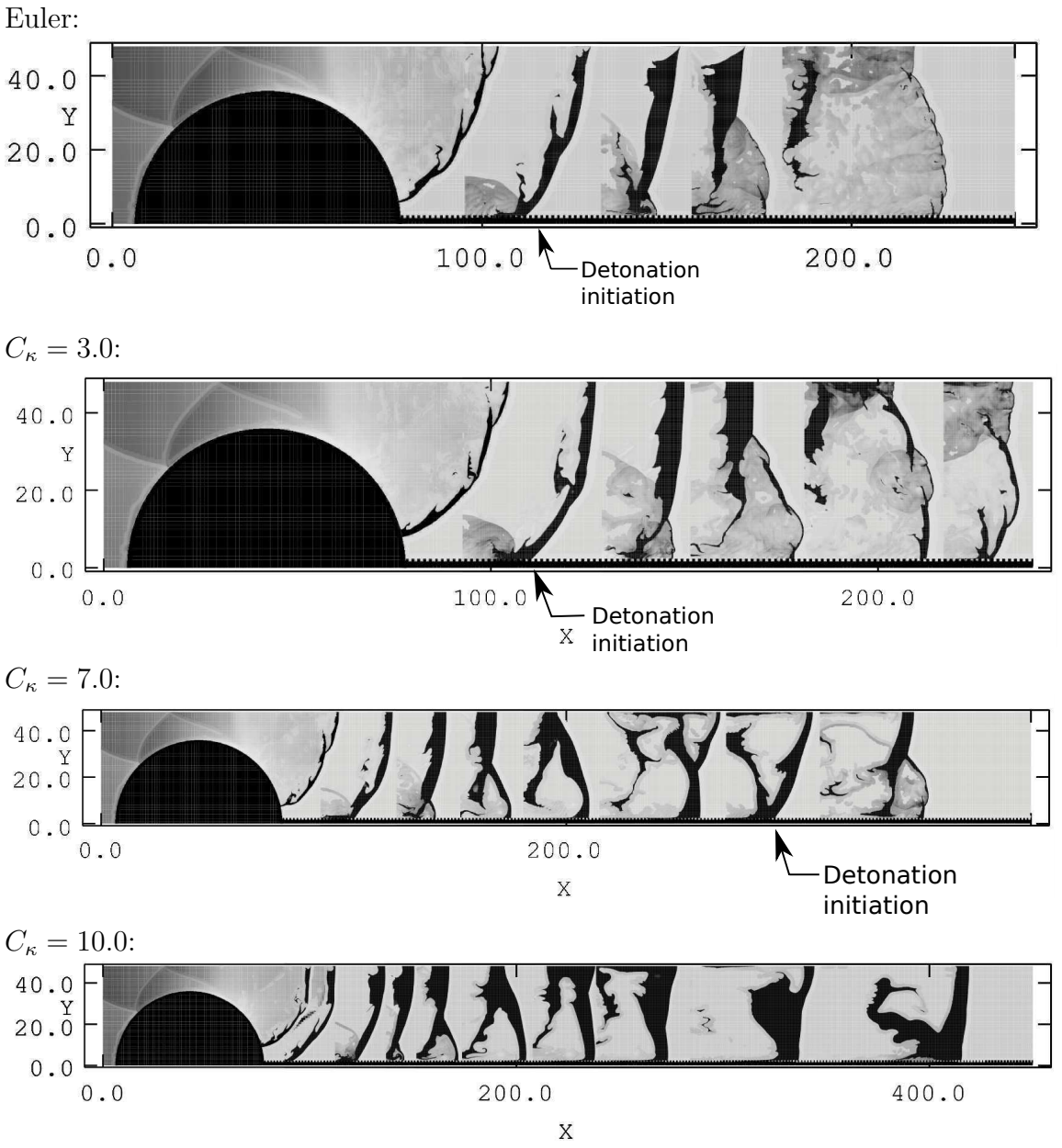

Figure 6.8: Density evolution for several values of C_κ and an Euler simulation at the same resolution ($b = 1/32$). Here, increasing C_κ was found to delay the onset of DDT to later shock reflections downstream. Note: dimensions are normalized by $\hat{\lambda}_{1/2}$.

occurs. In the Euler simulation, it can be seen that the detonation wave front contains many more triple points, and hence a smaller cell size, compared to the CLEM-LES simulation. This was also a fundamental observation and comparison made in the detonation propagation experiments, Chapter 5.

As C_κ was increased to an intermediate value, of 7.0, the onset of DDT occurs much later, even compared to $C\kappa = 6.7$. Figure 6.8 clearly shows a quenched detonation up until the reflected shock wave interacts with the roughness plate a second time. Next, as C_κ is increased to 10.0, DDT is not observed in the numerical simulation. In the density evolution, presented in Figure 6.8, the reaction zone clearly remains decoupled from the leading shock wave throughout the simulation. At the first shock reflection with the roughness plate, there are some hot spots which become entrained into a forward jet and burn turbulently behind the resulting Mach shock. This combustion, however, is insufficient to re-establish detonation.

As was done for the $C_\kappa = 6.7$ case, x-velocity measurements were acquired for all C_κ values along the top wall and roughness plate. These are shown in the top and bottom frames of Figure 6.9, respectively. Also shown are the x-velocity measurements collected from the Euler simulation, and also the experiment [13]. For $C_\kappa = 3.0$ and the Euler simulation, the x-velocity of the wave along the roughness plate oscillates about the CJ-velocity from the moment of initial shock collision with the plate in the wake of the obstacle. This confirms the existence of detonation propagation along the roughness plate. For $C_\kappa = 7.0$ the first interaction with the roughness plate gives rise to x-velocity measurements near the CJ-value. However, the velocity of the shock-reaction zone has a decaying trend beyond this initial reflection event, much below the CJ-value. Upon the shock wave reflection with the top wall, the velocity of the wave comes close to CJ, around $x \sim 200$, but does not transition to detonation. Subsequently, the x-velocity of the wave along the top wall decays below the CJ value. The x-velocity of the wave finally exceeds the CJ value at the second wave interaction with the roughness plate, around $x \sim 300$, thus confirming DDT. Finally, for $C_\kappa = 10.0$, the x-velocity of the wave, following the initial shock reflection at the

Table 6.2: Run times and number of supergrid cells and subgrid elements required for each DDT simulation.

Simulation	**Run time (hrs)**	**Number of supergrid cells**	**Number of subgrid elements**
$C_\kappa = 3.0$	165.5	1,059,396	7,815,872
$C_\kappa = 6.7$	149.2	1,241,260	9,604,288
$C_\kappa = 7.0$	234.5	2,444,368	21,620,864
$C_\kappa = 10.0$	251.2	2,762,632	27,531,200
Euler	13.3	1,925,464	

roughness plate, was close to the CJ-value. At later times, however, this wave, and also the wave along the top wall, clearly have a decaying trend up to $x \sim 250$, with velocities well below the CJ-value. For $x > 250$, slight increases in velocity are observed with each shock interaction with the roughness plate, followed by a period of decay. In this particular case, however, DDT does not occur through the duration of the simulation. In the next section, a formal comparison to experiment [13] is made for the $C_\kappa = 10.0$ case, which displayed qualitative features of the flow evolution very similar to that obtained experimentally.

Finally, in terms of performance, each CLEM-LES simulation had a run time of approximately 150 to 250 hours, all using 24 CPUs, which largely depended on the domain size and the duration of simulation required to observe DDT. This run time was found to be an order of magnitude greater than the Euler simulation, which had a run time of only 13 hours. This observation is consistent with the findings in Chapter 5. The run time for each simulation conducted in this chapter, and also the total number of supergrid cells and subgrid elements is shown in Table 6.2.

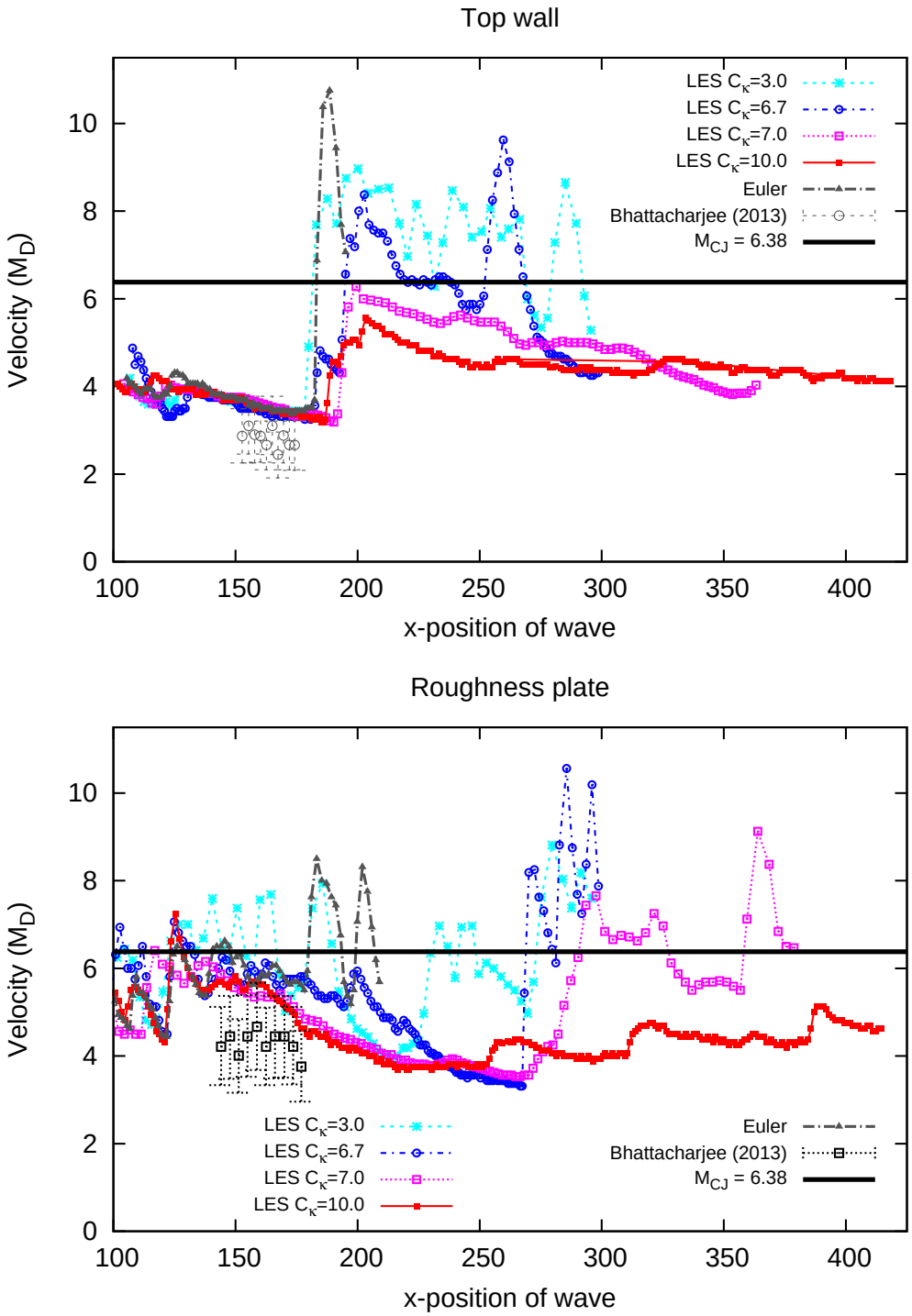

Figure 6.9: x-velocity of the leading shock for various C_κ values as a function of distance from the initial wave position, measured along the top wall (at $y = 48$) and also the roughness plate (at $y = 2.36$). These are shown in the top and bottom frames, respectively. Also shown are velocity measurements from experiment [13]. Note, the velocity M_D is normalized by the quiescent speed of sound ($\hat{c}_o$).

6.4 Discussion

6.4.1 Comparison to experiment

From numerical simulation, a C_κ value of 10.0 was found to match well the ignition behaviour of the shock reflection process, following the first interaction with the roughness plate, as observed in experiment [13]. In the experiment, whose evolution is shown in Figure 6.10, local ignition following the shock interaction at the roughness plate was found to become entrained into a forward jet. This allows for a region of burned gas to form behind the newly formed Mach shock, much like the evolution previously shown numerically in Figure 6.8. In this particular experimental case, DDT does not occur from the first shock reflection despite the near CJ-velocities observed by the wave in Figure 6.9, and also the enhanced turbulent combustion associated with the forward jetting behind the Mach shock. To qualitatively compare the numerical simulation from Figure 6.8 with the experiment [13], Schlieren images obtained experimentally are shown in Figure 6.10. The corresponding numerical images showing snapshots of the density gradient field are shown in Figure 6.11. Many features are noted throughout the evolution of the shock reflection process in the figure. Feature (1) is the incident shock, whose trailing combustion zone is clearly decoupled indicating a quenched detonation follows the interaction with the obstacle. This is evident by the thick region of shocked, but unreacted gas in Feature (2). Feature (3) is the reflected shock, which originates from the roughness plate. Feature (4) is the triple-point where the incident, reflected, and Mach shocks intersect. The Mach shock is denoted by Feature (5). Following the reflection process, hot spots ignite a region behind the Mach shock. This region is indicated in Feature (6). It should be noted that this particular feature is not observed in the experimental images of Figure 6.10. Feature (7), however, is a layer of hot spots that form along the roughness plate and is observed in both the numerical simulation and experiment. This combustion layer becomes entrained into a central vortex, Feature (8), located behind the Mach shock. This central vortex allows for efficient mixing of the hot

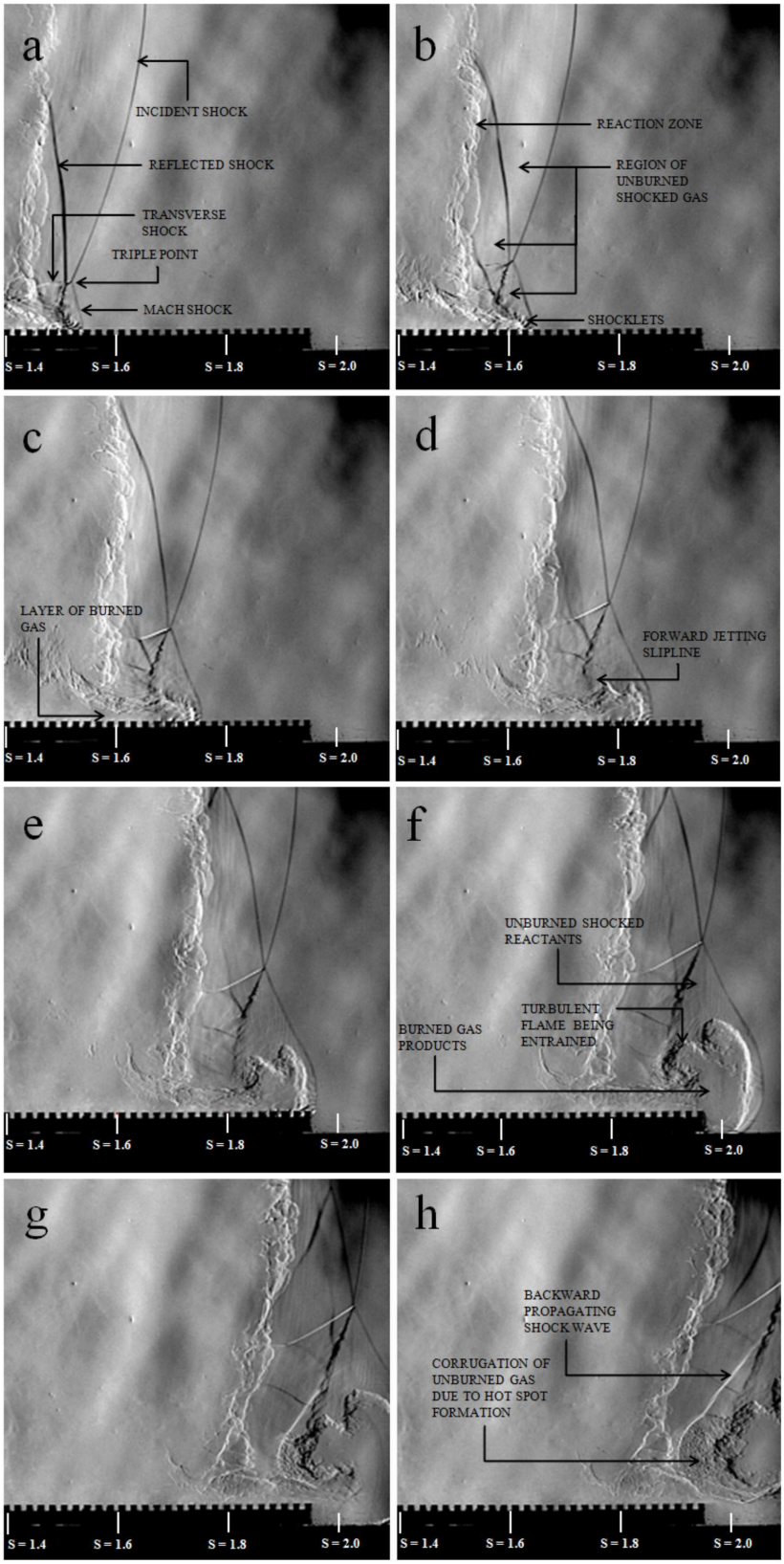

Figure 6.10: Experimental Schlieren image evolution [13] for the shock wave reflection process at the roughness plate shown numerically in Figure 6.11. The time in between images presented above is $\Delta\hat{t} = 11.53\mu s$.

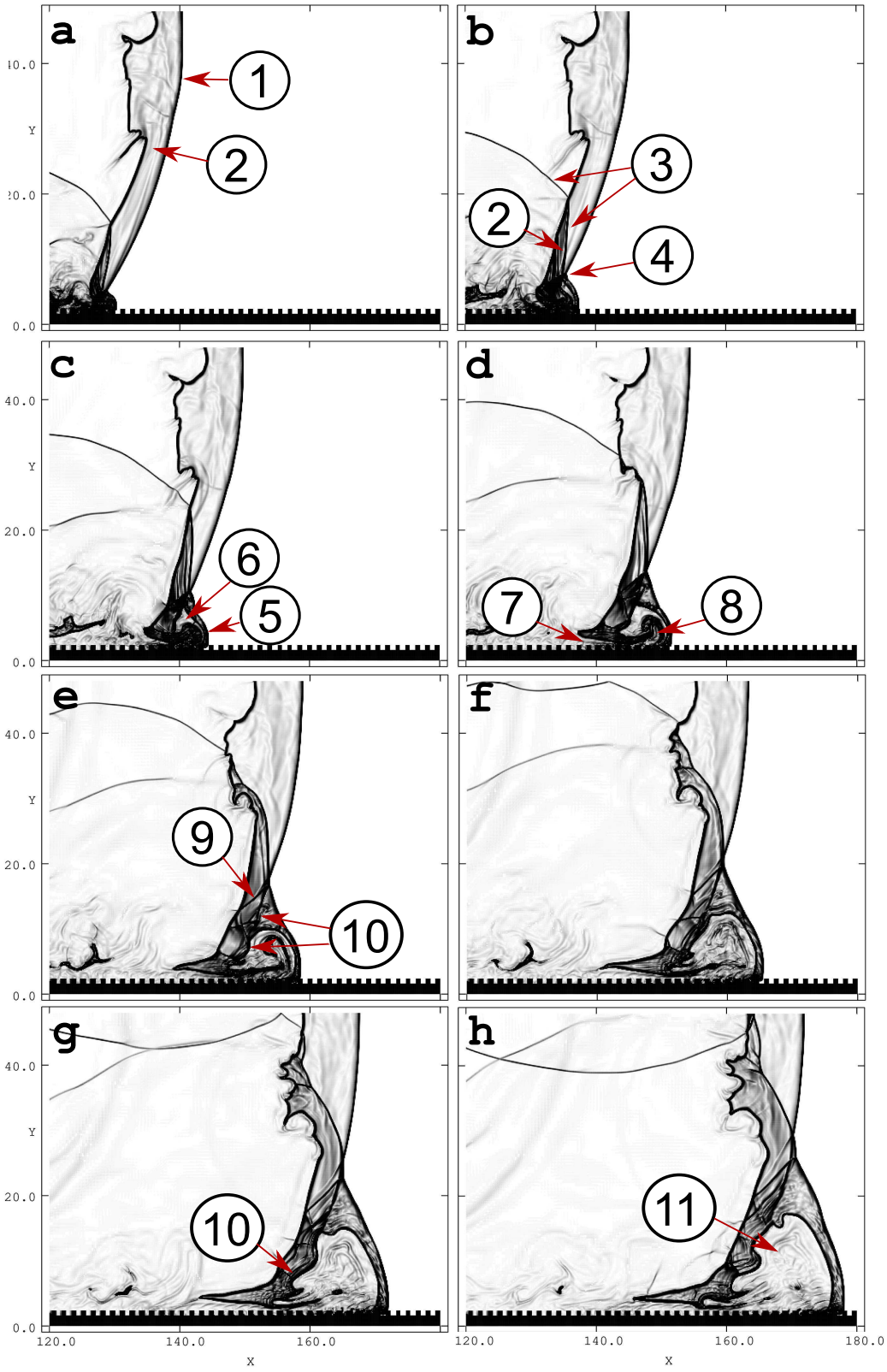

Figure 6.11: Numerical density gradient evolution for $C_\kappa = 10.0$ for the shock wave reflection process at the roughness plate. The corresponding experimental images are found in Figure 6.10. The time in between images presented above is $\Delta t = 1.0$ (11.87μs). Dimensions are normalized by $\hat{\lambda}_{1/2}$.

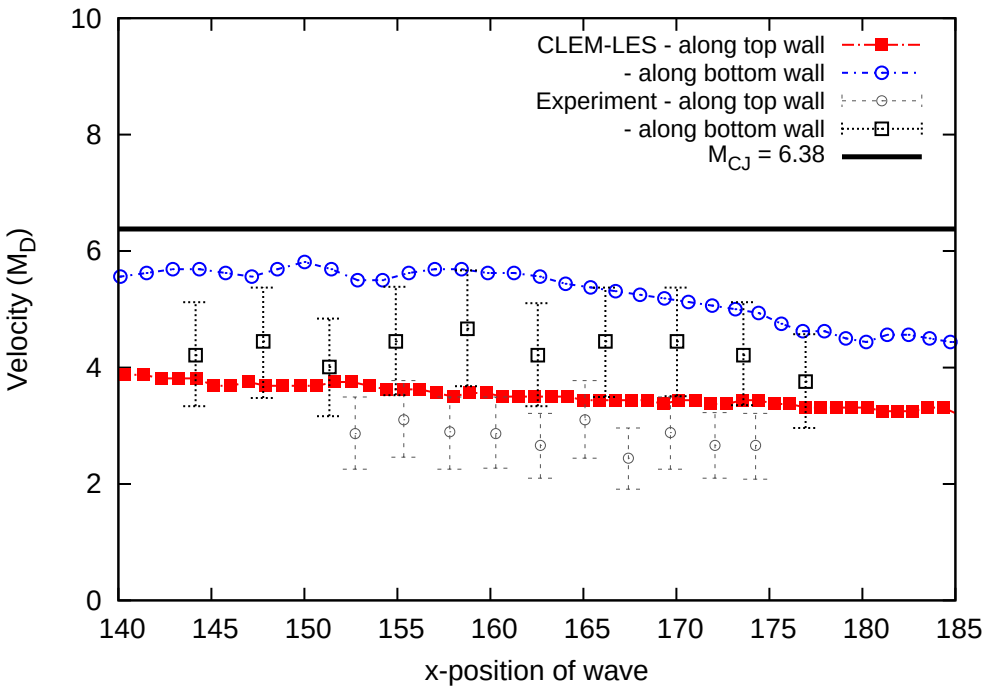

Figure 6.12: x-velocity of leading shock for $C_\kappa = 10.0$ as a function of distance from the initial wave position, measured along top and bottom walls and compared to Bhattacharjee [13].

spots, Features (6) and (7), with unburned gas behind the Mach shock. Feature (9) is a transverse shock wave which likely originates from combustion that occurs behind the Mach shock [13]. This transverse wave triggers Richtmyer-Meshkov and Kelvin-Helmholtz instabilities along the slip-line, Feature (10), which also acts to entrain combustion products into the central vortex behind the Mach shock. Finally, Feature (11) is a large region of burned products behind the Mach shock, which is separated from the bulk of the burned products in the wake of the wave by a large zone of unburned gas, much like the unburned pockets observed during irregular detonation propagation, previously indicated in Figures 5.17 and 5.20.

For quantitative comparison with the experiment [13], the x-velocities of the waves along the top wall and roughness plate are presented again for $C_\kappa = 10.0$ in Figure 6.12. This figure, however, shows only a zoomed-in portion of the wave speed obtained through the simulation to directly compare with wave speeds obtained experimentally. The full velocity history was presented previously in Figure 6.9. In

Figure 6.12 it is clear that the velocities of the waves along the top wall and roughness plate remain well below the CJ-value for both the simulation and experiment through the first reflection process. Although the numerically obtained wave speeds are slightly faster than the experimental wave speeds, they are still within experimental error. Furthermore, it is noted that the simulations do not account for losses to the walls, which may be present in the experiment.

6.4.2 Role of turbulence on mitigating DDT

In the current study, the turbulence intensity generated in the flow was varied through altering the C_κ variable. It was found that higher levels of turbulence intensity, in the form of subgrid kinetic energy (k^{sgs}), had the effect of mitigating DDT events following detonation interaction with a porous medium. As turbulent velocity fluctuations increase, the onset of DDT occurs at later shock reflections. With sufficiently high turbulence intensity, the fast-flame remains quenched throughout the duration of the simulation conducted here. Interestingly, one might assume the opposite behaviour since combustion rates are generally locally enhanced by turbulence, thus promoting DDT [66]. However, the action of the turbulent viscosity, a function of k^{sgs}, is to *smooth* the flow field, possibly promoting the decoupling of the reaction zone from the shock wave. It is possible that this behaviour may be an numerical artifact of the *eddy-viscosity model*. Alternatively, this behaviour may be physically explained by the fact that larger turbulent fluctuations lead to a larger variation of observed wave speeds along the wave front. This is especially true for large values of C_κ which favour detonation propagation wave speeds below CJ, as observed in Chapter 5. Thus, the unburned gas which enters the wave front may also have greater variation in ignition delays, which thus promotes the formation of unburned pockets in the wave of wave collisions. This particular behaviour of DDT mitigation is not observed when numerical diffusion is present in Euler simulations [39, 109], where such diffusion is found to promote DDT through increased mixing and combustion due to numerical errors. One fundamental difference for the CLEM-LES methodology, in the current

investigation, is that the reaction rate is resolved on the LEM scales. Thus, ν_t simply acts to diffuse, or transport, only the velocity fluctuations throughout the wave. Such an effect may thus contribute to favoured lower wave speeds on the front, while combustion rates respond accordingly. It is therefore possible that the results obtained here are physically sound. Furthermore, many investigations have demonstrated that sufficient turbulence intensity can actually act to extinguish flame propagation [101]. In the current investigation, it is possible that increased turbulence leads to the existence of a *well-stirred reactor* combustion regime, whereby turbulent motions act to distribute any hot spots away from the high temperature, and high pressure region behind the Mach shock and triple point, thus mitigating DDT. Furthermore, such large turbulent motions would also act to entrain combustion products from the wake into the central vortex, thus giving rise to the observed rapid burning behind the Mach shock. This shift in combustion regimes has also been postulated to give rise to the forward jetting of combustion products for this type of fast-flame acceleration behind an obstacle, in the absence of a roughness plate [62]. In terms of confirming the effect that turbulence has on mitigating DDT, controlled experiments would be required to further validate the results obtained here.

Chapter 7

Conclusions and Recommendations

7.1 Summary

In this work, a turbulent modelling strategy has been formulated for closing reaction rates on flows which are highly compressible, reactive, and contain rapid transients in pressure and energy. The strategy itself serves as extended work to a previously developed Linear Eddy Model formulation for Large Eddy Simulation [97–100] whose capabilities were limited to modelling only weakly compressible flows in multiple dimensions. In the current work presented here, a large focus has been to validate and verify the model performance in fundamental 1D problems, as detailed in Chapter 4 (and recently published [199]). Furthermore, the Compressible LEM-LES (CLEM-LES) strategy has been applied to model two-dimensional detonation propagation and flame acceleration leading up to DDT events, as detailed in Chapters 5 and 6, and validated accordingly.

To summarize, this novel modelling approach has been demonstrated to capture laminar and turbulent flame speeds, and also detonation initiation events in one-dimensional test cases. Furthermore, in the one-dimensional formulation described in Chapter 4, the strategy was found to retain the detonation and flame structures on the supergrid despite the low-Mach number assumption (see Section 3.2) applied

to the subgrid. These 1D verification and validation tests were compared to direct simulations of the 1D Navier-Stokes equations [199], previous standalone LEM computations [102], and also experimental observations of turbulent flame behaviour [101]. For two-dimensional flows, the CLEM-LES strategy was found to qualitatively and quantitatively capture experimental observations [13, 15] in terms of detonation cell structure and irregularity. Furthermore, experimental observations of fast-flame burning behaviour following detonation interaction with a porous medium (and roughness plate) [13] are also recovered through numerical simulation. To this effect, the strategy was also used to gain insight on how turbulent mixing rates influence the observed detonation propagation flow patterns, and also DDT events in a porous medium.

7.2 Conclusions

Since DNS is currently not amenable for most problems of practical interest, the CLEM-LES strategy was found to be an affordable alternative, with reasonable simplifications, in order to gain physical insight on laboratory-scale problems. To this effect, the strategy was found to address the turbulent scales of highly compressible combustion problems, which would normally be unattainable through traditional modelling techniques. Furthermore, its versatility allows the strategy to be applied to a range of combustion regimes. Its application is not limited to the problems outlined in Chapter 1, but can be applied to model any number of supersonic problems, where turbulent-scale mixing is important. Furthermore, CLEM-LES also proves advantageous over traditional Euler investigations. Euler methods have previously been shown to exhibit differing behaviour depending on the resolution applied. That is, Euler simulations can never be resolved to a grid independent solution, and often rely on sufficient numerical diffusion to account for turbulent mixing of burned and unburned fuel [27]. Instead, CLEM-LES has been demonstrated to produce grid-independent and resolved solutions in terms of expected qualitative and quantitative features.

Given the success of CLEM-LES for capturing experimental observations of multi-dimensional detonation propagation [13, 15] and fast-flame evolution problems [13], the strategy is promising for gaining insight into the physical influence of turbulent mixing rates on such problems. For planar detonation propagation in a thin channel, Chapter 5, numerical simulations have shown that turbulent mixing rates significantly influence the observed cell patterns and detonation structure. Furthermore, turbulent mixing rates were found to influence the variation of velocities experienced by the wave front. For increased levels of turbulence intensity, such turbulent wave fronts were found to favour local velocities below the CJ-value. This led to a favouring of much longer ignition delays, compared to ZND theory, for the unburned gas which passed through the front. This, in turn, contributed to the formation of unburned pockets in the wake, thus lengthening the overall hydrodynamic structure. Furthermore, the presence of such unburned pockets was found to give rise to larger and more irregular cell patterns. For the fast-flame simulations of Chapter 6, the obstacle and roughness plate setup was designed to isolate the triple point collision process present during turbulent detonation wave propagation. In this context, it was found that increased turbulence intensity had the effect of mitigating DDT. In fact, increased turbulence was found to prolong the number of shock reflections, downstream from the obstacle, required for a detonation to successfully initiate. Furthermore, at sufficiently high turbulence intensity, transition to detonation did not occur through the duration of the simulation conducted. This influence of turbulence on DDT events is in contrast to experimental observations of shock-flame interaction experiments where the presence of turbulence were found to promote DDT [66]. It is likely that in the porous medium simulation conducted here, increased turbulence led to a well-stirred reactor combustion regime, whereby turbulent motions act to distribute hot spots away from the high pressure region behind the triple point. This was recently believed to be the case for this type of fast-flame acceleration behind an obstacle in the absence of a roughness plate [62].

While the CLEM-LES methodology provides square-root to cube-root savings in computations compared to 2D or 3D DNS, it is still very expensive to implement on

personal computers efficiently for the purpose of resolving both pressure effects and diffusion/reaction that occurs on the subgrid. In Chapters 5 and 6, typical resolved two-dimensional simulations were run on at least 20 to 30 CPUs, in parallel, for 2 to 3 weeks. Thus, a full three-dimensional investigation would require massive parallelization, likely requiring several orders of magnitude more CPUs than the two-dimensional simulations conducted here. Despite this drawback, the solution methodology is a realizable alternative to DNS. If the solution framework is applied to the appropriate laboratory-scale problem, it can give well resolved solutions within a reasonable time frame. Finally, it should be noted that the CLEM-LES strategy is not limited to examining solely the roles of turbulence on such problems investigated here. With appropriate model calibration, any model parameter may be altered to gain physical insight on their effect while accounting for, and resolving, the turbulent-scales of the problem.

7.3 Contributions to Original Knowledge

The major contribution of the current work was to provide adequate closure of the reaction rate term, $\overline{\dot{\omega}}$, in Eq.(3.6) for modelling and understanding turbulent fast-flame and detonation behaviour. This has been achieved through adaption of the LEM-LES strategy to account for the effect of rapid pressure changes on the energy field of the subgrid domains in each supergrid cell. This adaption allows for correct ignition delays of hot spots, on the subgrid, to be accounted for in the presence of shock waves and strong expansions, which occur on the supergrid. The CLEM-LES strategy itself is to model the subgrid scales as one-dimensional samples of the local flow field with appropriate subgrid-supergrid coupling between pressure and energy evolution on both scales. Details of the CLEM-LES modelling approach have been presented in Chapter 3. This work has allowed for highly compressible and reactive problems to be solved via LES, without the need to assume a specific combustion regime.

In terms of contribution to original knowledge relating to irregular detonation propagation theory, the current work has supported previous postulation that turbulence gives rise to a large variation of shock-induced ignition delays, for unburned fuel passing through the wave structure [27]. This variation of ignition delays, manifested through a variation of local shock speeds, thus gives rise to the formation of unburned pockets in the wake of the detonation. In the current work, however, the role of turbulence intensity on the resulting cellular flow patterns, structure thickness, and irregularity were clarified. All of these qualitative features were found to be significantly altered by the degree of turbulence intensity present. For fast-flame propagation, recent work [62] has suggested that turbulent mixing was responsible for the rapid combustion observed behind a Mach shock which forms following a shock reflection process behind an obstacle. The current work has extended this knowledge by demonstrating conditions under which successful DDT occurs.

7.4 Recommendations

In light of the recent advancement of the LEM-LES strategy, its proven advantages, and potential applications, there remains many improvements to be made and aspects of the model performance to further investigate. The recommendations proposed here are to further advance the application of the CLEM-LES modelling strategy and to improve efficiency.

First, in terms of modelling performance, a major limitation of the CLEM-LES strategy remains the difficulty associated with diffusion of subgrid elements on supergrid boundaries to subgrid elements in neighbouring supergrid cells. Currently, diffusion of subgrid elements across supergrid cells has not been implemented; attempts at doing so have proven unsatisfactory. Thus the modelling strategy requires sufficient fluid motion, and thus convection of subgrid elements to neighbouring supergrid cells, in order to ensure flame propagation beyond a single supergrid cell. While this may not be problematic for the scenarios presented in this work, it may be problematic

for modelling flame propagation near walls. To date, this feature has not been implemented in LEM-LES strategies [97–100] and thus remains an open problem for future improvement.

Another fundamental improvement required for the strategy is to improve the advection procedure of subgrid elements to neighbouring supergrid cells. Currently the procedure, outlined in Section 3.2.5, is reported to lead to artificial spurious diffusion errors [119]. Another improvement to the LES strategy would be to implement better filter size control, as various sources propose that discontinuous errors can be reduced at fine-coarse grid interfaces in AMR-LES implementations. This would be achieved by maintaining a filter size $\bar{\Delta} \geq 4b$ [144]. The effect of maintaining a larger filter size compared to the minimum supergrid size on observed detonation and fast-flame behaviour has not yet been investigated in the LES strategy presented here. Furthermore, dynamic procedures to obtain the tuning constant C_κ could be explored as another improvement to the strategy, as is done in many other LES implementations [146, 147]. However, the reader should be cautioned that it is unclear if such dynamic approaches are appropriate for highly compressible flows. Finally, the subgrid formulation itself could be further improved by implementing compressibility to the subgrid itself. In this sense, a recent investigation has been exploring the possibility of combining subgrid stirring with a fully compressible 1D domain, in the context of *One-Dimensional Turbulence* (ODT) [200]. This particular application has been suitable for simulating the turbulent shock-flame interaction problem solely in a 1D configuration. To date this implementation has not yet been coupled with LES applications.

Finally, in terms of investigation on the role of turbulent mixing itself on highly compressible combustion, it remains an open question why the optimum C_κ value to match experiments is higher than theory predicts. It is possible that the two-dimensional nature of the simulations generates more back-scatter, resulting in less subgrid kinetic energy generated. Furthermore, the compressible nature of the phenomena investigated likely generates back-scatter through amplification of pressure

waves that originate from turbulent fluctuations on the small scales, which thus feed into larger low-frequency fluid motions [22]. As such, compressible problems may inherently require a higher C_κ value. After all, theory and confirming experiments [150] predict or find C_κ for flow regimes assumed in the incompressible and isotropic limit according to Kolmogorov's theory [149]. Furthermore, the current numerical simulations could be extended to 3D in order to determine whether a lower C_κ value matches the experiments, and to determine how much of an effect compressibility has on C_κ.

APPENDICES

Appendix A

CLEM-LES Flowcharts

This appendix provides the flowcharts that correspond to the CLEM-LES procedure, as detailed in Chapter 3. First, Appendix A.1 shows the flowchart for the overall CLEM-LES procedure, across one global time step on the supergrid, as detailed step-by-step in Section 3.3.3. Appendix A.2 contains the flowchart for the CLEM simulation, a sub-step of the overall procedure shown in Appendix A.1. Appendix A.3 shows the flowchart relevant to the re-gridding procedure described in Section 3.2.6, a sub-step of the CLEM simulation shown in Appendix A.2. Finally, Appendix A.4 shows the splicing procedure described in Section 3.2.5, also a sub-step of the overall CLEM-LES procedure shown in Appendix A.1.

A.1 CLEM-LES Procedure

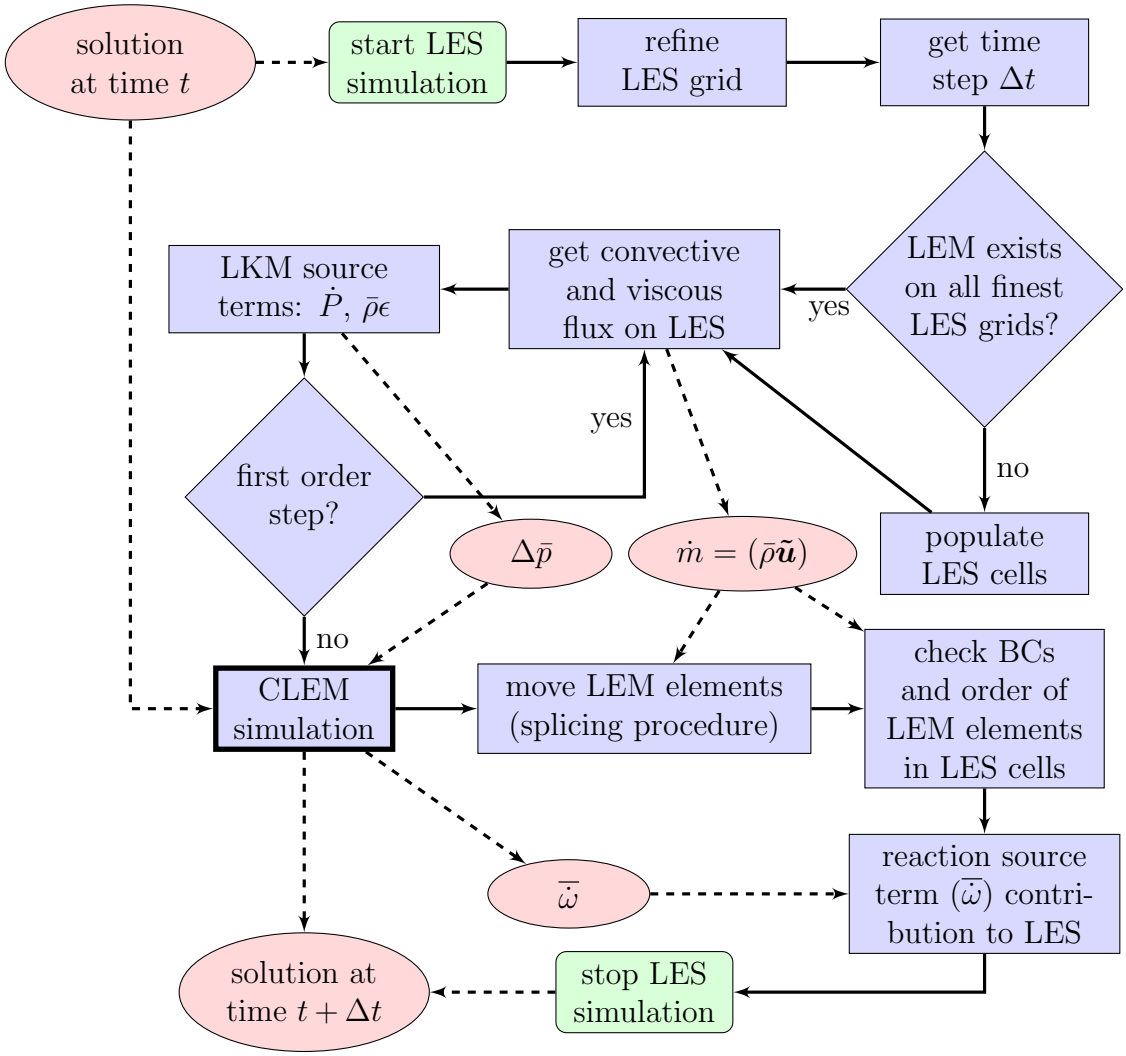

Figure A.1: Flowchart showing the overall CLEM-LES procedure, across one global time step on the supergrid, as detailed step-by-step in Section 3.3.3.

A.2 CLEM Simulation

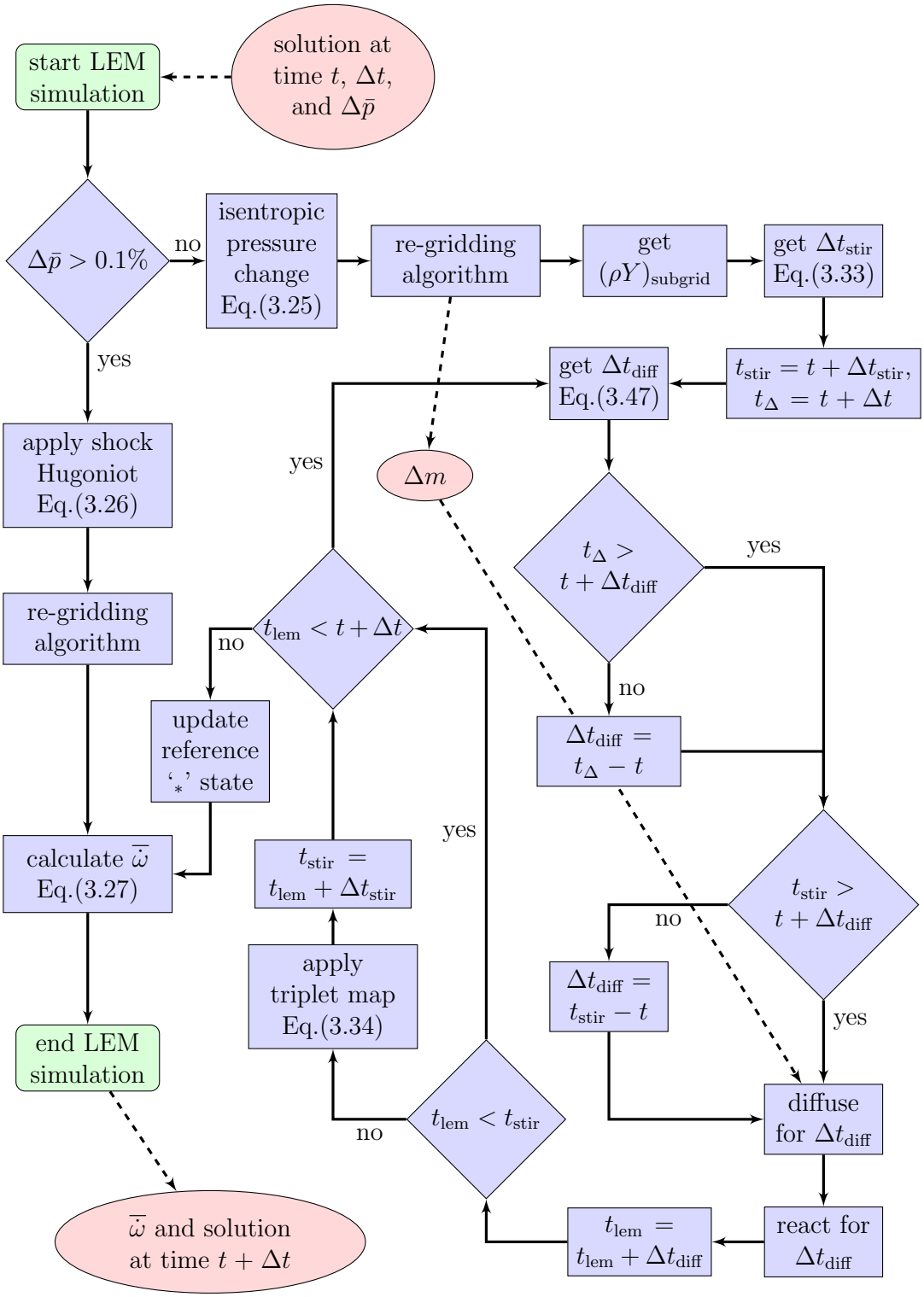

Figure A.2: Flowchart for the CLEM simulation.

A.3 Re-gridding Algorithm

Let N be number of LEM elements with index i before re-gridding
Let M be number of LEM elements with index j after re-gridding
Let V represent the 1-D volume of an LEM element

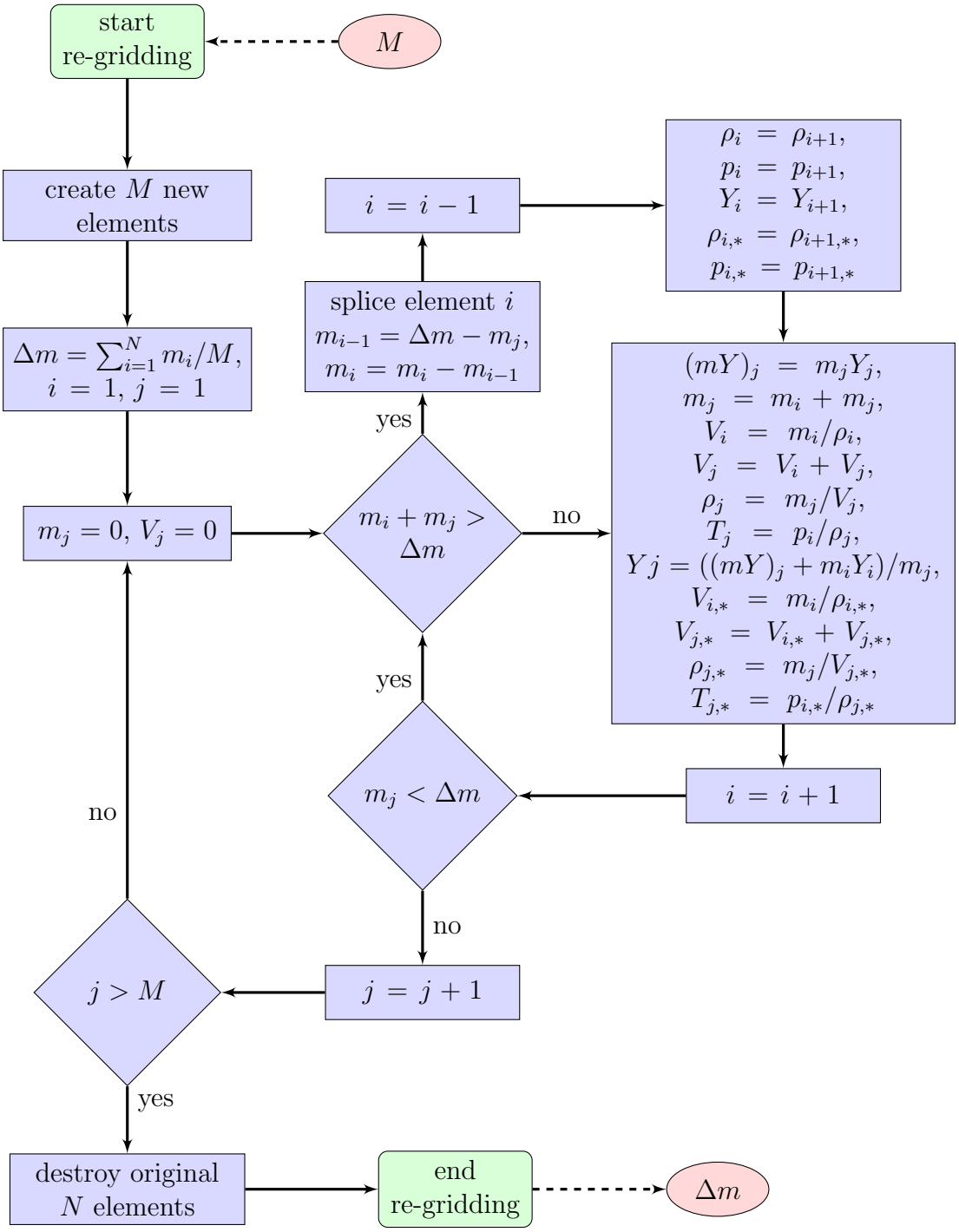

Figure A.3: Flowchart showing the re-gridding procedure described in Section 3.2.6.

A.4 Splicing Procedure

Let N be number of LES cell faces with index i
Let M be number of LEM elements with index j
Let Δm_i represent the amount of 1D 'mass' moved from face i

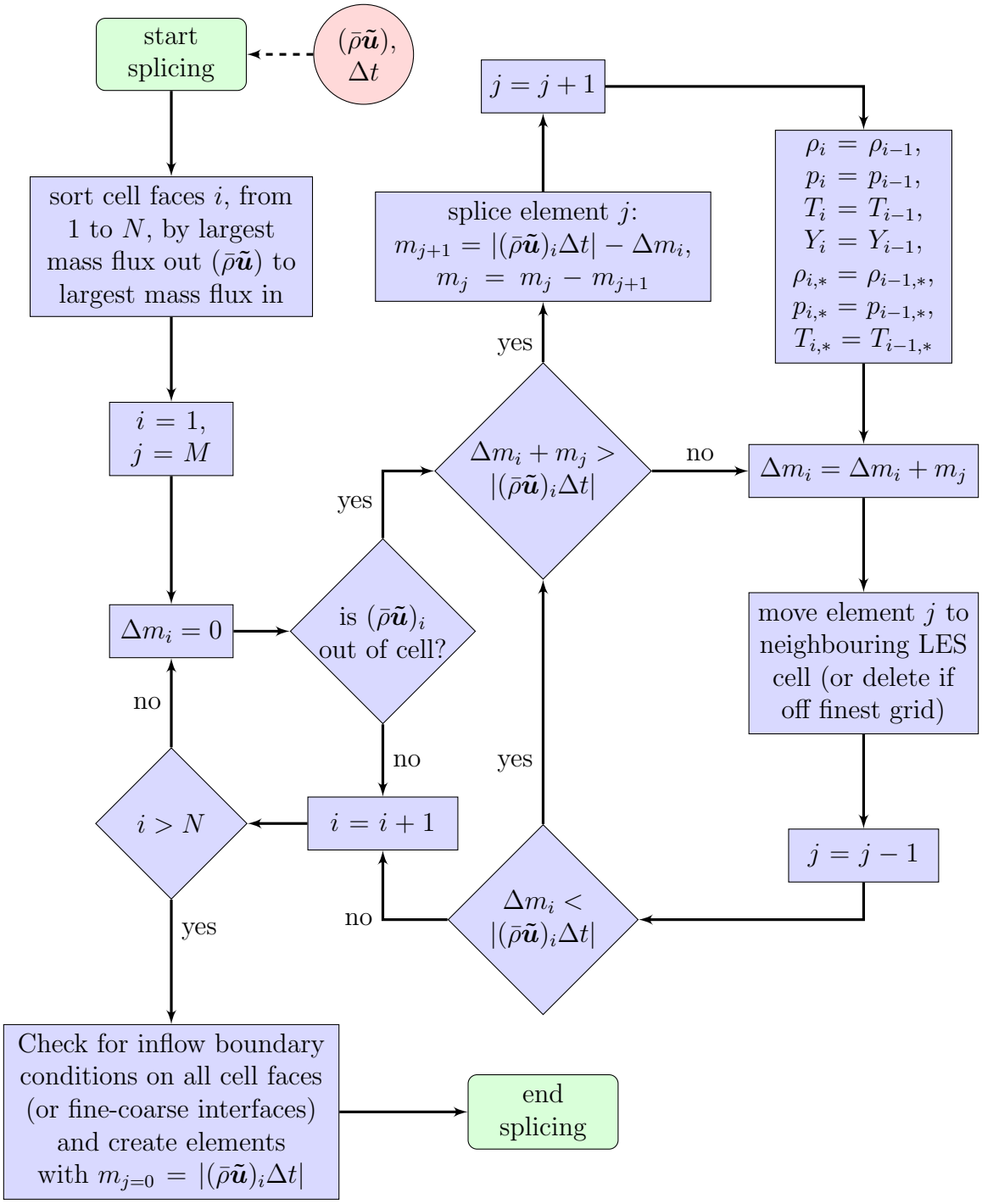

Figure A.4: Flowchart for the splicing procedure described in Section 3.2.5.

Appendix B

Determination of Model Parameters

B.1 Procedure

Below is a summary of the procedure used to determine the model constants listed in Tables 5.1 and 6.1 for methane combustion. First, various software packages [193, 201, 202] and kinetic mechanisms [194] are used to determine dimensional properties of the fuel-oxygen mixture, such as detonation velocity, half-reaction length, flame speed, activation energy, global heat release, and transport properties. These properties are then used to calibrate the non-dimensional one-step model, in Section 2.1.3, such that the detonation speed, half-reaction length, and flamespeed are matched accordingly. The formal procedure is as follows:

1. Use Cantera libraries [193] and the SD Toolbox [201] to get the CJ, 70% CJ, and VN states given the unburned composition of the gas mixture, initial pressure ($\hat{p}_o$), and initial temperature ($\hat{T}_o$). The CJ detonation velocity M_{CJ} is also determined using the SD Toolbox. For methane-combustion, the GRI-3.0 kinetic mechanism is used [194].

2. Obtain γ, transport properties, and total heat release ($\hat{Q}$). For the ratio of specific heats, γ is taken at the VN-state since the region of interest, where combustion occurs, is behind the shock. The transport properties ($\hat{\nu}$, L_e, P_r, and S_c) are also obtained at the VN-state. Then, given the detonation velocity, M_{CJ}, and γ, the total heat release can be obtained through the perfect gas expression, as derived in [16]:

$$\hat{Q} = \frac{\hat{c}_o^2}{2(\gamma^2 - 1)}\left(M_{CJ} - \frac{1}{M_{CJ}}\right). \tag{B.1}$$

3. Use the SD Toolbox ZND solver [202] to get the half reaction length, $\hat{\lambda}_{1/2}$. Specifically, this distance is taken as the distance from the shock to where the maximum temperature gradient occurs in the reaction zone. Example ZND temperature, density, pressure, and velocity profiles for stoichiometric methane-oxygen at $\hat{T}_o = 300$K and $\hat{p}_o = 3500$Pa using the GRI-3.0 mechanism [194] are shown below in Figure B.1.

4. Do constant volume ignition calculations using Cantera [193] at $\hat{T}_{VN} \pm 5\%$ to determine the global activation energy, $\hat{E}_a$, at the VN state. This is done by matching numerically obtained ignition times at $\hat{T}_{VN} \pm 5\%$ using the GRI-3.0 mechanism [194] with the analytical solution for ignition time associated with the one-step model obtained through high activation energy asymptotics [203]. Starting with the simplified governing equations in dimensional form, the system of Eqs.(2.18) to (2.21) for constant volume ignition can be reduced to to the system of ODEs:

$$\hat{\rho}\hat{c}_v\frac{d\hat{T}}{d\hat{t}} = -\hat{Q}\dot{\hat{\omega}} \tag{B.2}$$

$$\hat{\rho}\frac{dY}{d\hat{t}} = \dot{\hat{\omega}} = -\hat{\rho}\hat{A}Ye^{(-\hat{E}_a/\hat{R}\hat{T})}. \tag{B.3}$$

Following the approach of [203], the ignition delay ($\hat{t}_{ig}$) for a fuel mixture with initial temperature, $\hat{T}_o$, can be found to be

$$\hat{t}_{ig} \approx C\hat{T}_o^2 e^{(\hat{E}_a/\hat{R}\hat{T}_o)} \tag{B.4}$$

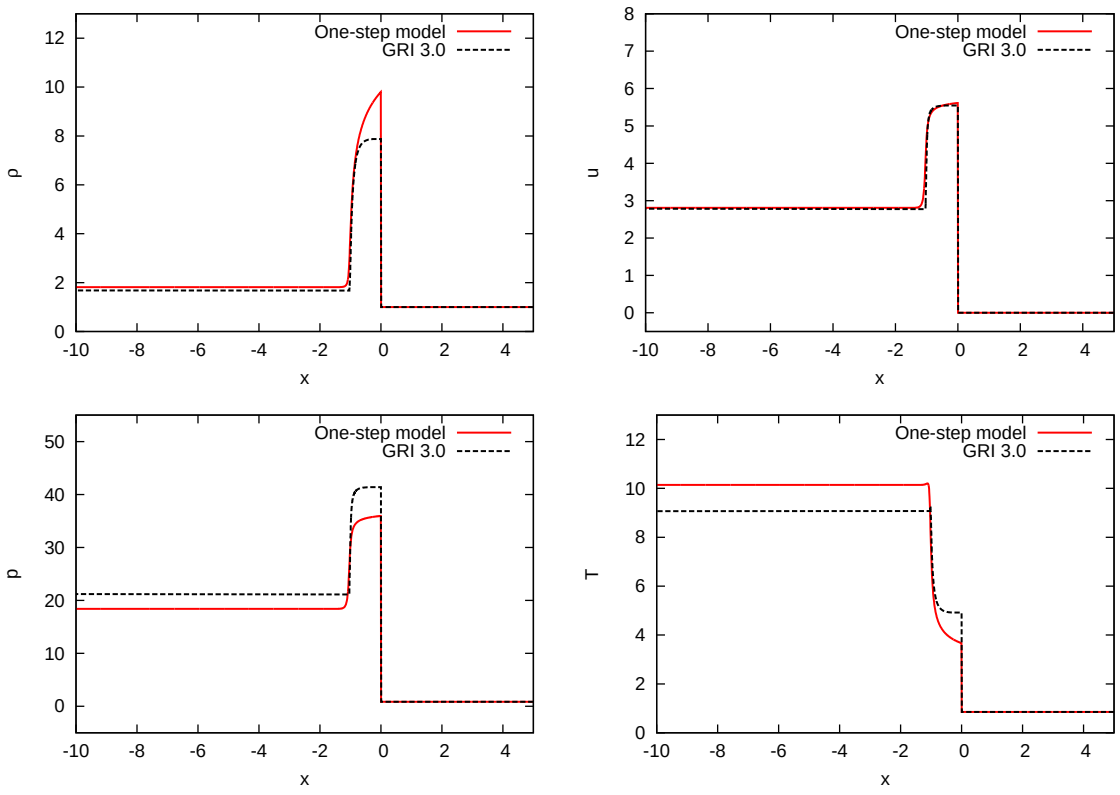

Figure B.1: ZND profiles computed for $CH_4 + 2O_2$ using the SD Toolbox ZND solver [202] and the GRI-3.0 mechanism [194], and also the One-step model (Eqs.(4.8) to (4.11)).

where C is a constant. Then, the activation energy, $\hat{E}_a$, can be determined by finding the ignition times at $\hat{T}_{VN} \pm 5\%$ and making use of Eq.(B.4). Then, since C is constant,

$$\frac{\hat{t}_{ig,+}}{\hat{t}_{ig,-}} = \frac{\hat{T}_{o,+}^2}{\hat{T}_{o,-}^2} \exp\left(\frac{\hat{E}_a}{\hat{R}\hat{T}_{o,+}} - \frac{\hat{E}_a}{\hat{R}\hat{T}_{o,-}}\right). \tag{B.5}$$

Then, solving for the activation energy yields

$$\hat{E}_a/\hat{R} = \frac{\ln\left(\hat{t}_{ig,+}/\hat{t}_{ig,-}\right) - \ln\left(\hat{T}_{o,+}^2/\hat{T}_{o,-}^2\right)}{1/\hat{T}_{o,+} - 1/\hat{T}_{o,-}}. \tag{B.6}$$

Finally, for $\ln\left(\hat{t}_{ig,+}/\hat{t}_{ig,-}\right) \gg \ln\left(\hat{T}_{o,+}^2/\hat{T}_{o,-}^2\right)$:

$$\hat{E}_a/\hat{R} \approx \frac{\ln\left(\hat{t}_{ig,+}\right) - \ln\left(\hat{t}_{ig,-}\right)}{1/\hat{T}_{o,+} - 1/\hat{T}_{o,-}}. \tag{B.7}$$

In fact, $\hat{E}_a/\hat{R}$ is simply the slope of a line which relates ignition time and temperature by taking the natural logarithm of Eq.(B.4). For example, this trend is shown for methane combustion in Figure B.2 where the quantity $\hat{t}_{ig}/\hat{T}_o^2$ is shown as a function of inverse temperature, $1/\hat{T}_o$, where $\hat{T}_o = \hat{T}_{vn} \pm 5\%$.

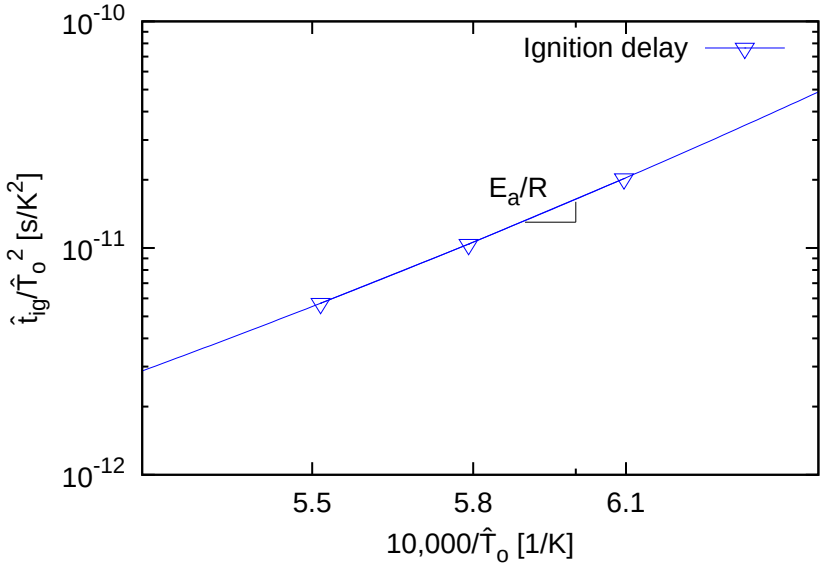

Figure B.2: Ignition delay times vs. inverse temperature for $CH_4 + 2O_2$ computed using the GRI-3.0 mechanism [194].

5. Acquire the flame speed at the 70% CJ state using a 1-D unsteady Lagrangian in-house code as described in Appendix C. The 70% CJ state is chosen since mixtures at the VN-state tend to auto-ignite before a steady-state flamespeed can be obtained. Also, the fast-flame in porous media and shock-flame interaction experiments often report wave speed deficits around 50 to 70% the CJ speed [55–58, 66], and is therefore a more appropriate estimate.

6. Non-dimensionalize the various parameters according to Section 2.1.3 and provide an initial guess for the pre-exponential factor A.

7. Solve for the ZND profile using the one-step model. Hence numerically integrate Eqs.(4.8) to (4.11).

8. Check if the half-reaction length ($\lambda_{1/2}$) is within 1% of that obtained in Step 3.

If not, provide a new guess for A and repeat step 7. The half-reaction length, $\lambda_{1/2}$, is determined from the shock location to where $Y = 0.5$. An example of a final acceptable ZND profile for methane combustion is shown in Figure B.1 and compared to the ZND profile obtained from the GRI-mechanism [194].

9. Solve the Eqs.(2.26) to (2.29) in 1D for a freely propagating flame (1D-NS simulation).

10. Check if the flamespeed S_L is within 1% of that obtained from Step 5. If not, scale the kinematic viscosity (ν) while holding L_e, P_r, and S_c constant and repeat step 9. An example of a final acceptable flamespeed for methane combustion through 1D-NS is shown in Figure B.3 and is compared to that obtained from the GRI-mechanism [194]. Also shown in the figure is the 1D-NS simulation conducted at several resolutions. The figure indicates grid independent results obtained at $b = \lambda_{1/2}/512$.

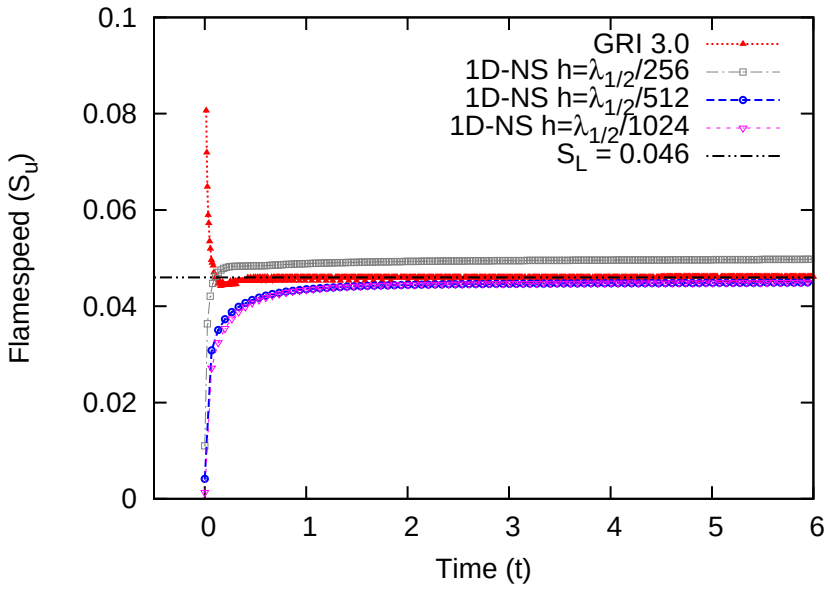

Figure B.3: Flame speeds computed for $CH_4 + 2O_2$ at the 70% CJ state using both the GRI-3.0 mechanism [194] and the 1D-NS strategy, which uses the One-step model.

B.2 Flow Chart

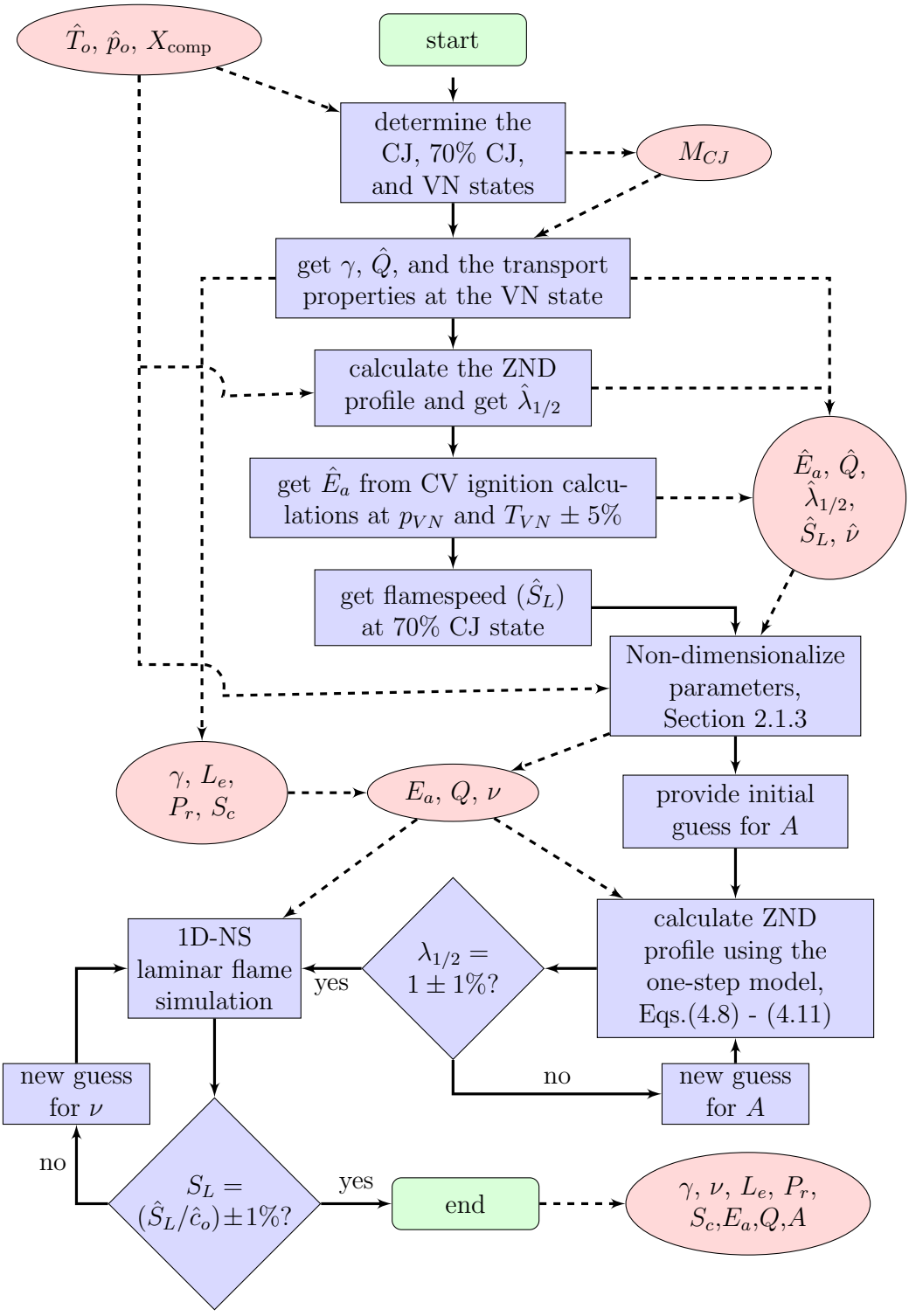

Figure B.4: Flowchart for the splicing procedure to determine model parameters.

Appendix C

uFlame: 1D Unsteady Lagrangian Flamespeed Simulator

C.1 Introduction

uFlame is a C++ program designed to simulate the *unsteady* evolution of a constant pressure flame using the Cantera 2.1 [193] libraries to incorporate detailed chemical kinetic mechanisms to compute realistic combustion rates and flame speeds across a wide range of fuel-air concentrations. The software also incorporates the Sundials [204] CVODE [205] libraries to compute large systems of stiff equations, necessary for the formulation presented below. The software is command-line driven, and thus scripted, through the UNIX shell interface. It is also parallelized using the OpenMP libraries [206]. Specific implementation and performance details can be found in [49]. This Appendix summarizes how the code is used to compute a stoichiometric methane-oxygen flame using the GRI-3.0 mechanism [194] as an example.

C.2 Governing Equations

The unsteady evolution of a flame is governed by the Navier-Stokes equations for a chemically reactive fluid augmented by the evolution of each chemical reactive species. In a fixed coordinate system, the conservation of total mass, mass of the ith species, momentum, and sensible enthalpy, as derived by Williams[103] respectively become:

$$\underbrace{\frac{D\hat{\rho}}{D\hat{t}}}_{\Delta \text{ total mass}} + \underbrace{\hat{\rho}\nabla\cdot\hat{\boldsymbol{u}}}_{\text{divergence of mass}} = 0 \tag{C.1}$$

$$\underbrace{\hat{\rho}\frac{DY_i}{D\hat{t}}}_{\Delta \text{ mass of specie } i} = \underbrace{\dot{\hat{\omega}}_i}_{\text{production rate}} - \underbrace{\nabla\cdot\hat{\rho}Y_i\hat{\boldsymbol{u}}_{d,i}}_{\text{diffusion}} \tag{C.2}$$

$$\underbrace{\hat{\rho}\frac{D\hat{\boldsymbol{u}}}{D\hat{t}}}_{\Delta \text{ momentum}} = \underbrace{-\nabla\hat{p}}_{\text{pressure gradients}} - \underbrace{\nabla\cdot\hat{\underline{\boldsymbol{\tau}}}}_{\text{shear stress}} + \underbrace{\sum_{i=1}^{N}\hat{\rho}_i\hat{\boldsymbol{f}}_i}_{\text{external forces}} \tag{C.3}$$

$$\begin{aligned}\underbrace{\hat{\rho}\hat{c}_p\frac{D\hat{T}}{D\hat{t}}}_{\Delta \text{ enthalpy}} = \underbrace{\frac{D\hat{p}}{D\hat{t}}}_{\Delta \text{ pressure}} &+ \underbrace{\nabla\cdot\hat{k}\nabla\hat{T} - \sum_{i=1}^{N}\hat{\rho}Y_i\hat{c}_{p,i}\hat{\boldsymbol{u}}_{d,i}\cdot\nabla\hat{T}}_{\text{diffusion}} - \underbrace{\sum_{i=1}^{N}\hat{h}_i^o\dot{\hat{\omega}}_i}_{\text{heat release}} - \underbrace{\nabla\cdot\boldsymbol{q}_{\text{rad}}}_{\text{radiation}} \\ &- \underbrace{\nabla\cdot R^o\hat{T}\sum_{i=1}^{N}\sum_{j=1}^{N}\frac{X_j\hat{D}_{T,i}}{\dot{\hat{\omega}}_i\hat{D}_{i,j}}(\hat{\boldsymbol{u}}_{d,i}-\hat{\boldsymbol{u}}_{d,j})}_{\text{Dufour effect}} + \underbrace{\phi}_{\text{dissipation}} + \underbrace{\sum_{i=1}^{N}\hat{\boldsymbol{u}}_{d,i}\cdot\hat{\rho}_i\hat{\boldsymbol{f}}_i}_{\text{external work}}\end{aligned} \tag{C.4}$$

C.3 The Simplified 1-D Model

To simplify the equations for freely propagating flames, the low-Mach number approximation [173] can be applied. In this approximation, for flows whose velocities are much slower than the speed of sound, pressure variations (gradients) are locally neglected near the flame surface, $\nabla p \approx 0$. In addition, unsteady pressure changes are also neglected. Thus, uFlame is designed to simulate constant pressure flame evolution. Further neglecting body forces, viscous dissipation and radiation transfer,

the resulting simplified system of equations to solve thus becomes:

$$\hat{\rho}\frac{DY_i}{D\hat{t}} = \dot{\hat{\omega}}_i - \frac{\partial(\hat{\rho}Y_i\hat{u}_{d,i})}{\partial\hat{x}} \tag{C.5}$$

$$\hat{\rho}\hat{c}_p\frac{D\hat{T}}{D\hat{t}} = \frac{\partial}{\partial\hat{x}}\left(\hat{k}\frac{\partial\hat{T}}{\partial\hat{x}}\right) - \sum_{i=1}^{N}\hat{\rho}Y_i\hat{c}_{p,i}\hat{u}_{d,i}\frac{\partial\hat{T}}{\partial\hat{x}} - \sum_{i=1}^{N}\hat{h}_i^o\dot{\hat{\omega}}_i. \tag{C.6}$$

In this form, the conservation evolution of each chemical specie and sensible enthalpy, along particle paths, has been decoupled from the conservation of momentum equation. Finally, the analysis can be further simplified if one uses a mass-weighted Lagrangian coordinate to follow the diffusion layer. This permits the elimination of the requirement of solving the continuity equation and the velocity field, since each mass element travels with its material velocity. The transformation follows the same approach as Rogg and Wang[207] where the Eulerian spatial coordinates are transformed into the mass-weighted Lagrangian coordinates, i.e.,

$$(\hat{x},\hat{t}) \rightarrow (\hat{m},\hat{t}). \tag{C.7}$$

In the transformation approach, the spatial coordinate, $\hat{x}$, is transformed into a mass-based coordinate, $\hat{m}$, by integrating the density from some reference coordinate, $\hat{x}_o$, to $\hat{x}$.

$$\hat{m}(\hat{x},\hat{t}) = \int_{\hat{x}_o}^{\hat{x}}\hat{\rho}(\hat{x},\hat{t})d\hat{x}. \tag{C.8}$$

Upon using this transformation and applying the assumptions described above, the conservation of mass of the ith specie and the conservation of energy respectively become:

$$\underbrace{\hat{\rho}\frac{\partial Y_i}{\partial\hat{t}}}_{\Delta\text{ mass of specie i}} = \underbrace{\dot{\hat{\omega}}_i}_{\text{production rate}} - \underbrace{\hat{\rho}\frac{\partial(\hat{\rho}Y_i\hat{u}_{d,i})}{\partial\hat{m}}}_{\text{diffusion}} \tag{C.9}$$

$$\underbrace{\hat{\rho}\hat{c}_p\frac{\partial\hat{T}}{\partial\hat{t}}}_{\Delta\text{ enthalpy}} = \underbrace{\hat{\rho}\frac{\partial}{\partial\hat{m}}\left(\hat{\rho}\hat{k}\frac{\partial\hat{T}}{\partial\hat{m}}\right) - \sum_{i=1}^{N}\hat{\rho}^2Y_i\hat{c}_{p,i}\hat{u}_{d,i}\frac{\partial\hat{T}}{\partial\hat{m}}}_{\text{diffusion}} - \underbrace{\sum_{i=1}^{N}\hat{h}_i^o\dot{\hat{\omega}}_i}_{\text{heat release}} \tag{C.10}$$

Note that partial derivatives with respect to time denote Lagrangian derivatives, i.e., keeping the mass coordinate constant. To solve the set of Eqs.(C.9)-(C.10) , an operator splitting technique [184] is applied, as detailed in Maxwell [49]. In this sense, the unsteady solution is first obtained for the inert *diffusion* terms across one time step. For this, the explicit Forward Euler method [185] is applied. Once the solution is updated, the production and heat release terms are solved across the same time step using the implicit Backward Euler method [185] which relies on Newton iteration.

C.4 Initial and Boundary Conditions

To initiate a flame, a hot-spot is specified in a reactive gas mixture and allowed to evolve temporally. The example reactive gas mixture is $CH_4 + 2O_2$ and is initialized at this composition everywhere ahead of the hot-spot. Also, the temperature and pressure are 1085.39K and 0.80atm in the unburned gas (i.e., the VN state). To determine the temperature and composition of the hot-spot, Cantera [193] is used to equilibrate the initial composition at constant enthalpy and pressure. The hot-spot is initially placed in 5% of the computational nodes, located from the right boundary. Thus the unsteady flame evolves from right to left. Also, to avoid computational difficulties associated with sharp gradients at startup, a smoothing function [208] is applied at the hot-spot surface, thus diffusing the temperature gradient across 6 computational cells. This initial profile is shown below in Figure C.1. Finally, the left boundary is kept fixed at the initial value while the right boundary has zero-gradients prescribed. Simulations are stopped before the flame reaches the left boundary.

C.5 Flame Evolution

To simulate the flame, 800 computational nodes are used, with a resolution of $\Delta m = 1.0 \times 10^{-6}\text{kg/m}^2$. At this resolution, the flame speed for this particular concentration

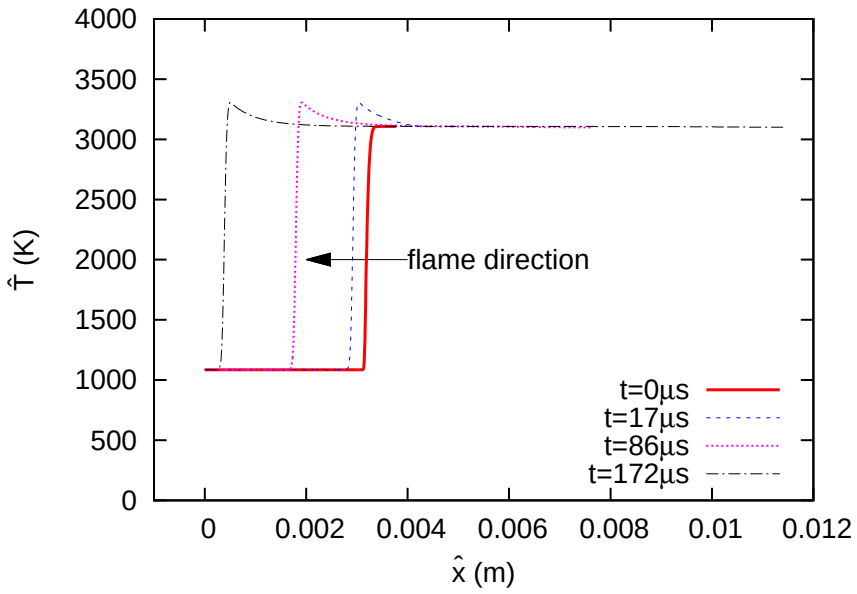

Figure C.1: Flame temperature profile evolution for CH_4+2O_2. The flame propagates to the left, while hot products expand to the right.

is converged, although different mixtures may require different resolutions. Also, the number of computational nodes must be sufficient to allow a steady flame speed to be developed. Figure C.1 shows the evolution of the flame temperature for 4 sequences until a steady profile is reaches. Figure C.2 shows the flame speed measured as a function of time for this mixture. The flame speed is measured directly by how much physical distance the flame travels as a function of time. The location of the flame is taken as the location where $\hat{T} > (\hat{T}_{VN} + 100)$K. The final steady state speed speed is taken as the average value over the last recorded 20 data points.

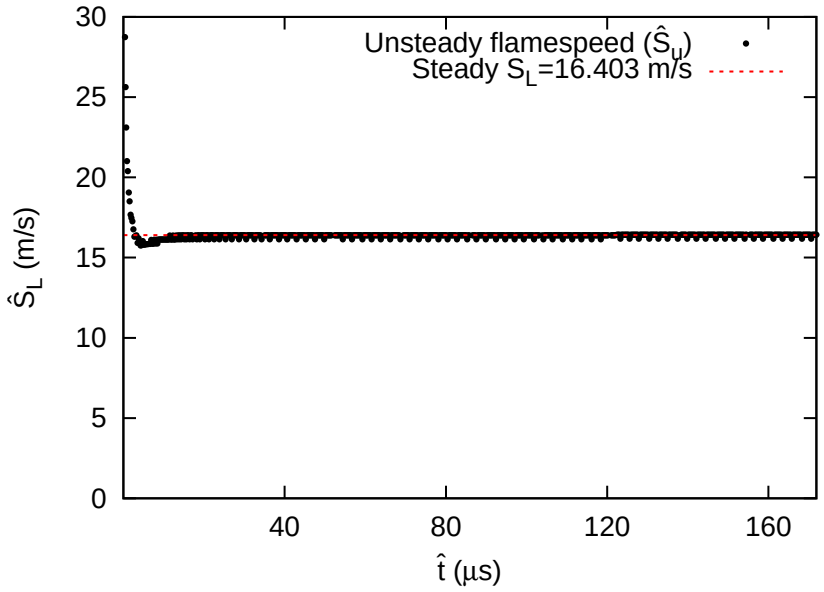

Figure C.2: Unsteady and steady flame speeds. The steady flame speed indicated is the average value over the last 20 data points.

Appendix D

Method for Computing Probability Density Functions

In order to evaluate the probability density functions presented in Section 5.4.4, the following procedure is applied. The procedure described here differs from a standard bin counting method, as velocity measurements may sometimes be collected experimentally at unequal time intervals. In particular, this was the case in Kiyanda and Higgins [15]. Thus, the procedure accounts for the amount of time a detonation wave spends at each velocity measurement in order to determine how probable a particular velocity is.

First consider a discreet set of velocities measurements:

$$\{D_1, D_2, ..., D_k, D_{k+1}, ..., D_{k+n}, ..., D_N\}.$$

Here, we are interested in computing the PDF(D) for a range of measurements, from D_k to D_{k+n} within the set. Suppose each measurement in the set has a corresponding time at which it was recorded. This set is then

$$\{t_1, t_2, ..., t_k, t_{k+1}, ..., t_{k+n}, ..., t_N\}.$$

The range of velocities to sample, for $n+1$ measurements, in order to compute the PDF is simply

$$\Delta D = D_{k+n} - D_k. \tag{D.1}$$

Then, the time spend by the detonation wave at the sample velocities is

$$t_{kn} = \sum_{i=k}^{k+n} t_i. \tag{D.2}$$

Next, the total time for all measurements is required. This is simply

$$t_N = \sum_{i=1}^{N} t_i. \tag{D.3}$$

The PDF can readily be determined since (t_{kn}/t_N) represents the fraction of time the wave spends in the interval ΔD. Thus

$$\mathrm{PDF}(\bar{D}) = \frac{(t_{kn}/t_N)}{\Delta D} \tag{D.4}$$

where $\bar{D}$ is the time-averaged velocity at which the PDF is evaluated for the interval:

$$\bar{D} = \frac{\sum_{i=k}^{k+n} D_i(t_{i+1} - t_i)}{t_{kn}}. \tag{D.5}$$

References

[1] Government of Japan, Report of Japanese Government to the IAEA Ministerial Conference on Nuclear Safety: The Accident at TEPCO's Fukushima Nuclear Power Stations, Tech. rep., Nuclear Emergency Response Headquarters (2011).

[2] Buncefield Major Incident Investigation Board, The Buncefield Incident 11 December 2005, Final Report Volumes 1 and 2, Buncefield Major Incident Investigation Board (2008).

[3] M. Johnson, The potential for vapour cloud explosions - lessons from the Buncefield accident, J. Loss Prevent. Proc. Ind. 23 (2010) 921–927.

[4] M. Ulutas, Soma mine disaster and the reality of privatization, Centre for Policy and Research on Turkey 3 (12) (2014) 15–23.

[5] J. Hsu, E. Duo, A. Poon, 1 August 2014, Deadly Gas-Pipeline Explosions Rock Taiwan, *The Wall Street Journal* (Accessed 2015).
URL `http://www.wsj.com/articles/gas-explosions-in-taiwan-kill-at-least-25-1406893177`

[6] Associated Press, 7 August 2013, Gas explosion destroys apartment block in Argentina, *The Guardian* (Accessed 2015).
URL `http://www.theguardian.com/world/2013/aug/07/gas-explosion-collapses-apartment-block`

[7] M. Johnson, Vapour Cloud Explosion at the IOC Terminal in Jaipur, 23rd Institution of Chemical Engineers Symposium on Hazards (Hazards XXIII), Southport, UK, 2012.

[8] W. A. Stewart, Sunrise propane blast, Crisis Response 5 (1) (2009) 18–19.

[9] L. Harding, 19 November 2007, More than 50 killed in Ukraine coal mine blast, *The Guardian* (Accessed 2015).
URL `http://www.theguardian.com/world/2007/nov/19/ukraine.international`

[10] D. M. Dawson, B. J. Brooks, The Esso Longford Gas Plant Accident: Report of the Longford Royal Commission, Tech. rep., Government Printer for the State of Victoria (1999).

[11] T. Poinsot, D. Veynante, Theoretical and Numerical Combustion, 2nd Edition, Edwards, 2005.

[12] N. Peters, Turbulent Combustion, Cambridge University Press, 2000.

[13] R. R. Bhattacharjee, Experimental investigation of detonation re-initiation mechanisms following a Mach reflection of a quenched detonation, Master's thesis, University of Ottawa, Ottawa, Canada (2013).

[14] R. R. Bhattacharjee, S. S. M. Lau-Chapdelaine, G. Maines, L. Maley, M. I. Radulescu, Detonation re-initiation mechanism following the Mach reflection of a quenched detonation, Proc. Combust. Inst. 34 (2013) 1893–1901.

[15] C. B. Kiyanda, A. J. Higgins, Photographic investigation into the mechanism of combustion in irregular detonation waves, Shock Waves 23 (2013) 115–130.

[16] W. Fickett, W. C. Davis, Detonation Theory and Experiment, Dover, 1979.

[17] R. Strehlow, The nature of transverse waves in detonations, Astronautica Acta 14 (1969) 539–548.

[18] M. I. Radulescu, The propagation and failure mechanism of gaseous detonations: experiments in porous-walled tubes, Ph.D. thesis, McGill University, Montreal, Canada (2003).

[19] J. M. Austin, The role of instability in gaseous detonation, Ph.D. thesis, California Institute of Technology, Pasadena, CA (2003).

[20] R. Strehlow, Gas phase detonations: Recent developments, Combust. Flame 12 (1968) 81–101.

[21] F. Pintgen, C. A. Eckett, J. M. Austin, J. E. Shepherd, Direct observations of reaction zone structure in propagating detonations, Combust. Flame 133 (2003) 211–229.

[22] M. I. Radulescu, G. J. Sharpe, J. H. S. Lee, C. B. Kiyanda, A. J. Higgins, R. K. Hanson, The ignition mechanism in irregular structure gaseous detonations, Proc. Combust. Inst. 30 (2005) 1859–1867.

[23] D. H. Edwards, A. T. Jones, The variation in strength of transverse shocks in detonation waves, J. Phys. D: Appl. Phys. 11 (1978) 155–166.

[24] V. A. Subbotin, Collision of transverse detonation waves, Combustion Explosion and Shock Waves 11(3) (1975) 411–414.

[25] V. N. Gamezo, A. A. Vasilev, A. M. Khokhlov, E. S. E S Oran, Fine cellular structures produced by marginal detonations, Proc. Combust. Inst. 28 (2000) 611–617.

[26] E. S. Oran, T. R. Young, J. P. Boris, J. M. Picone, A study of detonation structure: The formation of unreacted gas pockets, 19th Symp. (Int.) on Combustion, Haifa, Israel, 1982.

[27] M. I. Radulescu, G. J. Sharpe, C. K. Law, J. H. S. Lee, The hydrodynamic structure of unstable cellular detonations, J. Fluid Mech. 580 (2007) 31–81.

[28] G. S. Settles, Schlieren and Shadowgraph Techniques, Springer-Verlag, 2001.

[29] P. Mach, M. I. Radulescu, Mach reflection bifurcations as a mechanism of cell multiplication in gaseous detonations, Proc. Comb. Inst. 33 (2011) 2279–2285.

[30] V. N. Gamezo, D. Desbordes, E. S. Oran, Two-dimensional reactive flow dynamics in cellular detonation waves, Shock Waves 9 (1999) 11–17.

[31] G. J. Sharpe, Transverse waves in numerical simulations of cellular detonations, J. Fluid Mech. 447 (2001) 31–51.

[32] G. Cael, H. D. Ng, K. R. Bates, N. Nikiforakis, M. Short, Numerical simulation of detonation structures using a thermodynamically consistent and fully conservative reactive flow model for multi-component computations, Proc. R. Soc. Lond. A 465 (2009) 2135–2153.

[33] Y. Mahmoudi, N. Karimi, R. Deiterding, S. Emami, Hydrodynamic instabilities in gaseous detonations: comparison of Euler, Navier-Stokes, and large-eddy simulation, Journal of Propulsion and Power 30 No. 2 (2014) 384–396.

[34] J. L. Ziegler, R. Deiterding, J. E. Shepherd, D. I. Pullin, An adaptive high-order hybrid scheme for compressive, viscous flows with detailed chemistry, J. Comput. Phys. 230 (2011) 7598–7630.

[35] R. H. Kraichnan, Inertial ranges in two-dimensional turbulence, Phys. Fluids 10 (1967) 1417–1423.

[36] C. E. Leith, Diffusion approximation for two-dimensional turbulence, Phys. Fluids 11 (1968) 671–673.

[37] G. K. Batchelor, Computation of the energy spectrum in homogeneous two-dimensional turbulence, Phys. Fluids Suppl. II 12 (1969) 233–673.

[38] K. C. Gottiparthi, F. Genin, S. Srinivasan, S. Menon, Simulation of cellular detonation structures in ethylene-oxygen mixtures, in: 47th AIAA Aerospace Science Meeting and Exhibition, no. AIAA-2009-437, Orlando, Florida, 2009.

[39] M. I. Radulescu, B. M. Maxwell, The mechanism of detonation attenuation by a porous medium and its subsequent re-initiation, J. Fluid Mech. 667 (2011) 96–134.

[40] J. C. Chao, Critical deflagration waves that lead to the onset of detonation, Ph.D. thesis, McGill University, Montreal, Canada (2006).

[41] Y. J. Zhu, J. Chao, J. H. S. Lee, An experimental investigation of the propagation mechanism of critical deflagration waves that lead to the onset of detonation, Proc. Combust. Inst. 31 (2007) 2455–2462.

[42] G. A. Lyamin, V. V. Mitrofanov, A. V. Pinaev, V. A. Subbotin, Propagation of gas explosion in channels with uneven walls and in porous media, in: A. Borisov (Ed.), Dynamic Structure of Detonation in Gaseous and Dispersed Media, Vol. 153, kluwer, 1991, pp. 51–75.

[43] A. Teodorczyk, J. H. S. Lee, K. Knystautas, Propagation mechanism of quasi-detonations, 22nd Symp. (Int.) on Combustion, Pittsburg, PA, 1988.

[44] M. Arienti, J. E. Shepherd, A numerical study of detonation diffraction, J. Fluid Mech. 529 (2005) 117–146.

[45] C. A. Eckett, J. J. Quirk, J. E. Shepherd, The role of unsteadiness in direct initiation of gaseous detonations, J. Fluid Mech. 421 (2000) 147–183.

[46] M. I. Radulescu, B. M. Maxwell, Critical ignition in rapidly expanding self-similar flows, Phys. Fluids 22 No. 6.

[47] R. I. Soloukhin, Nonstationary phenomena in gaseous detonation, Proc. Combust. Inst. 12 (1969) 799.

[48] E. A. Lundstrom, A. K. Oppenheim, On the influence of non-steadiness on the thickness of the detonation wave, Proc. R. Soc. Lond. A 310 (1969) 463–478.

[49] B. M. Maxwell, M. I. Radulescu, Ignition limits of rapidly expanding diffusion layers: Application to unsteady hydrogen jets, Combustion and Flame 158 No. 10 (2011) 1946–1959.

[50] F. Pintgen, J. E. Shepherd, Detonation diffraction in gases, Combust. Flame 156 (2009) 665–667.

[51] B. Khasainov, H. N. Presles, D. Desbordes, P. Demontis, P. Vidal, Detonation diffraction from circular tubes to cones, Shock Waves 14 (2005) 187–192.

[52] R. Sorin, R. Zitoun, B. Khasainov, D. Desbordes, Detonation diffraction through different geometries, Shock Waves 19 (2009) 11–23.

[53] S. Ohyagi, T. Obara, S. Hoshi, P. Cai, T. Yoshihashi, Diffraction and re-initiation of detonations behind a backward-facing step, Shock Waves 12 (2002) 221–226.

[54] T. Obara, J. Sentanuhady, Y. Tsukada, S. Ohyagi, Re-initiation process of detonation wave behind a slit-plate, Shock Waves 18 (2008) 117–127.

[55] A. Makris, The propagation of gaseous detonations in porous media, Ph.D. thesis, McGill University, Montreal, Canada (1993).

[56] A. Makris, A. P. M. Kamel, J. Kilambi, R. Knystautas, J. H. S. Lee, Mechanisms of detonation propagation in a porous medium, in: A. L. Kuhl, J. C. Leyer, A. A. Borisov, W. A. Sirignano (Eds.), Dynamic Aspects of Detonation, American Institute of Aeronautics and Astronautics, 1993, pp. 363–380.

[57] A. Makris, H. Shafique, J. H. S. Lee, R. Knystautas, Influence of mixture sensitivity and pore-size on detonation velocities in porous-media, Shock Waves 5 (1995) 89–95.

[58] T. Slungaard, T. Engebretsen, O. K. Sonju, The influence of detonation cell size and regularity on the propagation of gaseous detonations in granular materials, Shock Waves 12 (2003) 301–308.

[59] C. Johansen, G. Ciccarelli, Modeling the initial flame acceleration in an obstructed channel using large eddy simulation, J. Loss Prevent. Proc. Ind. 26 (2013) 571–585.

[60] A. V. Gaathaug, K. Vaagsaether, D. Bjerketvedt, Experimental and numerical investigation of DDT in hydrogen-air behind a single obstacle, Int. J. Hydrogen Energy 37 (2012) 17606–17615.

[61] L. Maley, R. Bhattacharjee, S. S. M. Lau-Chapdelaine, M. I. Radulescu, Influence of hydrodynamic instabilities on the propagation mechanism of fast flames, Proc. Combust. Inst. 34 (2013) 645–651.

[62] L. Maley, On shock reflections in fast flames, Master's thesis, University of Ottawa, Ottawa, Canada (2015).

[63] G. Ciccarelli, S. Dorofeev, Flame acceleration and transition to detonation in ducts, Prog. Energy Combust. Sci. 34 (2008) 499–550.

[64] M. A. Liberman, M. F. Ivanov, A. D. Kiverin, M. S. Kuznetsov, A. A. Chukalovsky, T. V. Rakhimova, Deflagration-to-detonation transition in highly reactive combustible mixtures, Acta Astronautica 67 (2010) 688–701.

[65] H. D. Ng, J. Chao, Y. Ju, J. H. S. Lee, Combustion regimes subsequent to the reflection of a detonation from a perforated plate, Communications in Nonlinear Science and Numerical Simulation 13 (2008) 243–247.

[66] G. Thomas, R. Bambrey, C. Brown, Experimental observations of flame acceleration and transition to detonation following shock-flame interaction, Combust. Theor. Model. 5:4 (2001) 573–594.

[67] T. Scarinci, J. H. Lee, G. O. Thomas, R. Bambrey, D. H. Edwards, Amplification of a pressure wave by its passage through a flame front, in: A. L. Kuhl, J. C. Leyer, A. A. Borisov (Eds.), Dynamics of Heterogeneous Combustion and Reacting Sytems, Vol. 152 of Progress in Astronautics and Aeronautics, American Institute of Aeronautics and Astronautics, 1993, pp. 3–24.

[68] G. Thomas, A. Jones, Some observations of the jet initiation of detonation, Combust. Flame 120 (2000) 392–398.

[69] A. M. Khokhlov, E. S. Oran, G. O. Thomas, Numerical simulations of deflagration-to-detonation transition: The role of shock-flame interactions in turbulent flames, Combustion and Flame 117 (1999) 323–339.

[70] A. M. Khokhlov, E. S. Oran, Numerical simulations of detonation initiations, Combustion and Flame 119 (1999) 400–416.

[71] V. N. Gamezo, A. M. Khokhlov, E. S. Oran, The influence of shock bifurcations on shock-flame interactions and DDT, Combust. Flame 126 (2001) 1810–1826.

[72] S. Yu, S. Navarro-Martinez, Modelling of deflagration to detonation transition using flame thickening, Proc. Combust. Inst. 35 (2015) 1955–1961.

[73] N. C. Inc., BC Transit revolutionizes its services to welcome the 2010 winter olympics, Canadian Transit Forum 20 No. 2 (2010) 17–20.

[74] A. Vieira, H. Faria, R. Oliveira, N. Correia, A. T. Marques, H2 high pressure on-board storage considering safety issues, 2nd International Conference on Hydrogen Safety, San Sebastian, Spain, 2007.

[75] P. Wolanski, S. Wojcicki, Investigation into the mechanism of diffusion ignition of a combustible gas flowing into an oxidizing atmosphere, 14th Symp. (Int.) on Combustion, Pittsburg, PA, 1973.

[76] F. L. Dryer, M. Chaos, Z. Zhao, J. N. Stein, J. Y. Alpert, C. J. Homer, Spontaneous ignition of pressurized releases of hydrogen and natural gas into air, Combust. Sci. Tech. 179 (2007) 663–694.

[77] S. V. Golovastov, D. I. Baklanov, V. V. Volodin, V. V. Golub, K. V. Ivanov, An experimental study of the diffusion-controlled self-ignition of hydrogen in a channel, Russ. J. Phys. Chem. B 3 No. 3 (2009) 348–355.

[78] T. Mogi, Y. Wada, Y. Ogata, A. K. Hayashi, Self-ignition and flame propagation of high pressure hydrogen jet during sudden discharge from a pipe, Int. J. Hydrogen Energy 34 (2009) 5810–5816.

[79] P. Oleszczak, P. Wolanski, Ignition during hydrogen release from high pressure into the atmosphere, Shock Waves 20 (2010) 539–550.

[80] H. J. Lee, Y. R. Kim, S. H. Kim, I. S. Jeung, Experimental investigation on the self-ignition of pressurized hydrogen released by the failure of a rupture disk through tubes, Proc. Combust. Inst. 33 (2011) 2351–2358.

[81] J. Grune, K. Sempert, M. Kuznetsov, T. Jordan, Experimental study of ignited unsteady hydrogen releases from a high pressure reservoir, Int. J. Hydrogen Energy.

[82] A. Kessler, A. Schreiber, C. Wassmer, L. Deimling, S. Knapp, V. Weiser, K. Sachsenheimer, G. Langer, N. Eisenreich, Ignition of hydrogen jet fires from high pressure storage, Int. J. Hydrogen Energy 39 (2014) 20554–20559.

[83] T. Mogi, D. Kim, H. Shiina, S. Horiguchi, Self-ignition and explosion during discharge of high-pressure hydrogen, J. Loss Prevent. Proc. Ind. 21 (2008) 199–204.

[84] Y. F. Liu, F. N. Tsuboi, H. Sato, F. Higashino, A. K. Hayashi, Direct numerical simulation on hydrogen fuel jetting from high pressure tank, 20th Intl Colloquium on the Dynamics of Explosions and Reactive Systems, Montreal, Canada, 2005.

[85] Y. L. Liu, J. Y. Zheng, P. Xu, Y. Z. Zhao, H. Y. Bei, H. G. Chen, H. Dryver, Numerical simulation on the diffusion of hydrogen due to high pressure storage tanks failure, J. Loss Prevent. Proc. Ind. 22 (2009) 265–270.

[86] B. P. Xu, L. E. L. Hima, J. X. Wen, V. H. Y. Tam, Numerical study of spontaneous ignition of pressurized hydrogen release into air, Int. J. Hydrogen Energy 34 No. 14 (2009) 5954–5960.

[87] J. X. Wen, B. P. Xu, V. H. Y. Tam, Numerical study on spontaneous ignition of pressurized hydrogen release through a length of tube, Combust. Flame 156 (2009) 2173–2189.

[88] B. P. Xu, L. E. Hima, J. X. Wen, S. Dembele, V. H. Y. Tam, T. Donchev, Numerical study on the spontaneous ignition of pressurized hydrogen release through a tube into air, J. Loss Prevent. Proc. Ind. 21 (2008) 205–213.

[89] E. Yamada, S. Watanabe, A. K. Hayashi, N. Tsuboi, Mechanism of high-pressure hydrogen auto-ignition when spouting into air, Int. J. Hydrogen Energy 36 (2011) 2560–2566.

[90] B. J. Lee, I. Jeung, Numerical study of spontaneous ignition of pressurized hydrogen released by the failure of a rupture disk into a tube, Int. J. Hydrogen Energy 34 (2009) 8763–8769.

[91] M. V. Bragin, V. V. Molkov, Physics of spontaneous ignition of high-pressure hydrogen release and transition to jet fire, Int. J. Hydrogen Energy 36 (2011) 2589–2596.

[92] M. V. Bragin, D. V. Makarov, V. V. Molkov, Pressure limit of hydrogen spontaneous ignition in a T-shaped channel, 4th International Conference on Hydrogen Safety, San Francisco, USA, 2011.

[93] J. Grune, K. Sempert, M. Kuznetsov, T. Jordan, Experimental investigation of flame and pressure dynamics after spontaneous ignition in tube geometry, Int. J. Hydrogen Energy 39 (2014) 20396–20403.

[94] B. P. Xu, J. X. Wen, The effect of tube internal geometry on the propensity to spontaneous ignition in pressurized hydrogen release, Int. J. Hydrogen Energy 39 (2014) 20503–20508.

[95] N. Kitabayashi, Y. Wada, T. Mogi, T. Saburi, A. K. Hayashi, Experimental study on high pressure hydrogen jets coming out of tubes of 0.1-4.2 m in length, Int. J. Hydrogen Energy 38 (2013) 8100–8107.

[96] B. M. Maxwell, P. Tawagi, M. I. Radulescu, The role of instabilities on ignition of unsteady hydrogen jets flowing into an oxidizer, International Journal of Hydrogen Energy 38 (2013) 2908–2918.

[97] S. Menon, A. R. Kerstein, Turbulent Combustion Modeling: Advances, New Trends and Perspectives, Springer, 2011, Ch. 10: The Linear-Eddy Model, pp. 221–247.

[98] S. Menon, W. H. Calhoon, Subgrid mixing and molecular transport modeling in a reacting shear layer, 26th International Symposium on Combustion, Naples, Italy, 1996.

[99] V. K. Chakravarthy, S. Menon, Subgrid modeling of turbulent premixed flames in the flamelet regime, Flow, Turbulence and Combustion 65 (2000) 133–161.

[100] V. Sankaran, S. Menon, LES of scalar mixing in supersonic mixing layers, Proc. Combust. Inst. 30 (2005) 2835–2842.

[101] R. G. Abdel-Gayed, K. J. Al-Khishali, D. Bradley, Turbulent burning velocities and flame straining in explosions, Proceedings of the Royal Society of London A 391 (1984) 393.

[102] T. Smith, S. Menon, One-dimensional simulations of freely propagating turbulent premixed flames, Combustion Science and Technology 128 (1997) 99–130.

[103] F. A. Williams, Combustion Theory, 2nd Edition, Benjamin/Cummings Publishing Company Inc., Menlo Park, CA, 1985.

[104] R. W. Fox, P. J. Pritchard, A. T. McDonald, Introduction to Fluid Mechanics, 7th Edition, John Wiley and Sons, 2009.

[105] J. O. Hirschfelder, R. B. Bird, C. F. Curtis, Molecular Theory of Gases and Liquids, John Wiley, 1964.

[106] M. Short, J. J. Quirk, On the nonlinear stability and detonability limit of a detonation wave for a model three-step chain-branching reaction, J. Fluid Mech. 339 (1997) 89–119.

[107] D. A. Kessler, V. N. Gamezo, E. S. Oran, Multilevel detonation cell structures in methane-air mixtures, Proc. Combust. Inst. 33 (2011) 2211–2218.

[108] H. Ng, A. Higgins, C. Kiyanda, M. Radulescu, J. Lee, K. Bates, N. Nikiforakis, Nonlinear dynamics and chaos analysis of one-dimensional pulsating detonations, Combustion Theory and Modeling 9:1 (2005) 159–170.

[109] S. Lau-Chapdelaine, Numerical simulations of detonation re-initiation behind an obstacle, Master's thesis, University of Ottawa, Ottawa, Canada (2013).

[110] B. Borzou, B. Maxwell, M. I. Radulescu, Influence of the Reaction-to-Induction Length Ratio on the Stability of Cellular Detonations, 23rd Intl Colloquium on the Dynamics of Explosions and Reactive Systems, Irvine, CA, USA, 2011.

[111] C. Leung, M. I. Radulescu, G. J. Sharpe, Characteristics analysis of the one-dimensional pulsating dynamics of chain-branching detonations, Phys. Fluids 22: 126101 doi: 10.1063/1.3520188.

[112] S. Pope, Turbulent Flows, Cambridge University Press, 2000.

[113] R. Pecnik, V. E. Terrapon, F. Ham, G. Iaccarino, H. Pitsch, Reynolds-averaged Navier-Stokes simulations of the HyShot II scramjet, AIAA Journal 50 No. 8 (2012) 1717–1732.

[114] D. Muthusamy, O. R. Hansen, P. Middha, M. Royle, D. Willoughby, Modelling of hydrogen jet fires using CFD, 4th International Conference on Hydrogen Safety, San Francisco, USA, 2011.

[115] M. I. Radulescu, C. K. Law, The transient start of supersonic jets, J. Fluid Mech. 578 (2007) 331–369.

[116] R. Borghi, Recent Advances in the Aerospace Sciences, Plenum Press, 1985, Ch. 7: On the Structure and Morphology of Turbulent Premixed Flames, pp. 117–138.

[117] N. Peters, Laminar flamelet concepts in turbulent combustion, 21st Symp. (Int.) on Combustion, 1986.

[118] N. Peters, The turbulent burning velocity for large-scale and small-scale turbulence, J. Fluid Mech. 384 (1999) 107–132.

[119] V. Sankaran, Sub-grid combustion modeling for compressible two-phase reacting flows, Ph.D. thesis, School of Aerospace Engineering, Georgia Institute of Technology, Atlanta, Georgia (2003).

[120] T. Echekki, E. I. Mastorakos, Turbulent Combustion Modeling: Advances, New Trends and Perspectives, Springer, 2011.

[121] H. Pitsch, Large-eddy simulation of turbulent combustion, Annu. Rev. Fluid Mech. 38 (2006) 453–482.

[122] J. Janicka, A. Sadiki, Large eddy simulation of turbulent combustion systems, Proc. Combust. Inst. 30 (2005) 537–547.

[123] M. Berglund, C. Fureby, LES of supersonic combustion in a scramjet engine model, Proc. Combust. Inst. 31 (2007) 2497–2504.

[124] V. E. Terrapon, F. Ham, R. Pecnik, H. Pitsch, A flamelet-based model for supersonic combustion, Center for Turbulence Research Annual Research Briefs, 2009, pp. 47–58.

[125] X. Jianwen, L. Jialing, Application of flamelet model for the numerical simulation of turbulent combustion in SCRAMJET, International Conference on Methods of Aerophysical Research, Novosibirsk, Russia, 2008.

[126] M. Zbikowski, D. Makarov, V. Molkov, LES model of large scale hydrogen-air planar detonations: Verification by the znd theory, Int. J. Hydrogen Energy 33 (2008) 4884–4892.

[127] M. Zbikowski, D. Makarov, V. Molkov, Numerical simulations of large-scale detonation tests in the rut facility by the LES model, J. Hazard. Mater. 181 (2010) 949–956.

[128] C. Johansen, G. Ciccarelli, Numerical simulations of the flow field ahead of an accelerating flame in an obstructed channel, Combust. Theor. Model. 14 No. 2 (2010) 235–255.

[129] V. D. Sarli, A. D. Benedetto, G. Russo, S. Jarvis, E. J. Long, G. K. Hargrave, Large eddy simulation and PIV measurements of unsteady premixed flames accelerated by obstacles, Flow Turb. Combust. 83 No. 2 (2009) 227–250.

[130] A. R. Masri, S. S. Ibrahim, B. J. Cadwallader, Measurements and large eddy simulation of propagating premixed flames, Exp. Therm. Fluid Sci. 30 (2006) 687–702.

[131] C. Fureby, Large eddy simulation modelling of combustion for propulsion applications, Phil. Trans. R. Soc. A 367 (2009) 2957–2969.

[132] W. Breitung, C. Chan, S. Dorofeev, A. Eder, B. Gelfand, M. Heitsch, R. Klein, A. Malliakos, E. Shepherd, E. Studer, P. Thibault, Flame Acceleration and Deflagration-to-Detonation Transition in Nuclear Safety, OECD Nuclear Energy Agency, France, 2000.

[133] B. F. Magnussen, B. H. Hjertager, On mathematical models of turbulent combustion with special emphasis on soot formation and combustion, 16th Symp. (Int.) on Combustion, 1977.

[134] O. Colin, F. Ducros, D. Veynante, T. Poinsot, A thickened flame model for large eddy simulations of turbulent premixed combustion, Physics of Fluids 12 No. 7 (2000) 1843–1863.

[135] A. L. Kuhl, J. B. Bell, V. E. Beckner, K. Balakrishnan, Characterizing turbulent combustion fields in explosions, HPCMP Users Group Meeting, Portland OR LLNL-PROC-512235, Lawrence Livermore National Laboratory (2011).

[136] A. Aspden, N. Nikiforakis, S. Dalziel, J. B. Bell, Analysis of implicit LES methods, Comm. App. Math. and Comp. Sco. 3 No. 1 (2008) 103–126.

[137] A. Dauptain, B. Cuenot, T. J. Poinsot, Large Eddy Simulation of a supersonic hydrogen-air diffusion flame, Complex Effects in Large Eddy Simulation, Limassol, Cyprus, 2005.

[138] H. Koo, P. Donde, V. Raman, A quadrature-based LES/transported probability density function approach for modeling supersonic combustion, Proc. Combust. Inst. 33 (2011) 2203–2210.

[139] J. P. Drummond, P. M. Danehy, D. Bivolaru, R. L. Gaffney, S. A. Tedder, A. D. Cutler, Supersonic combustion research at NASA, Fall Technical Meeting Eastern States Section of the Combustion Institute, University of Virginia, 2007.

[140] J. F. Izard, A. Mura, Numerical Simulation of Supersonic Turbulent Combustion in a Scramjet Combustor Model, American Institute of Aeronautics and Astronautics, 2009.

[141] H. B. Wang, N. Q. N, M. B. Sun, H. Y. Wu, Z. G. Wang, A hybrid LES (Large Eddy Simulation)/assumed sub-grid PDF (Probability Density Function) model for supersonic turbulent combustion, Sci. China Tech. Sci. 54 (2011) 2694–2707.

[142] U. Schumann, Subgrid scale model for finite difference simulations of turbulent flows in plane channels and annuli, J. Comput. Phys. 18 (1975) 376–404.

[143] V. K. Chakravarthy, S. Menon, Linear eddy simulations of Reynolds number and Schmidt number effects on turbulent scalar mixing, Phys. Fluids 13 (2001) 488–499.

[144] S. B. Pope, Ten questions concerning the large-eddy simulation of turbulent flows, New Journal of Physics 6 (2004) 35.

[145] M. Vanella, U. Piomelli, E. Balaras, Effect of grid discontinuities on large-eddy simulation statistics and flow fields, Journal of Turbulence 9: 32 (2008) 1–23.

[146] G. D. Stefano, O. V. Vasilyev, D. E. Goldstein, Localized dynamic kinetic-energy-based models for stochastic coherent adaptive large eddy simulation, Physics of Fluids 20: 045102.

[147] W.-W. Kim, S. Menon, H. C. Mongia, Large-eddy simulation of a gas turbine combustor flow, Combustion Science and Technology 143:1-6 (1999) 25–62.

[148] D. K. Lilly, The representation of small-scale turbulence in numerical simulation experiments, NCAR Manuscript 281, National Center for Atmospheric Research (1966).

[149] U. Frisch, Turbulence: The Legacy of A. N. Kolmogorov, Cambridge University Press, 2000.

[150] J. R. Chasnov, Simulation of the Kolmogorov inertial subrange using an improved subgrid model, Phys. Fluids A 3 (1991) 188–200.

[151] T. von Karman, Progress in the statistical theory of turbulence, Proc. Natl. Acad. Sci. USA 34 No. 11 (1948) 530–539.

[152] Y. H. Pao, Structure of turbulent velocity and scalar fields at large wavenumbers, Phys. Fluids 8 (1965) 1063–1075.

[153] J. Meyers, M. Baelmans, Determination of subfilter energy in large-eddy simulations, Journal of Turbulence 5 (2004) 1–17.

[154] D. C. Leslie, G. L. Quarini, The application of turbulence theory to the formulation of subgrid modelling procedures, J. Fluid Mech. 91 (1979) 65–69.

[155] L. C. Berselli, T. Iliescu, W. J. Layton, Mathematics of Large Eddy Simulation of Turbulent Flows, Springer-Verlag, 2006.

[156] M. Lesieur, O. Metais, New trends in large-eddy simulations of turbulence, Ann. Rev. Fluid Mech. 28 (1996) 45–82.

[157] A. R. Kerstein, A linear-eddy model of turbulent scalar transport and mixing, Combust. Sci. Tech. 60 (1988) 391–421.

[158] A. R. Kerstein, Linear-eddy modeling of turbulent transport. II: Application to shear layer mixing, Combust. Flame 75 (1989) 397–413.

[159] A. R. Kerstein, Linear-eddy modeling of turbulent transport. Part 3: Mixing and differential molecular diffusion in round jets, J. Fluid Mech. 216 (1990) 411–435.

[160] A. R. Kerstein, Linear-eddy modeling of turbulent transport. Part 4: Structure of diffusion flames, Combust. Sci. Tech. 81 (1992) 75–96.

[161] A. R. Kerstein, Linear-eddy modeling of turbulent transport. Part V: Geometry of scalar interfaces, Phys. Fluids A 3 (1991) 1110–1114.

[162] A. R. Kerstein, Linear-eddy modeling of turbulent transport. Part 6: Microstructure of diffusive scalar mixing fields, Journal of Fluid Mechanics 231 (1991) 361–394.

[163] A. R. Kerstein, Linear-eddy modeling of turbulent transport. Part 7: Finite-rate chemistry and multi-stream mixing, J. Fluid Mech. 240 (1992) 289–313.

[164] P. A. McMurtry, S. Menon, A. R. Kerstein, A linear eddy sub-grid model for turbulent reacting flows: Application to hydrogen-air combustion, 24th Symp. (Int.) on Combustion, 1992.

[165] S. Menon, A. Patrick, A. McMurtry, A. R. Kerstein, Large Eddy Simulation of Complex Engineering and Geophysical Flows, Cambridge University Press, 1993, Ch. 14: A Linear-Eddy Mixing Model for Large Eddy Simulation of Turbulent Combustion, pp. 287–314.

[166] W. H. Calhoon, S. Menon, Subgrid modeling for reacting large eddy simulations, in: AIAA 34th Aerospace Sciences Meeting and Exhibition, no. 96-0516, Reno, NV, 1996.

[167] F. Mathey, J. P. Chollet, Subgrid-scale model of scalar mixing for large eddy simulations of turbulent flows, in: B. Galperin, S. A. Orszag (Eds.), Direct and Large-Eddy Simulation II, Kluwer Academic, 1997, pp. 103–114.

[168] I. Porumbel, Large eddy simulation of bluff body stabilized premixed and partially premixed combustion, Ph.D. thesis, School of Aerospace Engineering, Georgia Institute of Technology, Atlanta, Georgia (2006).

[169] S. Menon, P. A. McMurtry, A. R. Kerstein, J. Y. Chen, Prediction of NOx production in a turbulent hydrogen-air jet flame, Journal of Propulsion and Power 10 No. 2 (1994) 161–168.

[170] S. Menon, A. R. Kerstein, Stochastic simulations of the structure and propagation rate of turbulent premixed flames, 24th Symp. (Int.) on Combustion, 1992.

[171] T. Smith, S. Menon, Model simulations of freely propagating turbulent premixed flames, 26th Symp. (Int.) on Combustion, 1996.

[172] W. H. Calhoon, S. Menon, G. Goldin, Comparison of reduced and full chemical mechanisms for nonpremixed turbulent h2-air jet flames, Combust. Sci. Tech. 104 (1995) 115–141.

[173] S. Paolucci, On the filtering of sound from the Navier-Stokes equations, Tech. rep., Livermore, CA (1982).

[174] Y. B. Zeldovich, Y. U. Raizer, Physics of Shock Waves and High-Temperature Hydrodynamic Phenomena, Dover, 2002.

[175] J. Hinze, Turbulence, 2nd Edition, McGraw-Hill, 1975.

[176] J. H. Jeans, An Introduction to the Kinetic Theory of Gases, Cambridge University Press, 1940.

[177] D. Bradley, How fast can we burn?, 24th Symp. (Int.) on Combustion, 1992.

[178] S. Sannan, T. Weydahl, A. R. Kerstein, Stochastic simulation of scalar mixing capturing unsteadiness and small-scale structure based on mean-flow properties, Flow Turbulence Combust. 90 (2013) 189–216.

[179] S. A. E. G. Falle, Self-similar jets, Monthly Notices of the Royal Astronomical Society 250 (1991) 581–596.

[180] R. D. Richtmyer, K. W. Morton, Difference Methods for Initial-Value Problems, Interscience Publishers, New York, 1967.

[181] B. van Leer, Towards the ultimate conservative difference scheme iii. upstream-centered finite-difference schemes for ideal compressible flow, J. Comput. Phys. 23 (1977) 263–275.

[182] S. A. E. G. Falle, J. R. Giddings, Numerical Methods for Fluid Dynamics IV, Oxford University Press, 1993, Ch. Body capturing using adaptive cartesian grids, pp. 337–343.

[183] S. cannon, V. Adumitroaie, K. McDaniel, C. Smith, Les software for the design of low emission combustion systems for vision 21 plants, CFDRC Report No. 8321/2, CFD Research Corporation (2001).

[184] R. J. Leveque, Finite Volume Methods for Hyperbolic Problems, Cambridge University Press, New York, 2002.

[185] J. C. Tannehill, D. A. Anderson, R. H. Pletcher, Computational Fluid Mechanics and Heat Transfer, 2nd Edition, Series in computational and physical processes in mechanics and thermal sciences, 1997.

[186] S. M. Mitran, Adaptive mesh refinement computation of turbulent flows pitfalls and escapes, in: N. V. Pogorelov, E. Audit, P. Colella, G. P. Zank (Eds.), Numerical Modeling of Space Plasma Flows: ASTRONUM 2008, Vol. 406, ASP Conf. Series, 2009, pp. 249–254.

[187] D. A. Kessler, V. N. Gamezo, E. S. Oran, Simulations of flame acceleration and deflagration-to-detonation transitions in methane-air systems, Combust. Flame 157 (2010) 2063–2077.

[188] M. Short, G. J. Sharpe, Pulsating instability of detonations with a two-step chain-branching reaction model: theory and numerics, Combust. Theor. Model. 7(2) (2003) 401–416.

[189] S. Browne, Z. Liang, J. E. Shepherd, Detailed and Simplified Chemical Reaction Mechanisms for Detonation Simulation, Fall Technical Meeting Western States Section of the Combustion Institute, Stanford University, 2005.

[190] B. E. Launder, Second-moment closure and its use in modelling turbulent industrial flows, Int. J. Numer. Meth. Eng. 9 (1989) 963–985.

[191] D. P. Combest, P. A. Ramachandran, M. P. Dudukovic, On the gradient hypothesis and passive scalar transport in turbulent flows, Ind. Eng. Chem. Res. 50 (2011) 8817–8823.

[192] K. Hanjalic, B. Launder, Modelling Turbulence in Engineering and the Environment: Second-Moment Routes to Closure, Cambridge University Press, Cambridge, UK, 2011.

[193] D. G. Goodwin, Cantera (Accessed 2013).
URL `http://code.google.com/p/cantera/`

[194] G. P. Smith, D. M. Golden, M. Frenklach, N. W. Moriarty, B. E. Eiteneer, M. Goldenberg, C. T. Bowman, R. K. Hanson, S. Song, W. C. Gardiner, V. V. Lissianski, Z. Qin, Gri-mech 3.0 (Accessed 2013).
URL `http://www.me.berkeley.edu/gri_mech/`

[195] S. Srinivasan, S. Menon, Linear eddy mixing model studies of high karlovitz number turbulent premixed flames, Flow, Turbulence and Combustion 93 (2014) 189–219.

[196] M. Short, Theory and modeling of detonation wave stability: A brief look at the past and toward the future, 20th International Colloquium on the Dynamics of Explosions and Reactive Systems, Montreal, Canada, 2005.

[197] R. H. Kraichnan, Inertial-range transfer in two- and three-dimensional turbulence, J. Fluid Mech. 47 (1971) 525–535.

[198] S. D. Danilov, D. Gurarie, Quasi-two-dimensional turbulence, Physics-Upsekhi 43 no. 9 (2000) 863–900.

[199] B. M. Maxwell, S. A. E. G. Falle, G. Sharpe, M. I. Radulescu, A compressible-LEM turbulent combustion subgrid model for assessing gaseous explosion hazards, J. Loss Prevent. Proc. Ind. 36 (2015) 460470.

[200] Z. Jozefik, A. R. Kerstein, H. Schmidt, Simulation of shock-turbulent deflagration and detonation regimes using one-dimensional turbulence, Combust. Flame doi: 10.1016/j.combustflame.2015.10.035.

[201] S. Browne, J. Ziegler, J. E. Shepherd, Numerical solution methods for shock and detonation jump conditions, GALCIT Report FM2006.006, California Institute of Technology: Aeronautics and Mechanical Engineering (2008).

[202] S. Kao, J. E. Shepherd, Numerical solution methods for control volume explosions and ZND detonation structure, GALCIT Report FM2006.007, California Institute of Technology: Aeronautics and Mechanical Engineering (2008).

[203] J. D. Buckmaster, G. S. S. Ludford, Lectures on Mathematical Combustion, SIAM, 1983.

[204] A. C. Hindmarsh, P. N. Brown, K. E. Grant, S. L. Lee, D. E. Serban, D. E. Shumaker, C. S. Woodward, SUNDIALS: Suite of nonlinear and differential/algebraic equations solvers, ACM Transactions on Mathematical Software 31 no. 3 (2005) 363–396.

[205] S. D. Cohen, A. C. Hindmarsh, CVODE: A stiff/nonstiff ODE solver in C, Computers in Physics 10 no. 2 (1996) 138–143.

[206] OpenMP, Openmp.org (Accessed December 2014).
URL `http://openmp.org/wp/`

[207] B. Rogg, W. Wang, Run-1DL User Manual, Lehrstuhl fur Stromungsmechanik Institut fur Thermo-und Fluiddynamik, Ruhr-Universitat Bochum, D-44780 Bochum, Germany, 1995.

[208] R. Knikker, A. Dauptain, B. Cuenot, T. Poinsot, Comparison of computational methodologies for ignition of diffusion layers, Combust. Sci. Tech. 175 no. 10 (2003) 1783–1806.